Accuracy and stability analysis of finite-volume methods on unstructured spherical grids for shallow water oceanic models

by

Fabrício Rodrigues Lapolli
May 2023

A thesis submitted to the the Graduate Program of Applied Mathematics of the University of São Paulo in partial fulfilment of the requirements for the degree of Philosophy Doctor in Applied Mathematics

Advisor: Pedro da Silva Peixoto

During the development of this work the author received financial grants by the Brazilian Coordination for the Improvement of Higher Education Personnel (CAPES) PRINT project - Call no. 41/2017, Grant 88887.694523/2022-00, the São Paulo Research Foundation (FAPESP) Grant 2021/06176-0, and the Brazilian National Council for Scientific and Technological Development (CNPq), Grants 140455/2019-1 and 303436/2022-0.

Instituto de Matemática e Estatística

Accuracy and stability analysis of finite-volume methods on unstructured spherical grids for shallow water oceanic models

Fabrício Rodrigues Lapolli

Esta versão definitiva da tese contém as correções e alterações sugeridas pela Comissão Julgadora durante a defesa realizada por Fabrício Rodrigues Lapolli em 24/7/2023.

Comissão Julgadora:

- Prof. Dr. Pedro da Silva Peixoto - IME-USP
- Prof. Dr. Pedro Leite da Silva Dias - IAG-USP
- Prof. Dr. Ricardo Camargo - IAG-USP
- Dr. Peter Korn - MPIM
- Prof. Dr. Daniel Ruprecht - TUHH

To my family and friends

Acknowledgments

My heartfelt thanks to the reader of this document, and specially to the defence committee. Initially, I would like to acknowledge the help given through the financial support given by the Brazilian Coordination for the Improvement of Higher Education Personnel (CAPES) PRINT project - Call no. 41/2017, Grant 88887.694523/2022-00, the São Paulo Research Foundation (FAPESP) Grant 2021/06176-0, and the Brazilian National Council for Scientific and Technological Development (CNPq), Grants 140455/2019-1 and 303436/2022-0.

I would like to express my deep and sincere gratitudes towards my supervisor, Prof. Dr. Pedro Peixoto, for giving me the help and opportunity, whilst also providing guidance throughout my time in IME-USP. I also had the pleasure to work with my colleagues, Jeferson Brambatti Granjeiro, Luan da Fonseca Santos, which helped me throughout my doctorate. Special thanks to the late Prof. Dr. Saulo Barros, which was an invaluable professor for my career development. Furthermore, CNPq financial help was critical for the fruition of this work.

My sincere thanks also goes to Prof. Dr. Ilson Carlos Almeida da Silveira, and Prof. Dr. Paulo Calil, whose prior guidance shaped me during my masters and undergraduate. I appreciate my friends, Guilherme Antonio, Witor Ferraz, Leandro Patricio, Vadim Harlamov, who are sharing this journey with me with love and support. My family, in particular my brother and his family, Vinicius Rodrigues Lapolli, was also an important person for all the success in my life and I humbled and glad to have him as my family and my niece Eduarda Lapolli, which is the light shining in this world.

Finally, I am sincerely in debt to my love, caring, and supporting girlfriend 김보성 (Kim Bosung), who helped me a lot during rough times. It was an immense comfort to know she was there for me. She is one of the most important people in my life and I have nothing, but gratitude for everything.

Table of Contents

List of Tables

List of Figures

Resumo

Fabrício Rodrigues Lapolli. Accuracy and stability analysis of finite-volume methods on unstructured spherical grids for shallow water oceanic models. Tese. Instituto de Matemática e Estatística, Universidade de São Paulo, São Paulo, 2023.

Uma importante ferramenta ao nosso alcance para a avaliação da robustez dos Modelos de Circulação Globais (GCM) é a compreensão da discretização horizontal do core dinâmico sob o regime de aproximação de água rasa e seu uso nas grades respectivas. Nessa tese, a acurácia e a estabilidade de diferentes métodos usados, ou com uso adequado, em modelos oceânicos não estruturados considerando o regime de água rasa foram avaliadas. Esse trabalho uni os esforços feitos durante a qualificação apresentada em 2021 até o trabalho finalizado. Também junto a esse segue um artigo a submetido ao Journal of Ocean Modelling. Nesse trabalho foi avaliado os esquemas de grade A (NICAM), B (FeSOM 2.0) e esquemas de grade C: TRiSK nos triângulos, discretização horizontal de MPAS-O e de ICON. Duas grades foram utilizadas: uma grade padrão não-otimizada (MODSTD) e a Spherical Circumcentre Voronoi Tessellation (SCVT) do artigo submetido. Os presentes resultados mostraram que os esquemas possuem diferentes desempenhos em relação à acurácia, sendo os esquemas de grade A e B apresentando ao menos uma acurácia de ordem 1 nos operadores e na sua integração no tempo. Mesmo assim, o esquema de grade A mostrou-se suscetível às manifestações de oscilações numéricas na grade MODSTD, podendo elas contaminarem a grade e consequentemente prejudicar a solução. Enquanto isso, os esquemas de grade C mostraram, dependendo da grade utilizada, uma dificuldade em aproximar os operadores de água rasa. Além disso, a teoria de representação de ondas inércio-gravitacionais em grade regulares mostrou-se podendo ser extendida aos esquemas não-estruturados, onde se foi encontrado da menor para a maior representação os esquemas: A, B e C, respectivamente. Dos esquemas C, TRiSK nos triângulos mostrou ser o que mais se aproximava à forma contínua da solução, seguido por MPAS e ICON. Em relação à estabilidade, o esquema A mostrou possuir as propriedades mais estáveis. Entretanto, as oscilações desse esquema mostraram influenciar nessa estabilidade, i.e. enquanto MODSTD a estabilidade permanecia constante com a mudança de profundidade, seu uso na grade SCVT mostrou-se haver uma perda de estabilidade à medida que a altura equivalente era maior. Finalmente, em um esforço para compreender os efeitos das oscilações numéricas no modelo 3D ICON, simulações com e sem filtro biharmônico foram utilizados. Notamos que as oscilações presentes não foram suficientes para desestabilizar o modelo, mas elas foram responsáveis por prejudicar na dinâmica do modelo. Esse prejuízo foi identificado na perda da energia cinética das correntes. Além disso, uma perda na energia cinética turbulenta fora também observado, podendo ser parcialmente responsável pela perda de energia do sistema de correntes.

Palavras-chave: Modelo de água rasa, NICAM, FeSOM 2.0, MPAS-O, ICON-O, Instabilidade numérica

Abstract

Fabrício Rodrigues Lapolli. Accuracy and stability analysis of finite-volume methods on unstructured spherical grids for shallow water oceanic models. Thesis. Instituto de Matemática e Estatística, Universidade de São Paulo, São Paulo, 2023.

One important tool at our disposal to evaluate the robustness of Global Circulation Models (GCMs) is to understand the horizontal discretization of the dynamical core under a shallow water approximation and its respective grid. In this thesis, we evaluate the accuracy and stability of different methods used in, or adequate for, unstructured ocean models considering shallow water models. Our work draws a path from the early qualifying dissertation presented in 2021 and the finalized work along with a submitted paper. We evaluated A-(NICAM), B-grid (FeSOM 2.0), and C-grid schemes: one concerning the TRiSK discretization in triangles, the other on hexagons (MPAS) and the ICON horizontal discretization using a modified standard non optimized grid (MODSTD) and a Spherical Circumcentre Voronoi Tessellation (SCVT) grid. Our results show that the schemes have different accuracy capabilities, with the A- (NICAM) and B-grid (FeSOM 2.0) schemes providing at least 1st order accuracy in most operators and time integrated variables, while the C-grid (TRiSK, ICON and MPAS) schemes display more difficulty in adequately approximating the horizontal dynamics depending on the grid use. However, A-grid has shown to be susceptible to the manifestation of computational waves on the MODSTD grid that could contaminate and damage the solution. Moreover, the theory of the inertia-gravity wave representation on regular grids can be extended for our unstructured based schemes, where from least to most accurate we have: A-, B, and C-grid, respectively. Considering only C-grid schemes, TRiSK on triangles most accurately represent the inertia-gravity waves, followed by MPAS and ICON. In terms of stability, we see that the A-grid scheme displays the best stability properties. However, the scheme's stability has shown to be influenced by its grid, due to the manifestation of the spurious numerical waves. In contrast, both B-grid and ICON displayed the least stability of all schemes. Finally, in an effort to understand the effects of potential instabilities in ICON, we note that the full 3D model without a filtering term does not destabilize as it is integrated in time. However, the present spurious oscillations are responsible for decreasing the kinetic energy of the oceanic currents. Furthermore, an additional decrease of the currents' turbulent kinetic energy is also observed, which may play an important role in the weakness of the oceanic currents.

Keywords: Shallow water model, NICAM, FeSOM 2.0, MPAS-O, ICON-O, Numerical Instability

Chapter1

Introduction

The interest in weather and climate research has been growing rapidly due to the increased climate change, whose long-term effects are already been observed (e.g. Rignot and Thomas, 2002; Carton et al., 2005; Church and White, 2006), which may lead to irreversible changes in the climate. Additionally, drastic short term effects are becoming more frequent, which in turn may lead to severe consequences, such as material damages or a substantial loss of life. In light of this situation, there is an increasing demand to prioritize the minimization of the climate impact of current economic activities.

The importance of this field has been underscored by two recent recognitions. In 2018, in economics for a work that aimed to develop "an integrated assessment model, i.e. a quantitative model that describes the global interplay between the economy and the climate" (RSAS, 2018). Subsequently, in 2021, a second prize was awarded for the use of climate models as a way to quantify and predict global warming (RSAS, 2021).

These climate models are invaluable tools for understanding and projecting climate change. Despite there being some level of criticism for these tools, due to its level of uncertainty (Cowtan et al., 2015), they have been known to provide reliable results for the use in research and weather prediction (Hausfather et al., 2020). Thus, it is highly desirable to keep pushing the boundaries on this field and aim to improve these models.

Indeed, these efforts lead to our understanding being significantly expanded since the inception of climate models. Currently, are comprised of several components, such as atmospheric, ocean, ice, and land. The atmospheric and ocean components are subdivided into a physical core and a dynamical core. The physical core model incorporates parameterizations for factors such as the thermodynamical and dynamical impact of radiation, precipitation, cloud and ice processes, as well as unresolved sub-grid scale motion. On the other hand, the dynamical core model is responsible for solving the governing fluid and thermodynamic equations on resolved scales, which are typically larger than the cell size.

In the particular case of the dynamical core, the continuous governing equations of weather and climate models possess numerous physical properties, including mass conservation, energy conservation, potential vorticity conservation, and more. It is important for a dynamical core to contemplate these properties in order to provide reliable simulations. To further discuss the topic, we provide a background history on the development of these weather and climate models.

1.1 Modelling history

In 1950, the first successful numerical model was developed by Charney et al. (1950) on the ENIAC computer and utilized the barotropic vorticity equation, which are simplified

equations free of gravity waves. They incorporated a significant contribution by Courant et al. (1928) (republished in English in Courant et al. (1967)), in which was shown that the ratio between the time step and spatial resolution times the signal speed (or wind speed) is bounded above, in order for the model to remain stable. This criterion, known as CFL (Courant-Friedrichs-Lewys) criteria, remains fundamental today.

These early models were simplified and focused on the atmosphere. However, advances were also being made in the field of oceanic modelling. Significant advancements emerged for the general oceanic circulation theory through the seminal works of Sverdrup (Sverdrup, 1947), Stommel (Stommel, 1948), and Munk (Munk, 1950). Subsequent research also contributed to the understanding of the ocean vertical structure and its associated density driven circulation (Robinson and Stommel, 1959).

These developments helped the creation of the Bryan-Cox model (Bryan and Cox, 1967). Although their model was not the first oceanic model created (e.g. Bryan, 1963; Veronis, 1963), their tool was coupled with an atmospheric model, creating the first atmosphere-ocean coupled model (Manabe and Bryan, 1969).

Both ocean and atmospheric models at the time used a different positioning for their variables on a horizontal grid, but no consistent definition was made for these positioning, until Arakawa and Lamb (1977). They defined grids varying from A-E grids (Figure 1.1). Further research on these designs have shown that the C-grid was found to be the most accurate representation of inertia-gravity waves (e.g. Dukowicz, 1995; Konor and Randall, 2018a,b).

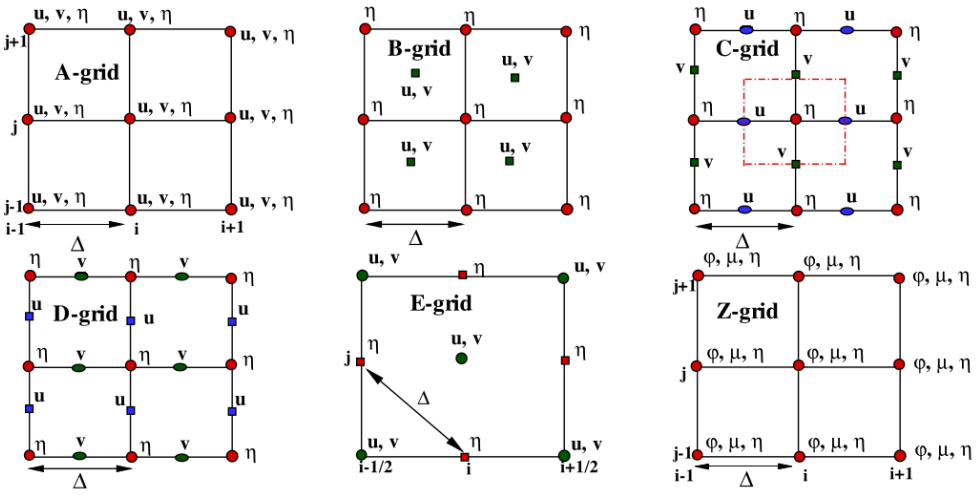

Figure 1.1: Different Arakawa grids. Source: Rajpoot et al. (2012)

Most ocean and atmospheric models so far used a finite difference approach for their models, but the use of spectral methods, i.e. methods based on the Fourier Transform, was popularizing among modellers. This method is far more accurate than the finite difference. However, this increased accuracy sacrificed computational cost. Despite this, the use of semi-lagrangian and semi-implicit methods allowed longer time steps, hence, diluting the overall cost of computation (Randall et al., 2018a).

Additionally, global grids of the finite difference method, presented a substantial issue, the accumulation of points on the poles. This grid is an orthogonal quadrilateral grid with a spatial step based on the longitude and latitude of the grid, thus the real distance of each point of this grid decreased latitudinally as it reaching the poles.

Because of these issues, researchers sought viable alternatives in hope to eliminate or minimize this problem, such as the overset composite grids (Phillips, 1957), cubed spheres (Sadourny, 1972), icosahedral grids (Williamson, 1968; Sadourny et al., 1968). All previously suggested alternatives. However, there were some problems that thwarted the use of these geometries at the time. One such problem was the computational limitation. Variables in lat-lon grids could be stored in large arrays for computation, which was not easily feasible in other geometries. Another issue was related to the grid optimization. Most of the alternative grids had an unstructured nature, and the distortion of the cells could concentrate errors at some points of the grid. Hence, the Spectral Method became almost unchallenged for many years. It is worth noting that some point accumulation also happened in the global grids of the spectral methods, however to a much less degree. Furthermore, a special grid was eventually devised for these methods that could avoid this singularity (Hortal and Simmons, 1991).

At the early dawn of the digital age, it was hypothesized that the computational power in a single CPU would double every couple of years. However, in the present day, we are witnessing signs of a slowdown in this trend (Schaller, 1997). As a result, this delay shifted the focus from developing computers of a single processor to multiple processors. For context, the Cray-1 was a revolutionary supercomputer of the 1970s, containing the vector processing system[1]. It contained a single CPU node of 80 MHz (Russell, 1978). On the other hand, in 2020, The Fugaku supercomputer was ranked first for the most powerful supercomputer with 158,976 CPU nodes of 2.2 GHz (Kodama et al., 2020).

Therefore, methods that are able to easily parallelize could benefit from these many nodes. However, the Spectral Method faces challenges in terms of inter-processor communication and does not readily benefit from parallelization, unlike gridpoint methods. Therefore, the previously popularized spectral method started being substituted back to the gridpoint method.

The previously utilized lat-lon grids were very useful, in that they had many properties that were beneficial for the dynamical core. Lat-lon grids, however, had some obstacles that prevented the optimization of the parallelization. As a result, alternative grids were sought as to circumnavigate these obstacles, but also to maintain many of the properties of the dynamical core. These properties, as mentioned by Staniforth and Thuburn (2012), are: conservation of mass, which is highly desirable for long range climate predictions, as to accurately describe some of the models tracers; accurate representation of balanced flows and its adjustment, in which several important atmospheric and ocean flow is in a state of quasi balanced/geostrophic state and dispersing inertia-gravity waves; absence or limitation of computational modes, discretization processes include some solutions in the equations that are non-physical, creating oscillations that are purely numerical, which may interact with the physical modes (through nonlinear terms), potentially causing unrealistic results; the ability to mimic basic geometrical or mathematical properties of the continuous equations,

[1] an implementation that allows for a CPU to operate efficiently with one-dimensional arrays.

including, for example, energy, vorticity, and enstrophy conserving properties.

Many grids were considered as potential candidates, such as the cubed sphere, Yin-Yang, Kite grids, etc (Staniforth and Thuburn, 2012). But one of the most popularized grids are the spherical geodesic dual icosahedron-dodecahedron derived grids. They are tessellated either by triangular cells or quasi-hexagonal (mix between pentagons and hexagons) cells. Their use is highlighted by their flexibility to distort around the sphere. Notable models that use these grids are: Tomita A-grid model (Tomita et al., 2001), used in NICAM; Danilov B-grid (Danilov et al., 2017), used in FESOM2.0; TRiSK C-grid (Thuburn et al., 2009; Ringler et al., 2010), used in MPAS and MPAS-O; and Korn C-grid (Korn and Linardakis, 2018), used in ICON-O (Korn, 2017).

NICAM A-grid, A-grid hereafter, is a developed atmospheric model used with a grid optimization on the triangular icosahedral grid. It contains a simple staggering design, but it provides an efficient and high accurate model. FeSOM 2.0 B-grid, B-grid hereafter, is an ocean model using, again, the triangular icosahedral mesh with a slightly different B-grid structure. It is slightly more complicated than the previous model, but it still is quite a flexible grid, and it avoids some issues present in the A-grid (Discussed in Chapter 3). TRiSK's C-grid, TRiSK hereafter, is a scheme used for both ocean and atmospheric component models. Both models use the quasi-hexagonal dual mesh of the icosahedron. The scheme is able to satisfy many important prerequisites for an ideal dynamical core. It is a very promising, but there still remains a few problems that needs to be addressed (Refer Chapter 3). Korn's C-grid scheme, ICON hereafter, solved some of these issues, by relying on some special operators in which he coined as admissible reconstructions Korn (2017). It is particularly advantageous for triangular grids. It is what used in the current oceanic component of ICON. We further discuss these schemes in Chapter 3.

These schemes, however, are prone to mesh distortion, which is known to impact the overall performance of the model (Peixoto, 2016). In addition, the operations resolved in the triangular tessellation allows for the manifestation of computational oscillations due to their inherent structure. These oscillations could irreversibly damage the model if not treated. Lastly, as we are achieving finer resolution with our technological advance, one important issue is with the model stability. The instability noted by Hollingsworth et al. (1983) is once again resurging (e.g. Gassmann, 2013; Bell et al., 2017; Peixoto et al., 2018; Gassmann, 2018), and is now an important point to consider for current models.

It is clear that the scientific community has not converged towards a single best choice of grid and scheme. The deeper understanding of these schemes is still a matter to be pursued, with many questions to be addressed. Of major importance are questions related to accuracy and stability of such schemes, as well as adequate representation of relevant ocean/atmospheric dynamics features.

1.2 Objective

We aim to present a general thorough comparison in accuracy and in stability between horizontal discretization methods used in global models relying on unstructured triangular icosahedral spherical grids. The schemes are the A-grid (Tomita et al., 2001), B-grid (Danilov et al., 2017), TRiSK-MPAS (Ringler et al., 2010), and ICON (Korn and Linardakis, 2018).

1.2.1 Specific Objectives

To achieve that, we aim to:

1. Analyse the properties of the triangular icosahedral grid and its dual Pentagonal/Hexagonal grid;

2. Investigate the accuracy of the operators involved in the solution of the nonlinear shallow water equations for all schemes;

3. Analyse the normal modes of the linear shallow water equations on the grids;

4. Analyse the near grid scale instabilities;

Of utmost importance, this work targets to shed more light on the problem of development of numerical methods for ocean models that rely on unstructured grids. Knowing the characteristics of existing schemes is a key step towards development of new methods and/or convergence of the scientific community to the most adequate numerical model formulation.

1.3 Organization

This thesis is organized as follows. In Chapter 2 we describe and analyse the triangular icosahedral grid. In Chapter 3 we present a description of the methods and an analysis of the shallow water operators' accuracies. In Chapter 4 we analyse the presence of the near grid scale instabilities.

In Chapter 5, we show the main results submitted to the Journal of Ocean Modelling. It incorporates some results from the previous chapters, but with some differences. The first difference is that the paper utilizes a different grid optimization than the ones previously used. This change is important, since many models today utilize some form of grid optimization (discussed in Chapter 2). Secondly, the scheme used in Chapter 3 uses the TRiSK scheme in the primal (triangular) grid, however, in Chapter 5 we utilized the scheme used in MPAS-O, i.e. we used the dual (quasi-hexagonal) grid. Finally, our work was done in collaboration with the Max-Planck Institute für Meteorology. Hence, we analysed the presence and effects of near grid numerical oscillations on the full 3D ICON-O.

Finally, in Chapter 6 we conclude our work. Here, we discuss the path undertaken throughout the PhD program and necessary steps towards more reliable and efficient models.

Chapter2

Icosahedral Grid Analysis

For many years, the main choice of grid was the lat-lon grid, i.e. a grid composed of quadrilateral tiles equispaced around the globe (Figure 2.1). This grid was capable of satisfying most of the ideal properties of a dynamical core. However, it suffered from some problems. The most notable is that it has a poleward clustering of cells, in which the grid size sharply decreases toward the pole, creating a singularity. This poleward increase of resolution would change the Rossby Radius of Deformation[1], proportionally, while in earth's dynamics this radius would not change so abruptly with latitude. Therefore, this change in radius could potentially generate numerical waves of different speeds not present on the real earth. More importantly, for explicit time integration methods (e.g. leapfrog, RK44), this singularity would heavily cap the time step at the poles, requiring a lot of computational power to simulate a rough resolution at the equator.

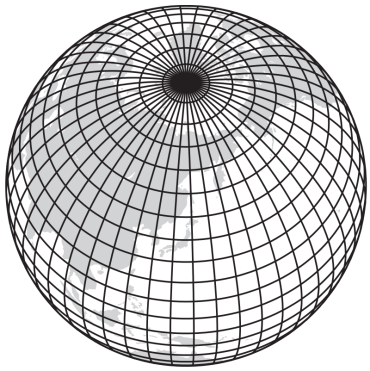

Figure 2.1: Illustration of lat-lon grid, obtained from Williamson (2007)

To avoid the problems of the lat-lon grid, it was necessary to find a mesh that could provide a regularity in the resolution throughout the surface of the sphere (Earth).

Geometrically, there are 9 regular polyhedra, i.e. a solid whose faces are identical in shape and size, and all angles equal. Out of these, however, only 5 are convex[2]: tetrahedron, hexahedron (cube), octahedron, icosahedron, and the dodecahedron. These are called the Platonic Solids (Figure 2.2).

Research has shown that, in general, solids with smaller faces will have a reduced distortion on the grid when transforming from the surface of the polyhedron to the surface of the sphere (White et al., 1998). Thus, making the icosahedron and dodecahedron providing the smallest distortion with the transformation. Hence, making them well suited for a basis solid for climate modelling.

[1] $R_d = c/(f_0 \Delta x)$ or $R_d = \sqrt{c/(2\beta)}$ at the equator, where β is from the β-plane.

[2] any set of two points inside the polyhedron will draw a line that would still be inside the polyhedron

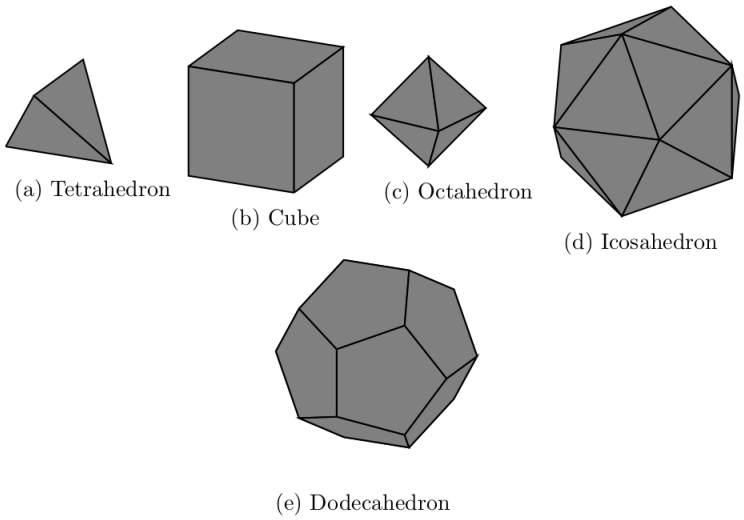

Figure 2.2: Platonic Solids

Regardless, these solids are too rough for practical use, the finest is the dodecahedron with around 4546 km of edge length. Hence, some subdivision of the faces must be performed in order to increase the grid's resolution.

In order to refine the solid to generate a viable grid, we subdivide the triangle through the midpoints of each edge. As illustrated in Figure 2.3, for each face, we connect the midpoints of the original grid, forming new inscribed triangles. The vertices of these new triangles are then projected onto the sphere and thus forming a new grid. We repeat this process enough times as needed until the desired resolution is achieved.

It should be noted that, on the plane, this process creates new equilateral triangles, thus maintaining the domain uniformity. On the sphere, however, when we project the points onto it, we create a distortion in the triangles (Figure 2.3.d). Any grid refining process of any solid on the sphere will produce a distortion of the mesh. Nonetheless, this refining process of the icosahedron has the smallest maximum-minimum length size ratio, of around 1.2 (Staniforth and Thuburn, 2012).

However, this standard way of refining a grid is not optimal and some optimization is desired as to either better distribute the distortion around the domain, or to increase the operators' accuracy. Tomita et al. (2001), for example, created a process that allowed the grid to be smoother by connecting the mesh points with "springs", hence the process was called Spring Dynamics. Heikes and Randall (1995b) created another optimization, moving the vertices of the grid in order to improve the accuracy of a discrete Laplacian operator. This method is now known as HR95. A rather popular optimization used is the Spherical Voronoi Tessellation (SCVT) which is used by many models. It aims to move the vertices of the grid, such that these vertices are the barycentric points of the dual mesh (Miura and Kimoto, 2005).

Regardless of optimization, all meshes have an associated figure known as a dual mesh. This is constructed by connecting the centre of the cells of the (primal) mesh. This concept of the dual grid is used in most numerical schemes. For example, NICAM model has its main variables defined on the centre of the dual mesh, while FESOM2.0, MPAS, and ICON-O

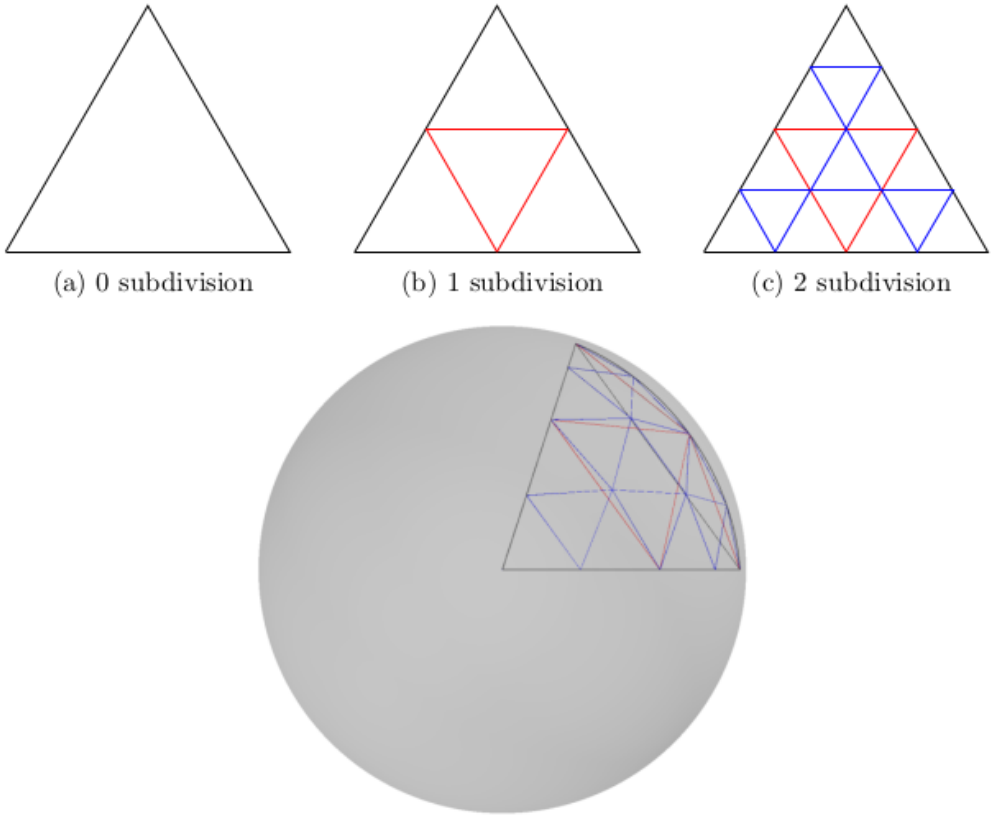

(a) 0 subdivision (b) 1 subdivision (c) 2 subdivision

(d) Sphere

Figure 2.3: Triangle subdivision

uses both primal and dual cells of the grids, in order to better achieve the accuracy of the operators without much interpolation. We note that these models consider different dual grids. Both NICAM and FESOM2.0 consider the dual cell connecting the barycentre of the primal mesh, while MPAS and ICON-O connect the circumcentres of the primal cells to obtain the dual cell. Another important remark is that the dual mesh of the triangular tilling, i.e. the quasi-hexagonal mesh, is the primal mesh for the MPAS model.

As previously stated, the use of these tessellations are highly beneficial for numerical schemes, as both have a degree of flexibility associated. The triangular grid, in particular, allows for the mesh to delineate sharp boundaries of the oceans, such basins, estuaries, coastal areas, inlets, and islands. In addition to that, the ocean presents a wide range of dynamical spectrum phenomena, with the high wavenumber dynamics occurring at the continental shelf and low wavenumber at the open ocean. This flexibility enables to refine areas of high/fast dynamics without needing to refine the whole domain. For these reasons, the triangular grid is quite popular among coastal ocean modelling, but uncommon for global modelling.

In this chapter, we will introduce the grid notation, which will be used throughout this dissertation. Our focus will ultimately be to evaluate the cell distortion of an icosahedral based grid. We will analyse an ensemble of parameters of the grid: area distribution, edge midpoint displacement, and grid distortion and alignment (concepts from Peixoto (2013)).

Our primal grid used will be triangular tiling derived from the icosahedral grid. For that, we will use an optimized algorithm known as Jigsaw Software (Engwirda, 2014).

2.1 Triangular Grid

2.1.1 Notation

In this section, it is important for us to define a few important points regarding the grid that will be used throughout the documentation. We will use a similar notation as Korn and Linardakis (2018).

Every vertex $\mathbf{v} \in \mathcal{V}$ is connected by edges $e \in \mathcal{E}$ to form a triangular cell $K \in \mathcal{C}$, where $\mathcal{V}$, $\mathcal{E}$, and $\mathcal{C}$ are the set of vertices, edges and triangular cells. The boundary of a cell K is denoted as ∂K and the boundary of an edge e is denoted by ∂e. These elements, when bold (e.g. $\mathbf{v}$, $\mathbf{e}$, $\mathbf{K}$) will denote the point on the sphere.

We will be representing the duality with a hat symbol $\widehat{(\cdot)}$. Therefore, generically, the dual grid cell will be represented by $\hat{K} \in \hat{\mathcal{C}}$, where $\hat{\mathcal{C}}$ is the set of dual cells on the sphere. For the purpose of this document, we will be dealing with a dual cell formed by either the barycentre or the circumcentre points of the neighbouring triangles. For each case, respectively, we shall also include the superscripts $(\cdot)^{(b)}$ and $(\cdot)^{(c)}$. Occasionally, we will omit these superscripts and let reader aware by the context.

The elements $v_1, v_2, \cdots, v_n \in \bigcup_{e\in\partial K} \partial e$ will be ordered in a counterclockwise rotation of their respective cell (the same ordering will be used in case of the dual cell). $v_1, v_2 \in \partial e$ or $\partial \hat{e}$ will be in an order, such that, the associated unit vector $\mathbf{t}_e$ along the edge, will be from v_1 to v_2. These unit vectors will be defined at the midpoint $\mathbf{e}$ of e. Furthermore, these tangent vectors will have an associated normal $\mathbf{n}_e$ with its direction perpendicular to $\mathbf{t}_e$, s.t. $\mathbf{n}_e \times \mathbf{t}_e = \mathbf{e}$. We also define control values associated with the direction of these vectors:

$$
\begin{aligned}
n_{e,K} &= -\text{sgn}\ \langle \mathbf{n}_e, \mathbf{K} - \mathbf{e} \rangle, \\
t_{e,v} &= -\text{sgn}\ \langle \mathbf{t}_e, \hat{\mathbf{K}}_v - \mathbf{e} \rangle.
\end{aligned}
$$

This implies that $n_{e,k}$ will be 1 if the $\mathbf{n}_e$ has a direction outwards of the cell K and -1 if it points inward.

Each edge e will have its length $|e|$ calculated as a distance on the unit sphere. In other words:

$$
|e| = d(\mathbf{v}_1, \mathbf{v}_2) = 2\sin^{-1}\frac{|\mathbf{v}_1 - \mathbf{v}_2|}{2} \quad \mathbf{v}_1, \mathbf{v}_2 \in \partial e \tag{2.1}
$$

A similar calculation will be performed for the edge length of $\hat{e}$.

Each cell K will have an area $|K|$, calculated as:

$$
|K| = A(\mathbf{v}_1, \mathbf{v}_2, \mathbf{v}_3) = 4\tan^{-1}\sqrt{\left|\tan\frac{s}{2}\tan\frac{s - d(\mathbf{v}_1, \mathbf{v}_2)}{2}\tan\frac{s - d(\mathbf{v}_2, \mathbf{v}_3)}{2}\tan\frac{s - d(\mathbf{v}_3, \mathbf{v}_1)}{2}\right|}, \tag{2.2}
$$

where v_1, v_2, v_3 are the vertices of the cell K and $s = 1/2[d(\mathbf{v}_1, \mathbf{v}_2) + d(\mathbf{v}_2, \mathbf{v}_3) + d(\mathbf{v}_3, \mathbf{v}_1)]$. For a dual cell $\hat{K}$ with reference vertex $v = \hat{\mathbf{k}}$, we will perform:

$$|\hat{K}| = \sum_{\hat{e} \in \partial \hat{K}} A(\mathbf{K}_1, \mathbf{K}_2, \hat{\mathbf{K}}). \qquad K_1, K_2 \in \partial \hat{e} \tag{2.3}$$

A notation summary can be found in Table 2.1.

Table 2.1: Notation Summary

K, L	Primal cells
e, $\hat{e}$	primal and dual edge
∂K	edge set of cell K
∂e	vertex set of edge e
$\hat{K}^{(b)}$, $\hat{L}^{(b)}$, $\hat{K}^{(c)}$, $\hat{L}^{(c)}$	Dual cells
$\hat{e}^{(b)}$,$\hat{e}^{(c)}$	Dual edge
e	Primal edge
$\mathcal{C}$	Set of primal cells sets
$\mathcal{V}^{(b)}$, $\mathcal{V}^{(c)}$	Set of dual cells
$\mathcal{E}$	Set of primal edge sets
$\hat{\mathcal{E}}^{(b)}$,$\hat{\mathcal{E}}^{(c)}$	Set of dual edge sets
$e = K\|L$	edge e between K and L

2.1.2 Construction

To construct the icosahedron, we consider three orthogonal rectangles on $\mathbb{R}^3$, as illustrated in Figure 2.4. These rectangles have side 1 and $\tau = (\sqrt{5}+1)/2$, where τ is the golden ratio. The vertices v of these rectangles belong to the icosahedron, so that $v \in \mathcal{V}$.

Now, for each vertex $v_i \in \mathcal{V}$, we connect it with $v_j \in B_r(v_i) \cap \mathcal{V}$, where $B_r(v_i)$ is the ball with radius $r = \min_{v_j \in \mathcal{V} \setminus \{v_i\}}(|v_i - v_j|)$ centred at v_i. Specifically, each vertex is connected by five other vertices.

For each connection, we can then obtain our edges $e \in \mathcal{E}$. To obtain the circumcentre, let us again take $v_i \in \mathcal{V}$, and $v_j, v_k \in B_r(v_i) \cap \mathcal{V}$, with the same radius previously created. If $v_i, v_j, v_k \in B_r(v_i) \cap B_r(v_j) \cap B_r(v_k)$, then these three vertices define our triangle. Since each triangle is equilateral, we can easily obtain the circumcentre $K \in \mathcal{C}$.

Using the notation of Tomita et al. (2001), this will define our g_0 grid. To obtain g_1, for a triangle $K \in \mathcal{C}_0$ we connect its midpoint elements $\mathbf{e} \in \partial K \cup \mathcal{E}_0$ of each face, forming new triangles. This will form four additional triangles with $\mathcal{E}_0 \subset \mathcal{V}_1$. Doing this for all faces, we created a new generation of the mesh. This procedure can be repeated i-th times, in order to obtain g_i grid.

The grid used in this research will differ slightly from the standard way of mesh generation. For each bisection, the vertices of the grid are projected onto the sphere, until the desired mesh is achieved. We will project the elements onto the sphere only when we achieve

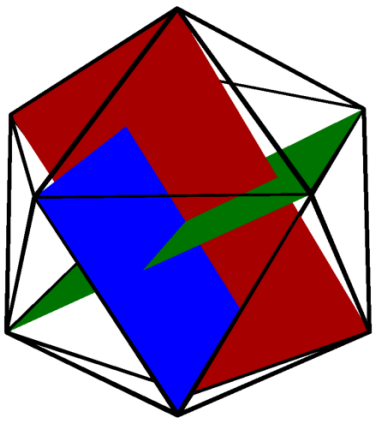

Figure 2.4: Icosahedron with its three orthogonal rectangles.

the desired resolution, as to accentuate the distortions of the grid and better observe the behaviour of the schemes in a distorted grid. We will call it MODSTD grid.

Regardless, from this process of bisection, we can define the number of faces and edges by $\#\mathcal{C} = 20 \times 4^i$ and $\#\mathcal{E} = 30 \times 4^i$, respectively. Euler's formula also dictates that:

$$\#\mathcal{C} + \#\mathcal{V} - \#\mathcal{E} = 2$$

The Table 2.2 lists the number of elements up to a level g_6, which will be used in further chapters.

Table 2.2: Number of cells, vertices and edges for each grid.

Grid	$\#\mathcal{C}$	$\#\mathcal{V}$	$\#\mathcal{E}$
g_0	20	12	30
g_1	80	42	120
g_2	320	162	480
g_3	1280	642	1920
g_4	5120	2562	7680
g_5	20480	10242	30720
g_6	81920	40962	122880

2.2 Grid Properties

As previously mentioned, this subdivision process will inevitably break the homogeneity of the grid and create distortion of the grid. A first evidence of this distortion is how the length of each edge is in comparison to the length of the largest edge of the domain (Figure 2.5.A). A similar comparison can be performed when analysing the circumcentre distance between neighbouring cells (Figure 2.5.B).

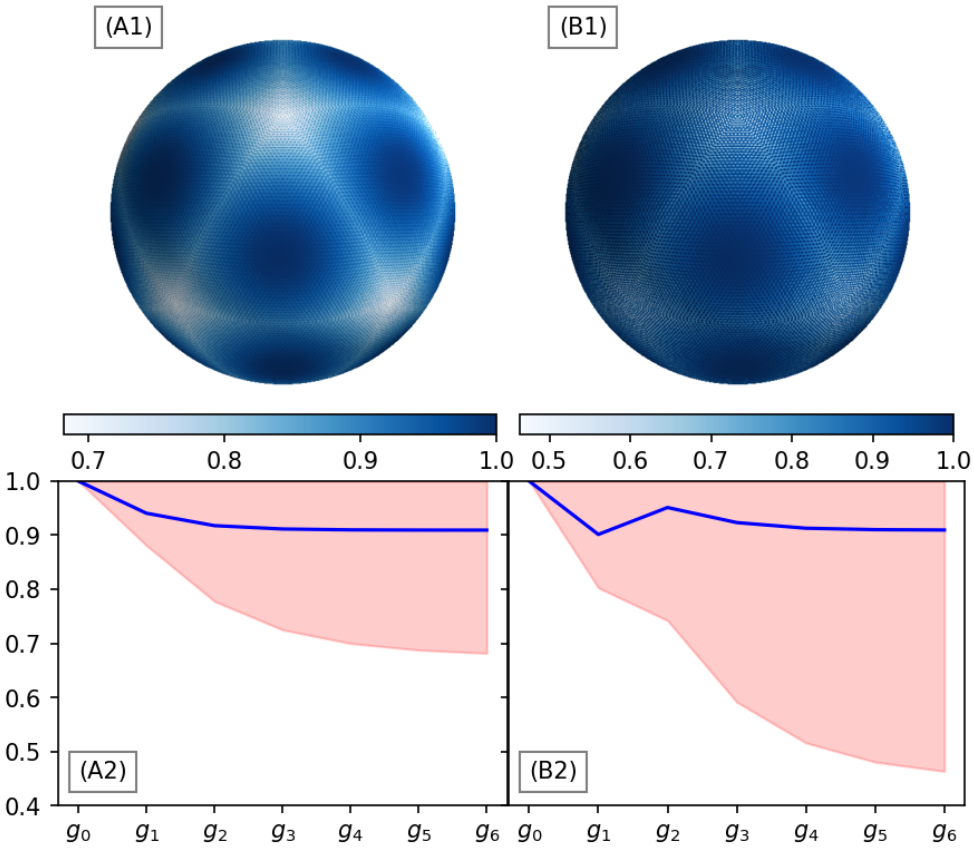

Figure 2.5: Normalized arc length of primal (A) and dual (B) edge. The shaded area in the lower panels represent the range of the minimum and maximum length, and the line represents the mean value.

The first bisection produces the largest difference in lengths in the grid. The minimum normalized edge length decreases from 1 to around 0.88, while the average of the domain is from 1 to around 0.94 (Table 2.3). Each subsequent bisection is slower than the previous. The difference between each value decreases by a factor of 2 for the minimum edge length of the domain. The average field difference decreases much faster (the ratio $g_6 - g_5/(g_5 - g_4)$ is of around 23/3). In that case, if we expect a consistent decrease, we expect the minimum/average normalized edge length value to converge to 0.675/0.909.

The circumcentre distance also has its largest decrease in the first bisection (Figure 2.5.B2). The minimum/average value of the field decreases from 1/1 to 0.8/0.9 (Table 2.3). Unlike the edge length ratio, the bisection g_1 to g_2 increase the field average ratio of the circumcentre distance. However, further bisection behaves similar to the other parameter, decreasing, but slower at each subdivision. This brake is found to be of an order of 2 for the minimum value and an order of 3 for the average value of the field. Assuming that this break is consistent to these orders, then the minimum/average values will likely converge to approximately 0.447/0.909. Therefore, though the average is similar to the primal edge length, the circumcentre distance, or dual edge length, is more affected by the bisection.

Observing the spatial structure of the parameters in a g_6, we see that both behave quite

Table 2.3: Minimum/mean normalized edge length and circumcentre distance.

	$\frac{\lvert e\rvert}{\max\lvert e\rvert}$	$\frac{\lvert e^{\perp}\rvert}{\max\lvert e^{\perp}\rvert}$
g_0	$1.0000.10^{0}/1.0000.10^{0}$	$1.0000.10^{0}/1.0000.10^{0}$
g_1	$8.8104.10^{-1}/9.4058.10^{-1}$	$8.0276.10^{-1}/9.0143.10^{-1}$
g_2	$7.7787.10^{-1}/9.1766.10^{-1}$	$7.4249.10^{-1}/9.5114.10^{-1}$
g_3	$7.2513.10^{-1}/9.1149.10^{-1}$	$5.9164.10^{-1}/9.2333.10^{-1}$
g_4	$7.0001.10^{-1}/9.0986.10^{-1}$	$5.1623.10^{-1}/9.1285.10^{-1}$
g_5	$6.8785.10^{-1}/9.0940.10^{-1}$	$4.8080.10^{-1}/9.1022.10^{-1}$
g_6	$6.8187.10^{-1}/9.0934.10^{-1}$	$4.6381.10^{-1}/9.0950.10^{-1}$

similarly (Figure 2.5.A1 and Figure 2.5.B1). The regions of the original g_0 present the small ratios of the grid, with the smallest occurring at the regions of the original vertices. In contrast, the centre of the faces (of the original g_0) shows the largest ratios. The largest distortions, therefore, are located within these g_0 edges. It is evident that the primal and dual edge suffer from these distortions in the same regions, though the dual edge seems much more affected.

In comparison to other grids, according to (Figure 3 of Peixoto, 2016), the SCVT optimization has a continued decrease of this ratio, without an apparent slow-down. However, its minimum values for up to g_6 are substantially higher than ours (larger than 0.7). The HR95 optimization is also much better in this respect, as it not only does not lose continuously its uniformity, but also, again, has a convergent value higher than ours (minimum values near 0.8). According to Miura and Kimoto (2005), the standard mesh also behaves similarly as the HR95, having a minimum ratio around 0.85.

Another useful parameter to observe is the offset between the midpoint of primal and dual (circumcentre) edges and between the circumcentre and barycentre of the triangular cell (Figure 2.6). The original grid, as expected, should not present any distance between these points as the solid is composed only of equilateral triangles (Table 2.4). The fist bisection will create a distortion in the grid. This distortion produces an offset of these points. The largest offset is at the g_1. The mean/maximum normalized midpoint edge offset value is of 0.0016/0.0031, while the cell centre distance is 0.24/0.33. Subsequent bisections, decrease both parameters continuously with a second order convergence. This convergence is also present in HR95, but not in SCVT (Figure 3 of Peixoto, 2016).

When observing its spatial distribution on the sphere, we notice some similarities. As the primal/dual edge length ratio, both of these parameters have their largest values near the original edges of the solid, which implies for its distortion. The lowest values are located near the centre of the face of the icosahedron. A noteworthy difference that should be highlighted is that the edges of the cell along the original g_0 edges and the edges neighbouring the original g_0 vertices have a small normalized distance between edges. This will likely have an impact on the error distribution of some operators dependent on these edges.

Another important analysis of grid structure to analyse is the cell areas of the grid. There are three main areas to analyse, the primal and dual cell area, and the edge area, which is calculated using the edge neighbouring points circumcentre and vertex point. This resulting area and its distribution in its normalized form is presented in Figure 2.7 and

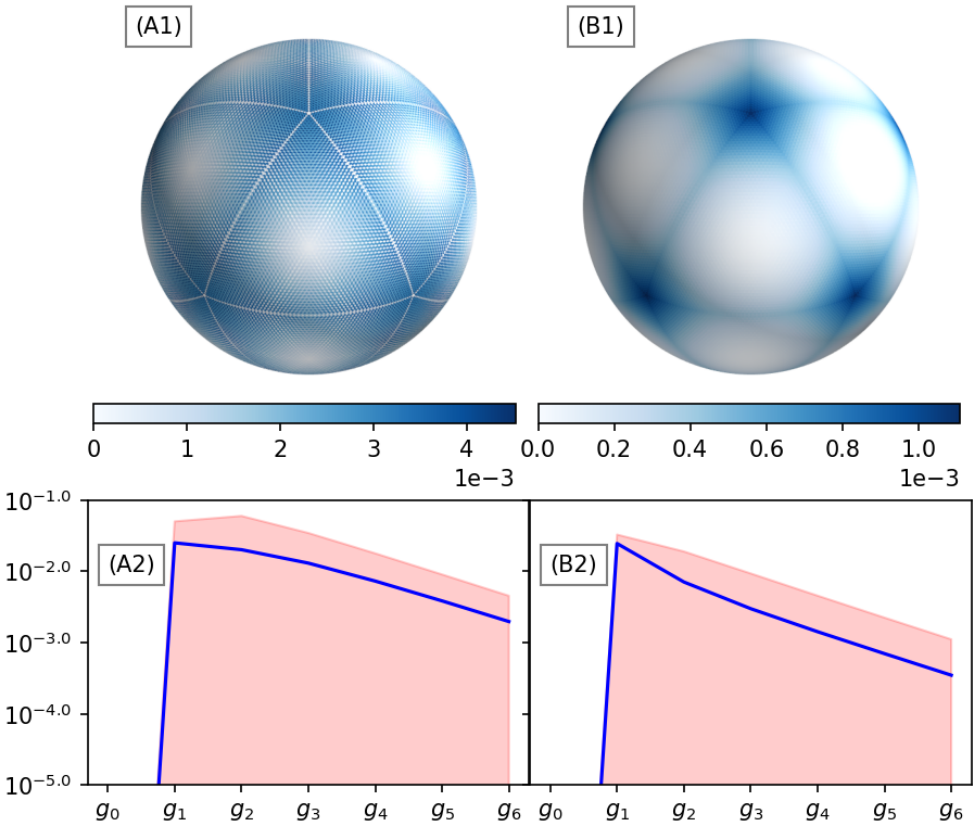

Figure 2.6: Mean primal-dual- edge point distance (A), and circumcentre and centroid point distance (B).

Table 2.5. All values start 1 (implying their homogeneity in the icosahedron). The first bisection introduces the most expressive loss of uniformity for the primal grid, decreasing in 0.17/0.13 for the minimum/average of the area field. As with the other parameters, the loss for subsequent bisection is diminished. In contrast, for both the edge area and the dual area, the largest difference occurs at the bisection g_1 to g_2 and g_2 to g_3, decreasing 0.089/0.044 and 0.115/0.033.

However, all the areas seems to converge in their minimum and average values, since there is a slow-down of this loss. The minimum/average of the primal area field from g_5 to g_6 is 6.4/4.15 times slower than g_4 to g_5. For both the dual and edge area, the $g_5 \to g_6$ is 2/4 slower than $g_4 \to g_5$. At the current rate, we expect that the minimum area of each field to be: 0.501, 0.355, and 0.479, for the primal, edge, and dual area, respectively. However, the average field normalized area is expected to be 0.8288 for all fields.

When observing their distribution around the sphere, we notice the same pattern as our other analysis, in other words, the worst results (small values) are in regions near the original g_0 edges and vertices of the icosahedron. The best results (large values) are located near the centre of each face of the solid.

In comparison to other grids, Miura and Kimoto (2005) found that for tested grids, the normalized dual area of most grids perform better than ours. The HR95 has the largest ratio without any decrease as our grid. However, the SCVT is one of the worst performing, and

Table 2.4: Mean/Maximum distance between primal and dual edge midpoints and between cell circumcentre and barycentre.

	$(e - e^{\perp})/\max\|e\|$	$K - K_c$
g_0	$0.0000.10^{0}/0.0000.10^{0}$	$0.0000.10^{0}/0.0000.10^{0}$
g_1	$1.5688.10^{-2}/3.1377.10^{-2}$	$2.4463.10^{-2}/3.2617.10^{-2}$
g_2	$6.1112.10^{-3}/1.7637.10^{-2}$	$7.0561.10^{-3}/1.8918.10^{-2}$
g_3	$1.9510.10^{-3}/4.8197.10^{-3}$	$2.9828.10^{-3}/9.2951.10^{-3}$
g_4	$5.4254.10^{-4}/1.2099.10^{-3}$	$1.4178.10^{-3}/4.5387.10^{-3}$
g_5	$1.4266.10^{-4}/3.0349.10^{-4}$	$6.9924.10^{-4}/2.2360.10^{-3}$
g_6	$3.6557.10^{-5}/7.5891.10^{-5}$	$3.4840.10^{-4}/1.1090.10^{-3}$

Table 2.5: Mean/Maximum distance between primal and dual edge midpoints and between cell circumcentre and barycentre.

	$\|K\|/\max\|K\|$	$A_e/\max A_e$	$\|\hat{K}\|/\max\|\hat{K}\|$
g_0	$1.0000.10^{0}/1.0000.10^{0}$	$1.0000.10^{0}/1.0000.10^{0}$	$1.0000.10^{0}/1.0000.10^{0}$
g_1	$8.3117.10^{-1}/8.7337.10^{-1}$	$9.1115.10^{-1}/9.5557.10^{-1}$	$8.8525.10^{-1}/9.6721.10^{-1}$
g_2	$6.5935.10^{-1}/8.4008.10^{-1}$	$6.8392.10^{-1}/8.8519.10^{-1}$	$6.9457.10^{-1}/9.2371.10^{-1}$
g_3	$5.7625.10^{-1}/8.3163.10^{-1}$	$5.0365.10^{-1}/8.4302.10^{-1}$	$5.6523.10^{-1}/8.5331.10^{-1}$
g_4	$5.3778.10^{-1}/8.2951.10^{-1}$	$4.2462.10^{-1}/8.3236.10^{-1}$	$5.1708.10^{-1}/8.3498.10^{-1}$
g_5	$5.1947.10^{-1}/8.2897.10^{-1}$	$3.8876.10^{-1}/8.2969.10^{-1}$	$4.9691.10^{-1}/8.3035.10^{-1}$
g_6	$5.1056.10^{-1}/8.2884.10^{-1}$	$3.7176.10^{-1}/8.2902.10^{-1}$	$4.8775.10^{-1}/8.2918.10^{-1}$

has continuous decrease in this ratio, yet it has a better performance on the g_6 grid showing a ratio of around 0.6. The distribution of our normalized dual area show high similarities with the HR95, with the largest area difference near original vertices.

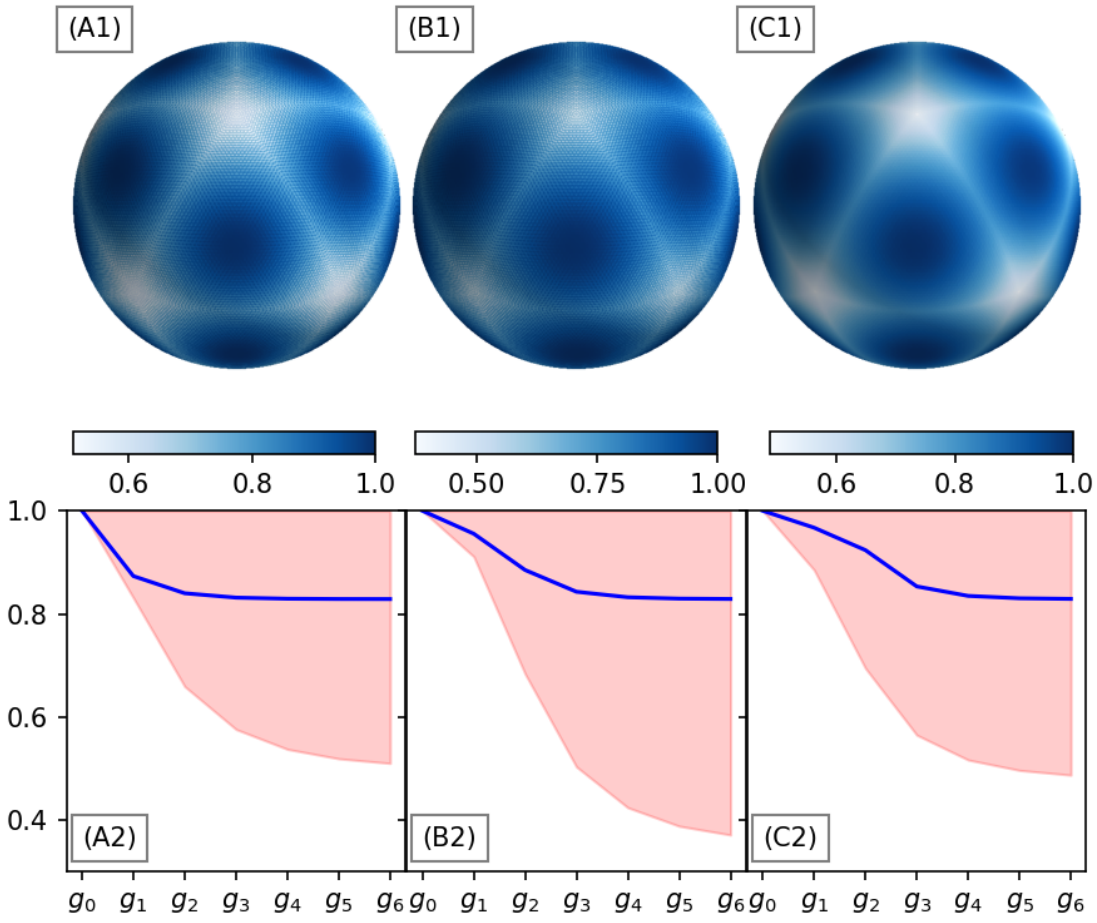

Figure 2.7: Normalized area of the triangles (A), edge (B), dual grid(C), and the g_6 grid triangle area.

2.3 Distortion and Alignment

The distortion and alignment index parameters were calculated from the definitions of Peixoto and Barros (2013). Suppose a Voronoi cell is composed of n even vertices $\{v_i\}_{1\leq i\leq n} \in \mathcal{V}$. Define $d_{i,j} = d(v_i, v_j)$, so the alignment index is:

$$\Xi = \frac{1}{n\bar{d}} \sum_{i=1}^{n/2} |d_{i+1+n/2,i} - d_{i+n/2,i+1}| + |d_{i+1,i} - d_{i+n/2+1,i+n/2}|, \tag{2.4}$$

where $\bar{d} = (1/n)\sum_{i=1}^{n} d_{i,j+1}$. For cells with odd number of vertices $\Xi = 0$. The distortion parameter is:

$$\Theta = \frac{\sqrt{\frac{1}{n}\sum_{e\in\partial K}(|e| - |\bar{e}|)}}{|\bar{e}|}, \tag{2.5}$$

where $|\bar{e}| = \sqrt{(1/3)\sum_{e\in\partial K}|e|^2}$.

It should be noted that since triangles all have an odd number of vertices, then $\Xi = 0$ for all cells. Therefore, the alignment index will be calculated on the Voronoi grid. The distortion, however, will be done on our primal grid.

The results are present in Figure 2.8 and Table 2.6. The g_0 grid, since it is composed of only equilateral triangles, shows a zero distortion in the mesh and a perfect (1) alignment of the dual grid. The first bisection, as with the other parameters, show a large distortion, increasing the minimum/average distortion to 0.046/0.061 and average alignment increases to 0.286. It should be noted that, at this point, the dual grid has the presence of pentagons (12, in fact), and these pentagons will bring the minimum alignment to zero for all g_i. For grids finer than g_1 we observe a decrease in the distortion of the primal mesh. From g_1 to g_2, the average distortion decreases 0.0182, but the maximum increases 0.0137. Further refinements have a slower change in both the average and the maximum distortion. The change in both average and maximum distortion for $g_5 \to g_6$ is about 4 times slower than $g_4 \to g_5$. The alignment decreases for all subdivisions. It also slows-down with the refinement, with an order close to 2. For the same constant rate, the expected average/maximum distortion will be of around 0.023/.0786 and the average alignment will be of $9.13.10^{-4}$.

Table 2.6: Average alignment and average/maximum distortion. The minimum alignment disregards the cells where $\Xi = 0$.

g_i	Ξ	Θ
g_0	$1.0000.10^{0}$	$0.0000.10^{0}/0.0000.10^{0}$
g_1	$2.8576.10^{-1}$	$4.5618.10^{-2}/6.0824.10^{-2}$
g_2	$2.3783.10^{-1}$	$2.7418.10^{-2}/7.4523.10^{-3}$
g_3	$1.5024.10^{-1}$	$2.4193.10^{-2}/7.7243.10^{-2}$
g_4	$8.2947.10^{-2}$	$2.3352.10^{-2}/7.7831.10^{-2}$
g_5	$4.3349.10^{-2}$	$2.3132.10^{-2}/7.7967.10^{-2}$
g_6	$2.2131.10^{-2}$	$2.3077.10^{-2}/7.8000.10^{-2}$

When observing the spatial distribution of the both fields, we again see that the largest distortions are confined near the g_0 edges and vertices (Figure 2.8.A1). Near the centre of the faces of the original icosahedron, we see a decrease in the distortion of the cell.

The alignment, however, shows a different behaviour. The best values are near these regions of g_0, but instead of showing a smooth gradient, as had presented the distortion, it is presented as a confined region of large alignment. A dual cell located at a point in the original g_0 will be symmetrical along the segments of this edge. This centre of this cell will have two segments of this original edge, and since it is symmetrical along the edge, the dual edges opposite to one another will have the same length. Due to this symmetry, this cell will have a large alignment.

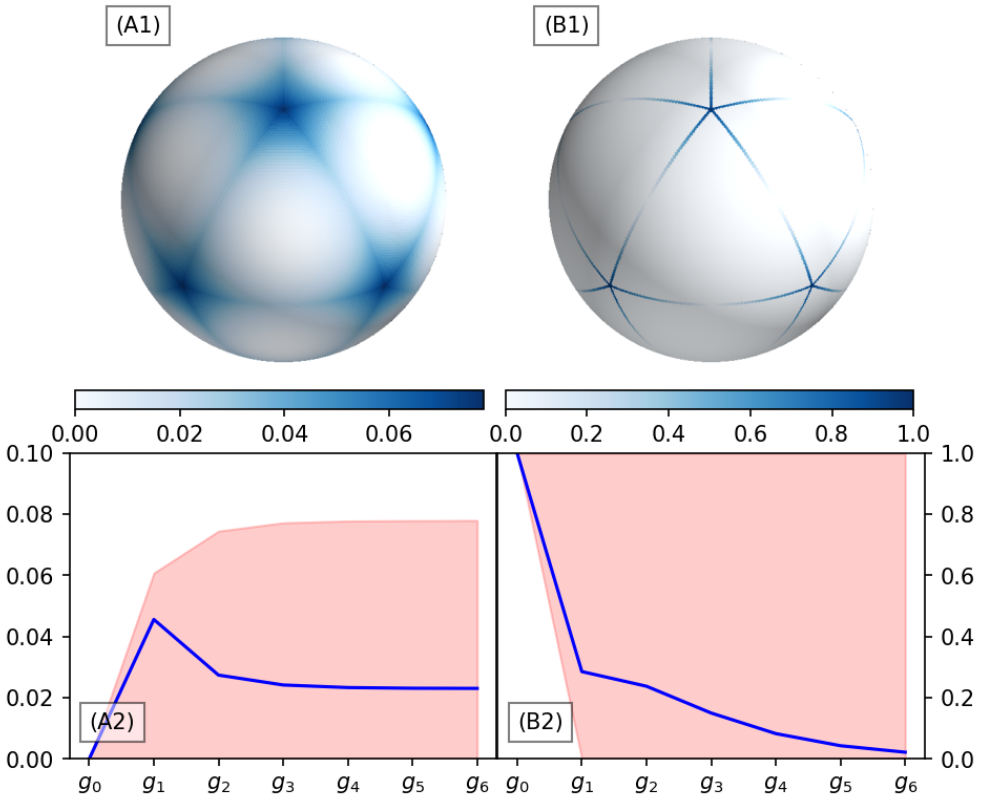

Figure 2.8: Triangle distortion (A), and dual grid alignment (B), Triangle distortion distribution on g_6.

In comparison to other grids, Peixoto and Barros (2013) found that the mean alignment of the standard icosahedral g_6 grid is of around 0.55. Further grid subdivisions, notwithstanding, impacts substantially the alignment of the grid. It is also shown that this grid has various patterns of low and high alignments values. Ours, in contrast, are mostly restricted to the original icosahedron edges.

2.4 Concluding Remarks

Our grid shows that it is quite affected by the refinement process. There is, as expected, an abrupt loss of homogeneity. Some primal grid parameters present a recovery as the grid is bisected. Other parameters do not seem to worsen with refinement. The dual mesh alignment, however, present a decline with each bisection. There are two main issues pointed by Peixoto (2016):

- the vertices/cell circumcentre are not necessarily the centroid of the dual/primal cell,
- non coincidence of the primal and dual edge midpoint.

The first, according to the author, will have a direct impact on the accuracy of operators of the next chapter. Although our defined grid does not have this coincidence of points on

the primal mesh, they converge as the grid is refined. The second point causes the Laplacian operator to be inconsistent, which is solved by using the HR95.

Concerning the optimizations, our results provide similar results with Miura and Kimoto (2005), Peixoto and Barros (2013) and (Figure 3 of Peixoto, 2016). Spatially, it appears as that the distortions associated with the grid are more closely related to the HR95, rather than the standard icosahedral grid, despite not using optimization. On average, our alignment present better results than the standard icosahedral grid.

Like all other grids, ours also show signs of imprinting. We expect that this imprinting will be the main responsible for the operator accuracy error in our grid. We expect that the loss of alignment, in particular, will provide even poorer results for operators defined in these cells. In the next chapter (Chapter 3), we will evaluate these operators for the Shallow Water Equations in our grid.

Chapter3

Shallow Water Analysis

A suitable grid choice is only one key piece of a well thought numerical weather or climate model. Another important consideration is the choice of an appropriate numerical scheme, and, alongside, the grid staggering. When determined, those choices should go through a battery of tests, as a way to determine their advantages and limitations. It is common to define such a model on one of the simplest set of system of equations available, the Shallow Water Equations:

$$\frac{\partial h}{\partial t} + \nabla \cdot \mathbf{u} = 0 \tag{3.1a}$$

$$\frac{d\mathbf{u}}{dt} + f\mathbf{k} \times u + \nabla\Phi + \kappa\nabla^2 u + F = 0 \tag{3.1b}$$

where $d/dt = \partial/\partial t + \mathbf{u} \cdot \nabla$ is the material derivative, $\Phi = g(h + b)$, g is gravitational acceleration, f, is the Coriolis parameter, h is the mass field, b is the bathymetry, $\mathbf{u}$ is the vector field, denominated as wind/current velocity, κ is the biharmonic coefficient, and F is the external forces.

There is a large interest to provide some conservation properties, such as energy, vorticity, and enstrophy. The above system of equations has a non-linearity term (advective term) that present issues in conserving these quantities. Therefore, it is usual to reformulate this term as:

$$\mathbf{u} \cdot (\nabla \mathbf{u}) = \zeta \mathbf{u} + \nabla E_k,$$

where $\zeta = \hat{\mathbf{k}}\nabla \times \mathbf{u}$ is the relative vorticity and $E_k = |\mathbf{u}|^2/2$ is the kinetic energy. Now, the momentum equation can then be written as:

$$\frac{\partial \mathbf{u}}{\partial t} + \omega\mathbf{k} \times \mathbf{u} + g\nabla\Phi + \nabla E_k = 0, \tag{3.2}$$

where $\omega = \zeta + f$ is the absolute vorticity. It is also not uncommon to write $\omega(\mathbf{k} \times \mathbf{u}) = q(\mathbf{k} \times \mathbf{u}h)$, where $q = \omega/h$ is the potential vorticity.

Regardless of the choice of the momentum equation, the two primary unknowns/variables are the h and $\mathbf{u}$, which are a scalar and a vector field, respectively. It is crucial to define where these variables will ultimately be positioned, i.e. which *grid staggering* to use. Initially, Arakawa and Lamb (1977) defined 5 possible staggering grids from "A" to "E". Randall (1994) defined a new one which he coined "Z", but used other variables derived from $\mathbf{u}$.

The A-grid is one of the simplest suggested staggering. It is considered a non-staggered grid, since all variables coincide at the vertices of the grid. On traditional grids, it requires

many averaging operations, such that the resulting operators could be defined again at the vertices. This averaging would, inevitably, "hide" the physical waves associated with 1-grid scale. Another huge drawback of this scheme is the presence of computational modes on the 2-grid scale interval. These waves are not only present, but are also easily excited, making the scheme unconditionally unstable. It is, therefore, required the addition of a smoothing filter to mitigate these waves and provide stability to the model. This smoothing attenuate waves of large wavenumbers impacting their representation on this scale (Figure 3.1.A).

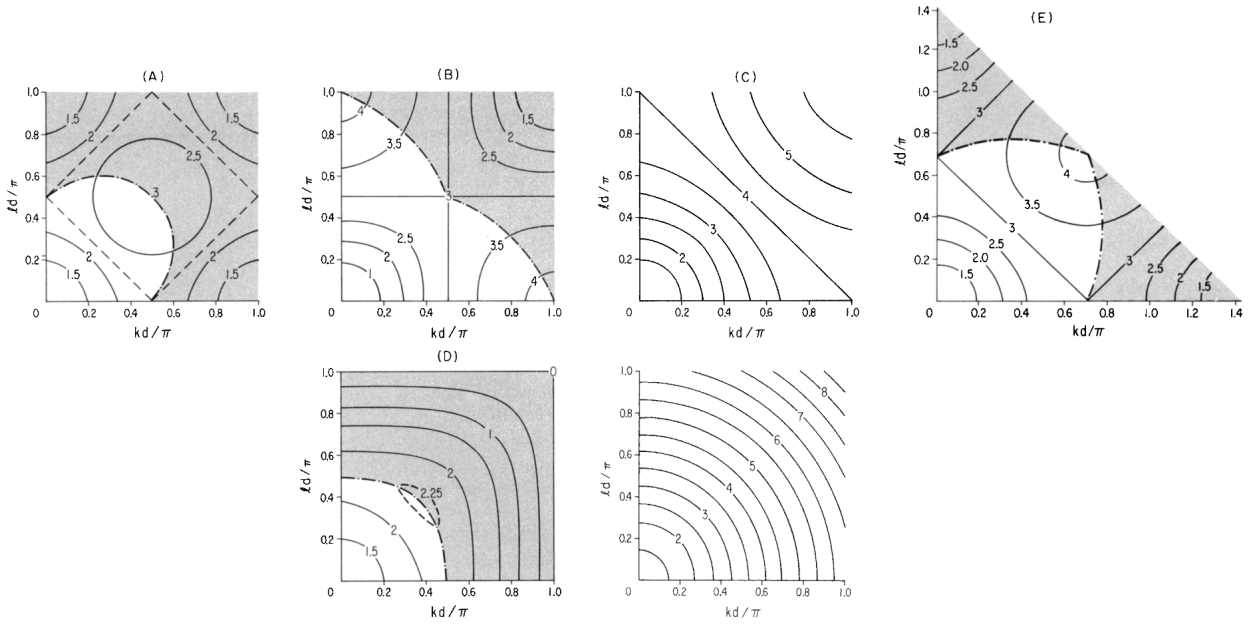

Figure 3.1: Contours of non-dimensional frequency $|\mathbf{u}|/f$ for schemes (A)-(E) by each component of non-dimensional wave number. The lower right corner panel is the true wave representation. Source Arakawa and Lamb (1977)

.

A slightly more complex staggering is the type B-grid. This staggering has its mass variable points positioned at the vertices, while its vector variable points are located at the faces of the primal cells. On traditional structured grids, it also requires averaging, however, in contrast to the A-grid, this averaging occurs on the orthogonal complement axis, e.g. $\partial h/\partial x$ requires averaging on the y-axis. In this staggering, there is also a smoothing of the waves on the 1 grid scale for this direction. However, for the other axis, no averaging is required, and, consequently, there will be a presence of waves in this scale. These numerical waves are associated with spurious pressure modes on the system. Similar to the A-grid, it will be necessary the use of a damping filter to remove this noise. This damping again will attenuate waves of large wavenumbers.

The C-grid, in contrast, is yet more complex than the previous types. The vector field is separated, and each orthogonal component is allocated to the edges. For structured grids, the zonal component is located at the midpoint of the vertical (lines of same longitude) edges, and the meridional components are positioned at the midpoint of the horizontal edges (lines of same latitude). The mass variable h is located at the face (centre) of the cell. This

positioning provides an accurate representation of the geostrophic adjustment, portraying well inertia gravity waves of near grid scale frequency (Figure 3.1.C). The largest drawback is that this separation of the vector components requires the field to be reconstructed, in order to calculate the Coriolis Force term. The reconstruction of the field will not be exact and will, therefore, add another layer of uncertainty in the equations.

Other grid positioning will also present many problems. The D-grid needs substantial averaging, which impacts the wave dispersion much more strongly than the A-grid (Figure 3.1.D). The E-grid has a positioning issue that, for some specific conditions, it might behave as the A-grid. Finally, The Z-grid has similar benefits as the C-grid, but it uses variables that are derivative from the h and $\mathbf{u}$. It, thus, demands for a solution of a Poisson equation for each time step to retrieve the original variables, making the whole scheme quite costly.

Despite the necessity of vector reconstruction, the advantage of a more accurate inertia wave dispersion representation made C-grid popular. A good deal of research was done to provide an effective vector reconstruction that maintained important conservative properties of the core (e.g. Arakawa and Lamb, 1977). However, the rise of unstructured grids for global modelling, in particular for ocean modelling, required new strategies for devising the Coriolis Term. One main issue is the lack of orthogonality between edges, which could potentially create new terms and produce new sources of computational noise that could make the model unstable. One solution is to use finite-element strategies, which was popular among ocean modellers for triangular tilling (e.g. TELEMAC, COMPAS, FESOM1.4). These methods can provide satisfactory results in their spatial and time range needed. They have, however, a large computational cost, making them unfeasible for finer grids.

Another alternative is the use of finite-volume methods, a rather new concept in the geophysical fluid modelling community. The basis of these methods is to consider the cells as volume representations within the cells and calculate the flux out and in of these cells. It is mostly guaranteed at least the conservation of mass. For climate modelling, we wish to achieve other conservation properties such as energy.

An early finite-volume scheme for icosahedron was devised by Tomita et al. (2001) with an A-grid staggering. This scheme became the basis of the Japanese Non-hydrostatic Icosahedral Atmospheric Model (NICAM). Their model avoided many shortcomings at the time, such as the vector reconstruction problem. Since the staggering of choice required some use of filter technique, it also solved many issues with noise. Not all grids, however, were optimal for the model. The standard icosahedral grid was found to be inconsistent to use in their model. There was an apparent noise surging due to the inconsistency of the mass equation operators. They solved this issue using a special kind of optimization known as Spring Dynamics.

Subsequently, based on the work of Arakawa and Lamb (1981), a couple of papers suggested a new scheme for discretizing the shallow water equations on an arbitrary polygon for a staggering of type C on the sphere (Thuburn et al., 2009; Ringler et al., 2010). This scheme, known as TRiSK, became the basis for the Los Alamos Laboratory and the National Center for Atmospheric Research (COSIM) Model for Prediction Across Scales (MPAS) in both atmospheric and oceanic component. Their model, however, used the dual of the icosahedral grid, which is composed of pentagonal-hexagonal tiling.

The reason why the icosahedral dual was used instead, was because C-grid triangular meshes requires a special treatment. This tiling presents a substantial noise in a 1-grid interval pattern known as a *chequerboard* pattern. It is specially dominant on flows dominated by

slow geostrophic dynamics (Figure 3.2), which can contaminate the domain and damage the solution.

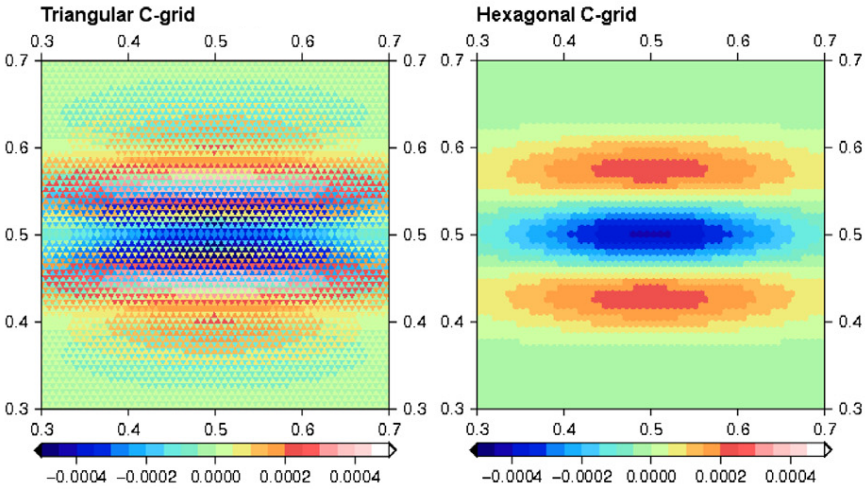

Figure 3.2: Geostrophic adjustment divergence on the h field for both the triangular and its dual C-grid meshes. Source: Gassmann (2011)

Le Roux et al. (2005) studied this problem for planar grids and diagnosed that an unbalance in the Degrees of Freedom (DOFs) of height and velocity would evoke this pattern. He realized that it is necessary, although not sufficient, that the velocity DOFs be twice as many as the height DOFs.

Weller et al. (2012) analysed the TRiSK scheme using different geometries and observed that, it indeed, showed the same pattern in either the vorticity (quasi-hexagonal mesh) or divergence (triangular mesh). They unsuccessfully suggested a different geometry that would satisfy the condition imposed by Le Roux et al. (2005). They found that this grid would present an even stronger noise, which they would conclude that an anisotropic resolution would also play an important role on the noise generation.

Gassmann (2011) was able to better elucidate this problem. She assumed an equilateral triangular mesh on the plane and the representation of the canonical basis as $(\mathbf{i}, \mathbf{j}) = (\mathbf{j}_1, \mathbf{j}_2, \mathbf{j}_3)$ with $\mathbf{j}_i$ a normal unit vector associated with the edge e_i pointing away from the cell (Figure 3.3). She realized that, in other to avoid the numerical pattern, we require:

$$v_1 + v_2 + v_3 = 0, \tag{3.3}$$

where v_i is the scalar velocity associated with $\mathbf{j}_i$. A solution proposed by the author is that we can guarantee this relation if the divergence can be reformulated as an average of the divergence of three overlapping rhombi in the triangular cell.

Some authors have, thus, developed schemes and/or filters to damp these modes (e.g. Gassmann, 2011; Wolfram and Fringer, 2013). However, the useful conservation properties of a scheme would eventually be eliminated with use of these methods.

Korn and Danilov (2016), in an effort to develop an ocean model that would remove this noise and also retain the useful physical conservation properties, developed a scheme that integrated notions of finite volume and finite difference methodology, leading to a mimetic

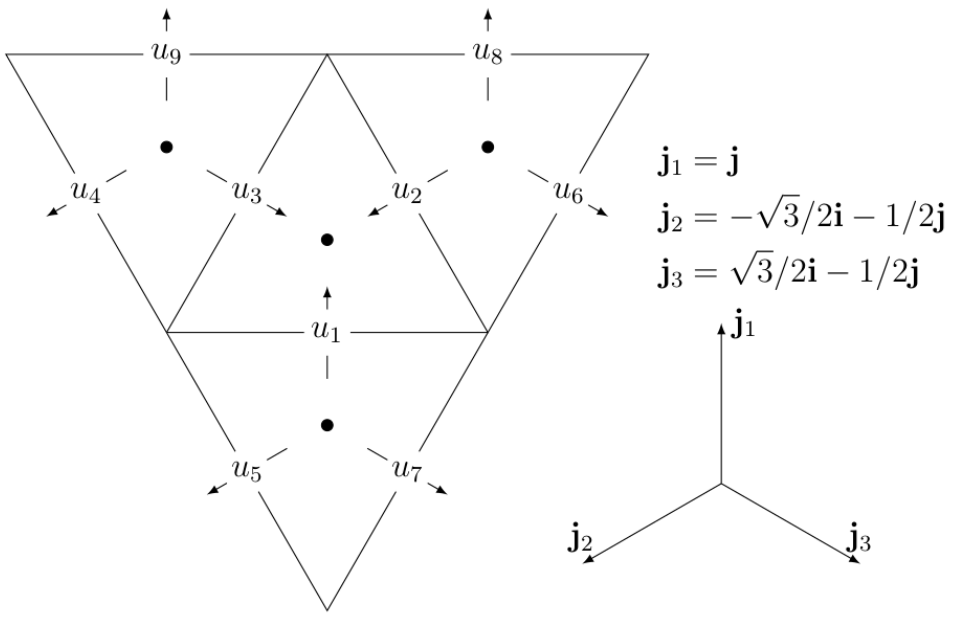

Figure 3.3: Example of equilateral triangular cells with velocity vectors

discretization. This became the basis of the Icosahedral Nonhydrostatic (ICON) ocean component model Korn (2017). However, his discretization requires a matrix inversion for each time step (as does some finite element schemes). This is quite costly, so the authors used a technique known as matrix lumping which removes the inversion requirement, and, thus, making the scheme faster. There is a drawback of losing some conservation properties, but the underline robustness of the model is maintained.

A scheme devised by Danilov et al. (2017) on a B-grid tiling also present the same issue with excessive DOFs. However, in contrast, to the C-grid, it does not need to concern with the velocity reconstruction, since the full velocity vector field is placed on the triangular nodes. Moreover, their scheme is free from pressure modes, which dominates A-grid schemes. Despite this, the excessive DOFs leads to spurious inertial modes, which requires filtering to reduce, breaking possible conservation of the model. This scheme became the basis of the Finite VolumE Sea-Ice Model (FESOM) 2.0.

Thus, no scheme presents an optimal solution for practical use, specially on a triangular mesh. Additionally, due to the novelty of the new technology, there is a lack of work regarding the comparison of these new schemes. So, we pose the following questions: How does A-C grid staggering behave on the sphere? How are their accuracy affected by distortion and noise?

To answer these questions, in this chapter we will provide a comparison between three staggering types: A-, B-, and C-grid. For A- and B-grid, we will study the schemes of Tomita et al. (2001) and Danilov et al. (2017), respectively. To compare with the C-grid, we will study both TRiSK (Ringler et al., 2010) and ICON-O (Korn and Danilov, 2016).

Prior to tackle these objectives, in the next section (Section 3.2) we will provide in details the discretization of the operators used in each scheme. In Section 3.3 we will provide the spatial error accuracy of the spatial operators and in Section 3.3.3 the accuracy of the

time integrated accuracy of the variables. The physical modes of TRiSK and ICON will be analysed in Section 3.4. Finally, an application of the plausible real world scenario will be used in Section 3.5.

3.1 Discrete Grid Spaces

To be able to provide the dicretizations for the schemes, we need to define the spaces where we will perform our calculations. Particularly, for the primal and dual cells, we define:

$$\mathcal{H}_{\mathcal{E}} \coloneqq \{v : \mathcal{E} \to \mathbb{R}, v : e \mapsto v_e\} \tag{3.4}$$
$$\mathcal{H}_{\mathcal{C}} \coloneqq \{p : \mathcal{C} \to \mathbb{R}, p : K \mapsto p_K\} \tag{3.5}$$
$$\mathcal{H}_{\mathcal{V}} \coloneqq \{\hat{p} : \mathcal{V} \to \mathbb{R}, \hat{p} : V \mapsto \hat{p}_V\} \tag{3.6}$$
$$\mathbf{H}_{\mathcal{C}} \coloneqq \{\mathbf{p} : \mathcal{C} \to \mathbb{R}^3, \mathbf{p} : K \mapsto \mathbf{p}_K\} \tag{3.7}$$
$$\mathbf{H}_{\mathcal{V}} \coloneqq \{\hat{\mathbf{p}} : \mathcal{V} \to \mathbb{R}^3, \hat{\mathbf{p}} : \hat{K} \mapsto \hat{\mathbf{p}}_{\hat{K}}\}. \tag{3.8}$$

The last two spaces are defined for vector fields, while the first three spaces are for scalar fields. We endow these spaces with inner products for the use in ICON scheme:

$$\langle v^1, v^2 \rangle_{\mathcal{H}_{\mathcal{E}}} \coloneqq \sum_e |e||\hat{e}| v_e^1 v_e^2, \qquad \forall v^1, v^2 \in \mathcal{H}_{\mathcal{E}} \tag{3.9}$$
$$\langle p^1, p^2 \rangle_{\mathcal{H}_{\mathcal{C}}} \coloneqq \sum_K |K| p_K^1 p_K^2, \qquad \forall p^1, p^2 \in \mathcal{H}_{\mathcal{C}} \tag{3.10}$$
$$\langle \hat{p}^1, \hat{p}^2 \rangle_{\mathcal{H}_{\mathcal{V}}} \coloneqq \sum_V |V| \hat{p}_V^1 \hat{p}_V^2, \qquad \forall \hat{p}^1, \hat{p}^2 \in \mathcal{H}_{\mathcal{V}} \tag{3.11}$$

and

$$\langle \mathbf{p}^1, \mathbf{p}^2 \rangle_{\mathbf{H}_{\mathcal{C}}} \coloneqq \sum_K |K| \mathbf{p}_K^1 \mathbf{p}_K^2, \qquad \forall \mathbf{p}^1, \mathbf{p}^2 \in \mathbf{H}_{\mathcal{C}} \tag{3.12}$$
$$\langle \hat{\mathbf{p}}^1, \hat{\mathbf{p}}^2 \rangle_{\mathbf{H}_{\mathcal{V}}} \coloneqq \sum_V |V| \hat{\mathbf{p}}_V^1 \hat{\mathbf{p}}_V^2, \qquad \forall \hat{\mathbf{p}}^1, \hat{\mathbf{p}}^2 \in \mathbf{H}_{\mathcal{V}}. \tag{3.13}$$

3.2 Discrete Operators

The nonlinear frictionless momentum and mass equations in the vector invariant form have three primary differential operators, namely divergence, vorticity, and gradient. For the first two, suppose $\mathbf{F}$ is continuous differentiable, and V and Σ are regions that can be discretized in a piecewise continuous arbitrary polygon of N sides, then we can, for all schemes, employ the Gauss Theorem:

$$\int_V \nabla \cdot \mathbf{F} dV = \oint_S \mathbf{F} \cdot \mathbf{n} dS \approx \sum_{i=1}^{N} \mathbf{F}_i \cdot \mathbf{n}_i l_i \tag{3.14}$$

and the Stokes theorem:

$$\int_{\Sigma} \nabla \times \mathbf{F} dV = \oint_{\partial\Sigma} \mathbf{F} \cdot \mathbf{t} dS \approx \sum_{i=1}^{N} \mathbf{F}_i \cdot \mathbf{t}_i l_i. \tag{3.15}$$

Dividing by the area/volume of the cell, we obtain the average of the divergence and vorticity, respectively.

The gradient of a scalar function f is a vector field, whose components are the partial derivatives of a point $\mathbf{p}$. It can be defined as:

$$(\nabla f(\mathbf{p})) \cdot \hat{\mathbf{n}} = \frac{\partial f}{\partial \hat{\mathbf{n}}}(\mathbf{p}) \tag{3.16}$$

Each scheme will have its own formulation of the aforementioned operators. Nonetheless, they are all consistent with the provided definitions.

3.2.1 A-grid

The A-grid, derived from Tomita et al. (2001), has all its variables defined on the vertices of the triangles. We require an interpolation of these variables at the dual edge midpoint so to apply the theorems (Figures 3.4). The correspondent dual edge will be the midpoint edge of the dual cell, whose vertices are the triangle barycentre. To simplify the notation, we will assume on this section that $\hat{e} = \hat{e}^{(b)}$.

First, let $h \in \mathcal{H}_v$ and $\mathbf{u} \in \mathbf{H}_v$. Then, our interpolations are of the following:

$$\overline{\mathbf{u}}^K = \frac{1}{3} \sum_{v \in \bigcup_{e \in \partial K} \partial e} \mathbf{u}_v \tag{3.17}$$

$$\overline{h}^K = \frac{1}{3} \sum_{v \in \bigcup_{e \in \partial K} \partial e} h_v. \tag{3.18}$$

and on the edge of the dual grid:

$$\widetilde{\mathbf{u}}^{\hat{e}} = \frac{1}{2} \sum_{K \in \partial \hat{e}} \overline{\mathbf{u}}^K \tag{3.19}$$

$$\widetilde{h}^{\hat{e}} = \frac{1}{2} \sum_{K \in \partial \hat{e}} \overline{h}^K. \tag{3.20}$$

The operators are defined on the dual mesh pentagonal-hexagonal mesh:

$$|\hat{K}| \mathbf{div}^{(\mathrm{A})} \mathbf{u}_{\hat{K}} = \sum_{\hat{e} \in \partial \hat{K}} \widetilde{\mathbf{u}}^{\hat{e}} \cdot \hat{\mathbf{n}}_{\hat{e}} |\hat{e}| n_{\hat{e},\hat{K}} \tag{3.21}$$

$$|\hat{K}| \mathbf{vort}^{(\mathrm{A})} \mathbf{u}_{\hat{K}} = \sum_{\hat{e} \in \partial \hat{K}} \widetilde{\mathbf{u}}^{\hat{e}} \cdot \hat{\mathbf{t}}_{\hat{e}} |\hat{e}| t_{\hat{e},\hat{K}} \tag{3.22}$$

$$|\hat{K}| \mathbf{grad}^{(\mathrm{A})} h_{\hat{K}} = \sum_{\hat{e} \in \partial \hat{K}} \widetilde{h}^{\hat{e}} \hat{\mathbf{n}}_{\hat{e}} |\hat{e}| n_{\hat{e},\hat{K}} - \sum_{\hat{e} \in \partial \hat{K}} h_K \hat{\mathbf{n}}_{\hat{e}} |\hat{e}| n_{\hat{e},\hat{K}}. \tag{3.23}$$

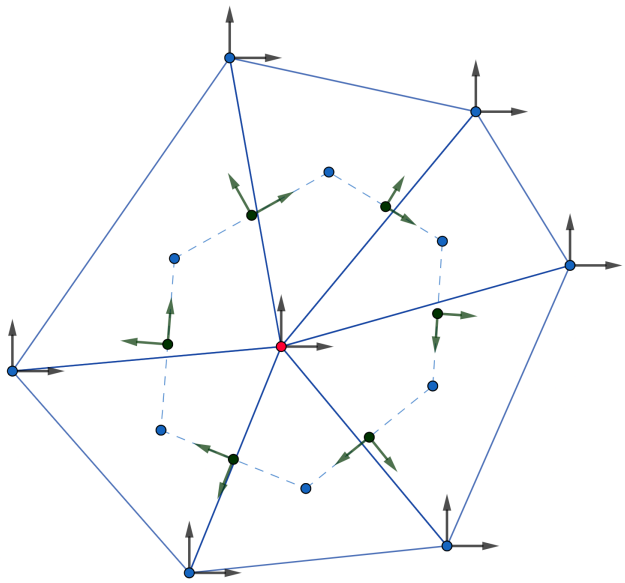

Figure 3.4: Hexagonal cell of an A-grid

The second term of the gradient is a correction term, so that homogenous fields are zero. Additionally, Tomita et al. (2001) argues that if the grid point vertex $\mathbf{v} \in \mathcal{V}$ coincides with the gravitational centre of the dual control volume $\widehat{\mathcal{C}}$, these operators would be consistent and have an increased accuracy.

The kinetic energy is defined at the same points and, therefore, the definition is simply:

$$E_K^{(\mathrm{A})} = \frac{|\mathbf{u}|^2_{\hat{K}}}{2}, \tag{3.24}$$

so that we will have an exact operator.

We recall that this method *as is* is unstable, since the A-grid discretization allows for the presence of spurious numerical oscillations known as pressure modes. Therefore, we require the application of some filter to damp these waves. Following the authors, we will use a biharmonic filter, defined as the divergence of the gradient of the vector field. In order to position the biharmonic field at the triangle vertices, we define a different gradient operator, which is positioned at the triangle barycentre. To compute the gradient, we interpolate the velocity at the midpoint edge of the triangles $\widetilde{\mathbf{u}}^e$ (do not confuse with the interpolation at the midpoint of the dual cell $\widetilde{\mathbf{u}}^{\hat{e}}$). This new gradient, we define as $\mathbf{grad'}^{(\mathrm{A})}$:

$$|K|\mathbf{grad'}^{(\mathrm{A})}\ \mathbf{u}_K = \sum_{e\in\partial K} \widetilde{\mathbf{u}}^e \mathbf{n}_e |e| n_{e,K}, \tag{3.25}$$

where $\widetilde{\mathbf{u}}^e = 1/2 \sum_{v\in\partial e} \mathbf{u}_v$. The divergent is applied to the resulting value. We will then have a diffusion operator $\nabla^2 = \Delta$ positioned at the vertices of the triangles. The same process is applied twice to get the biharmonic.

3.2.2 B-grid

This scheme from Danilov et al. (2017) has the mass field located at the vertices and the vector field at the barycentres of the triangle (Figure 3.5). Our dual edge will have its vertices at the neighbouring triangle barycentres and the neighbouring primal edge midpoint. The dual edge area will then be the third part of the sum of the neighbouring triangles:

$$|\hat{K}^{(b_2)}| = \frac{1}{3} \sum_{K \in \bigcup_{\hat{e} \in \partial \hat{K}} \partial \hat{e}} |K|. \tag{3.26}$$

Now, our dual cell will have 1/3 of the area of the sum of its neighbour triangles. The resulting cell will have around 12 to 14 edges. In this section, we will assume $\hat{K}^{(b_2)} = \hat{K}$.

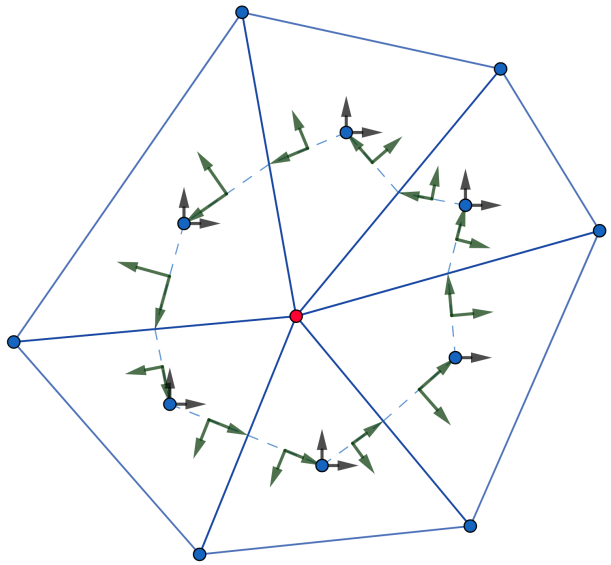

Figure 3.5: Hexagonal cell of an B-grid

First, let $h \in \mathcal{H}_v$ and $\mathbf{u} \in \mathbf{H}_\mathcal{C}$, then the necessary interpolation can be performed as follows:

$$\widetilde{h}^e = \frac{1}{2} \sum_{v \in \partial e} h_v$$

The primal operators (divergence, gradient and vorticity) are defined on this grid as follows:

$$|\hat{K}| \mathbf{div}^{(\mathrm{B})} h\mathbf{u}_v = \sum_{\hat{e} \in \partial \hat{K}} \sum_{K \in \partial \hat{e}} \widetilde{h}^K \mathbf{u}_K \cdot \hat{\mathbf{n}}_e d(\hat{\mathbf{e}}, \mathbf{K}), \tag{3.27}$$

$$|\hat{K}| \mathbf{vort}^{(\mathrm{B})} \mathbf{u}_v = \sum_{\hat{e} \in \partial \hat{K}} \sum_{K \in \partial \hat{e}} \mathbf{u}_K \cdot \hat{\mathbf{t}}_e d(\hat{\mathbf{e}}, \mathbf{K}), \tag{3.28}$$

$$|K| \mathbf{grad}^{(\mathrm{B})} h_K = \sum_{e \in \partial K} \widetilde{h}^e \mathbf{n}_e |e| \tag{3.29}$$

where $d(\hat{\mathbf{e}}, \mathbf{K})$ is the distance between the primal edge midpoint e and the triangular barycentre K and $\widetilde{h}^K$ is an interpolation on the barycentre of the triangular cells following (3.18). Note that $\mathbf{vort}^{(\mathrm{B})}$ is defined on the vertex v. To use in the momentum equation, we need to interpolate $\omega_v = (\mathbf{vort}^{(\mathrm{B})}\mathbf{u}_v + f_v)$ on the barycentre K using (3.18).

In contrast to the A-grid, The kinetic energy requires an interpolation, in order to employ $\mathbf{grad}^{(\mathrm{B})}$. Since the variables $\mathbf{u}$ are defined on the barycentre of the triangle, we define the following operator:

$$E_k^{(\mathrm{B})} = \frac{1}{6|\hat{K}|} \sum_{K \in \bigcup_{\widehat{e} \in \widehat{K}} \partial \widehat{e}} |K||\mathbf{u}_K|^2. \tag{3.30}$$

Similar to the A-grid, this scheme also requires some filter to reduce the noise, in order to stabilize the method. Following Danilov et al. (2017), we again use the biharmonic operator, however, in this case, the points are defined in the centre of the triangles. Thus, we define this operator on the B-grid as:

$$\Delta \mathbf{u} \approx (\mathbf{diff}^{(\mathrm{B})}\ \mathbf{u})_K = \sum_{K,L \in \bigcup_{e \in \partial K} \partial e} \mathbf{u}_K - \mathbf{u}_L. \tag{3.31}$$

This operator is applied twice to get the biharmonic.

3.2.3 C-grid

Both schemes on this section use the Voronoi Diagram as the dual of our primal. In this case, the circumcentre of the primal cell will be considered the centre of the cell: $\hat{K} = \hat{K}^{(c)}$.

Since each velocity component on the C-grid is not the complete vector, we let the following: $u \in \mathcal{H}_{\mathcal{E}}$ with $u_e = \mathbf{u}_e \cdot \hat{\mathbf{n}}_e$. We can then, define our divergence and vorticity similar as the previous:

$$(\nabla \cdot \mathbf{u})(\mathbf{K}) \approx (\mathbf{div}^{(\mathrm{C})}\ u)_K \coloneqq \frac{1}{|K|} \sum_{e \in \partial K} u_e |e| n_{e,K} \tag{3.32a}$$

$$(\mathbf{k} \cdot \nabla \times \mathbf{u})(\mathbf{v}) \approx (\mathbf{curl}^{(\mathrm{C})}\ u)_v \coloneqq \frac{1}{|\widehat{K}|} \sum_{e \in \partial \widehat{K}} u_e |\widehat{e}| t_{e,\widehat{K}} \tag{3.32b}$$

These operators are defined on the cell centres of the primal grid, in the divergence case, and the dual grid, in the case of the vorticity.

In the case of ICON, we can implicitly define its gradient as the negative adjoint of the divergent operator (da Veiga et al., 2014). In other words, for $h \in \mathcal{H}_{\mathcal{C}}$:

$$\langle \mathbf{div}\ u, h \rangle_{\mathcal{H}_{\mathcal{C}}} = -\langle u, \mathbf{grad}\ h \rangle_{\mathcal{H}_{\mathcal{E}}}. \tag{3.33}$$

Explicitly, for both schemes, we can define the discrete gradient as:

$$(\nabla h)(\mathbf{e}) \cdot \mathbf{n}_e \approx (\mathbf{grad}^{(\mathrm{C})}\ h)_e = \frac{h_K - h_L}{|\hat{e}|} n_{e,K}, \quad e = K|L. \tag{3.34}$$

A few other properties, we can define on these discretizations are:

1. $(\mathbf{curl}\ \mathbf{grad}\ h)_v = 0,\ \forall v \in \mathcal{V}$
2. $(\mathbf{curl}\ u)_v = -(\widehat{\mathbf{div}}\ u)_v,\ \forall v \in \mathcal{V}$

The divergence operator has at most a first order convergence for most cell geometries (Peixoto and Barros, 2013). For some polygons, such as squares, it can increase to a second order. However, in the case of triangles, it is known to present this first order only. In the case of this geometry, it is argued that it is because of the odd number of sides present, which is likely linked to the fact of geometry being *non-aligned*.

For the use of the icosahedral or its dual, the *chequerboard* pattern will still be present (Figure 3.2). In the case of triangles, it is present in the divergent. For its dual, it will be present in the vorticity operator, due to the property (2).

We can analyse the vorticity of our primal grid, by analysing the results of Peixoto and Barros (2013) for the divergence on the dual grid. On their analysis, it is expected that this operator would reach at most a 1st order approximation. If they were aligned, however, it would reach a 2nd order approximation. In essence, it is to be expected that our vorticity operator to have its convergence linked with the alignment of cells.

For the gradient operator, in equilateral triangles, it is expected to achieve a 2nd order convergence, since for these cells, the primal edge midpoint of the cells are equivalent to their dual edge midpoints. So, for distorted meshes, we will have a greater distance between these midpoints, and, therefore, a decrease on the convergence of the operator.

The following sections will deal with the other operators. Both reconstruction method and kinetic energy operators are computed differently for TRiSK and ICON.

3.2.3.1 TRiSK

The TRiSK method is inspired by the method of Arakawa and Lamb (1981), which is a weight based method. It reconstructs the tangent velocity of the whole Coriolis term of (3.64). In order to conduct the method, we restate the term as follows:

$$(f + \omega)\mathbf{k} \times u = q u^{\perp} h, \tag{3.35}$$

where $u^{\perp} = \mathbf{k} \times u$. We assume that our perpendicular velocity is a weighted combination of the normal velocities as:

$$|\hat{e}|(uhq)_e = \sum_{e' \in V_e} w_{e,e'} \widetilde{q}^{e'} \overline{h}^{e'} |e'| u_{e'}, \qquad V_e = \bigcup_{K \in \partial \widehat{e}} \partial K \tag{3.36}$$

where $w_{e,e'}$ is a weight scalar, $\tilde{q}^{e'}$ and $\overline{h}^{e'}$ are interpolations on the edge e' of the potential vorticity and sea level height, respectively. The weight scalar is computed as follows:

$$w_{e,e'} t_{e,v'} = \left(\sum_v R_{K,v} - \frac{1}{2} \right) n_{e',K} \tag{3.37}$$

where $\sum_v R_{K,v}$ is the sum of normalized areas traversing from e' to e. The vertex v' is chosen to be the last vertex encountered in the path from e' to e.

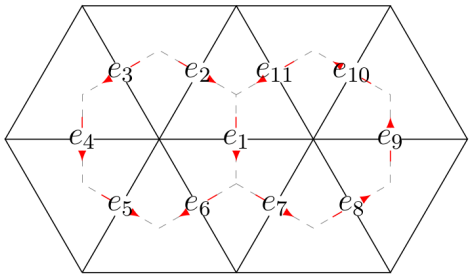

Figure 3.6: TRiSK example illustration

Thuburn et al. (2009) calculated the reconstruction on triangles in a linear shallow water equations with two different methods. The first method utilized the primal cell edges to calculate the weights. For example, to calculate the perpendicular velocity at e_1 as illustrated in Figure 3.6, we will have:

$$\begin{aligned}|\hat{e}_1|(uhq)_{e1} = w_{e_1,e_{11}}|e_{11}|u_{e_{11}}\overline{h}^{e_{11}}\widetilde{q}^{e_{11}} + w_{e_1,e_2}|e_2|u_{e_2}\overline{h}^{e_2}\widetilde{q}^{e_2} \\ + w_{e_1,e_6}|e_6|u_{e_6}\overline{h}^{e_6}\widetilde{q}^{e_6} + w_{e_1,e_7}|e_7|u_{e_7}\overline{h}^{e_7}\widetilde{q}^{e_7}.\end{aligned}$$

The second method, used the dual cells edges. For example, to calculate the same edge e_1:

$$\begin{aligned}|\hat{e}_1|(uhq)_{e1} = w_{e_1,e_7}|e_7|u_{e_7}\overline{h}^{e_7}\widetilde{q}^{e_7} + w_{e_1,e_8}|e_8|u_{e_8}\overline{h}^{e_8}\widetilde{q}^{e_8} \\ + w_{e_1,e_9}|e_9|u_{e_9}\overline{h}^{e_9}\widetilde{q}^{e_9} + w_{e_1,e_{10}}|e_{10}|u_{e_{10}}\overline{h}^{e_{10}}\widetilde{q}^{e_{10}} \\ + w_{e_1,e_{11}}|e_{11}|u_{e_{11}}\overline{h}^{e_{11}}\widetilde{q}^{e_{11}} + w_{e_1,e_2}|e_2|u_{e_2}\overline{h}^{e_2}\widetilde{q}^{e_2} \\ + w_{e_1,e_3}|e_3|u_{e_3}\overline{h}^{e_3}\widetilde{q}^{e_3} + w_{e_1,e_4}|e_4|u_{e_4}\overline{h}^{e_4}\widetilde{q}^{e_4} \\ + w_{e_1,e_5}|e_5|u_{e_5}\overline{h}^{e_5}\widetilde{q}^{e_5} + w_{e_1,e_6}|e_6|u_{e_6}\overline{h}^{e_6}\widetilde{q}^{e_6}.\end{aligned}$$

We shall denote the former as TRiSK1 and the latter as TRiSK2.

The interpolation of $\tilde{q}_e$ is done in a way as to provide energetic neutrality to the operator (Ringler et al., 2010). Therefore, for a fixed e, we require that:

$$\widetilde{q}^{e'} = \frac{\overline{q}^{e} + \overline{q}^{e'}}{2}, \qquad e' \in \bigcup_{K \in \partial\widehat{e}} \partial K \tag{3.38}$$

where the interpolated variables are:

$$\overline{q}^{e} = (1/2)\sum_{\hat{K}\in U_e} q_{\hat{K}} \qquad U_e = \bigcup_{\widehat{K}\in\partial\widehat{e}} \widehat{K} \tag{3.39}$$

$$\overline{h}^{e} = \frac{1}{A_e}\sum_{K\in V_e} h_K A_{e,K} \qquad V_e = \bigcup_{K\in\partial e} K \tag{3.40}$$

On the original work, the kinetic energy operator (E_k) was defined on Voronoi Diagrams; however, Weller et al. (2012) provided a modification, which applied to non-voronoi type grids as:

$$(E_k)_K = \frac{1}{|K|} \sum_{e \in \partial K} A_{e,K} u_e^2 \tag{3.41}$$

which can be considered a barycentric interpolation around the edges of the triangle.

3.2.3.2 ICON-O

We start by rewriting (3.64) in its weak/variational form. For that, we multiply the vector invariant form (3.2), by a couple of test functions ψ, ϕ:

$$\left\langle \frac{\partial h}{\partial t}, \psi \right\rangle_{L^2} = -\langle \nabla \cdot h\mathbf{u}, \psi \rangle_{L^2}, \tag{3.42a}$$

$$\left\langle \frac{\partial \mathbf{u}}{\partial t}, \boldsymbol{\phi} \right\rangle_{\mathbf{L}^2} = -\langle \omega \mathbf{u}^{\perp}, \boldsymbol{\phi} \rangle_{\mathbf{L}^2} - \langle \nabla \Phi, \boldsymbol{\phi} \rangle_{\mathbf{L}^2} - \langle \nabla \mathrm{K}, \boldsymbol{\phi} \rangle_{\mathbf{L}^2}, \tag{3.42b}$$

where have that $\langle \mathbf{A}, \mathbf{B} \rangle := \int_\Omega \mathbf{A} \cdot \mathbf{B} dS$ and $\langle f, g \rangle := \int_\Omega f g dS$. We are assuming that both h and $\mathbf{u}$ are differentiable.

Next, we will define the concept of admissible reconstructions. Models with staggered variables require reconstructions in a way to connect these variables located at different points, so that we can perform the computations. These admissible reconstructions are configured in a way as to retain many properties of the model. For that, we define the following linear maps:

$$\mathcal{P}_\mathcal{G} : \mathcal{H}_\mathcal{E} \to \mathbf{H}_\mathcal{C} \tag{3.43}$$

$$v \mapsto \mathcal{P}_\mathcal{G} v \tag{3.44}$$

with $\langle \mathcal{P}_\mathcal{G} v, \phi \rangle_{\mathbf{H}_\mathcal{C}} = \langle v, {\mathcal{P}_\mathcal{G}}^T \phi \rangle_{\mathcal{H}_\mathcal{E}}$, where ${\mathcal{P}_\mathcal{G}}^T$ is the transpose operator. To be able to connect the vertices to edges, we define:

$$\hat{\mathcal{P}}_\mathcal{G} : \mathcal{H}_\mathcal{E} \to \mathbf{H}_\mathcal{V} \tag{3.45}$$

$$v \mapsto \mathcal{P}_\mathcal{G} v. \tag{3.46}$$

To get the connection from the vertex to the edge points that will provide a tangential flux, we define the $\hat{\mathcal{P}}_\mathcal{G}^\dagger$:

$$\hat{\mathcal{P}}_\mathcal{G}^\dagger : \mathbf{H}_\mathcal{C} \to \mathcal{H}_\mathcal{E} \tag{3.47}$$

$$v \mapsto \hat{\mathcal{P}}_\mathcal{G}^\dagger v. \tag{3.48}$$

Both $\hat{\mathcal{P}}_\mathcal{G}$ and $\hat{\mathcal{P}}_\mathcal{G}^\dagger$ is going to be used for the vector reconstruction.

It is important to note that the domain and range of both operators have different dimensions (Section 2); therefore, they are not isomorphic and, consequently, non-invertible. With these maps, we can finally define the admissible reconstruction. From Korn and Linardakis (2018):

Definition 3.2.1. Let $\mathcal{M}_\mathcal{G} := {\mathcal{P}_\mathcal{G}}^T \mathcal{P}_\mathcal{G}$ and $\hat{\mathcal{M}}_\mathcal{G} := \hat{\mathcal{P}}_\mathcal{G}^\dagger \hat{\mathcal{P}}_\mathcal{G}$. The $(\mathcal{P}_\mathcal{G}, \hat{\mathcal{P}}_\mathcal{G}, \hat{\mathcal{P}}_\mathcal{G}^\dagger)$ is an admissible reconstruction if:

1. $\mathcal{P}_\mathcal{G}$, $\hat{\mathcal{P}}_\mathcal{G}$ reproduces constants;
2. $\mathcal{P}_\mathcal{G}$ and ${\mathcal{P}_\mathcal{G}}^\dagger$ provide unique and first order accurate fluxes;
3. The null space $\mathcal{N}_{\mathcal{M}_\mathcal{G}} := \{v \in \mathcal{H}_\mathcal{E} : \mathcal{M}_\mathcal{G} v = 0\}$ coincides with the divergence noise space $N := \{v \in \mathcal{H}_\mathcal{E} : \text{ sgn}(\textbf{div } v_K) \neq \text{sgn}(\textbf{div } v_L) \text{ and } |\textbf{div } v_K| \approx |\textbf{div } v_L|, \forall e = K|L\}$;
4. $\mathcal{M}_\mathcal{G}$ is strictly positive definite on the image space;
5. $\widehat{\mathcal{M}_\mathcal{G}}$ is skew symmetric;

According to the authors, the property (1) "allows to avoid dealing with discontinuous fluxes", while property (2) allows for a more accurate model and increase the stability of the model. The imposition (3) deals with the chequerboard pattern for the triangular primal grid. To produce an operator with filtering properties, we aim for one in which the image and its kernel are orthogonal, i.e. $\langle \mathcal{M}_\mathcal{G} v, u \rangle_{\mathcal{H}_\mathcal{E}} = 0$, $v \in \mathcal{H}_\mathcal{E}$, $u \in \mathcal{N}_{\mathcal{M}_\mathcal{G}} \subset \mathcal{H}_\mathcal{E}$. That would make $\mathcal{H}_\mathcal{E} = \mathring{\mathcal{H}}_\mathcal{E} \bigoplus \mathcal{N}_{\mathcal{M}_\mathcal{G}}$. Therefore, for a velocity $v = u + \gamma \implies \mathcal{M}_\mathcal{G} v = \mathcal{M}_\mathcal{G} u \in \mathring{\mathcal{H}}_\mathcal{E}$. The requirement 4 is necessary to invert the operators, to retrieve the variables h and $\mathbf{u}$ and, finally, 5 imposes that the Coriolis term should not contribute with energy to the system.

By using this method of admissible reconstructions and connecting different discrete spaces, we can now create a viable discretization for each operator of the vector invariant shallow water equations. The details of the discretization of each term can be seen in Korn and Linardakis (2018), but in essence:

$$\langle \textbf{div } hu, \psi \rangle_{L^2} \rightsquigarrow \langle \textbf{div } {\mathcal{P}_\mathcal{G}}^T h \mathcal{P}_\mathcal{G} u, \psi \rangle_{\mathcal{H}_\mathcal{C}} = \langle \text{div } \mathcal{M}_\mathcal{G} hu, \psi \rangle_{\mathcal{H}_\mathcal{C}} \tag{3.49a}$$

$$\langle (f+\zeta)\mathbf{k} \times u, \phi \rangle_{\mathbf{L}^2} \rightsquigarrow \langle \hat{\mathcal{P}}_\mathcal{G}^\dagger (f+\zeta) \hat{\mathcal{P}}_\mathcal{G} \mathbf{k} \times u, \phi \rangle_{\mathcal{H}_\mathcal{E}} = \langle \hat{\mathcal{M}}_\mathcal{G} (f+\zeta)\mathbf{k} \times u, \phi \rangle_{\mathcal{H}_\mathcal{E}} \tag{3.49b}$$

$$\langle \textbf{grad } \Phi, \phi \rangle_{\mathbf{L}^2} \rightsquigarrow \mathcal{M}_\mathcal{G} \langle \textbf{grad } \Phi, \phi \rangle_{\mathcal{H}_\mathcal{E}} \tag{3.49c}$$

$$\langle \textbf{grad } E_k, \phi \rangle_{\mathbf{L}^2} \rightsquigarrow \mathcal{M}_\mathcal{G} \langle \textbf{grad } \frac{|\mathcal{P}_\mathcal{G} u|^2}{2}, \phi \rangle_{\mathcal{H}_\mathcal{E}}. \tag{3.49d}$$

$$\langle \frac{\partial}{\partial t} \mathbf{u}, \phi \rangle_{\mathbf{L}^2} \rightsquigarrow \langle \frac{\partial}{\partial t} \mathcal{M}_\mathcal{G} u, \phi \rangle_{\mathcal{H}_\mathcal{E}} \tag{3.49e}$$

The discretized weak form of the system (3.42) is, then:

$$\langle \frac{\partial}{\partial t} h, \psi \rangle_{\mathcal{H}_\mathcal{C}} = -\langle \textbf{div } \mathcal{M}_\mathcal{G}[h, u], \psi \rangle_{\mathcal{H}_\mathcal{C}} \tag{3.50a}$$

$$\langle \frac{\partial}{\partial t} \mathcal{M}_\mathcal{G} u, \phi \rangle_{\mathcal{H}_\mathcal{E}} = -\langle \widehat{\mathcal{M}_\mathcal{G}}[\omega, u] u, \phi \rangle_{\mathcal{H}_\mathcal{E}} - \langle \mathcal{M}_\mathcal{G} \textbf{grad } \Phi, \phi \rangle_{\mathcal{H}_\mathcal{E}} - \langle \mathcal{M}_\mathcal{G} \textbf{grad} \frac{|\mathcal{P}_\mathcal{G} u^2|}{2}, \phi \rangle_{\mathcal{H}_\mathcal{E}}, \tag{3.50b}$$

The authors show that this equation conserves energy, vorticity and enstrophy.

Note that to get the approximate solution of the algorithm, it is necessary to calculate the inversion of the mass matrix $\mathcal{M}_\mathcal{G}$ at each time step. This requires a high computational

cost. To bypass this problem, we use a lumping, i.e. the substitution of the mass matrix by a diagonal matrix. We can let $\mathcal{M_G}^{-1} \approx I$. Korn and Danilov (2016) studied this form of lumping and noted that it does not expressively affect the solutions on the triangular grid.

What is left for us to define, are the linear maps betweens the spaces that compose the admissible reconstruction. The original authors used the Perot's reconstruction, since it had all the aforementioned properties.

3.2.3.3 Perot's Reconstruction

These reconstructions were developed by Perot (2000). He showed that this method is at least first order accurate and maintain the energy conservation regarding the Coriolis term. Korn and Danilov (2016) and Korn and Linardakis (2018) have shown that the method has a filtering property on the divergence, and it is strict positive-definite. These properties demonstrate that this reconstruction is admissible. We can define these operators as:

$$Pv_K := \frac{1}{|K|} \sum_{e \in \partial K} v_e |e| d(\mathbf{e}, \mathbf{K}) \mathbf{n}_e \tag{3.51a}$$

$$P^T F_{\hat{e}} := \frac{1}{|\hat{e}|} \left[\sum_{K \in \partial \hat{e}} \mathbf{F}_K d(\mathbf{e}, \mathbf{K}) \right] \cdot \mathbf{n}_{\hat{e}} \tag{3.51b}$$

The dual reconstruction is defined as the following:

$$\hat{P} v_{\hat{K}} := \frac{1}{|\hat{K}|} \sum_{e \in \partial \hat{K}} v_e |\hat{e}| \mathbf{e} \times d(\mathbf{e}, \hat{\mathbf{K}}) \mathbf{n}_e \tag{3.52a}$$

$$\hat{P}^\dagger F_e := \frac{1}{|e|} \left[\sum_{\hat{K} \in \partial e} \mathbf{F}_{\hat{K}} d(\mathbf{e}, \hat{\mathbf{K}}) \right] \cdot \mathbf{n}_e \tag{3.52b}$$

We can also show that the Perot Reconstruction removes the chequerboard pattern by using Gassmann (2011) argument. Let $(\mathbf{j}_1, \mathbf{j}_2, \mathbf{j}_3)$, and v_i be the velocity variable on the i-th component of the trivariate coordinate (as in Figure 3.3). We have the triangle K_1 composed of the edges $\{e_1, e_2, e_3\}$, K_2 of $\{e_1, e_5, e_7\}$, K_3 of $\{e_2, e_6, e_8\}$, and K_4 of $\{e_3, e_4, e_9\}$. The Perot map on the triangles, is, then:

$$\begin{aligned}
Pv_{K_1} &:= \frac{1}{3}(u_1 \mathbf{j}_1 + u_2 \mathbf{j}_2 + u_3 \mathbf{j}_3) \\
Pv_{K_2} &:= \frac{1}{3}(u_1 \mathbf{j}_1 + u_5 \mathbf{j}_2 + u_7 \mathbf{j}_3) \\
Pv_{K_3} &:= \frac{1}{3}(u_8 \mathbf{j}_1 + u_2 \mathbf{j}_2 + u_6 \mathbf{j}_3) \\
Pv_{K_4} &:= \frac{1}{3}(u_9 \mathbf{j}_1 + u_4 \mathbf{j}_2 + u_3 \mathbf{j}_3),
\end{aligned}$$

Where we used the fact that $A_e = 1/3|K|$. Then, for an equilateral grid, we have a simple average of all edges of each triangle projected in the centre. Now, the transposed map is then:

$$P^T(Pu)_1 := \frac{1}{3}[u_1 - \frac{1}{2}(u_2 + u_5) - \frac{1}{2}(u_3 + u_7)]$$
$$P^T(Pu)_2 := \frac{1}{3}[-\frac{1}{2}(u_1 + u_8) + u_2 - \frac{1}{2}(u_6 + u_3)]$$
$$P^T(Pu)_3 := \frac{1}{3}[-\frac{1}{2}(u_1 + u_9) - \frac{1}{2}(u_2 + u_4) + u_3].$$

Divergent can, therefore, be calculated as:

$$\textbf{Div } P^T(Pv) = \frac{1}{3}[D_1 + D_2 + D_3]$$

where D_1, D_2, and D_3 are the divergences on three rhombi overlapping the triangle K_1. This shows that the Perot reconstruction on an equilateral mesh satisfies the condition of Gassmann (2011), since the divergence of each triangular cell K can be restated as the average of the rhombi overlapping this cell. On a curved surface, however, that might not necessarily be true. In particular, $A_e \neq |\hat{e}||e|/2$, and, therefore, the previous argument is made invalid for a spherical grid. Hence, the aforementioned property will act only as an approximation. Nonetheless, since the spherical excess of a grid tends to 0 as it gets refined, then the filtering capability of the reconstruction is expected to improve for each bisection.

3.3 Error Analysis

To be able to compare both schemes, we analyse the error of their spatial operators and variables. We are mainly focusing on the norm 2 and the infinity norm. Following Ringler et al. (2010), we define the errors as:

$$L_2 = \sqrt{\frac{S((f_n(j) - f_r(j))^2)}{S(f_r^2(j))}} \tag{3.53a}$$

$$L_\infty = \frac{\max_j |f_n(j) - f_r(j)|}{\max_j |f_r(j)|}, \tag{3.53b}$$

assuming $S(f_r^2(j)) \neq 0$ and $\max_j |f_r(j)| \neq 0$, where:

$$S = \frac{\sum_{j=1}^{N_j} f(j)A(j)}{\sum_{j=1}^{N_j} A(j)}. \tag{3.54}$$

In the case of geostrophic balance, where **div** $uh = 0$, we will substitute $S(f_r^2(j))$ and $\max_j |f_r(j)|$ by 1.

3.3.1 Test Cases

For our analysis we will use four different test cases (TC0, TC1, TC2). Each case has its own importance and details of their use will be cleared below. Global parameters are set as to match the earths' parameter:

1. radius $r \equiv 6.37122 \times 10^6$ m,
2. rotation frequency $\Omega \equiv \frac{2\pi}{86400} \approx 7.292 \times 10^{-5}$ s^{-1},
3. acceleration of gravity $g \equiv 9.80616$ m s^{-1}.

Latitude and Longitude will be denoted as θ and ϕ.The mentioned testcases are described as follows:

3.3.1.1 Test Case 0

TC0 is the standard nonlinear geostrophic balance case from Williamson et al. (1992). The generalized initial conditions are, given an arbitrary choice of $\alpha \in (0, \pi/2)$, by:

$$(u_\phi)_0 = u_0 \cos\theta \cos\alpha + \cos\phi \sin\alpha \tag{3.55a}$$
$$(u_\theta)_0 = -u_0 \sin\phi \sin\alpha \tag{3.55b}$$

where $u_0 = 2\pi/(12\text{days})$. The height field is initialized as:

$$h = h_0 - \frac{1}{g}\left(a\Omega u_0 \frac{u_0^2}{2}\right)(-\cos\phi\cos\theta\sin\alpha + \sin\theta\cos\alpha)^2, \tag{3.56}$$

with $h_0 = 2.94 \times 10^4/g$. The Coriolis parameter is also given by:

$$f = 2\Omega(-\cos\phi\cos\theta\sin\alpha + \sin\theta\cos\alpha). \tag{3.57}$$

The bathymetry field is trivial, i.e. $b = 0$. In our work, we analyse the above equations on the parameter $\alpha = 0$.

The spatial distribution of u, h, and **grad** h can be observed in Figure 3.7. The divergence field is not shown, since the field is geostrophic, and, therefore, **div** $u = 0$.

This case is a steady state solution, where we know that the solution would be the same for all integrated times. This makes it easier to evaluate the error of variable ($\mathbf{u}$,h). We will use this case to compare with all operators from all schemes, as they will have a direct impact on the error evolution of the variables.

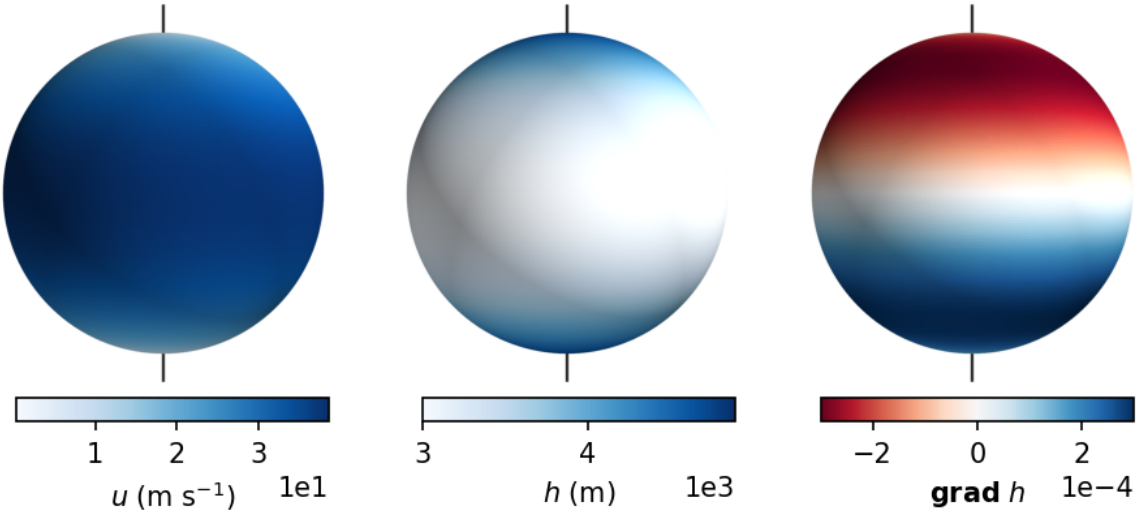

Figure 3.7: Zonal (u) component of the velocity vector field, mass field (h), and its respective gradient.

3.3.1.2 Test Case 1

This is a special case from Tomita et al. (2001) to test the spatial operators of its scheme. We define two test functions as:

$$\alpha(\phi, \theta) = \sin(\phi), \tag{3.58}$$
$$\beta_{m,n}(\phi, \theta) = r^2 \cos(m\phi) \cos^4(n\theta). \tag{3.59}$$

Then the variables $\mathbf{u}$ and h are defined as:

$$\mathbf{u} = \alpha \nabla \beta \tag{3.60}$$

We will evaluate this condition with the parameters set as $m = n = 1$. The spatial distribution of the spherical vector field, and its divergent, can be seen in Figure 3.8. These do not have analytical solutions, so we are not aiming to evaluate their error integrated in time.

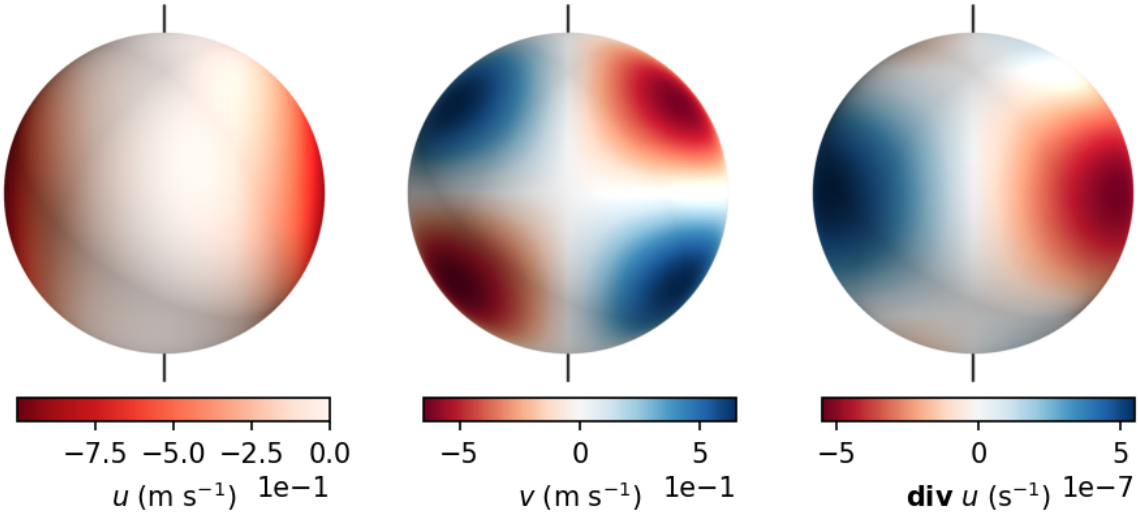

Figure 3.8: Zonal (u) and meridional (v) component of velocity vector field, and the divergence of the velocity.

3.3.1.3 Test Case 2

This case is also from Williamson et al. (1992). It is a zonal flow over an isolated mountain. It is defined as follows:

$$b = b_0(1 - r/R), \tag{3.61}$$

where $b_0 = 2 \times 10^3$ m, $R = \pi/9$,

$$r = \min(R^2, \sqrt{(\phi - \phi_c)^2 + (\theta - \theta_c)^2}),$$

$\phi_c = -\pi/2$, $\theta_c = \pi/6$. The mass variable is a constant $h = 5960$ m and the velocity is a zonal flow, similar to TC0:

$$(u_\phi)_0 = u_0 \cos\theta \tag{3.62}$$
$$(u_\theta)_0 = 0, \tag{3.63}$$

where $u_0 = 20$ m s^{-1}. The bathymetry is seen in Figure 3.9.

This testcase is useful to verify the dynamical evolution of the scheme. There is no known analytical solution.

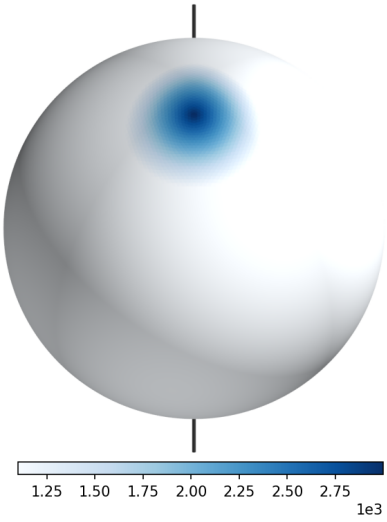

Figure 3.9: Bathymetry.

3.3.2 Spatial and Time Accuracy

In this section, we will present the error operators of all the terms in the system of shallow water equations. We will divide our results for the A-, B-grid and the C-grid TRiSK and ICON.

3.3.2.1 Divergence

The divergence operator is known to have at most a second order convergence (Peixoto and Barros, 2013). This is true for squares; however, for triangles the Gauss' Theorem will only be at most first order. This is likely because of the non-alignment of the cells, since it has an odd number of edges. On quasi-hexagonal cells, it is shown that the convergence rate for rougher grids is close to second order. However, since the refinement increases the cell misalignment, this convergence is lost. Thus, finer grids will have a convergence close to the first order.

Our A- and B-grid schemes will have its operator defined on the dual grid, which are cells of 5 to 6 edges for the former, or 10 to 12 edges for the latter. On both of these cases, it is expected that the operator will have a second order convergence, at least for the first few grid generations (g_i). Since the cells of our grid have an alignment similar to the standard grid (Peixoto and Barros, 2013), we expect the convergence to slow down to a first order for finer grids. Additionally, the presence of intense imprinting on our grid is likely, since our mesh shows strong signs of distortion (Section 2).

In the case of the C-grid, we expect both schemes to have a first order convergence. Additionally, ICON will likely show less noise, than the traditional operator (TRiSK). However, since our grid is highly distorted, some noise might not be completely removed.

We will display the error of both TC0 and TC1. We can then evaluate both convergence and distribution of the error in a trivial and non-trivial divergence field.

A- B-grid

Both schemes show a similar convergence rate for both cases (Table 3.1 and Figures 3.10 and 3.11). They display a near second order on L_2 norm. There is also second order on the L_∞; however, only up to g_5 on TC0 for the B-grid, and g_4 on TC1 for both schemes. For the geostrophic case, the error from g_5 to g_6 has a difference of around 40% for the B-grid, slightly less than first order. For the TC1, on the other hand, there is a decrease of 45% and 53% for the A-grid and 39% and 45% for the B-grid for the grid refinement of g_4 to g_5 and g_5 to g_6. It is also evident from the error observation that the B-grid displays an overall smaller error.

Table 3.1: Maximum Divergence error for A-/B-grid for each grid generation for all Test Cases.

g-level	TC0	TC1
g_0	0/0	$6.6106.10^{-8}/4.7567.10^{-10}$
g_1	0/0	$2.1633.10^{-7}/7.9352.10^{-8}$
g_2	$7.1409.10^{-8}/1.7669.10^{-8}$	$7.2038.10^{-8}/2.2101.10^{-8}$
g_3	$2.6386.10^{-8}/8.9528.10^{-9}$	$1.9842.10^{-8}/6.2014.10^{-9}$
g_4	$7.6860.10^{-9}/2.4695.10^{-9}$	$5.4219.10^{-9}/2.3443.10^{-9}$
g_5	$2.4493.10^{-9}/6.3977.10^{-10}$	$2.5248.10^{-9}/1.4390.10^{-9}$
g_6	$8.6826.10^{-10}/3.8031.10^{-10}$	$1.3836.10^{-9}/7.9291.10^{-10}$

Both schemes also present a similar error distribution on the sphere (Figure 3.10 and Figure 3.11). For TC0, the largest errors are located near the edges of g_0. Additionally, it is evident a pattern of a zonal variation on the face of each g_0 triangle, where the smallest errors are located on the centre of each face. In this case, the main difference between schemes is that the error sign is flipped (A-/B-grid shows a positive/negative error). For TC1, there is a large error on the edges of g_0. There is also a second expected error pattern which matches with the magnitude of the true field (Figure 3.8). However, this pattern is dwarfed by the much larger error of the edges. The main issue is likely again due to the cell misalignment.

For the A-grid, our results are similar to the ones provided by Tomita et al. (2001) on the standard icosahedral grid. It is likely that the provided divergent operator of the authors is not as highly affected by the grid distortion as the ones of Danilov et al. (2017), since for particular conditions it still provided with near second order convergence. However, the absolute the error was still smaller for the B-grid. This could be explained by the use of a larger stencil, i.e. the dual cell contains 10 to 12 edges, which could positively impact the divergence approximation. Regardless, There is a refinement issue which makes the operator lose its order of convergence. The non-linear geostrophic case seems less impacted, since the field that it is trying to approximate is homogenous, but the main culprit of the convergence loss could be associated due to the mismatch between the grid vertex and the associated barycentre of the dual cell.

C-grid

Both schemes have a similar rate of convergence, being near first order for both norms (Table 3.2 and Figures 3.12 and 3.13). For TC0, both schemes accelerate the convergence to near first order and have very similar absolute errors. For TC1, on the other hand, TRiSK

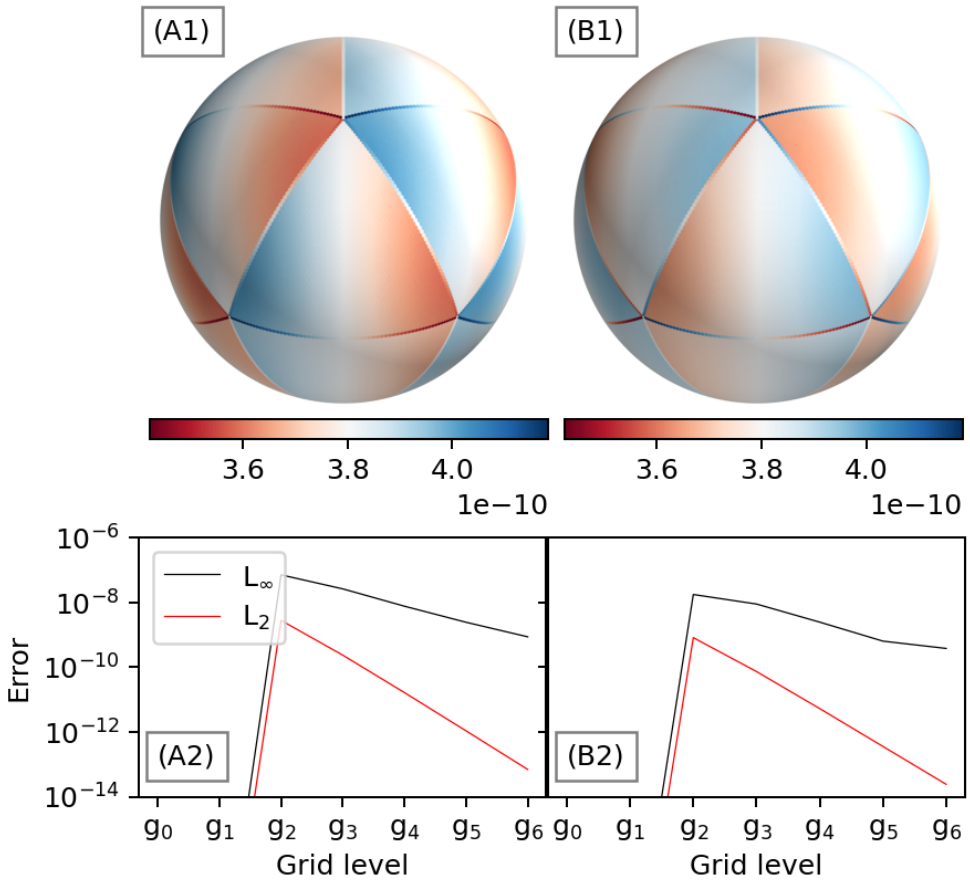

Figure 3.10: Spatial distribution (1) and plot for different levels (2) of the error of the divergence operator for TC0 for both A- (A) and B- grid (B).

is also near first order through all grid refinements, however, ICON's scheme maintains a second order convergence up to g_3. Further refinements show deceleration of the error, the minimum value is $g_4 \rightarrow g_5$, when the error decreases by only 40%. However, there is a slight acceleration from $g_5 \rightarrow g_6$, when the error decreases by 48%, indicating that the operator will reach a first order convergence. Although both absolute errors are similar, the standard divergence operator shows, surprisingly, a slight smaller error than ICON, even though the latter has a larger stencil.

The spatial error distribution shows clearly the presence of a chequerboard pattern for the traditional operator for both testcases (Figure 3.12 and Figure 3.13). This magnitude of this noise is larger near the vertices of the original icosahedron. This error pattern seems linked with the triangle distortion, since from Figure 3.14 it can be seen that for large distortions there is a larger magnitude of the error on both positive and negative sides. Additionally, on TC1, the expected pattern of the divergence field with its error is not observed, due to the mesh being contaminated by the noise.

On the other hand, ICON's operator seems to provide some improvement on the operator. For TC0, this improvement is modest and much of the noise is still present in the grid (Figure 3.12.B1). A much larger correction is displayed in TC1. As expected, there is still some noise

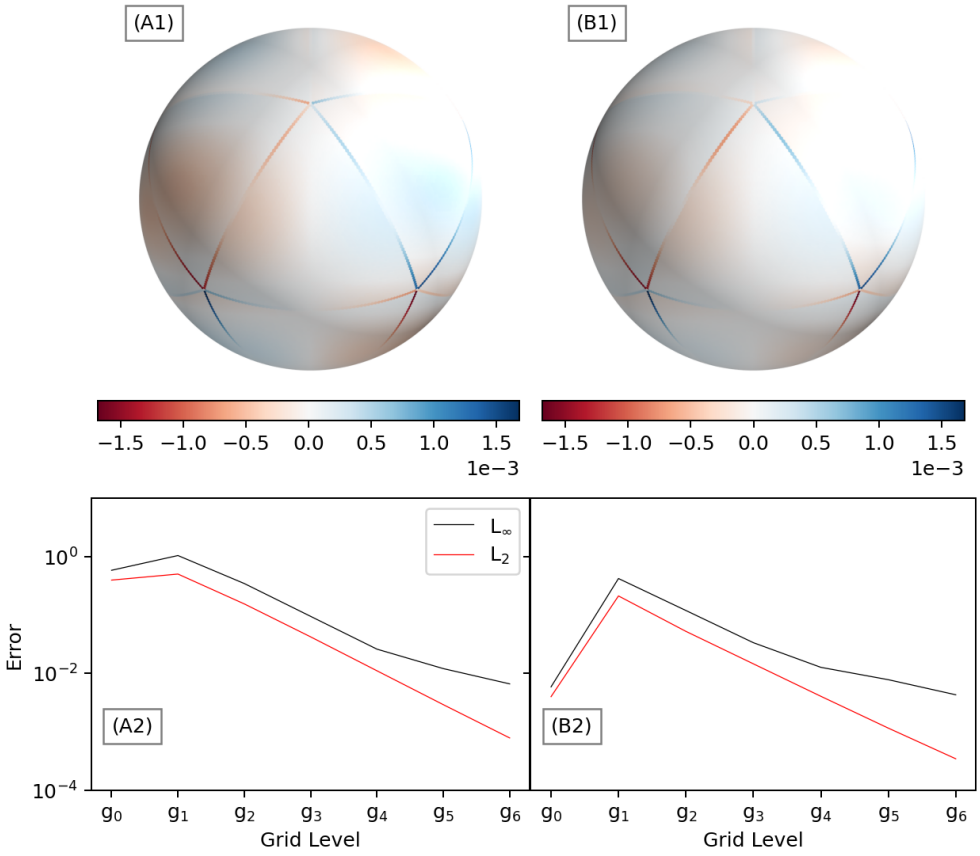

Figure 3.11: Same as Figure 3.10, but for TC1.

present on the grid, which is located near some vertices of g_0 (Figure 3.13.B1). As observed in Figure 3.14, these errors are associated with the grid distortion. This indicates that, although the noise can be removed of the operator, its efficiency is largely impacted by the grid distortion. The reason why some vertices are affected than others, might be due to the magnitude of the vector field, since the noise is larger near regions of large velocities.

Overall Comparison

Grid imprinting is an inherent behaviour of the operator on the grid. The error results of A-/B-grid are similar to the ones obtained by both Tomita et al. (2001) and Peixoto and Barros (2013). The former scheme is less subjected by the grid quality compared to the latter scheme. This, on the other hand, displays a deceleration in both tested cases. A similar behaviour occurs with ICON, likely due to its extended stencil. The simpler standard operator of TRiSK, albeit, not apparently affected by the distortion, presents a lower convergence rate than ICON. As though seemingly unexpected that the absolute error of TRiSK being larger than ICON, this is likely the consequence of the combined extreme grid distortion of the vertex and the chosen initial condition. Other tested conditions (not displayed) shows that ICON does actually portray not only a better convergence, but also an overall absolute error smaller than the traditional operator. Since the use of the standard grid by Korn and Linardakis (2018) portrays this result for the tested TC0, it is likely that a better distribution

Table 3.2: Maximum Divergence error for TRiSK/ICON for each grid.

g-level	TC0	TC1
g_0	0/0	$2.9340.10^{-1}/8.8583.10^{-1}$
g_1	$1.8475.10^{-3}/1.8639.10^{-6}$	$1.6882.10^{-1}/4.3079.10^{-1}$
g_2	$1.9999.10^{-3}/2.1115.10^{-3}$	$8.3112.10^{-2}/1.3168.10^{-1}$
g_3	$1.2830.10^{-3}/1.4322.10^{-3}$	$4.0739.10^{-2}/3.6644.10^{-2}$
g_4	$6.6764.10^{-4}/7.8719.10^{-4}$	$2.0110.10^{-2}/1.6423.10^{-2}$
g_5	$3.3579.10^{-4}/4.0722.10^{-4}$	$9.9936.10^{-3}/9.9437.10^{-3}$
g_6	$1.6819.10^{-4}/2.0656.10^{-4}$	$4.9792.10^{-4}/5.4589.10^{-4}$

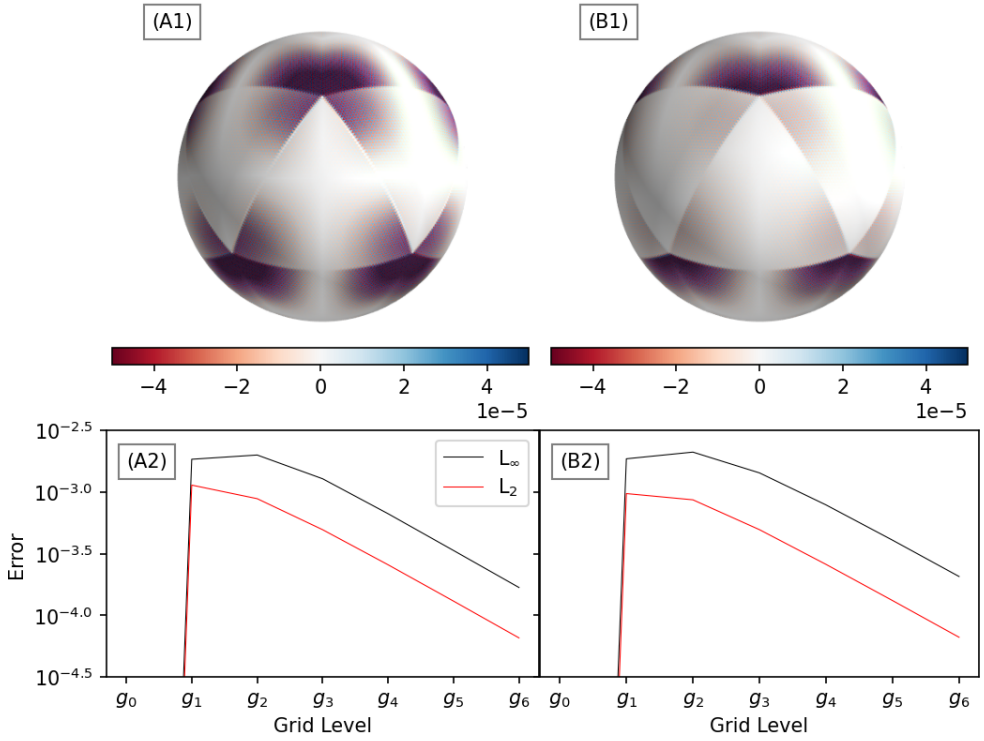

Figure 3.12: Spatial distribution (1) and plot for different levels (2) of the error of the divergence operator for TC0 for both TRiSK- (A) and ICON (B).

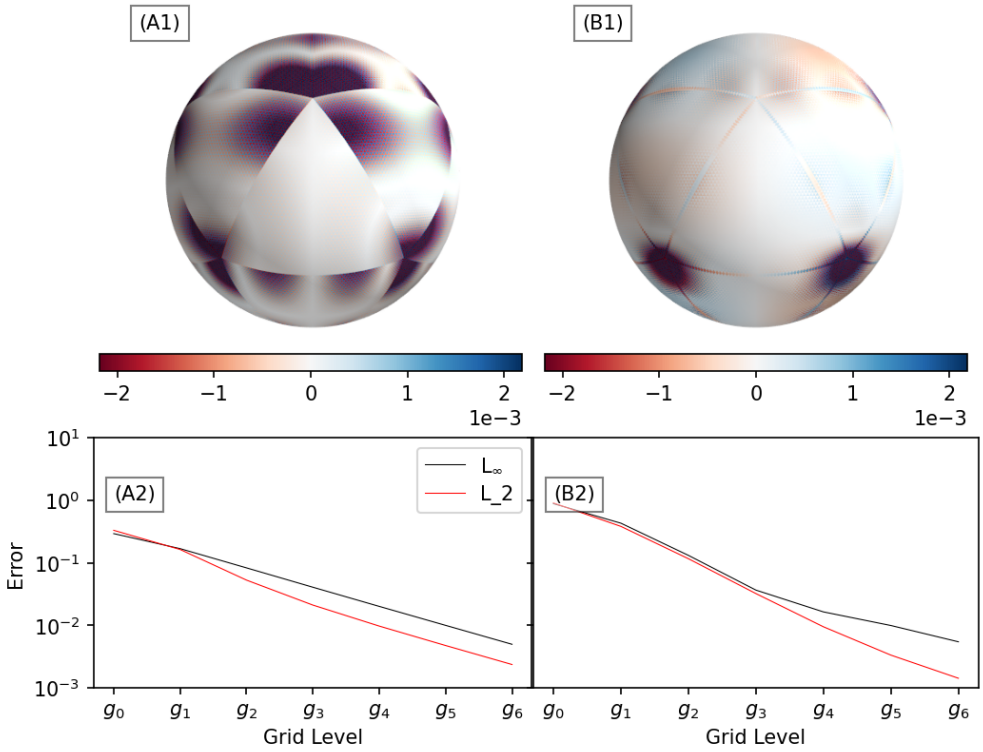

Figure 3.13: Same as Figure 3.12, but for TC1

of the error on the grid, will provide overall better results.

The noise of the triangular tiling of TRiSK is apparent in our results. ICON provides a partial correction of this noise. This correction seems to fail where there is a combination of the strong cell distortion couples with the magnitude of the field. Additionally, for geostrophic dynamics, the filtering capability has its worst performance, since the noise should be at its most intense. On the other schemes; however, where the operator is defined on the dual cell, this pattern is not displayed.

Essentially, all operators are affected by the grid quality, either of the primal or the dual cell. Therefore, a good choice of mesh, which decreases the distortion, will provide an improvement on these results.

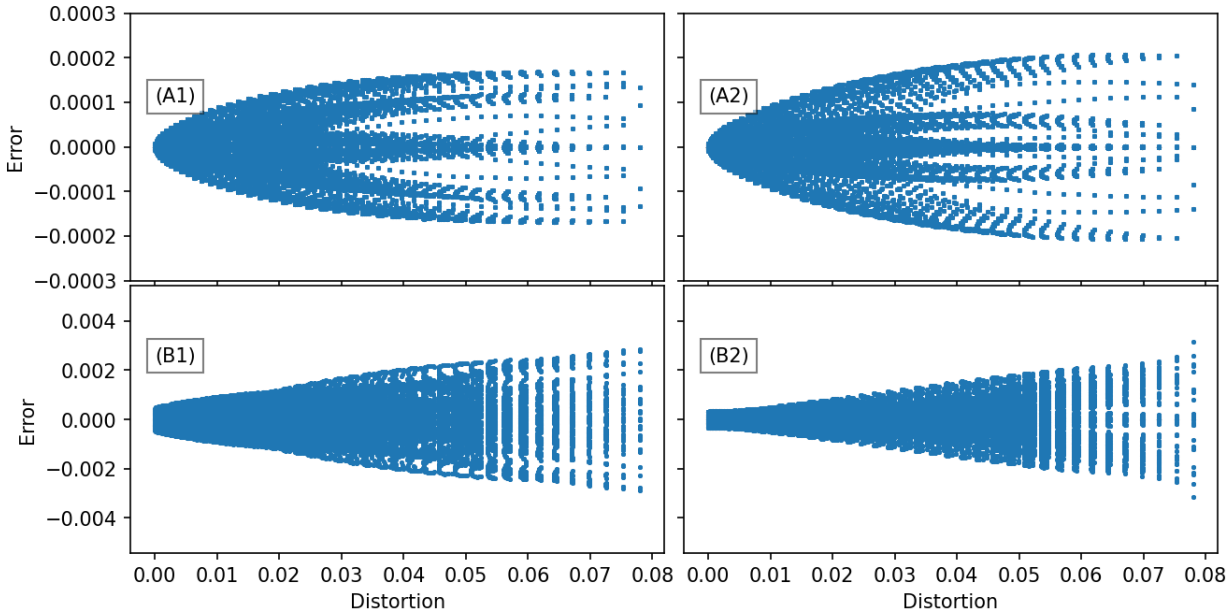

Figure 3.14: Divergent error by triangle distortion for TC0 (1) and TC1 (2) for TRiSK (A) and ICON (B).

3.3.2.2 Gradient

The gradient operator has a similar calculation as the divergent for the both A-/B-grid. Since the A-grid scheme has the computation on the vertices, we would expect a similar convergence rate. Opposite to it, the B-grid scheme has the operator performed on the barycentre of the triangles. Since there is a similarity between both divergence and gradient, we expect a behaviour similar to the divergent operator of TRiSK. In particular, the error distribution will likely be contaminated by noise and also the convergence rate will be at most first order without being much affected by the distortion, specially because the point where it is computed is the barycentre rather than the circumcentre.

Both C-grid schemes are defined similar to a midpoint differentiation method. This is expected to be second order. This is expected only if the computed point is halfway between each of the values to be computed. Since our grid is deformed, there is an offset between the primal and dual edge midpoint, and, therefore, it is likely that the second order will not be reached with this additional source of error. It is also likely to be a noise associated with the computation, since the gradient computed in this scheme is associated to a single vector direction, which is normal to the edge.

A- B-grid

Both schemes show a very different response to the gradient operator (Table 3.3). The A-grid has a L_∞ convergence rate near second order up to g_4. Further refinements lead to a slow-down of the convergence to near second order, where the slowest change is g_5 to g_6, when the error decreases in only 40%. However, the L_2 convergence stays consistent near second order (Figure 3.15.A2). These results are consistent with the ones obtained by Tomita

Table 3.3: Maximum Gradient Energy error for A- and B-grid.

g-level	A-grid	B-grid
g_0	$2.2888.10^{0}$	$5.5970.10^{-1}$
g_1	$3.6278.10^{-1}$	$2.3208.10^{-1}$
g_2	$8.3234.10^{-2}$	$1.0599.10^{-1}$
g_3	$2.1639.10^{-2}$	$4.8515.10^{-2}$
g_4	$5.5264.10^{-3}$	$2.3694.10^{-2}$
g_5	$2.5210.10^{-3}$	$1.1786.10^{-2}$
g_6	$1.5164.10^{-3}$	$5.8747.10^{-3}$

et al. (2001) with the standard grid, despite our grid having a lesser quality. Regardless, the absolute error of this scheme is larger than B-grid. As it is expected, this latter operator, has a first order convergence for both L_∞, and L_2 (Figure 3.15.B2), which is similar to the convergence of the divergence operator of TRiSK.

The spatial error distribution is also quite different (Figure 3.15). The A-grid operator shows a clear grid imprinting, as did its divergence. There are two patterns to be observed, the first and more evident, is the large error delineating the original edges of g_0. The second is a meridional (latitudinal) variation of the error, where the smallest error is located near the face centre of the grid and increasing with latitude. This is similar to Figure 3.10, except it was a zonal variation. B-grid, in contrast, shows a chequerboard pattern, although not clearly visible by observing the normed error of the vector. The most visible pattern of the error is that it is more intense near the triangle faces of g_0. However, the error pattern does seem connected with the vertices of g_0, despite its strong distortions, which was a result observed on the divergence of TRiSK (Figure 3.12).

C-grid

The gradient operator has a first order convergence from up to g_2 for both norm. Surprisingly, this convergence accelerates to near second order for finer grids, with the error g_5 to g_6 reducing by 77.7% (Table 3.4 and Figure 3.16).

Table 3.4: Maximum Gradient Energy error for each grid.

g-level	TC0
g_0	$1.0847.10^{-2}$
g_1	$6.2230.10^{-3}$
g_2	$3.4133.10^{-3}$
g_3	$9.4113.10^{-4}$
g_4	$2.4210.10^{-4}$
g_5	$6.1378.10^{-5}$
g_6	$1.3640.10^{-5}$

When observing the spatial distribution of the error, we observe that the errors on the centre of the triangle faces of g_0 are the smallest (Figure 3.16.C). This region is where there is the smallest amplitude of the gradient operator (Figure 3.7). The variation of this error is

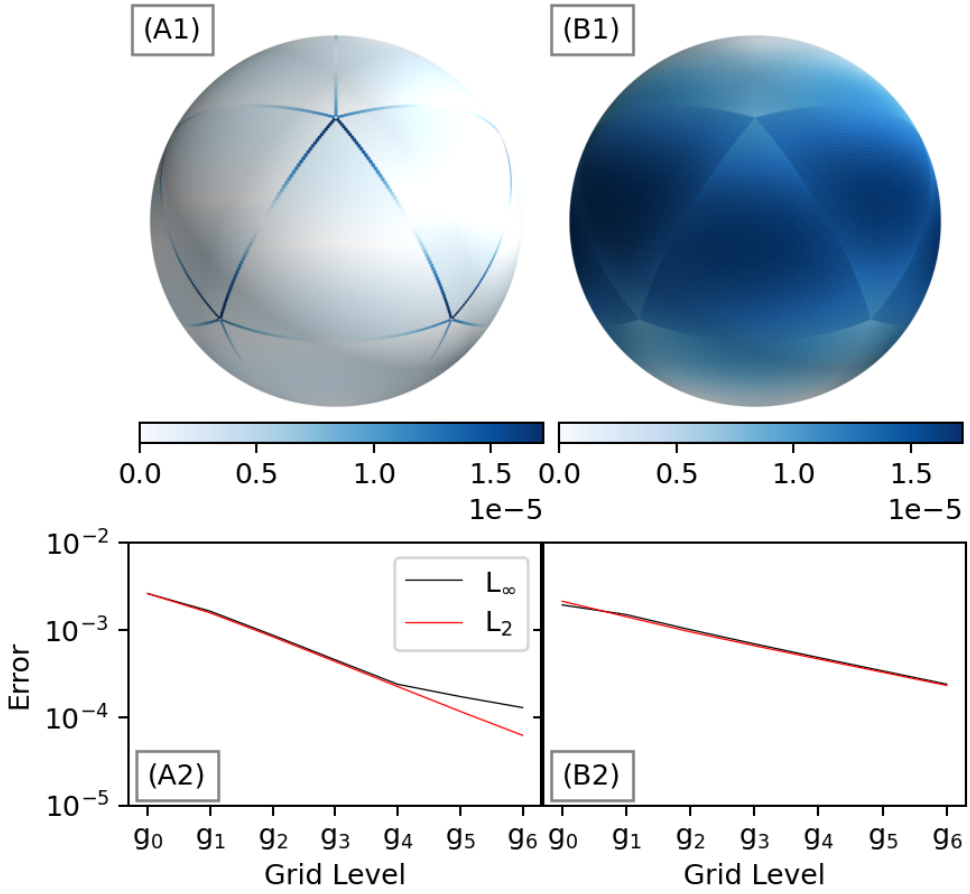

Figure 3.15: Spatial distribution error (1) and error plot for different grid refinements (2) of gradient operator for TC0 for both A- (A) and B- grid (B).

mostly meridional, with the largest magnitudes at the top of the triangle. Another observed error pattern is that the error is largest where the edge is closely parallel to the longitudinal lines. For edges more orthogonal to these lines, the error is smaller. Additionally, the error pattern also shows a distribution similar to the noise of the triangular chequerboard pattern. Some error behaviour seems to have a close relation with the edge midpoint offset of the grid (Figure 3.16.B), since it can be observed that some points of larger offset have larger errors. However, For edges with a distance larger than 6×10^{-5}, the majority of the points with large offset do not show a clear relation between the error and the distance.

Overall Comparison

All schemes show widely different behaviour of approximating the operator. The A-grid provides a similar behaviour with its divergent operator. Therefore, similar interpretations can be drawn from it: an impact from the grids quality, ranging from the error convergence to the presence of imprinting. The B-grid noise presence was expected, due to the similarities between computation of this operator and the divergent. The lack of relation between the error and the distortion of the cell, might be explained due to the fact the gradient of this scheme is defined at the barycentre of the cell. From the theory, the expected point the centre

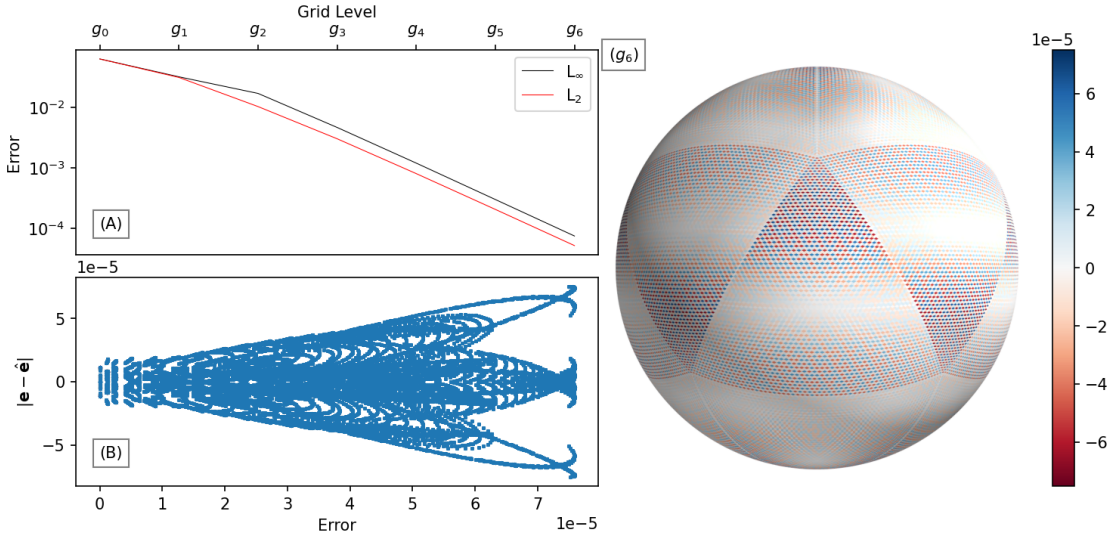

Figure 3.16: Spatial distribution of the error for the $g_6(g_6)$, maximum and second norm error plot for different grid refinements (A), and distribution of the error by the distance between primal and dual edge midpoint of the gradient operator for TC0 for the C-grid.

of mass, which is likely free from the distortion. Therefore, regardless of the distortion of the grid, this behaviour was expected.

The C-grid scheme acted, surprisingly, with a convergence error better than anticipated. This behaviour might be due to the fact that, although $|\mathbf{e} - \hat{\mathbf{e}}| \neq 0$, the distance between these points tends to 0 (Figure 2.6.A). Additionally, our convergence order of 2/2 for L_2/L_∞ is better than the computed by Peixoto (2016), which at best found 2/1 and at worst $0/-1$. Additionally, it is evident that there is a relation between the error and the normal vector direction, since the gradient direction is predominantly meridional which seems to coincide with the edges of larger error.

3.3.2.3 Kinetic Energy

As all variables of the A-grid are defined on the vertex of the mesh, then the kinetic energy operator is exact for this scheme. On the other hand, The B-grid requires and interpolation to be performed, in order to place the velocities on the vertices of the triangle, which in turn will make the gradient of the kinetic energy on the barycentre of the triangle tiling. The computation of this operator behave as a barycentric interpolation (which is a weighted average of all the neighbour points). However, due to the large number of points to be interpolated in the vertices; therefore, it is expected some grid imprinting on the operator, which goes in opposition to mass interpolation of the triangle, requiring only three points. If the vertices were the barycentric centre of the dual cell, we would have expected that the error of this interpolation would convert to a second order. However, since there is mismatch between these points, we assume that the additional error would pose an obstacle for the convergence.

The C-grid schemes has different computation for E_k. TRiSK's scheme comes from Weller

Table 3.5: Maximum kinetic energy error for B-grid for each grid.

g-level	TC0
g_0	274.6762
g_1	67.2432
g_2	25.6115
g_3	7.33677
g_4	1.92377
g_5	1.15875
g_6	0.64761

et al. (2012), which is barycentric interpolation to the circumcentre of the triangle (requiring to calculate the edge areas). As such, we expected a consistent interpolation in second order, which has been said by the aforementioned authors that this interpolation is more accurate for these non-Voronoi type grids. ICON, in contrast, utilizes Perot reconstruction to interpolate the velocities on the circumcentre of the triangular cell, and then compute the kinetic energy. Its use by Peixoto (2016) on Voronoi grids found that it converges to a second order. However, Perot (2000) have identified for triangles that this scheme first-order accurate. This indicates that we will likely expect that the kinetic energy operator might have a worse performance than TRiSK kinetic energy computation.

B-grid

The B-staggering scheme starts with a near second order convergence for the L_∞ norm up to the g_1. It slows down slightly up to g_4, but still remained near second order. However, up to g_6 it slowed down once more to a near first order convergence. In contrast, L_2 remained consistent, converging near second order on all iterations.

The spatial distribution of the error shows a pattern similar to other operators. The largest errors are found at regions near g_0 edges (Figure 3.17)). Note that these regions displays a small area in comparison to the grid (Figure 2.7.C), but also a large misalignment. In contrast, the grid pentagons, which are generated at the g_0 vertices, present small errors. This indicates that a large amount of cell vertices might negatively impact the interpolation of the grid.

C-grid

Both C-grid schemes show a second order convergence for both norms. The difference found on both schemes is that TRiSK show an error one order of magnitude less than ICON (Table 3.6).

This difference of behaviour in both schemes is also evident. For TRiSK, large errors seems closer to regions of large cell distortion (g_0 vertices). ICON, on the other hand, has its largest errors at the centre of the original g_0 triangles. Note that these regions are the less distorted ones, but also has the largest areas of the triangle. This might indicate that the ICON scheme is more susceptible to the overall area of the triangle rather than the distortion. Despite this, it is also worth noting that these regions are where the largest magnitude of velocity is located. Therefore, it is also possible that the operator is correlated by the magnitude of the interpolant, which could explain why only one sign of the error is

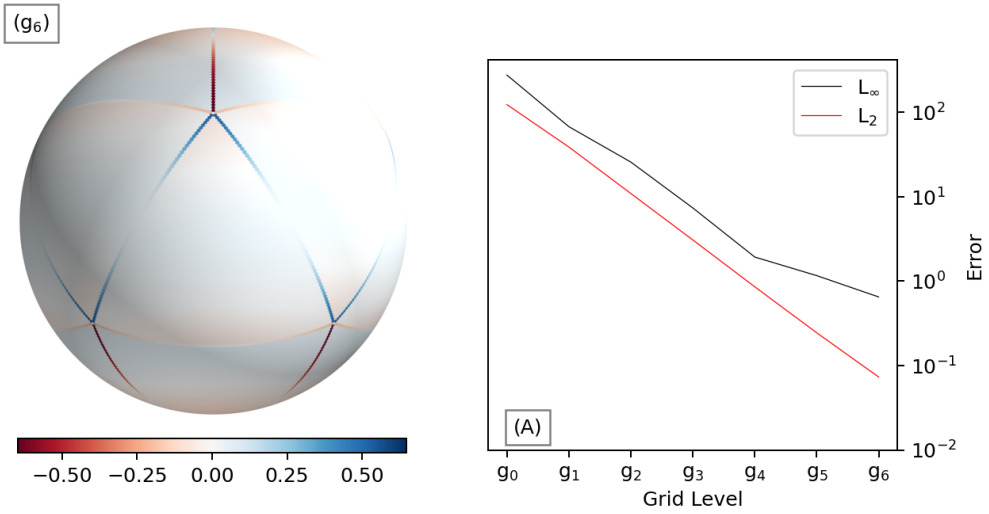

Figure 3.17: Spatial distribution error (g_6), and maximum and second norm error plot for each grid refinement (A) of the Kinetic Energy for the TC0 for the B-grid.

Table 3.6: Maximum kinetic energy error for TRiSK/ICON for each grid.

g-level	TC0
g_0	0.0000/79.0000
g_1	2.2066/27.3284
g_2	$4.8240.10^{-1}$/6.5064
g_3	$1.0380.10^{-1}$/1.6969
g_4	$2.4565.10^{-2}$/$4.2438.10^{-1}$
g_5	$6.2123.10^{-3}$/$1.0541.10^{-1}$
g_6	$1.5634.10^{-3}$/$2.6302.10^{-2}$

shown.

Overall Comparison

It is evident that the operator performs better on C-grid operator rather than B-grid, despite the vector components of the TRiSK and ICON being separated. The implementation of Weller et al. (2012) for the TRiSK operator on triangles has the best performance, as it is expected. This method outperforms even Perot's formula. Recall that, TRiSK's operator uses the spherical edge area $A_{e,K}$ to perform the calculation, while ICON uses the combination of primal-dual edge length $|e|d(\mathbf{e}, \mathbf{K})$. The area of the former, provide more information than only the length, and; therefore, might pose a better interpolation. It should be noted, however, that the former operator calculates E_k only for the normal component. ICON's E_k operator use the total vector component, which is interpolated by Perot's reconstruction.

The spatial error of the grids also displays a quite distinct behaviour. The grid imprinting of B-grid is very well present and similar to the operators. This indicates that this operator is susceptible to misalignment of the cell, due to its barycentric interpolation. If such a computation were to be performed on triangular cells, it is likely that it would be less

susceptible to it. However, a similar behaviour occurs in TRiSK. This susceptibility likely occurs because the velocity vectors are decomposed in each edge and the Kinetic Energy is computed in each edge separately and then interpolated in the triangle. ICON's absence of such a structure likely occurs, since the kinetic energy is computed after the vector is reconstructed in the circumcentre of the triangular cell.

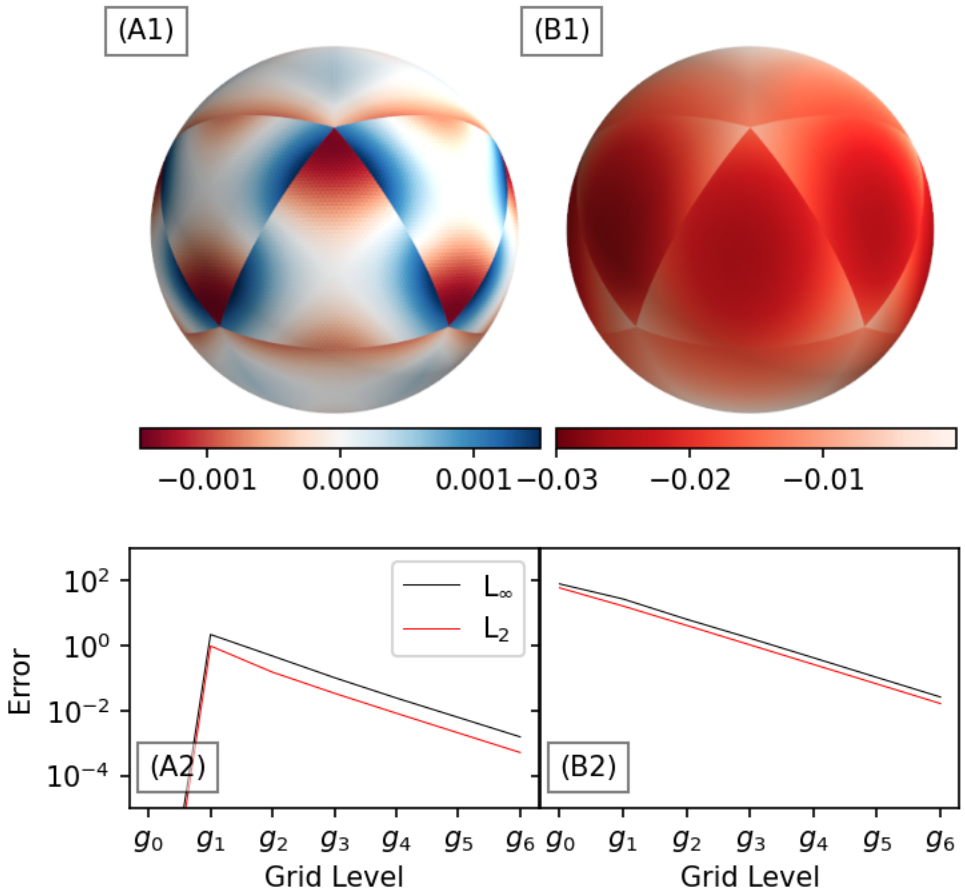

Figure 3.18: Spatial distribution error on g_6 grid (1), and maximum and second norm error plot for different grid refinements (2) of the kinetic energy operator for TC0 for both TRiSK (A) and ICON (B).

3.3.2.4 Coriolis Term

In this section, we will only analyse the C-grid scheme, since this operator requires a reconstruction of the velocity vector (A- and B- grid schemes already have the complete vector field defined on the same point). Prior to analyse the operator, we will verify the inconsistency index, which is defined as:

$$\chi = \|\mathbf{t}_e^n - \mathbf{t}_e\|,$$

where $\mathbf{t}_e^n$ is the numerical tangent vector and $\mathbf{t}_e$ is the analytical tangent vector. This index was presented by Peixoto (2016) which stated that for a method to be consistent on the spherical grid, it is required that it converges to 0 for larger resolutions. We have presented

Table 3.7: Maximum inconsistency index for TRiSK1/TRiSK2 for each grid.

g-level	
g_0	$2.1084.10^{-1}/1.9980.10^{-1}$
g_1	$1.8595.10^{-1}/5.9912.10^{-2}$
g_2	$1.9292.10^{-1}/1.0994.10^{-1}$
g_3	$3.5464.10^{-1}/4.2010.10^{-2}$
g_4	$4.7141.10^{-1}/3.1397.10^{-2}$
g_5	$5.4062.10^{-1}/2.5171.10^{-2}$
g_6	$5.7824.10^{-1}/2.3131.10^{-2}$

two TRiSK methods, which uses the weights of the primal or the dual cell, respectively. We will present an inconsistency index for both of those.

The first method present no convergence on both norms, except from g_0 to g_2 where there is a slight decrease in error for L_∞ and near first order convergence for L_2 (Table 3.7 and Figure 3.19). A continuous refinement from g_2 to g_6 shows a stagnation of the error for around 10^{-1} on L_2. However, L_∞ shows an increase in error from $1.9.10^{-1}$ in g_2 to $5.782.10^{-1}$ in g_6, an almost 3 times increase in error.

TRiSK2, on the other hand, shows a slightly better performance on both norms. Up to g_2 there is not an evident convergence of the error; however, from g_2 to g_3, we observe an almost 60% decrease in error for the L_∞, which slows down with further refinement, eventually stagnating. The error from g_5 to g_6 show a decrease only 8% in L_∞. For the L_2 norm, however, from g_2 to g_5 there is a convergence of near second order, which slows down to a near first order in $g_5 \rightarrow g_6$.

For both methods, their error distribution on the distribution are quite similar. The largest errors are found near the g_0 edges. The edge that shares the original g_0 edge displays a smaller error than their neighbours. The most noteworthy difference is that TRiSK1 displays an error decreasing radially from the original g_0 vertices. Contrary to it, TRiSK2 shows a confined error at the aforementioned regions, displaying a pattern similar to the grid imprinting described for the dual cell on the other schemes.

For the former method, we might argue that it seems closely related to the triangle distortion (Figure 2.8.A), since there is close match with large errors and worse triangle distortions. In contrast, TRiSK2 seems to have close relation with cell alignment. The large alignment band at the g_0 edges reflects the band of small error at the same region. It is likely that the dual edge that shares an aligned cell with a poor aligned one is the reason of large errors found for this method.

There is some evidence that the grid quality interferes with the accuracy of each method. Despite TRiSK2 showing a better performance, both tested schemes displays a 0th order convergence for the maximum norm. Peixoto (2016) have shown that, for some grids, TRiSK may improve on its accuracy. Therefore, it is possible that utilizing a different, TRiSK might improve on its convergence. However, Thuburn et al. (2009) also have shown that TRiSK2 contains non-zero frequencies on the geostrophic modes (which we will revisit in Section 3.4). For this reason, it is unreliable the application of the operator for time integration testing.

We will now evaluate the nonlinear Coriolis term error for both schemes with TC0. This

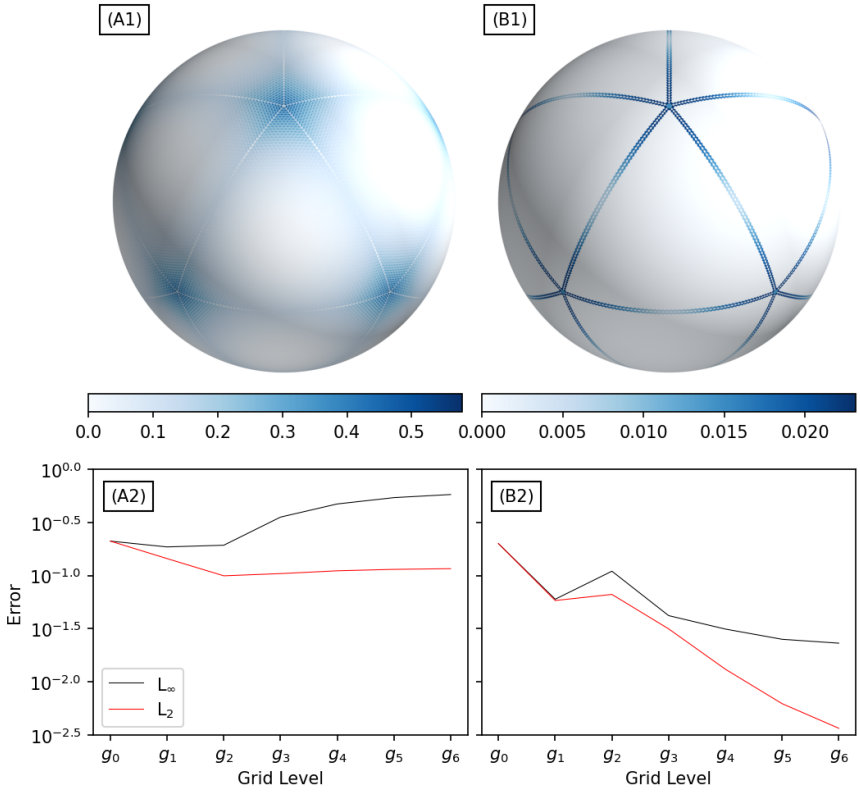

Figure 3.19: Inconsistency index spatial distribution error on g_6 (1), and maximum and second norm error plot (2) for both TRiSK1 (A) and TRiSK2.

operator, we recall, is defined as $qu^{\perp}h$, which consists of an interpolation of h to the vertices of the grid and the computation of the relative vorticity ζ. We will perform this test only for TRiSK1 and ICON, due to the issues mentioned above of TRiSK2.

Similar to the inconsistency index, the Coriolis term of TRiSK does not indicate a convergence of the error on either norms. Moreover, L_∞ displays a slight increase in error from $5.05.10^{-4}$ in g_2 to $13.86.10^{-4}$ in g_6, more than twice. ICON, however, displays a consistent convergence rate for both norms. L_2 consistently converge near second order, while L_∞ is near first order, with g_5 to g_6 presenting the lowest decrease of around 52%.

TRiSK1 shows a larger error concentrated around the vertices g_0 (Figure 3.20). There is, however, a slight difference in pattern around these vertices. The error seems to vary predominantly meridional. ICON, on the other hand, present a similar distribution as TRiSK2, with the largest errors restricted to the original icosahedral edges. Opposite to TRiSK2, the edges that coincide with g_0 also present large errors.

The Coriolis term of both schemes is likely controlled by the reconstruction, since we see no convergence on TRiSK1, while ICON has a pattern similar to TRiSK2. It is likely that this similarity is explained by the fact that both schemes are computed considering weights of the neighbouring dual cells. However, the weights are better adjusted for our grid such that ICON's reconstruction operator consistently converge.

Peixoto (2016) had proposed the Perot method to substitute TRiSK's reconstruction for the quasi-hexagonal tiling, with the argument to provide a consistent method. His method

Table 3.8: Nonlinear Coriolis maximum error for TRiSK1/ICON for each grid for TC0.

g-level	
g_0	$1.4440.10^{-3}/1.2318.10^{-3}$
g_1	$6.7610.10^{-4}/4.3780.10^{-4}$
g_2	$5.0573.10^{-4}/1.7573.10^{-4}$
g_3	$7.5572.10^{-4}/7.3100.10^{-5}$
g_4	$1.0607.10^{-3}/3.1222.10^{-5}$
g_5	$1.2715.10^{-3}/1.4078.10^{-5}$
g_6	$1.3863.10^{-3}/6.6354.10^{-6}$

also have a similar convergence. This shows the robustness of the accuracy of the reconstruction method in comparison to the traditional TRiSK scheme.

The Coriolis term seems highly sensitive to the reconstruction scheme chosen. For all tested scheme, the distortion and cell alignment is the primary drive for the accuracy of reconstruction.

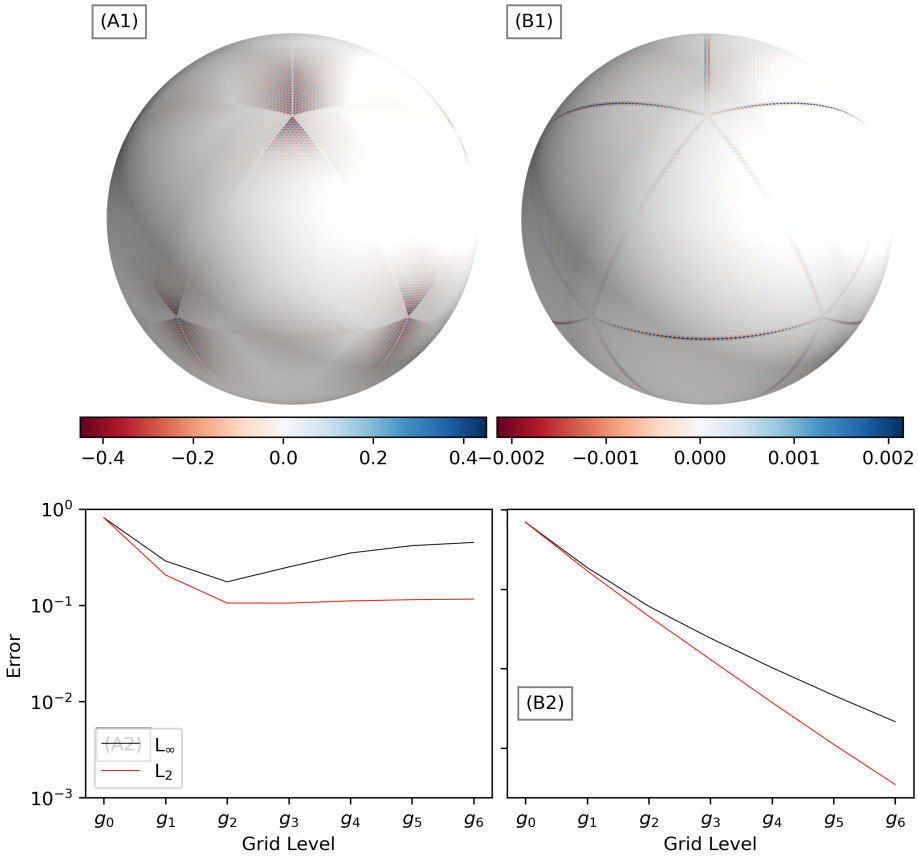

Figure 3.20: Nonlinear Coriolis error term spatial distribution for g_6 grid (1), and maximum and second norm error plot for each grid refinement (2) for TRiSK1 (A) and ICON (B).

3.3.3 Variable Error

To evaluate the accuracy of both scalar (h) and vector ($\mathbf{u}$) field, we will run our model with the initial conditions of the TC0. We will use the time integration method of Runge-Kutta order 4 (RK44), with a time step of 400 seconds. The maximum time integrated will be 15 computer days. Since TC0 is in geostrophic balance, the fields are expected to remain stationary.

To compute the error of the vector field, we will consider the total vector error, i.e. $|\mathbf{u}^n - \mathbf{u}|$, to compute L_2, L_∞, in the case of A- and B-grid. For C-grid, we will compute the errors similar to the scalar field, i.e. $|u^n - \mathbf{u} \cdot \mathbf{n}|$. To display the spatial distribution of the error, we will only use the zonal velocity, which will be the dominant field. To do that for both C-grid scheme, we will reconstruct the vector at the triangle's circumcentre using the Perot's operator (Pv_K).

We remark that ICON requires the computation of the inverse of its admissible reconstruction operator. This operation is computational costly. Therefore, we will use the lumping mass matrix in which we will assume that the inverse is a diagonal matrix, i.e. $\mathcal{M}_\mathcal{G}{}^{-1} = \mathbf{I}\lambda$. In particular, we will consider $\lambda = 1$ (Korn and Danilov, 2016; Korn and Linardakis, 2018).

Since TC0 is mostly stationary, nonlinearity should be absent in this scheme. In that

regard, A- and B-grid should be the best performing schemes. However, due to the issues of inconsistency presented by Tomita et al. (2001), we expect strong noise to appear in our grid, which will likely damage the accuracy of the variables. Moreover, since the B-grid scheme has some operators defined at the barycentres of the triangles, the accuracy of the variables will likely not be the most optimal. Regardless, both schemes necessarily require a filter to remove unwanted noise, which will negatively impact the accuracy. Despite this, we expect both C-grid methods to have a lower accuracy, specially because of necessity of the vector reconstruction of the Coriolis term. Moreover, it is likely that ICON will have a better performance, since TRiSK's reconstruction fails to present a convergence of the error.

In regard to the spatial distribution, since the C-grid scheme will not contain filtering techniques in their discretizations, near grid scale oscillations will likely be present. Since TRiSK contain no type of correction of the chequerboard pattern, opposite to ICON; it is, therefore, likely that this noise will be also present within the solution of scalar field.

A- B-grid

Both schemes exhibit a vastly different result. The A-grid (Figure 3.21) accelerates its convergence of the error up to g_3 for both norms, where the error from g_2 to g_3 has near second order convergence, i.e. decreasing in almost 79% and 86% for h and $\mathbf{u}$, respectively (Table 3.9 and Figure 3.9). However, L_∞ slows down with further refinements. It is observed that the scalar field error maximum norm increases 66% from g_5 to g_6, while the vector field has only a 2% increase. The L_2 norm also slows down, but remain convergent with a first order with grids finer than g_3.

Table 3.9: Maximum variable error for A-/B- grid

	$L_\infty(h)$	$L_\infty(\mathbf{u})$
g_0	$1.9105.10^{-2}/5.1995.10^{-1}$	$5.3933.10^{-1}/84.575.10^{0}$
g_1	$4.0315.10^{-2}/1.1123.10^{-1}$	$4.2177.10^{-1}/6.5812.10^{-1}$
g_2	$2.5001.10^{-2}/8.5065.10^{-3}$	$1.6146.10^{-1}/9.5452.10^{-2}$
g_3	$3.1830.10^{-3}/3.2516.10^{-3}$	$2.3112.10^{-2}/5.1187.10^{-2}$
g_4	$1.4166.10^{-3}/8.7003.10^{-4}$	$1.1346.10^{-3}/1.1827.10^{-2}$
g_5	$3.1994.10^{-4}/2.0436.10^{-4}$	$2.7379.10^{-3}/3.2065.10^{-3}$
g_6	$5.3236.10^{-4}/5.5774.10^{-5}$	$2.8187.10^{-3}/1.1818.10^{-3}$

On the other hand, for the B-grid scheme (Figure 3.22), it is observed a slight acceleration up to g_2 for both norms and fields. The L_∞ decreases in more than 99% and 85% for both h and $\mathbf{u}$. Further refinements are met with a slow-down of the error, but as intense as A-grid. Both variables in both norms retain a near second order convergence without clear signs of braking. For g_5 to g_6 in L_∞, in particular, the error decrease in 72% and 63% for both h and $\mathbf{u}$.

When observing the error distribution of the spatial error, we observe that the A-grid is fully contaminated with noise in the mass field h. This noise seems more intense near the vertices of g_0. In a Further analysis of this noise, we observed that the noise is generated at each time step of the integration at the edges of g_0. This noise is then transported westward, without damping, until the whole grid is contaminated, despite the presence of hyperviscosity.

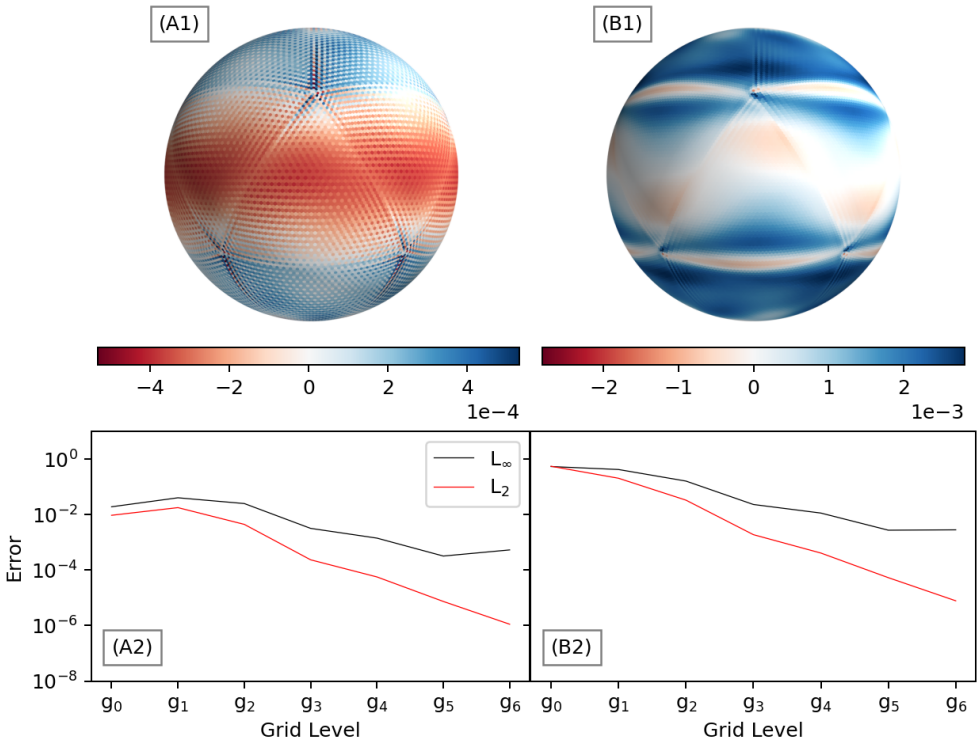

Figure 3.21: Mass (A) and zonal velocity (B) field spatial distribution error on g_6 (1), and maximum and second norm error plot (2) for TC0 for the A-grid scheme.

If we remove this filter, the integration destabilizes prior to the 15th day.

B-grid, however, displays no presence of any noise on the grid. The error pattern of both variables show a zonal oscillatory pattern of wavenumber of around five. The grid imprinting at the g_0 edges, which was identified at the operators, is also present in both fields. However, the magnitude of the error is much smaller than the surrounding error

We remark that a noise was also described by Tomita et al. (2001) in their work, though they only performed an analysis without using any form of filter. They have not thoroughly explained the reason for such a noise, but they have shown that the use of a grid in which there is a consistency and an improvement of the accuracy of the operators leads to a noise reduction. They reasoned, that the use of a spring dynamics grid was more consistent with their model. We provided a similar discretization in Appendix A, where we moved both vertices and triangle barycentres, such that vertices coincide with the mass centre of the dual cell. It is clear that the noise present is not generated at the momentum equation, since there is a presence of a filter. This noise is purely generated at the mass equation, likely in the divergence operator. This explains why the noise is much more prominent at the scalar field rather than the vector field.

The B-grid, on the other hand, does not display such visible oscillations. For TC0, this scheme outperforms A-grid's scalar field error by 1 order of magnitude. B-grid's error is comparable to the A-grid in a spring dynamics grid (Tomita et al., 2001). This suggests that the scheme provides a better flexible to grid quality, while A-grid is highly sensible to it.

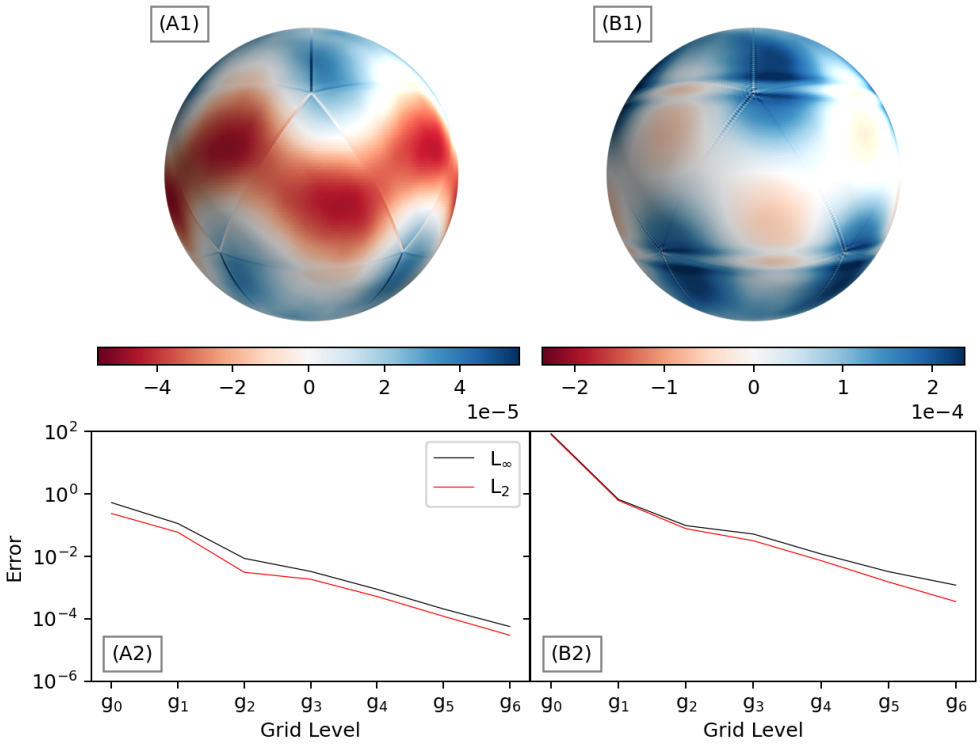

Figure 3.22: Same as Figure 3.21, but for the B-grid scheme.

C-grid

Both schemes show a well-behaved error control. TRiSK has an increase of the error up to g_2 for both fields and norms. From g_2 the error begin converging. The mass field L_∞ has its largest decrease from g_2 to g_3 of about 80%. It, then, slows-down, but remain convergent to near first order, with the error decreasing by 51%. The L_2 follows a similar behaviour. The vector field has its convergence near second order constant to the all grid levels. There is a slight slow down from g_5 to g_6, where the error decrease around 64%, less than second order, but more than first.

ICON's scheme has a similar error pattern. The mass field starts converging from grid

Table 3.10: Maximum variable error for TRiSK/ICON

	$L_\infty(h)$	$L_\infty(\mathbf{u})$
g_0	$2.2277.10^{-3}/4.9853.10^{-3}$	$1.6387.10^{-1}/2.7624.10^{-1}$
g_1	$2.2089.10^{-2}/3.6300.10^{-2}$	$2.9333.10^{-1}/1.2704.10^{0}$
g_2	$4.9740.10^{-2}/1.6902.10^{-2}$	$4.5466.10^{-1}/2.2850.10^{-1}$
g_3	$1.0317.10^{-2}/6.3856.10^{-3}$	$7.0111.10^{-2}/1.0780.10^{-1}$
g_4	$5.2617.10^{-3}/3.5896.10^{-3}$	$1.3362.10^{-2}/3.2745.10^{-2}$
g_5	$1.8232.10^{-3}/8.3187.10^{-4}$	$2.1799.10^{-3}/1.0314.10^{-2}$
g_6	$8.9341.10^{-4}/2.8325.10^{-4}$	$7.8181.10^{-4}/3.5797.10^{-3}$

level g_1, but we observe a more consistent convergent pattern from g_3. The largest decrease in error for L_∞ is from g_5 to g_6 of around 51%, i.e. near first order. L_2 is shown to have the same behaviour. Moreover, the vector field starts converging also from g_1, and we observe a consistent convergence of near second order, with the last refinement decreasing in 65%, less than second, but more than first order.

The largest differences between schemes occur in their distribution around the sphere. The mass field of TRiSK has a clear presence of chequerboard type pattern, which is larger near the vertices of the icosahedron; however, some errors are accentuated near the edges of the tropics. The vector field error displays an overall zonal pattern with wavenumber five around the sphere. Nevertheless, there is a presence of a clear noise on the sphere, which looks parallel to some edges of g_0. Additionally, there is a clear grid imprinting around these icosahedron edges that are slightly more pronounced closer to the poles.

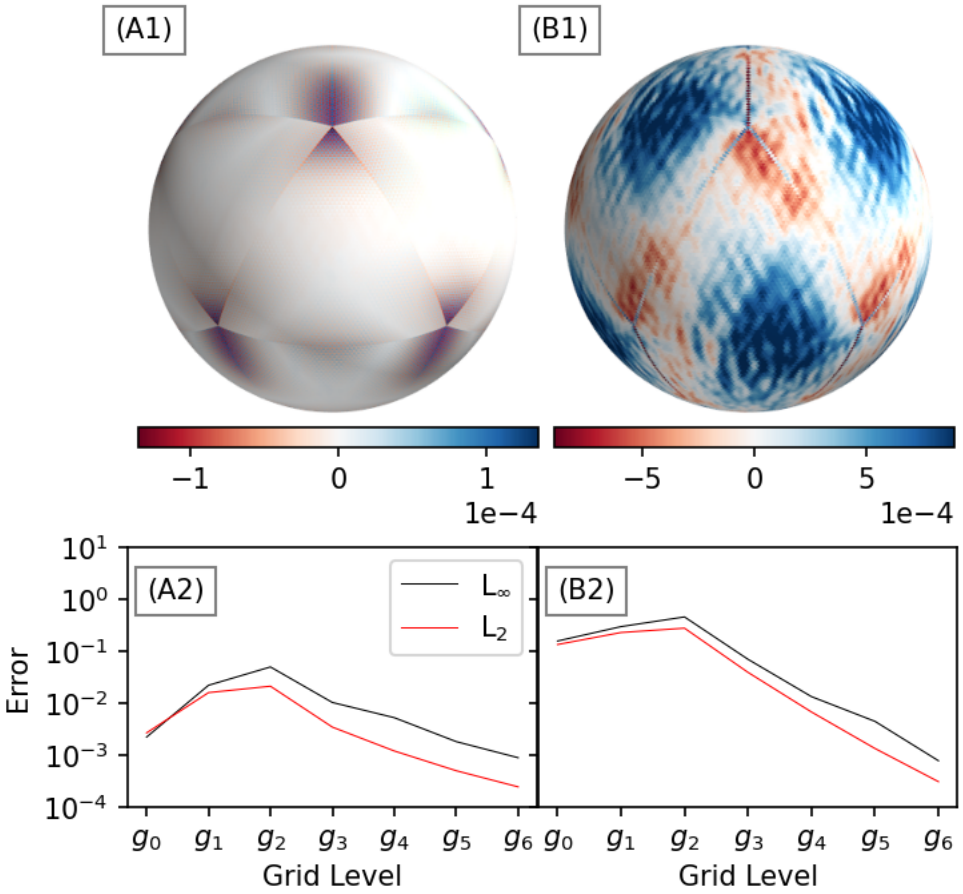

Figure 3.23: Mass (A) and zonal velocity (B) field spatial distribution error on g_6 (1), and maximum and second norm error plot (2) for TC0 for the TRiSK scheme.

On the other hand, there is no clear noise visible in ICON's scalar field, as one should expect. The visible pattern of this error field is the presence of zonal waves with a wavenumber of five, where one side of the equator will have its sign flipped in comparison to the other side. In addition, the g_0 edges at the tropics contain have a slightly larger error than its

surrounding. The vector field also has this wavenumber pattern present; however, similar to TRiSK's vector field error, it contains some level of noise on the grid. This noise is slightly less pronounced than TRiSK. Also, similar to the scalar field, slightly larger errors are present near the g_0 edges in the tropics.

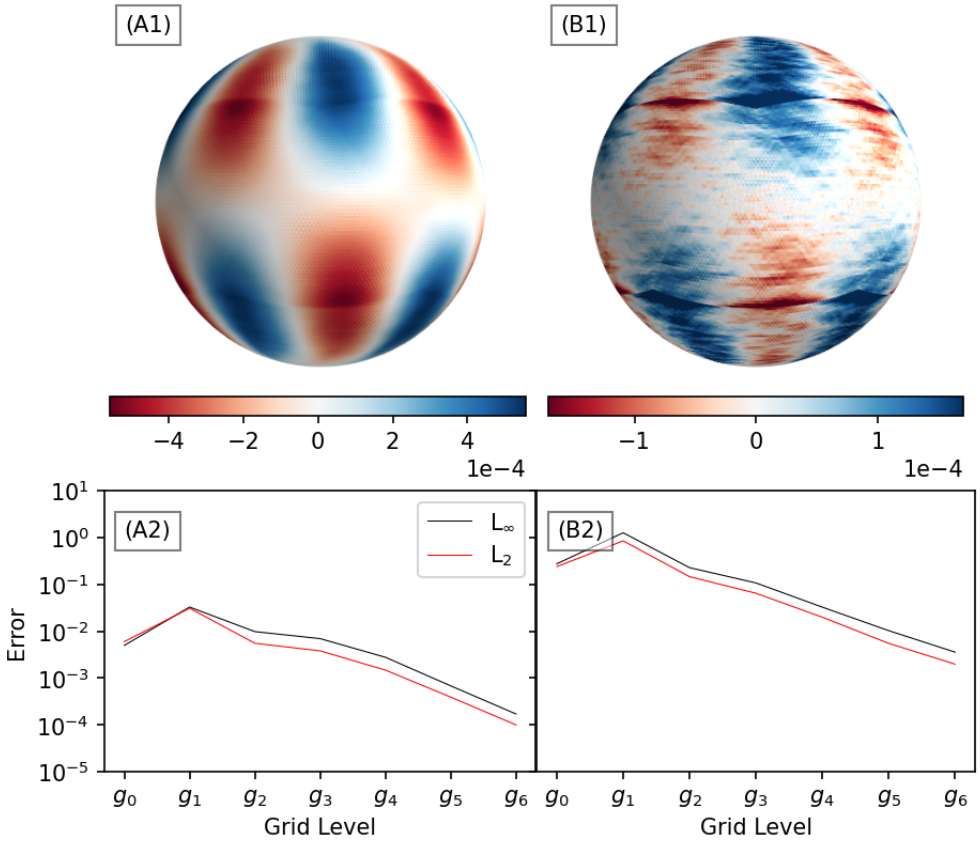

Figure 3.24: Same as Figure 3.23, but for ICON.

Overall Comparison

The A-grid presents the worst performance of the tested schemes. Its noise amplification is not damped by the filter. All the other schemes show at least a first order convergence. However, the scheme of B-grid has an error magnitude smaller than either C-grid schemes. This could have many causes, such as the filter used, the complete vector field being defined exactly, the choice of discretizations being at least first order and some near second order, but a more in depth investigation is required to evaluate these potential causes.

Additionally, the zonal wavenumber pattern for the mass field is observed in both B-grid and ICON. This pattern is also obtained by Korn and Linardakis (2018). Therefore, despite our grid having a worse distortion than the standard icosahedron, both schemes, ICON in particular, are robust enough so that the geostrophic balance is properly computed in time.

A-grid, however, is shown to not properly simulate the condition as the noise in these distorted are intense enough to contaminate the grid, making the scheme useful only for some specific grids (Appendix A). TRiSK, on the other hand, the noise does not seem to

affect heavily on the simulation, since it still converges. However, the poor performance of the reconstruction could likely impact heavier conditions that require more of the nonlinear components.

3.4 Normal Modes

In order to evaluate differences in TRiSK1, TRiSK2 and ICON, we will conduct normal mode test following Thuburn et al. (2009) and Weller et al. (2012). To achieve that, we use the linear form of (3.1b):

$$\frac{\partial h}{\partial t} = -h_0 \nabla \cdot \mathbf{u}, \tag{3.64a}$$

$$\frac{\partial \mathbf{u}}{\partial t} = -f_0 \mathbf{k} \times u - \nabla \Phi. \tag{3.64b}$$

Let $\mathbf{A}$ be the linear action of the shallow water equations on the sphere. Let $\mathbf{x} = (h, \mathbf{u}) = [\mathbf{x}_i]_i$, where $\mathbf{x}_i = (0, \cdots, 0, 1, 0, \cdots, 0)$ where it is 1 on the i-th component and 0 on the rest. Then:

$$\mathbf{A}\mathbf{x} = \mathbf{B}.$$

We then calculate eigenvalue (λ) and eigenvector ($\mathbf{v}$) of the matrix $\mathbf{B}$. Since we know that $\lambda = \alpha e^{i\omega\Delta t}$, we can then solve for ω which is the frequency.

We will consider the f-sphere, where $f_0 = 1.4585 \times 10^{-4}\ s^{-1}$, $gH = 10^5\ \mathrm{m}^2.\mathrm{s}^{-1}$. We will integrate the equations using the g_2 grid with RK44 with a time step of 10 seconds, similar to Weller et al. (2012). The analytical curves are:

$$c[c^2 - f^2 - n(n+1)\frac{gH}{r}] = 0. \tag{3.65}$$

For all schemes, we calculated a total of 798 modes. For both TRiSK1 and ICON, we found 162 geostrophic modes with zero frequency (Figure 3.25), i.e. neutral modes, which are the same obtained by Thuburn et al. (2009) and Weller et al. (2012). TRiSK2 and ICON, shows overall a slower inertia-gravity waves than TRiSK1, with ICON displaying the most intense reduction. Since both schemes share the use of the dual grid to reconstruct the vector velocity field, therefore, this might be indicative of the decrease in the inertia-gravity wave propagation.

Additionally, both schemes also display a lower quantity of zero-frequency geostrophic modes (48 modes) than that expected by the theory (Le Roux et al., 2005). This has the potential effect, depending on the initial condition, of not being able to sustain the geostrophic balance. For ICON, a similar result was observed by Peixoto (2016), however, as the author argued, it does not appear that these modes display an expressive issue in the scheme.

On the other hand, on both TRiSK schemes, there is also the presence of a *frequency jump* near the 50th mode. According to Thuburn et al. (2009), this jump is associated with a spurious branch of the inertio-gravity waves.

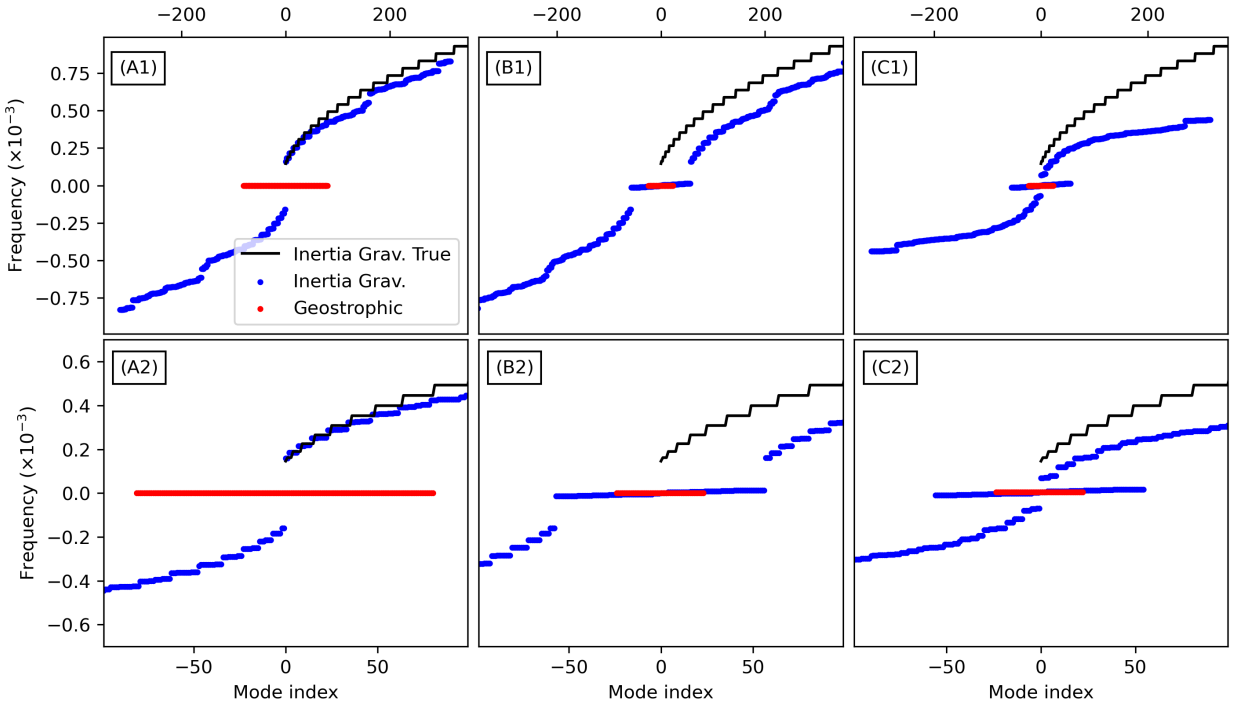

Figure 3.25: Normal modes on the f-sphere for TRSK1 (A), TRSK2 (B), and ICON (C) on the full range (1) and zoomed around the geostrophic portion (2). The red lines are the geostrophic modes, the blue lines are given the inertia-gravity modes.

ICON scheme, in contrast, does not display this jump and has a smoother transition to higher frequencies. However, ICON also displays a much slower frequency of inertio-gravity waves for the higher modes than the other schemes. The dual reconstruction is partly the culprit of such a loss of speed. The $\mathcal{M}_G$ on the divergence is likely also responsible to not only also to brake some of these waves, but also to make to eliminate the jump. Since the TRiSK2 displays this jump, this spurious branch is, therefore, probably associated with the chequerboard noise of the divergent operator.

The reader should be aware that in our work, we did not thoroughly investigate the associated eigenvectors of the analysis. However, we briefly observed for all schemes, some associated with the neutral geostrophic modes possess a more symmetrical around the equator, while modes associated with higher frequency present a more noisy high wavenumber pattern around the sphere, following from the work of Weller et al. (2012). A potential verification is in future to check whether the spurious Rossby modes from the triangular C-grid are diminished with admissible reconstructions of the ICON scheme.

3.5 Mountain Case

This testcase considers an orographic forcing at midlatitudes. We aim to verify a more realistic approach to fluid behaviour in a rotational setting.

The models show a disturbance caused by the mountain that propagates in the eastern

direction. This propagation allows the surge of planetary waves on the Southern Hemisphere, which is largely present at day 15th (Figures 3.26 and 3.27). We observe, at this time, small scale noises throughout all schemes. These noises are more prevalent at the midlatitudes and, in particular, in both C-grid schemes.

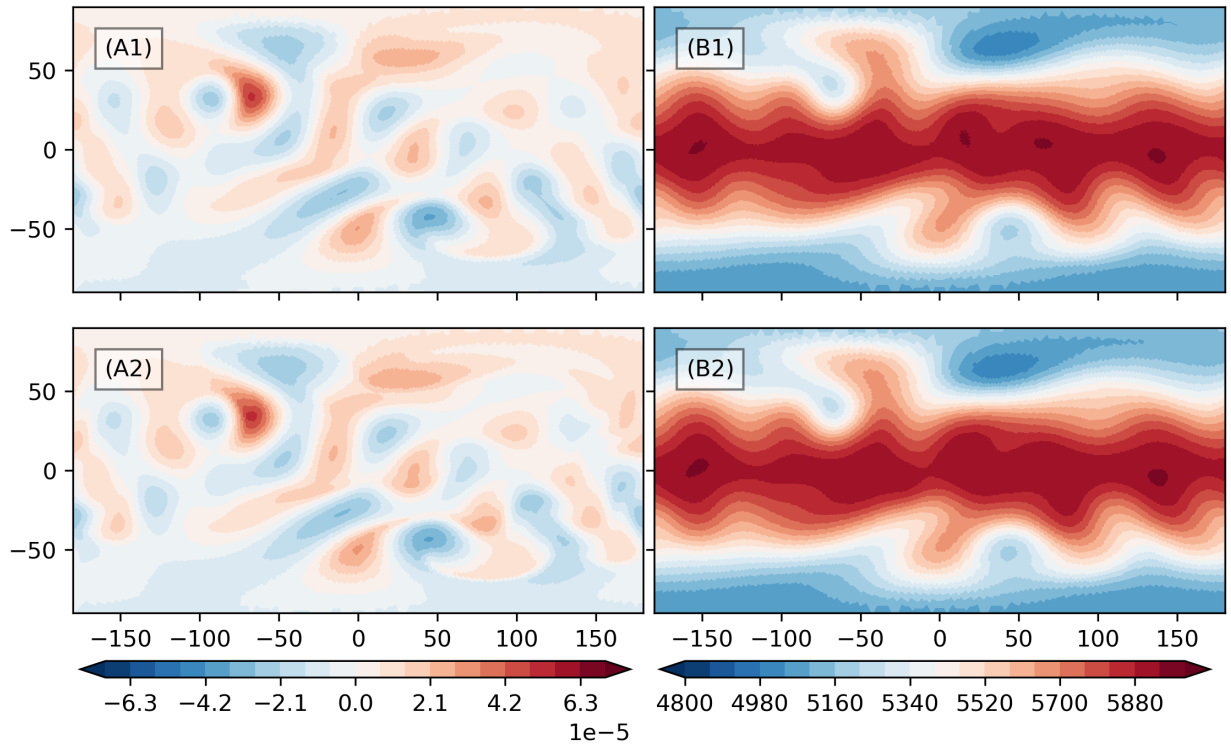

Figure 3.26: Mountain Test case day 15 for A-grid (A) and B-grid (B) for ζ (left panels) and Φ (left panels) variables.

We also note that near the mountain, where is a large positive concave vorticity feature, both C-grid schemes show a small frontal feature. Korn and Linardakis (2018) results (Figure 3.28) also show this phenomenon at g_7, while g_5 it is not as pronounced. The absence of this feature is noted on both A- and B-grid schemes. Therefore, this feature might be the consequence of an accurate small wave propagation of the schemes, which is smoothed by the filtering on the other simpler staggering schemes.

Further integration of the testcase lead to a stronger interaction of the planetary waves at day 50 (Figure 3.29), leading to a vortex shedding at the mountain location, and a constant source vortex emission. In this point, the differences of the schemes are higher. The noises previously present on A- and B-grid schemes dissipate, displaying a much smoother vorticity field. In contrast, both C-grid schemes show a much more detailed features of small scale waves. Between these latter schemes, TRiSK seems to display more detailed vorticity field than ICON. It is likely that the operators defined in ICON, which has a larger stencil, acts to smooth the operators, which was a result presented in the normal modes (Section 3.4). Despite that, TRiSK is heavily polluted by near grid scale noises. Although ICON also shows some noise, it is much less pronounced. This spurious oscillation is likely related to

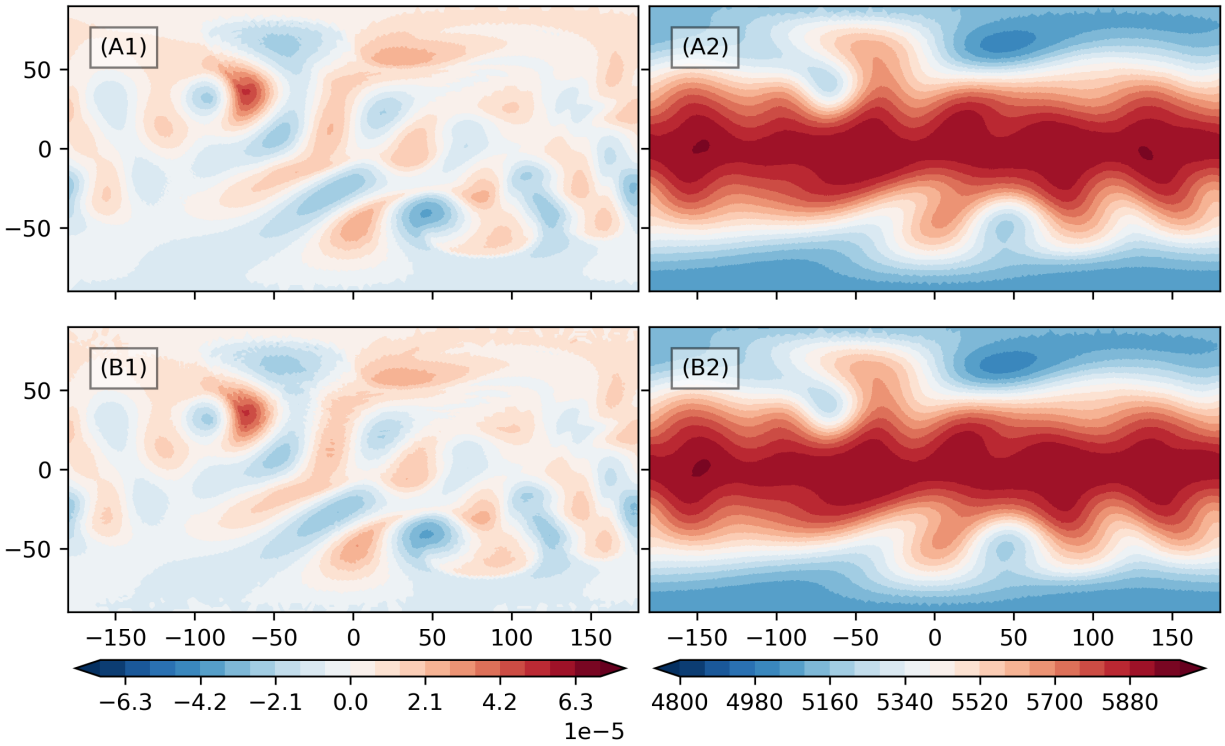

Figure 3.27: Mountain Test case day 15 for TRSK (A) and ICON (B) for v (left panels) and Φ (left panels) variables.

the chequerboard pattern of the divergence operator. This hypothesis was also presented by Weller et al. (2012), in which they stated that "the oscillations [...] are the manifestations of the computational Rossby modes caused by the excessive number of velocity DOFs in comparison to height".

3.5.1 Spectral Analysis

To visualize how well these features are presented, we show the kinetic energy spectrum on the sphere. This spectrum was done averaging the fields from day 16-50 using a g_5 grid. In the following section, we describe how the spectrum of the kinetic energy was obtained.

3.5.1.1 Description

Following Boer (1983), spherical harmonics are special functions defined on the surface of the sphere. A function $\psi(\lambda, \theta)$ can be expanded on the sphere as:

$$\psi(\lambda, \theta) = \sum_{n=0}^{N} \sum_{m=-n}^{n} \psi_n^m Y_n^m(\lambda, \theta), \tag{3.66}$$

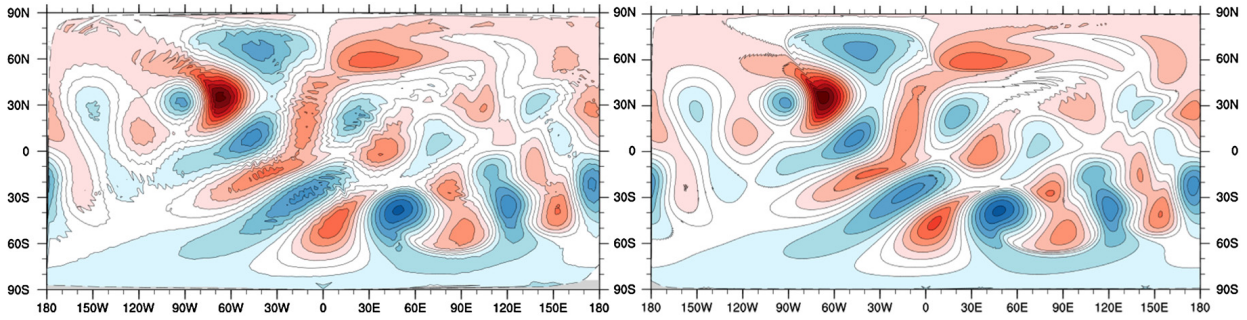

Figure 3.28: Mountain test case day 15 for ICON's scheme on g_5 (left) and g_7 (right). Source: Korn and Linardakis (2018).

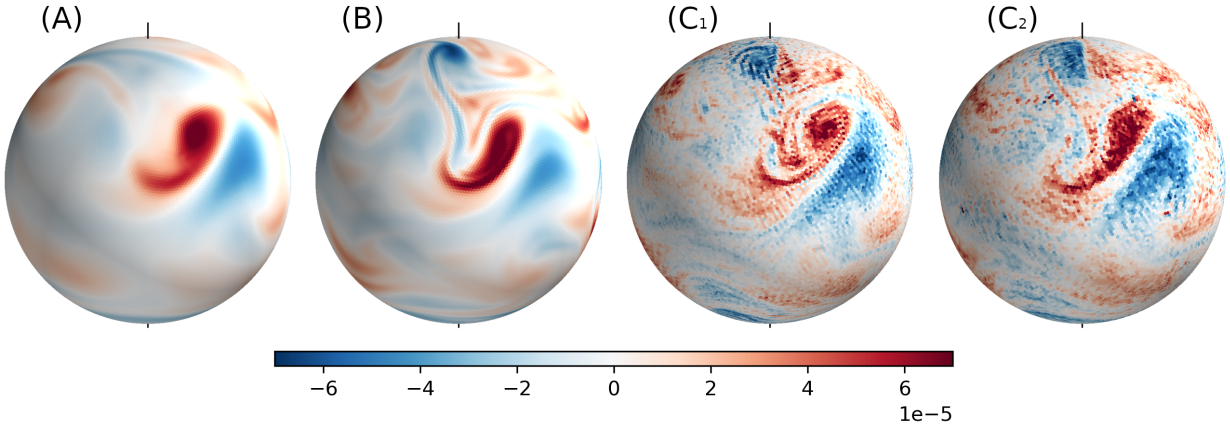

Figure 3.29: Relative vorticity field for the A-grid (A), B-grid (B), TRiSK (C_1), and ICON (C_2).

where this expansion is truncated and $Y_n^m(\lambda,\theta) = P_n^m(\mu)e^{im\lambda}$, and $P_n^m(\mu)$ is the associated Legendre Polynomial of order n defined as:

$$P_n^m(\mu) = \sqrt{\frac{2n+1}{2}\frac{(n-m)!}{(n+m)!}}\frac{\sqrt{(1-\mu^2)^m}}{2^n n!}\frac{d^{n+m}}{d\mu^{n+m}}(\mu^2-1)^n. \tag{3.67}$$

This way guarantee that the functions are orthogonal in the sphere.

We can then calculate the Kinetic Energy Spectra following Jakob-Chien et al. (1995):

$$\overline{(E_k)_n} = -\frac{r^2}{4n(n+1)}\left[\zeta_n^0(\zeta_n^0)^* + \delta_n^0(\delta_n^0)^* + 2\sum_{i=1}^{n}\zeta_n^i(\zeta_n^i)^* + \delta_n^i(\delta_n^i)^*\right]. \tag{3.68}$$

where $\overline{(E_k)_n}$ is the global mean spectra, ζ_n^j, δ_n^j and $(\zeta_n^j)^*$, $(\delta_n^j)^*$ are spectrum coefficients of the vorticity and divergence, and $(\cdot)^*$ is the complex conjugate.

Due to the optimization of the package, we are going to use *pyshtools*, a python package aimed to extract spectral coefficients. Subsequently, we will employ Equation (3.68) to compute the spectrum of the kinetic energy

3.5.1.2 Analysis

All schemes (Figure 3.30) show a very similar energy cascade for large wavenumbers. For high wavenumbers we observe an order from faster cascade to lower cascade is A-grid, B-grid, ICON, TRiSK. This goes in line with the previous observations. As A-grid has the worst representation for high wavenumbers, it is expected that it shows a worse energy behaviour. B-grid follows A-grid as it better represents high wavenumber waves, but not as well as C-grid. Lastly, C-grid shows that both TRiSK and ICON has an increase of energy near these high wavenumbers. ICON seems to have a slightly lower energy at this scale. Thus, it is likely that this energy behaviour might likely be linked with the grid scale oscillation of schemes.

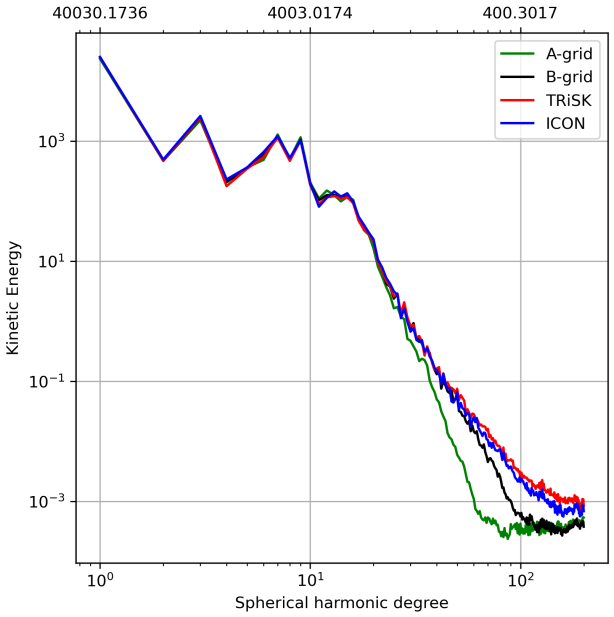

Figure 3.30: Spectral Analysis from the average of day 16 to 50.

3.6 Concluding Remarks

Our observations show that these schemes shares a lot of similarities. One very important similarity is their vulnerability to cell distortion. There seems to be a direct connection with the error and this grid property, and this likely impacts the convergence of the operators. This result is in agreement with Peixoto and Barros (2013).

The distortion of the grid is one of the reasons for the choice of an optimization, as means to minimize these problems. Even though the A- and B-grid shows first order convergence for the operators, there are critical issues due to the usage of this grid. Tomita et al. (2001), for example, have briefly showed that the standard icosahedral grid is highly inadequate for this scheme. We here have provided further evidence to attest to this inadequacy.

The C-grid schemes are also not immune to the effects of the grid. The main TRiSK discretization seems to not even converge its Coriolis operator. A second discretization of

TRiSK is shown to apparently have a first order convergence, but it does not have stable geostrophic modes, making it unusable. For these considerations, ICON seems to be a better alternative than TRiSK, since it does have a better convergence of the operators and minimizes some chequerboard pattern noise of the grid.

This noise is present in the B-grid and both C-grids. Regardless of the grid optimization, it will be present if the variable/operator be defined in the centre of the triangle cell. Although it is present on the B-grid, it does not affect heavily the solutions because this scheme requires an associated filter, which would remove any spurious oscillation. However, in C-grid it is present and has the potential to deteriorate the grid solution. ICON provided an efficient improvement of the oscillation. This scheme, however, has some limitations. It does not conserve energy, neither vorticity nor enstrophy with its lumping mass matrix. Some conservations are inherently built in TRiSK. Besides that, ICON seems to remove some grid scale features. This, however, could be an advantage for mitigating some instability (refer to Chapter 4).

In contrast, most small scale features are absent in the A- and B-grid schemes. Our results from the nonlinear mountain case show that 'we might require A-grid to have a finer resolution as to match with the results of the other schemes. B-grid, in that case, performs quite well, as it does show a good representation of the inertial gravity waves, but it does present small grid scale noise. It is possible that the same might be achieved by the C-grid schemes if they were to use diffusion.

It might be useful to consider using a different grid. It has not been shown how well these schemes perform on a Spherical Centroid Voronoi Tessellation for triangular cells. Many have used TRiSK in a hexagonal tessellation, but a triangular one. A-grid has been used on spring dynamics by Tomita et al. (2001), but we might argue that an SCVT grid will have a better performance, despite not being as flexible as used by the authors. The B-grid might also be improved on this grid.

Chapter4

Numerical Instability Analysis

The use of computation approximations for the shallow water equations provides a good resource for understanding the behaviour of fluid flow. However, these approximations can generate unphysical waves or spurious oscillations. These are potentially harmful, as some of these waves may amplify and crash the integration process. They have a variety of causes and may amplify through some conditions, such as the choice of time integration scheme, the proper choice of CFL condition or the associated with the staggering grids.

The schemes of Tomita et al. (2001) (A-grid) and Danilov et al. (2017) (B-grid) have some well known oscillations that are very unstable. The former is caused by excitation of pressure modes within the integration, while the latter is caused by the excessive DOFs of the velocity vector field. These issues cause uncontrollable growth of the height and velocity fields that eventually lead to instability, which will necessarily require some use of filter to remove the noise.

Most instabilities are well known and studied. Some, however, are still an open-ended problem. One such example is the one reported by Hollingsworth and Kallberg (1979). They observed uncontrollable behaviour in their energy/enstrophy conserving scheme, which lead to a decrease in the intensity of a jet stream in their model followed by an increase of the short wave kinetic energy in the system. The authors followed on a second paper (Hollingsworth et al., 1983) with a deeper analysis on this instability, which is now known as Hollingsworth or Hollingsworth-Kallberg instability, HK instability henceforth. It arises due to the 3D structure of the model, with the internal mode of the highest wavenumber being the trigger.

Subsequently, Gassmann (2013) have shown that the root of the problem lies in an unbalance between the advection term with its discretized vector invariant form. In other words, in theory:

$$\mathbf{u} \cdot \nabla \mathbf{u} = \mathbf{k}\zeta \times \mathbf{u} + \nabla E_k.$$

However, the discretization of the term of the Right-hand Side (RHS) are not necessarily equal with the Left-Hand Side (LHS), and this discrepancy may potentially lead to HK instability. The author was led to this conclusion by observing that the instability would arise even in a geostrophically balanced state. She also observed that in a quasi-geostrophic setting, this instability did not occur, since the equations filter out some inertia-gravity waves. Ultimately, the author makes a final suggestion to extend the stencil of the scheme, which could have a positive effect in reducing this cancellation error.

In a novel paper by Bell et al. (2017), they were able to provide a further understanding of the HK instability. Focused on oceanic flows on a plane, they assumed a few approximations, such as hydrostatic, adiabatic, f-plane, and Boussinesq. Since only the internal modes were of interest on this instability, they considered the ocean as a layered stack of barotropic fluid, resembling a layered model (Figure 4.1). As the instability would only be triggered by the

highest internal modes, it is then implied that the shallowest layer of the model would be the first to trigger the instability.

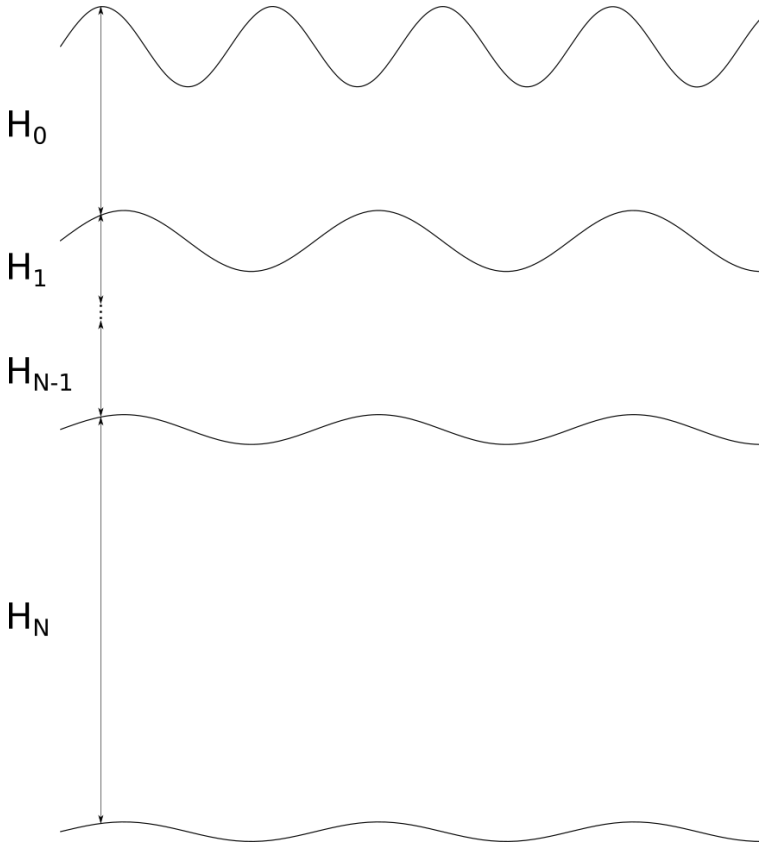

Figure 4.1: Illustration of a layered model.

Their results also found a connection between HK, and Froude and Rossby numbers, defined as:

$$R_o = \frac{U}{f_0 L} \tag{4.1}$$

$$F_r = \frac{U}{c}, \tag{4.2}$$

where U and L are, in this case, defined as $U = \max |\mathbf{u}|$ and $L = \min\{|e|, |\hat{e}|\}$. They found that the instability triggers faster for large values of R_o and F_r. The Froude Number dictates the shear of the fluid which goes in accordance with Gassmann (2013) which stated that the largest vertical shear will trigger faster the instability. Additionally, since the grid resolution impacts the Rossby Number, therefore, a larger resolution might also trigger the instability faster.

Subsequently, Peixoto et al. (2018) follows this work and analyse the instability in a curved geometry: quasi-hexagonal tiling (TriSK, Gassmann (2013), and Peixoto (2016) schemes), Cubed Sphere (Thuburn et al. (2014) scheme), and the ENDgame model (Wood et al., 2014). The stability of these methods were evaluated by the use of an adapted power method algorithm.

Their results show that all, but a version of the ENDgame, were in fact unstable. They also identified that HK on these grids follow predominantly the grid imprinting. They conclude their arguments by stating that, although there is a root problem for the triggering of the instability, other myriad of factors may work as either a catalyst or a damping of the instability. Furthermore, as it was previously mentioned in Bell et al. (2017), the resolution does not help to alleviate the symptoms of the instability, and it can, in turn, help to trigger it.

Recently, Gassmann (2018) also attacked this problem by utilizing a similar argument in a previous paper Gassmann (2011). She reasons that due to trivariate linear dependence constraint (3.3), the vector-invariant form and the advective form of the shallow water equations no longer exactly agree with each other in the discretization.

She also proposes a modified TRiSK scheme such that this trivariate constraint is met for the Coriolis term. In her previous work (Gassmann, 2013), she tried to alleviate the problem, but her success was limited to the equilateral triangular tiling. On a deformed mesh, however, she unfortunately failed to meet the constraint.

As it can be seen, there is not a definitive solution to the problem. Currently, the best way to circumnavigate this issue is to use some form of filtering, such as a diffusion operator. The inclusion of it poses some issues. Higher order diffusions are generally physically inconsistent. One form of inconsistency is that the conservation of angular momentum is often violated. Hence, its use is discouraged as it may result in unphysical solutions for long time integration. However, due to its simplicity, it is often used for some schemes. A- or B-grid schemes usually opt for these diffusion operators, which will eventually mitigate waves small scale waves. C-grid does not necessarily need to use filter, but with the HK instability, its use might be considered. Thus, for the use of hyperdiffusion operator, how much viscosity will we require for each scheme to be stable? Does ICON operators help to mitigate the instability issues?

To answer these questions, we will then evaluate the stability of each scheme studied in the previous chapters. We will apply the instability analysis method used by Peixoto et al. (2018) for each equivalent depth, and we will observe the spectrum of each scheme with and without such diffusion.

From a theoretical perspective, we expect the following order of schemes from more to less unstable: A-grid, B-grid, TRiSK, and ICON. We reason that since there is a pressure mode excitation inherent to the first scheme, then it is enough to be highly unstable. The second scheme requires less interpolation, but has a DOF unbalance, which would eventually lead to an instability. For some conditions, both C-grid schemes are not unstable, but it is shown that they could be for small equivalent depths. We expect ICON to be the more stable scheme, since it contains an operator that acts to damp some high frequency waves, and it also removes some noise present in the system.

4.1 Instability Analysis

4.1.1 Description Power Method

Prior to present our results, it is important to show an intuition behind the power method used for the analysis of the instability. This method is derived from Peixoto et al. (2018) and

aims to find the largest eigenvalue with its associated eigenvector of a matrix, which would translate to the dominant instability of a scheme.

It works as follows: let us assume an initial condition $\mathbf{x}^{(0)}$ under geostrophic balance $\bar{\mathbf{x}}$. If we then apply our shallow water scheme function $\mathbf{G}$, we will get the integration of the initial condition after a time step, i.e.

$$\mathbf{x}^{(1)} = \mathbf{G}(\mathbf{x}^{(0)}).$$

We expect that $\mathbf{x}^{(1)} = \mathbf{x}^{(0)}$, however, numerical deviation will be present. We can remove this deviation by letting:

$$\mathbf{x}^{(k+1)} = \mathbf{G}(\mathbf{x}^{(k)}) + \mathbf{F}, \tag{4.3}$$

where $\mathbf{F} = \bar{\mathbf{x}} - \mathbf{G}(\bar{\mathbf{x}})$. $\mathbf{F}$ will be a constant on the iterated solution, removing the numerical drift.

Let us now assume that our solution is $x^{(k)} = \bar{\mathbf{x}} + y^{(k)}$, where $y^{(k)}$ is a small perturbation. Substituting on (4.3):

$$\bar{\mathbf{x}} + y^{(k+1)} = \mathbf{G}(\bar{\mathbf{x}} + y^{(k)}) + \mathbf{F}.$$

Linearizing through Taylor Expansion, we obtain:

$$y^{(k+1)} = \mathbf{G}'(\bar{\mathbf{x}})y^{(k)} + \mathbf{F} + O(2),$$

where $\mathbf{G}'$ is the Jacobian gradient of numerical scheme operator. The value of this operator will tell us the behaviour of the numerical scheme. In other words, we can determine where and when the model will blow up by finding the eigenvalue and eigenvector of this operator.

This assumption relies on the fact that $y^{(k)}$ remains small so that the eigenvalue is found. However, there is a possibility that $y^{(k)}$ does not stay small enough before we find the eigenvalue, so we need to rescale the perturbations of the model. To do this, we apply a scaling factor similar to (4.3):

$$\mathbf{x}^{*} = \mathbf{G}(\mathbf{x}^{(k)}) + \mathbf{F}, \tag{4.4}$$

where our perturbation without the numerical drift will then be $\mathbf{r}^{(k+1)} = \mathbf{x}^{*} - \bar{\mathbf{x}}$. Now, we rescale our perturbation as:

$$\mathbf{x}^{(k+1)} = \alpha_{k+1}\mathbf{r}^{(k+1)} + \bar{\mathbf{x}}, \tag{4.5}$$

where $\alpha_k = \epsilon/||\mathbf{r}^{(k)}||$, $\epsilon > 0$ is a small constant.

Assuming the method converges, $\alpha_k \to \alpha$, then we can estimate our dominant eigenvalue as $\lambda = 1/\alpha$. In this case, the scheme will only be unstable if $\lambda < 1$. The growth rate ν of the scheme can be determined by the equation:

$$\lambda = e^{\nu \Delta t}, \tag{4.6}$$

and the e-folding time $T_e = 1/\nu$.

4.1.2 Scheme Stability

To analyse the instability, we will define an initial condition in geostrophic balance similar to TC0 (Section 3.3.1.1), but now the topography will act to retain the geostrophic balance:

$$b = -\frac{1}{g}\left(a\Omega u_0 - \frac{u_0^2}{2}\right)\sin^2\theta. \tag{4.7}$$

The sea level height will be a small constant $h = H_0$, such as to mimic the equivalent depth. The velocity will be unchanged:

$$u_\phi = u_0\cos(\theta). \tag{4.8}$$

We will be using a g_5 grid refinement, which has an average resolution of 480 Km.

Our analysis show that although A-grid is inherently unstable, its e-folding time is the largest of all schemes, reaching a maximum of 48 days at the 20 m equivalent depth (Figure 4.2). up to the 20 m equivalent depth, the scheme does not display a visible difference on the instability behaviour.

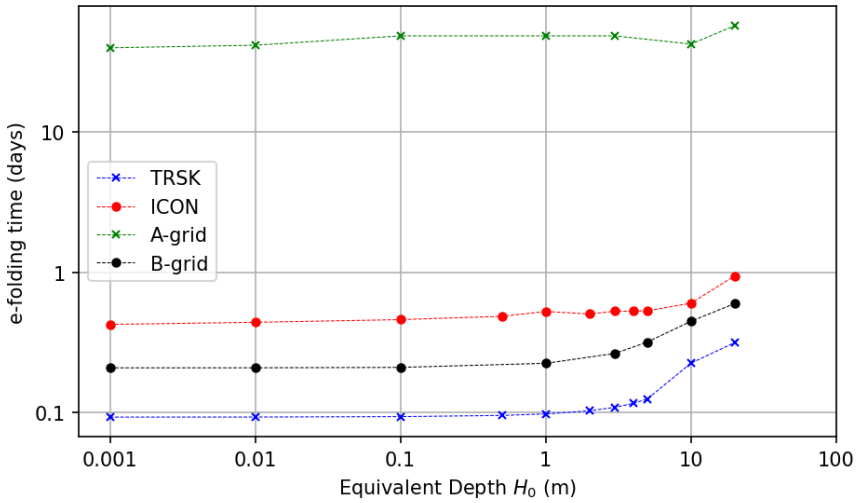

Figure 4.2: e-folding time by equivalent depth for both TRiSK and ICON.

In contrast, B- and both C-grid schemes are much more unstable for these shallow H_0. They do, however, improve on their stability drastically near the 10 m equivalent depth mark. From these schemes, TRiSK shows the worst e-folding time, reaching a minimum of 0.1 days for 0.001 m and a maximum of 0.46 day for 20 m. B-grid has a better result on this instability, although still very unstable. It has a minimum e-folding time analysed as 0.21 day for 0.001 m and a maximum of around 0.6 day for 20 m. ICON seems to outperform both of these other schemes, in particular TRiSK's scheme. It shows a minimum/maximum e-folding time at 0.001/20 m of around 0.6/1 day.

Comparing both C-grid schemes, we fix the 10 m equivalent depth and verify which C-grid operators are the most responsible for the stability of ICON (Figure 4.3). We observe that the **div** operator aid to improve the stability, increasing the e-folding time to around 0.25 day. Although it is not the main operator responsible for the instability, it already

shows signs of improvement by removing the chequerboard pattern. The Coriolis term of the momentum equation, on the other hand, has a massive improvement on stability, reaching 0.4 day of e-folding time. However, the kinetic energy does not show sign to improve on the stability of the equation. Even if we use both kinetic energy and Coriolis terms of ICON, we see a similar result as only using the Coriolis operator. This suggests that the largest source of instability of TRiSK is primarily due to how poorly it reconstructs the vector field on the grid.

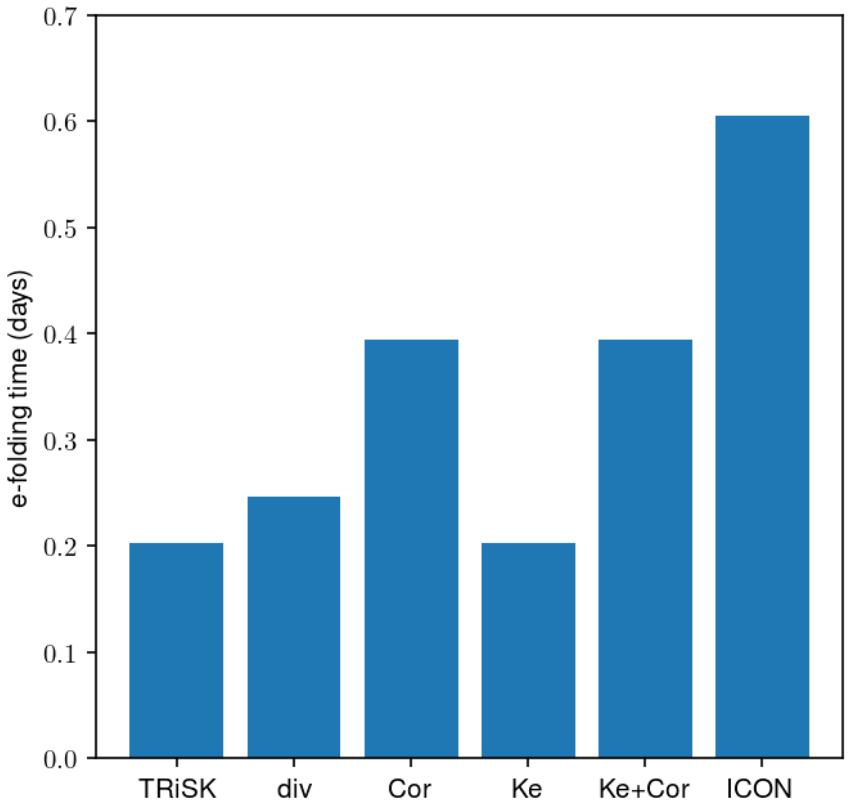

Figure 4.3: e-folding time by each operator component of ICON for $H_0 = 10$ m.

To understand how the instability is triggered on the grid, we analyse the associated eigenvector of the method of the most unstable mode. We will again verify the 10 m equivalent depth. All schemes seem to have a strong propensity of developing the instability around the edges and/or vertices of the icosahedra (Figures 4.4 and 4.5), similar to what was found by Peixoto et al. (2018).

When we observe the resulting eigenvector of the method for the 10 m equivalent depth, we can see where likely this instability is going to occur and what kind of pattern is going to present. These are seen in Figures 4.4 and 4.5. All schemes seem to have a strong propensity of developing the instability around the edges and/or vertices of the icosahedra, similar to what was found by Peixoto et al. (2018). A few differences are of particular interest. A-grid seems to develop a strong oscillation within the edges of the grid. This oscillation is likely the same oscillation found in the previous chapter and mentioned by Tomita et al. (2001). Therefore, it might be likely that the instability is due to the inconsistency of the divergence

operator on this kind of grid, rather than HK. Conversely, B-grid shows a propensity to develop instabilities near the vertices of g_0. These instabilities, however, appear to be near 2-grid intervals, which would be likely due to the instability of the staggering scheme rather than HK.

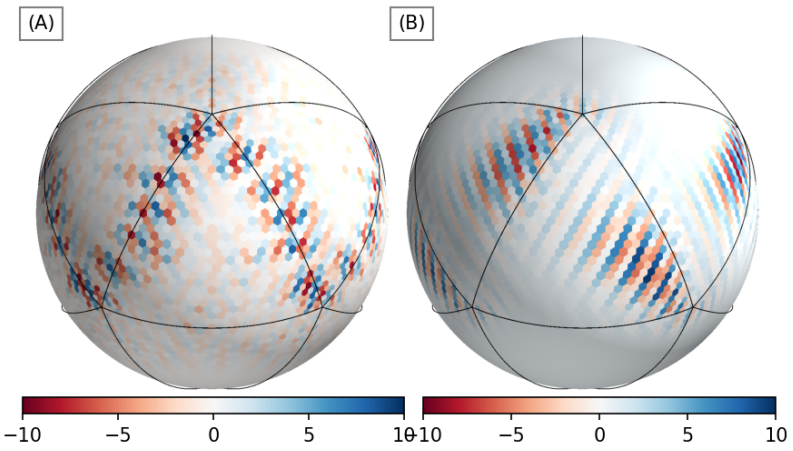

Figure 4.4: Eigenvector of h for A-grid (A) and B-grid (B).

Finally, C-grid shows the same pattern over g_0 edges. TRiSK's scheme seems to present an oscillation of 1-grid interval. ICON's eigenvector also displays a 1-grid interval oscillation, but much less apparent. It seems that the predominant oscillation is of around 2-grid interval. This indicates that TRiSK might actually have an HK instability, while ICON might could have HK instability, but other instability might appear earlier in the integration.

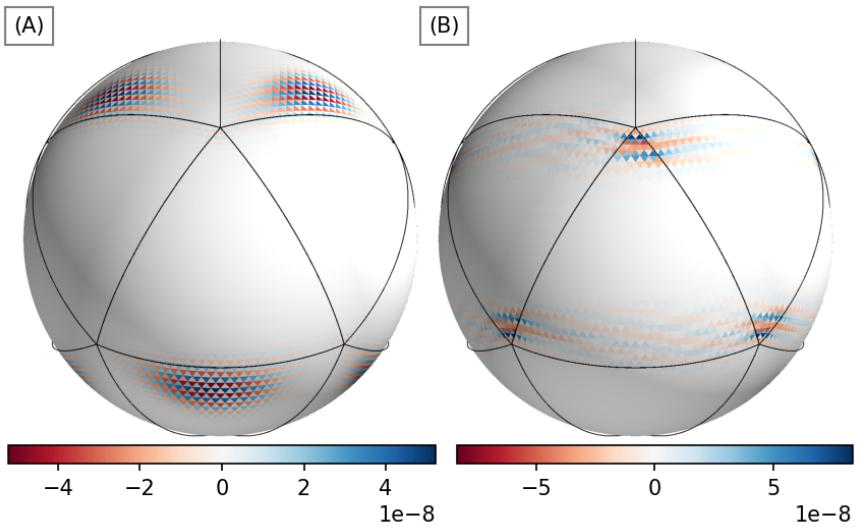

Figure 4.5: Eigenvector of h for TRiSK (A) and ICON (B).

To validate our analysis, we integrate these schemes on the 10 m equivalent depth. The A-grid scheme does not blow up after 15 days integration, while the B-grid scheme amplify its error near 3 day integration (Figure 4.6.A2 and Figure 4.6.B2). Despite the lack of noise

amplification with the time integration, error on g_5 shows a strong noise on the mass field, not particularly associated with the edges of g_0. A performed spectral analysis (Figure 4.7.A) on this field shows that we have a strong signal at the wavenumber of around 10, which is the interface between global scale and mesoscale. For higher wavenumber we see small prominences at around 2-grid interval, which is likely the noise associated with the field.

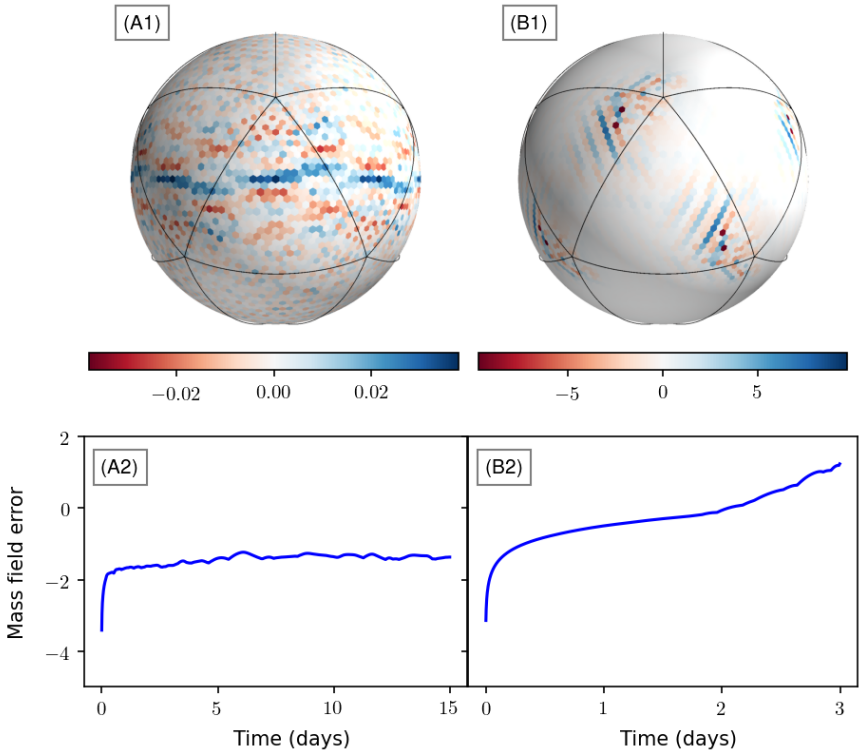

Figure 4.6: A-grid (A) and B-grid (B) scheme time integration (lower panels). The error spatial distribution of h mass variable is shown on the upper panels. B-grid is shown prior to blow up, while A-grid is shown after 15 days time integration.

However, with such a large e-folding time, we might only be able to observe some amplification after 1 year integration. The B-grid scheme, in contrast, display a strong noise emanating from the original vertices of g_0, as our analysis have previously predicted. This noise seems to match the wavelength of the analysis method we performed of around 2/3-grid interval. The same can also be observed on the spectrum analysis of its field (Figure 4.9.B). There, we can see, not only an increase of the 2/3-grid interval noise, but also a small 1-grid oscillation. Therefore, there are two types of numerical oscillation at play. One is associated with the DOF unbalance (2/3 grid interval) and the other due to HK instability (1 grid interval).

The time integration of C-grid schemes agrees with the e-folding time (Figure 4.8). TRiSK blows up near at around 0.36 day, while ICON blows up at around 4 days. TRiSK seems to have a large noise emanating from the vertices of g_0 which is not completely in line with the findings of the power method, but it is close to where it was supposed to be found. This oscillation is stationary and has a close to 1-grid interval (Figure 4.9.A). Likewise, ICON has an instability that somewhat matches with the power method; however, while TRiSK

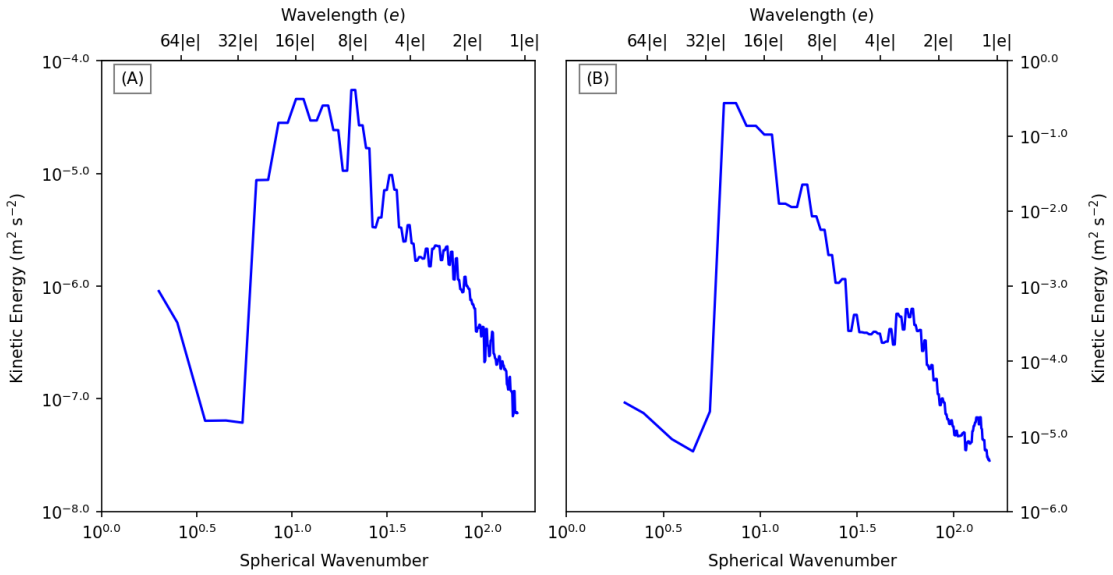

Figure 4.7: Spectral Analysis of A-grid (left) and B-grid (right) of the snapshots of Figure 4.6.

instability remain stagnated at the location where it was generated, ICON's instability is propagated eastward, in contrast to the B-grid scheme. This instability ranges from the 1/2 grid interval (Figure 4.9.B). Therefore, we see that TRiSK is highly affected by HK, and ICON's is less prone to this instability, but it can also be triggered.

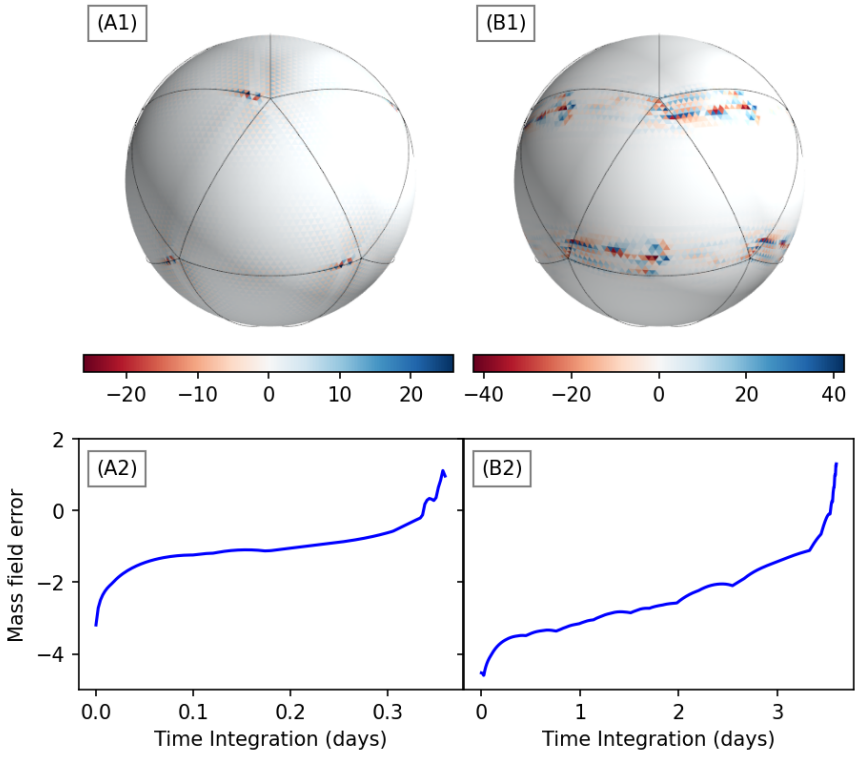

Figure 4.8: TRiSK (A) and ICON (B) time integration (lower panels). h mass variable prior to blow up

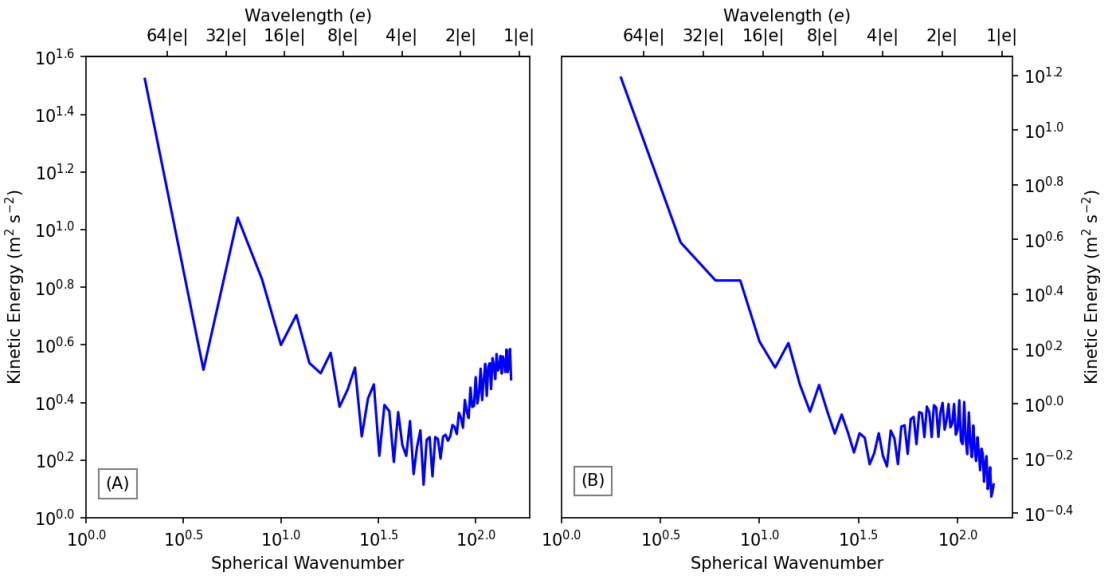

Figure 4.9: Spectral Analysis of TRiSK (left) and ICON (right) prior to blow up.

4.1.3 Applying hyperdiffusion

Before we apply the hyperdiffusion, we will present the discretization of the biharmonic operator. For the A-grid and B-grid, we will use the same operators utilized by the original authors, as we did in Chapter 3. For the C-grid scheme, we will seek a relation from Ringler and Randall (2002):

$$\Delta \mathbf{u} = \nabla(\nabla \cdot \mathbf{u}) + \nabla \times (\mathbf{k} \cdot \nabla \times \mathbf{u}). \tag{4.9}$$

Due to the duality of the operators, mentioned in chapter 3, our discretized operator is:

$$\Delta \mathbf{u} \approx \mathbf{grad}\ \mathbf{div}\ u_e - \mathbf{grad}^{\perp}\ \mathbf{vort}\ u_e. \tag{4.10}$$

This is going to be used for both TRiSK and ICON.

Now, we can answer the question of how much diffusion is required in order to stabilize the scheme. Therefore, we perform the power method for different viscosity coefficients using the 10 m equivalent depth (Figure 4.10).

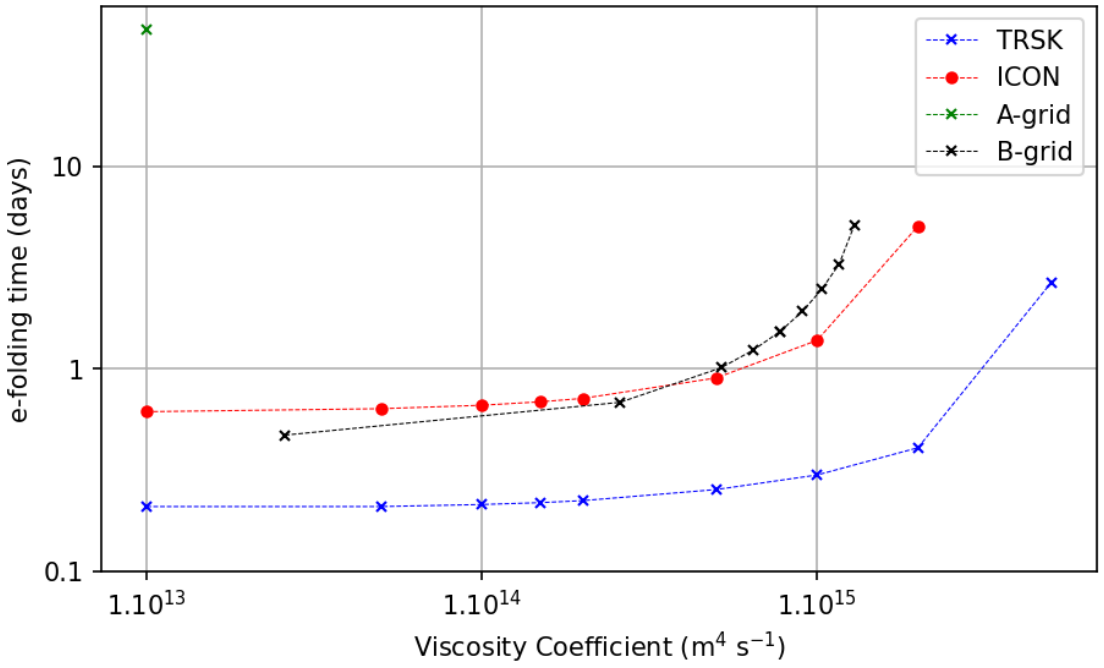

Figure 4.10: e-folding time per viscosity coefficient for TRiSK, ICON, A-, and B-grid schemes.

The A-grid is shown to have the largest e-folding time of the schemes of around 46 days with a coefficient of 10^{13} m^2s^{-1}. Utilizing a coefficient of 7.10^{13} m^2s^{-1} already stabilizes the scheme. Analysing the spectral analysis of the scheme using 10^{16} $m^2.s^{-1}$, we can see that the time integration after 15 days shows a longitudinal oscillation of around 10 waves near the equation. There is also no visual presence of a near grid scale noise on h. The same can be observed in the kinetic energy spectral analysis (Figure 4.13). The maximum energy found is

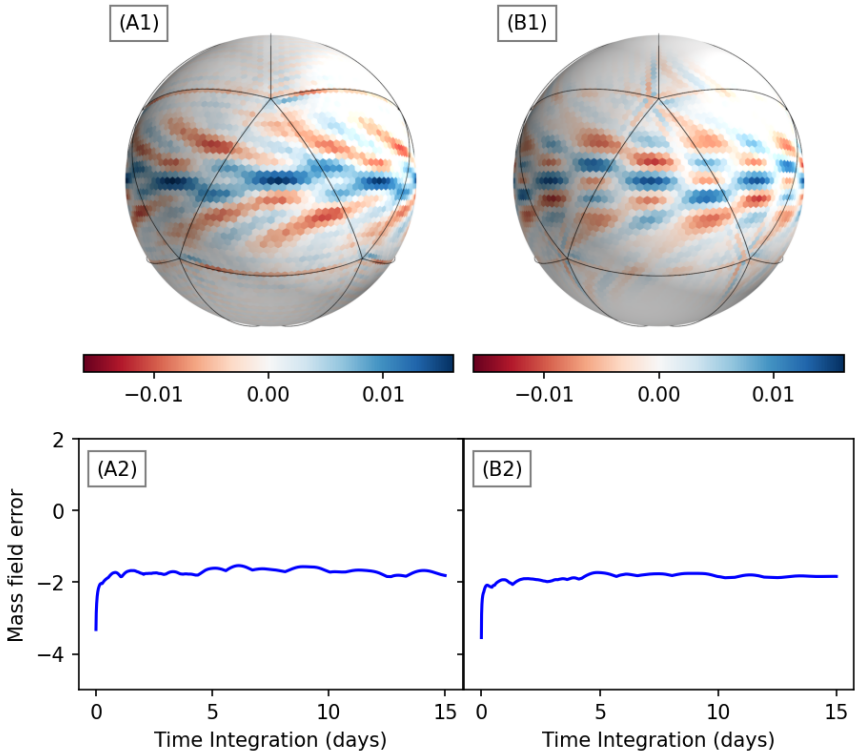

Figure 4.11: Time integrated solution for the mass field using biharmonic for the A- (left) and B- (right) grid schemes. Lower panels are the mass field error by time. The initial condition consists of a constant $h_0 = 10$m.

close to the spherical number 10, which is likely the same oscillation observed on the error. Higher wavenumbers show an almost linear decrease in kinetic energy.

B-grid has a low e-folding time (lower than ICON as already mentioned) for low viscosity, but increases rapidly and surpass ICON's scheme at around 5.10^{15} m^{2}s^{-1}. Its time integration is also quite stable, as did the A-grid, without much variation. After 15 days integration we observe a similar distribution of the error of h as did the A-grid with a large magnitude near the equator. A similar spectral analysis is, thus, observed for this scheme. A high energy around the wavenumber 10 and an almost linear decrease of energy.

For both TRiSK and ICON, there is a similar increase of e-folding. Their stability accelerate rapidly at 10^{15} m^{2}s^{-1} and both need a larger damping than both A-grid and B-grid scheme.

TRiSK, when integrated over time, has a larger time oscillation than the previous schemes. This oscillation has lower frequency than TC0 scheme. Its spatial error distribution shows a larger error around the midlatitude edges of g_0, where its instability was previously triggered. It can also be seen in this distribution that there is a presence of a near grid scale oscillation. This oscillation is still observed in the spectral analysis of the scheme (Figure 4.13). A similar observation can also be made for ICON. It also shows a large error near the midlatitude edges of g$_0$ with an apparent near grid scale oscillation. However, this oscillation is substantially smaller than TRiSK (Figure 4.13).

There are other differences beside this oscillation in the energy spectrum. It can be seen

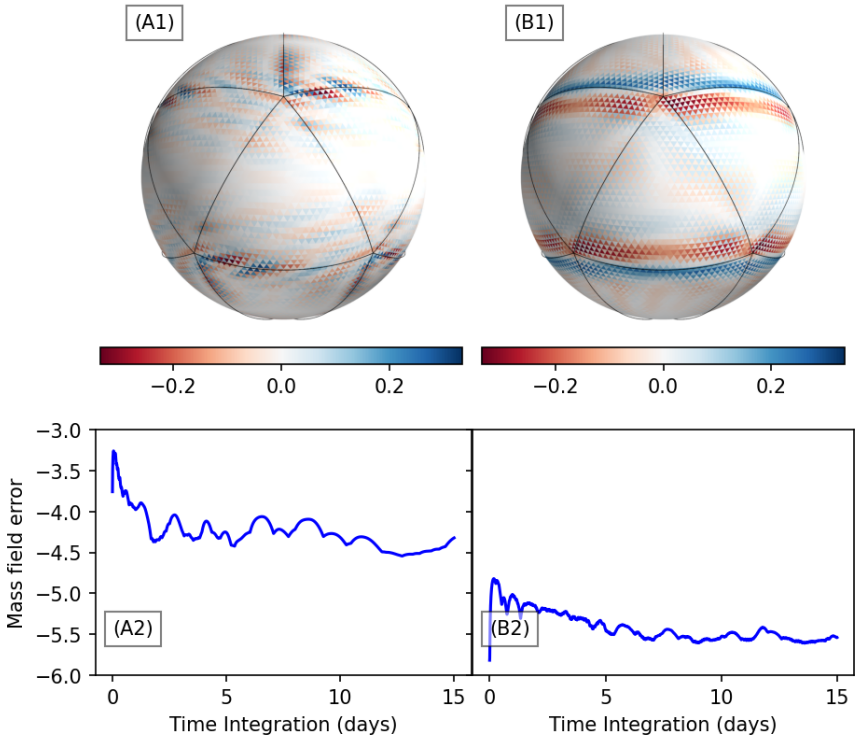

Figure 4.12: Time integrated solution for the mass field using biharmonic for both TRiSK (left) and ICON (right). Lower panels are the mass field error by time. The initial condition consists of a constant $h_0 = 10$m.

that while ICON has a maximum energy at wavenumber 10, similar to the previous schemes, TRiSK shows this maximum at around 30. ICON, however, show local maximum at the same point as TRiSK. For larger wavenumbers there is, then, an almost linear decrease in energy in the spectrum.

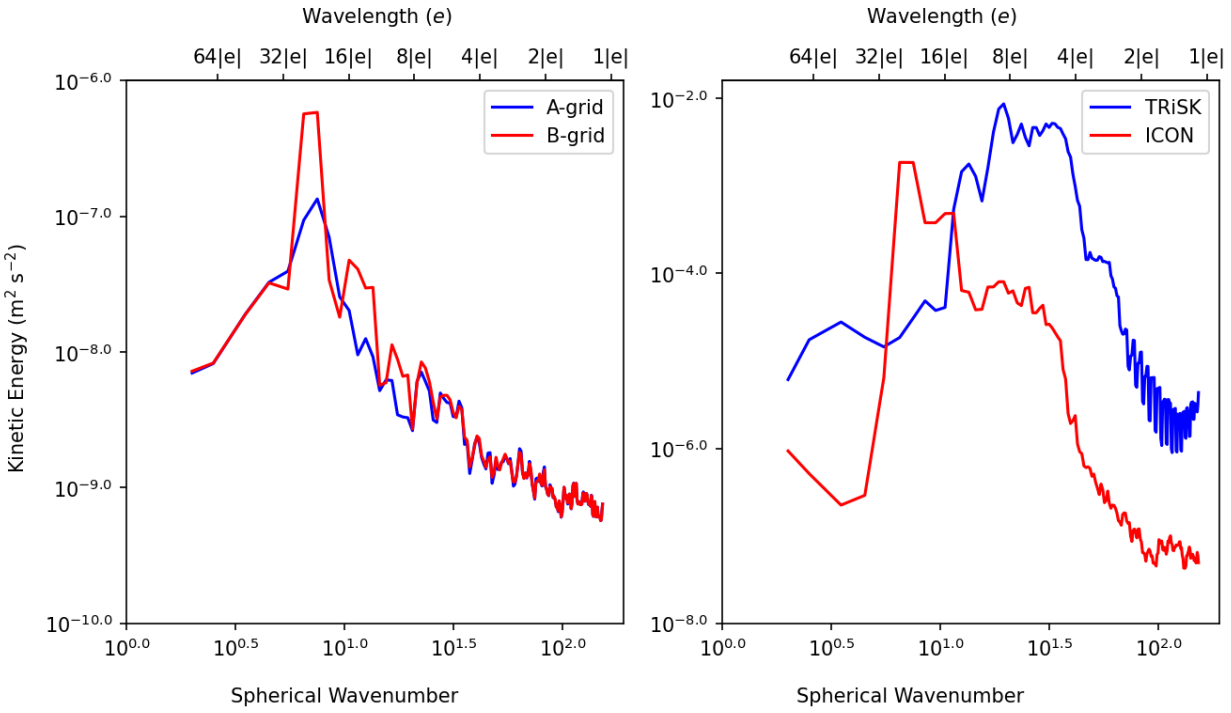

Figure 4.13: Kinetic Energy spectral analysis for both A- and B-grid (left) and TRiSK and ICON (right) at day 15 for all schemes with an equivalent depth of 10 m.

4.2 Concluding Remarks

All schemes have their stability attached to the grid properties. All, but A-grid, has the instability generated at the midlatitudes, in particular at the g_0 vertices, which has the largest, misalignment/distortion.

In the case of A-grid, a instability would likely be generated at the g_0 edges, but this instability is likely associated with the consistency of the operators. Regardless, this scheme has the largest stability. The inherent instability of A-grid scheme, due to the value interpolation, does not seem to be substantially affected by the equivalent depth, implying that HK is not the primary cause of the A-grids instability. It is likely that pressure mode excitation is the strongest cause of instability. The numerical inconsistency of the operators could potentially benefit the scheme to provide some stabilization.

B-grid, on the other hand, although is less stable than A-grid it is more stable than TRiSK and ICON (for some conditions). It shows a strong instability near at the g_0 vertices at the midlatitudes of the grid, which is propagated westward. It seems that this scheme in particular shows a combination of instabilities, since there is a noise excitation on both 1 and 2/3 grid intervals. There is an improvement of its stability with the increase of the equivalent depth. Therefore, it is likely that this grid not only suffers from the inherent instability of the staggering, but also with HK.

Finally, both C-grid staggering schemes shows slightly different behaviours. TRiSK has the lowest stability from the tested schemes. The reconstruction provided by Thuburn (2008)

and Ringler et al. (2010) definitely provide quite useful conservation properties, but it poorly reconstructs the velocity vector. Since there is also 1 grid excitation noise on the 1 grid interval, it is likely that there is a presence of the HK instability in this scheme. The diffusion aids to remove this oscillation, but due to the chequerboard pattern of the triangular grid, it seems difficult to completely remove it. Furthermore, this pattern seems to also contribute to generate the instability on the scheme. However, the primary contributor of the instability seems the vector reconstruction.

Therefore, the provided Perot's of ICON, not only seems to improve the accuracy of the method, but also improves on its stability. Most of its instability occurs on the 2-grid interval. It is likely that the averaging of the Perot's operators helps to mitigate most of the 1-grid noise. Furthermore, since C-grid has a better wave representation and that the noise removal not being perfect of the operators of ICON's scheme, thus we reason that this is the cause of why B-grid diffusion helps to faster improve on stability compared to ICON.

Chapter5

Accuracy and stability analysis of horizontal discretizations used in unstructured grid ocean models

In this chapter, we present our submitted paper to the Journal of Ocean Modelling, which combines the findings from this thesis and collaborative work conducted at the Max Planck Institute for Meteorology. It first presents a general comparison between different General Circulation Models, in terms of accuracy and stability. Secondly, it analyses the effects of near-grid numerical oscillations on the fully functioning 3D ICON ocean model component. The submitted paper can be found in Appendix B.

5.1 Introduction

Much of the scientific knowledge of the climate is largely due to the development of Earth System Models (ESMs), i.e. coupled models consisting of the atmosphere, ocean, sea ice, and land surface. The ocean, in particular, is a key component of these ESMs and a driver of the climate. Consequently, it is crucial to develop and improve such ocean models, with particular attention to global models (Randall et al., 2018b; Fox-Kemper et al., 2019).

These efforts, along with the atmospheric modelling community, allowed us to acquire important insights related to these numerical models, such as being able to compartmentalize models into what is termed dynamical cores along with several physical parametrizations (Thuburn, 2008; Staniforth and Thuburn, 2012). Combined, these form the main building blocks of the current operational ESMs. The dynamical core is defined as being responsible for solving the governing equations on the resolved scales of our domain (Randall et al., 2018b; Thuburn, 2008). For climate modelling, it is important that these cores are able to mimic important physical properties, such as mass and energy conservation, minimal grid imprinting, increased accuracy, and reliable representation of balanced and adjustment flow, which can be achieved by using a proper grid geometry and horizontal discretization (Staniforth and Thuburn, 2012). However, the use of unstructured grids may pose challenges in fulfilling these properties.

Traditional ocean models commonly used Finite Difference or Finite Volume discretization on regular structured grids (Fox-Kemper et al., 2019), e.g. NEMO (Gurvan et al., 2022), MOM6 (Adcroft et al., 2019). This approach was useful for the limited regional modelling. However, for global models it posed some problems. The most critical is the presence of singularity points at the poles, which constrained the timestep size for explicit methods, potentially making it unfeasible for use in high resolution models (Sadourny, 1972; Staniforth

and Thuburn, 2012; Randall et al., 2018b). Therefore, in recent years, a lot of effort has been put on the development of unstructured global oceanic models.

Given the success of triangular grids on coastal ocean models, one popular approach is the use of triangular icosahedral-based global models, i.e. using geodesic triangular grids. However, there are still present issues with triangular grids, in particular with the variable positioning considering a C-grid staggering. The C-grid staggering (Arakawa and Lamb, 1977) considers the velocity decomposed into normal components at the edges of a computational cell. On traditional quadrilateral meshes, this staggering was found to more accurately represent the inertia-gravity waves (Randall, 1994). On unstructured triangular grids, a spurious oscillation is present on the divergence field manifested as a *chequerboard pattern*, and it is present due to the excessive degrees of freedom (DOF) on the vector velocity field (Gassmann, 2011; Le Roux et al., 2005; Danilov, 2019; Weller et al., 2012). In theory, these can lead to incorrect results if not correctly filtered, or can potentially trigger instabilities.

This *chequerboard pattern* issue led modellers to avoid triangular grids. One potential solution, which is used by MPAS-O model, is to use the dual grid, based on hexagonal-pentagonal cells, formed by connecting the circumcentres of the triangles (defining a Voronoi grid dual to the triangulation). By relying on the orthogonality properties between the triangular and the dual quasi-hexagonal grid, the problem of the spurious divergence modes is avoided. However, the noise will appear on the vorticity field, where it is easier to filter (Weller et al., 2012).

Another potential solution to the chequerboard pattern on triangular grids is the use of filters on the divergence field in order to dampen these oscillations. However, these can potentially break the conservative properties of the model. A solution devised by the ICON-O ocean model community is the implementation of mimetic operators that required the preservation of some physical dynamical core properties, while, simultaneously, filtering the noise of the divergence field (Korn and Danilov, 2016; Korn, 2017; Korn and Linardakis, 2018). However, the added triangle distortion of the grid might not completely remove the noise, and, thus, the filtering property might be at most approximate.

In order to avoid the noise on the divergence field of triangular grids at all, a possibility is to avoid C-grid staggering. FeSOM 2.0 model, for example, uses the (quasi-) B-grid discretization in which the velocity vector field and the height field are allocated at the cells centre and vertices, respectively (Danilov et al., 2017). Alternatively, the NICAM atmospheric model, uses the A-grid discretization, which has all its fields positioned at the vertices of the grid (Tomita et al., 2001; Tomita and Satoh, 2004). Nonetheless, there are drawbacks from this solution. For example, both staggerings display spurious modes that are potentially unstable without treatment (Randall, 1994). The nature of these modes differs for each of the grid designs. The A-grid source of numerical noise is related to the manifestation of spurious pressure modes, whilst the B-grid allows the manifestation of spurious inertial modes due to excessive DOFs of the horizontal velocity (Tomita et al., 2001; Danilov et al., 2017).

Nonetheless, regardless of grid design, other artefacts may also be present. One particular spurious oscillation was detected on an energy-enstrophy conserving scheme (EEN) on an atmospheric model, leading to an instability (Hollingsworth et al., 1983). This kind of instability is dependent on the fastest internal modes of the model, the horizontal velocity and resolution of the model (Bell et al., 2017). Due to the presence of distortion on these

newer models, instability might be more easily triggered (Peixoto et al., 2018). This kind of noise is noticeable on atmospheric models, due to the large flow speeds of the atmosphere and the near to kilometre grid resolutions used in their simulations (Skamarock et al., 2012). Although the ocean dynamics are less energetic than the atmosphere, the higher distortion of the grids and the rapid increase of resolution towards submesoscale models make the effects of this noise more relevant. In fact, some models, such as the NEMO's EEN ocean model, identified this noise and its effects, which have shown significant effects on the model's mesoscale jets and submesoscale phenomena (Ducousso et al., 2017).

Considering the challenges discussed, this works aims at investigating and comparing the accuracy and stability of different horizontal discretizations used in global unstructured ocean models. First, the unstructured nature of the model's grid have different implications with respect to the computation of the underlying dynamics operators. As such, can we expect expressive differences in accuracy between A-, B- and C-grid models? Second, each of these grid designs are expected, from the theory, to perform differently when integrating them in time. Therefore, are the inertia-gravity wave dispersion representation similar to a structured grid case? Third, both the accuracy of the operators and the representation of the phenomena are expected to have an impact on the stability of the model. Consequently, which models are more prone to instability and which are easier to control?

To address these questions, we chose to evaluate both MPAS-O and ICON-O C-grid discretization schemes, due to their robustness and different approaches on computing the necessary operators; the FESOM2.0 for the B-grid scheme; and the NICAM A-grid scheme, which, to our knowledge, currently is not present in ocean models, but could be easily incorporated in existing ones. The investigation will be mostly focused on the rotating shallow water system of equations, but we will also evaluate some properties of the 3D ICON-O model. In section 5.2, we describe each of the aforementioned schemes. In section 5.3, we evaluate the accuracy and rate of convergence of each of these schemes. In section 5.4, we perform a time integration, in order to evaluate the accuracy of the integrated quantities and to observe some important properties of the models, such as the representation of inertia-gravity waves and the manifestation of near-grid scale oscillations under near realistic conditions. Finally, we evaluate the stability of the models under the effects of spurious grid scale oscillations and the effects of these oscillations in a 3D realistic oceanic ICON-O model.

5.2 Shallow Water models

In order to investigate these models, we test the schemes under the shallow water system of equations (Gill, 1982). This system is as follows:

$$\frac{\partial h}{\partial t} = -\nabla \cdot (\mathbf{u}h) \tag{5.1a}$$

$$\begin{aligned}\frac{\partial \mathbf{u}}{\partial t} &= -\mathbf{u} \cdot \nabla \mathbf{u} - \nabla \Phi - f\mathbf{u}^{\perp} + F \\ &= -\nabla(\Phi + E_k) - \omega u^{\perp} + F\end{aligned} \tag{5.1b}$$

where h and $\mathbf{u}$ are the height (scalar) and velocity (vector) fields of the system; f is the Coriolis parameter; $\omega = \zeta + f$ is the absolute vorticity; ζ is the relative vorticity or curl; $\Phi = g(b+h)$ is the geopotential, g is the acceleration of gravity, and b is the bathymetry; $\mathbf{u}^{\perp} = \hat{\mathbf{k}} \times \mathbf{u}$ is the perpendicular vector field $\mathbf{u}$ and $\hat{\mathbf{k}}$ is the vertical unit vector; and $E_k = |\mathbf{u}|^2/2$ is the kinetic energy. The right-hand most side of (5.1b) is known as the vector invariant form of the system of equations.

On this section, we present an introduction to each model and how they interpolate their quantities of the shallow water operators. On the next section, Section 5.3, we describe how each model compute each of the shallow water operator.

5.2.1 Discrete Framework

The models were evaluated with the Spherical Centroidal Voronoi Tessellation (SCVT) optimization (Miura and Kimoto, 2005) between the second (g_2) and eighth (g_8) refinements of the icosahedral grid (Table 5.1). This optimization has the property of having its vertices coincide with the barycentre of the dual cells, quasi-hexagonal (red lines of Figure 5.1). Despite this grid having loss of uniformity with refinement, for oceanic applications, it provides an additional analysis, since the unstructured grid is useful for contouring continental regions of the earth.

	Circ. distance (Km)	Edge length (Km)
g_2	1115	1913
g_3	556	960
g_4	278	480
g_5	139	250
g_6	69	120
g_7	35	60
g_8	17	30

Table 5.1: Spatial resolution of the SCVT grid, considering the average distance between triangles circumcentre and the average edge length in Km.

The structure of the grid domain will consist of triangular cells (primal grid) $K \in \mathcal{C}$ with edges $e \in \mathcal{E}$. The set of edges of a particular cell K is represented by ∂K. The vertices in the endpoint of these edges are represented by ∂e. Occasionally, when necessary, the edges may be denoted as $e = K|L$ where it is positioned between cells K and L. The dual cells will be denoted by the $\widehat{(\cdot)}$ symbol. The dual cells and edges, for example, are denoted as $\widehat{K} \in \widehat{\mathcal{C}}$ and $\hat{e} \in \widehat{\mathcal{E}}$, respectively. Furthermore, the centre/midpoint position of the elements will be denoted by the boldface, e.g. the cell circumcentre position $\mathbf{K}$, and the length or area of the respective elements will be denoted by $|\cdot|$, e.g. $|e|$, $|\widehat{K}|$ is the edge length and dual cell area, respectively.

We note that the relationship between the primal and dual mesh will differ depending on the model discretization definitions. Some models use circumcentre of the triangle to construct the dual mesh. The resulting relationship will be a Delaunay triangulation (for the

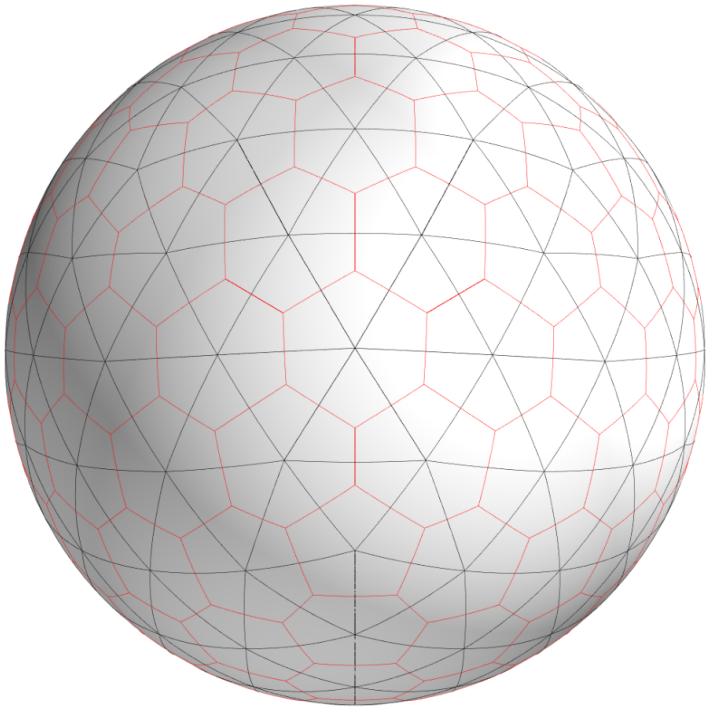

Figure 5.1: SCVT primal (black lines) and dual (red lines) g_2 grid.

primal) and a Voronoi diagram (for the dual), making their edges orthogonal to each other, which can be exploited by these models.

Additionally, normal ($\mathbf{n}_e$) and tangent ($\mathbf{t}_e$) vectors are positioned at the edge $\mathbf{e}$ or $\hat{\mathbf{e}}$, such that $\mathbf{n_e} \times \mathbf{t_e} = \mathbf{e}$. The former vector is normal to e, while the latter is parallel to it. These definitions are summarized in Table 5.2.

5.2.2 NICAM (A-grid)

The NICAM model is a non-hydrostatic atmospheric-only model developed at AICS, RIKEN. Its development aimed to develop a high-performance global model (Tomita and Satoh, 2004). The model has been shown to produce accurate results for simulations with a 3.5 km mesh size, and recent developments aim to pursue sub-kilometre grid scales (Miyamoto et al., 2013).

NICAM's dynamical core's horizontal component is based on the A-grid discretization, in which all variables are located at the grid vertices (Figure 5.2). The discretization of this scheme allows only for mass conservation. Other quantities, specially related to the velocity equation, can not be conserved. This is because this scheme allows for spurious pressure modes, which may destabilize the model, thus, requiring filtering.

Additionally, small scale oscillations may also be present due to the grid imprinting, which may also decrease the model's stability (Tomita et al., 2001). These oscillations, however, can be remedied with a proper grid optimization. One important requirement is that the dual cell centre coincide centre of mass coincide with the vertex of the grid, guaranteeing

Symbol	Description
$\mathcal{C}$	Set of primal cells
$\mathcal{E}$	Set of primal edges
K, L	primal grid cells
∂K	Set of edges of cell K
$e = K\|L$	primal edge
n_e , t_e	Normal and tangent vectors on edge e
∂e	Set of vertices of edge e
$\widehat{\mathcal{C}}$	Set of dual cells
$\widehat{\mathcal{E}}$	Set of dual edges
$\widehat{K}$, $\widehat{L}$	dual grid cells
$\partial\widehat{K}$	Set of edges of cell $\widehat{K}$
$\hat{e} = \widehat{K}\|\widehat{L}$	dual edge
$n_{\hat{e}}$, $t_{\hat{e}}$	Normal and tangent vectors on edge $\hat{e}$
$\partial\hat{e}$	Set of vertices of edge $\hat{e}$

Table 5.2: Definitions of the grid structure.

consistency of the discretization of the operators.

Moreover, NICAM's A-grid discretization compared to the MPAS-O shallow water scheme this scheme has been shown to display a higher resilience when non-linearities are present, implying that it can better treat some types of instabilities than other models (Yu et al., 2020). Therefore, despite this scheme not have originally been developed for oceanic purposes, It can be suitably implemented in such applications.

5.2.2.1 Interpolating operators

To compute the operations in the shallow water system, we need that the position of these operators coincide with the variables, i.e., at the vertices. Therefore, the computation must be performed on the dual cell. To do this, it is necessary to interpolate the variables at the dual edge midpoint. We do this by first interpolating at the circumcentre of the primal cell:

$$\widetilde{h}^K = \frac{1}{|K|}\sum_{v\in\partial e_K} w_v h_v, \tag{5.2a}$$

$$\widetilde{\mathbf{u}}^K = \frac{1}{|K|}\sum_{v\in e_K} w_v \mathbf{u}_v, \tag{5.2b}$$

where w_v is the sectional triangular area formed by the circumcentre and the opposite vertices of the cell (See Figure 2 of Tomita et al. (2001)). This interpolation, known as the barycentric interpolation, will provide us with a second order accurate interpolation. A second order interpolation to the edge midpoint can then be met by averaging neighbouring primal cells:

$$\widetilde{h}^{\hat{e}} = \frac{1}{2}(h_K + h_L), \tag{5.3a}$$

$$\widetilde{\mathbf{u}}^{\hat{e}} = \frac{1}{2}(\mathbf{u}_K + \mathbf{u}_L). \tag{5.3b}$$

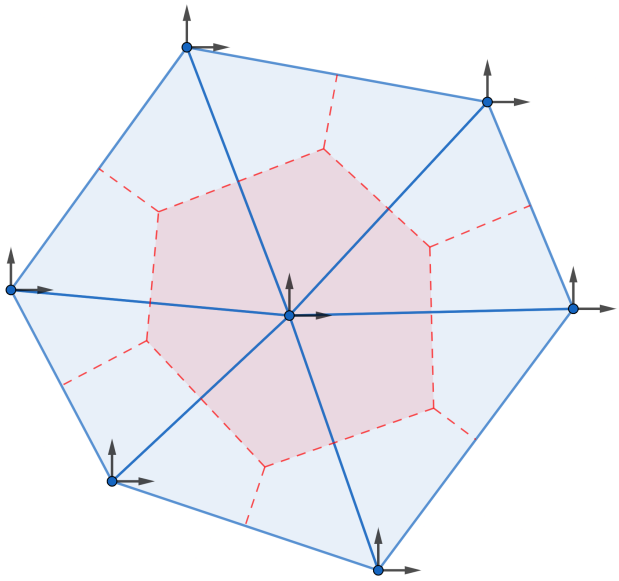

Figure 5.2: A-grid cell structure. The blue circles on the vertices are the height scalars points and the arrows are the components of the velocity vector points.

5.2.3 FESOM (B-grid)

FESOM 2.0, developed in the Alfred Wegener Institute, contains ocean (Danilov et al., 2017) and ice (Danilov et al., 2015, 2023) components only. The model is an update from its previous 1.4 model (Wang et al., 2008). The new model was developed to provide faster simulations compared to its 1.4 predecessor (Scholz et al., 2019), which is partly owed to the change from Finite Element Methods to Finite Volume discretization (Danilov et al., 2017).

In addition to its updated components and faster simulations, FESOM 2.0's horizontal discretization of the dynamical core is based on the Arakawa B-grid staggering (Arakawa and Lamb, 1977). It is important to note that there is no true analogue of the B-grid on triangles (Danilov, 2013), and such a discretization has been coined as quasi-B-grid. However, due to the similarities in the positioning of the fields in the cell, in this work, we will describe this discretization only as B-grid.

Contrary to the aforementioned A-grid, this discretization is free of pressure modes. However, it allows for the presence of spurious inertial modes, due to its excessive degrees of freedom (Danilov et al., 2017). Thus, again, requiring the use of filters to remove these oscillations.

In addition to the B-grid discretization, FESOM's grid design plays a crucial role in computing the operators necessary for FESOM's horizontal discretization. It creates a dual cell by connecting the triangles' barycentre with its edge midpoint, creating a cell with 10 to 12 edges (Figure 5.3).

5.2.3.1 Interpolation operators

This grid allows computing the operators by only interpolating the height field at the edges when needed to compute the gradient at the cells' barycentre. Given an edge e, with vertices

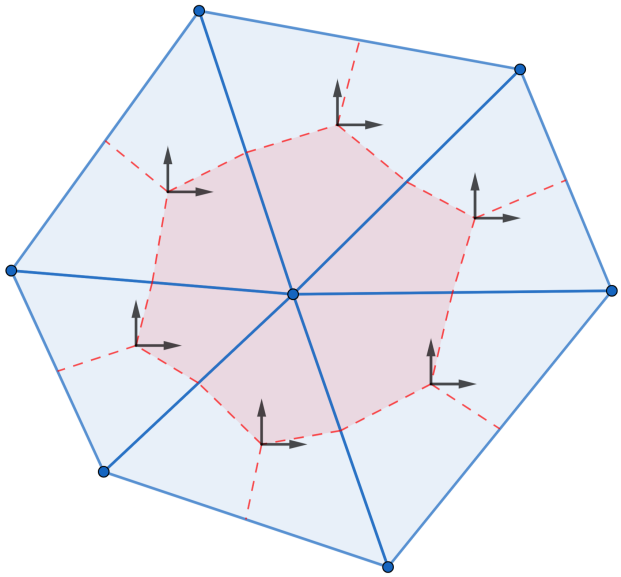

Figure 5.3: B-grid cell structure. The blue circles on the vertices are the height scalars points, and the arrows on the triangle centre are the components of the velocity vector points.

$\widehat{K}, \widehat{L} \in \partial e$, then the interpolation is defined as:

$$\widetilde{h}^e = \frac{1}{2}(h_{\widehat{K}} + h_{\widehat{L}}), \tag{5.4}$$

thus achieving a second order interpolation on the edge.

FESOM's horizontal momentum discretization is provided with three alternative computations of the momentum equations: two in its flux advective equation form, one computed at the centre of mass of the triangular cell and the other computed at the vertex, and one in a vector-invariant form, which is computed at the vertices of the grid. The two forms computed at the vertices would thus require to be interpolated at the centre of mass of the triangle with (5.4). It is also argued that the use of the flux advective form of the equation provides a small internal diffusion on the system (Danilov et al., 2015). However, there is a surprising lack of published work comparing these forms, indicating a need for a more in-depth research in the future. In this work, in order to ensure a fair comparison with the other schemes, we chose to compute this discretization using the vector invariant form of the equation.

5.2.4 MPAS-O (C-grid)

MPAS, an ESM from the Climate, Ocean and Sea Ice Modelling (COSIM) and National Center for Atmospheric Research (NCAR), comprises atmospheric, ocean, and ice components (Ringler et al., 2010; Skamarock et al., 2012; Hoffman et al., 2018; Turner et al., 2022). The oceanic component has been shown capable of accurately representing geophysical flows on meshes with a large variation of resolution (Ringler et al., 2013).

The horizontal discretization of the dynamical core of MPAS was developed for arbitrarily sided C-grid polygons (Thuburn et al., 2009; Ringler et al., 2010). It is inspired by the

Arakawa and Lamb's scheme (Arakawa and Lamb, 1981), which is capable of providing some conservative properties, such as total energy and potential vorticity, while also providing reliable simulations for these arbitrary grid structures without a breakdown of the time-integrated solutions, which has previously affected schemes using a quasi-hexagonal mesh (Staniforth and Thuburn, 2012).

Although this scheme could potentially be used for any arbitrarily sided polygonal mesh, the icosahedral based hexagonal grid was shown to provide the most accurate and well-behaved solutions (Weller et al., 2012). For example, analysis of this discretization has shown that the scheme can achieve at most first order accuracy for most of the operators, but a stagnation or divergent accuracy for others (Peixoto, 2016). Despite this, the model's noise is well controlled, while also maintaining its geostrophic modes with zero-frequency (Weller et al., 2012; Peixoto, 2016).

On this C-grid discretization (Figure 5.4), the velocity vector field is decomposed on the edges of our primal grid (triangular cells), where these velocities are normal to the dual grid (pentagonal or hexagonal cell), while the height field is collocated at the vertices of the grid. This minimizes the use of interpolating variables on this scheme. The only interpolation used is to calculate the perpendicular velocity and the kinetic energy, which will be better discussed in the following sections.

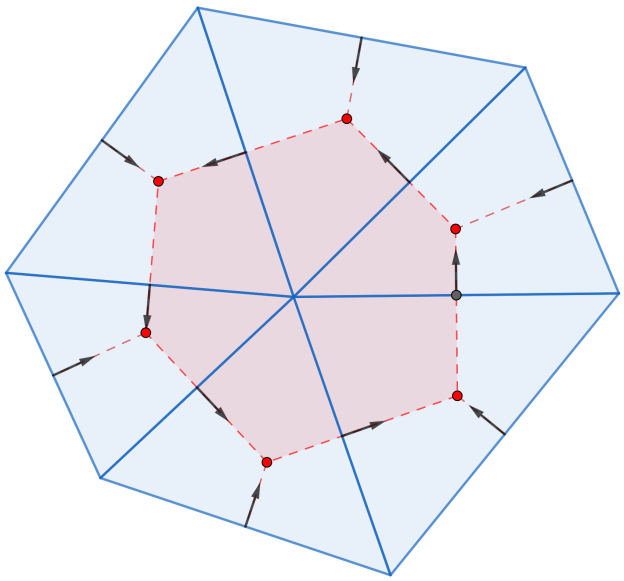

Figure 5.4: C-grid cell structure. Red circles on the vertices are the height scalar points, and the arrow on the edge midpoint is the decomposed velocity vector field.

5.2.5 ICON-O (C-grid)

The ICON numerical model is a joint project between the German Weather Service and the Max Planck Institute for Meteorology and consists of atmosphere, ocean (including biogeochemistry), land, and ice components (Giorgetta et al., 2018; Korn, 2017; Jungclaus et al., 2022). The ICON modelling team was not only able to successfully provide an accurate

simulation of geophysical flow, but also provided evidence that their model is within reach to accurately simulate ocean submesoscale flow (Hohenegger et al., 2023).

In the particular case of ICON's oceanic component, i.e. ICON-O, its horizontal discretization of the dynamical core is based on the mimetic methods approach, which is a practical way to discretize PDEs while taking into account fundamental properties of these equations (Brezzi et al., 2014). This philosophy, in theory, could allow for ICON depending on the truncation time to achieve the conservation of total energy, relative and potential vorticity, and potential enstrophy to some order of accuracy.

To accomplish these conservation properties under the mimetic methods, ICON-O uses the concept of admissible reconstructions $(\mathcal{P}, \hat{\mathcal{P}}, \hat{\mathcal{P}}^\dagger)$ (Korn and Linardakis, 2018). These are in charge of connecting variables at different points, acting as interpolation and reduction operations. They, i.e. the admissible reconstructions, are required to have some properties, such as providing unique and first-order accurate fluxes and having its nullspace coinciding with the space of divergence noise.

5.2.5.1 Interpolating operators

Operationally, ICON-O model uses the Perot operator. This function reconstructs the velocity field components of the edge midpoint to the triangle centre ($P = \mathcal{P}$), and subsequently project these reconstructed vectors to their original position at the edge midpoint ($P^T\mathcal{P}$) (Perot, 2000):

$$Pu_K = \frac{1}{K} \sum_{e \in \partial K} |e| u_e \mathbf{n}_e, \tag{5.5}$$

$$P^T u_e = \frac{1}{|\hat{e}|} \sum_{K \in \partial \hat{e}} d_{e,K} u_K \cdot \mathbf{n}_e. \tag{5.6}$$

The combination of operators is denoted as $M = P^T P$ and is key to compute the operators of the shallow water equations. This mapping, M, was found to filter the divergence noise of triangles without losing the aforementioned physical properties (Korn and Danilov, 2016; Korn, 2017; Korn and Linardakis, 2018). However, the operator has the potential to smooth high wavenumber phenomena (Korn and Danilov, 2016).

Additionally, there is also a set of operators that reconstructs the vector velocity field into the vertices of the grid ($\widehat{P} = \hat{\mathcal{P}}$) and reduce it back into the edge midpoints ($\widehat{P}^\dagger = \hat{\mathcal{P}}^\dagger$). This sequence is defined as:

$$\widehat{P} u_{\hat{K}} = \frac{1}{|\hat{K}|} \sum_{e \in \partial \hat{K}} |\hat{e}| u_e \mathbf{e} \times \mathbf{n}_{\hat{e}}, \tag{5.7}$$

$$\widehat{P}^\dagger u_e = \frac{1}{|\hat{e}|} \sum_{\hat{K} \in \partial e} d_{e,\hat{K}} u_{\hat{K}} \cdot \mathbf{n}_e. \tag{5.8}$$

Thus, the sequence $\widehat{M} = \widehat{P}^\dagger \widehat{P}$ allows us to compute the Coriolis term of the shallow water equations. This dual operator has shown to provide a non-zero spurious frequency geostrophic modes, which have been shown to create numerical waves in the system (Peixoto, 2016), and

	Institution	Staggering	Components	Conservation
NICAM	AORI, JAMSTEC, AICS	A-grid	Atm	TE
FESOM	AWI	B-grid	Oc	TE
MPAS	COSIM, NCAR	C-grid	Atm/Oc/Ice	PV, TE
ICON	DWD, Max-Planck	C-grid	Atm/Oc/Land/Ice	KE, TE, PV, Enst

Table 5.3: Summary of the main models to be compared with their respective components: Ocean (Oc), Atmosphere (Atm), Ice Dynamics (Ice) or Land; and their conservation properties: Total energy (TE), Kinetic Energy (KE), Potential vorticity (PV), and Enstrophy (Enst).

could potentially be damaging to the stability of the scheme (Peixoto et al., 2018). However, due to the filtering property of the operator M, these modes could be removed from the simulation due to their filtering property on the grid scale.

5.3 Accuracy of the Discrete Operators

We aim to analyse the truncation errors of each operator from Nonlinear Shallow Water Equations (5.1). To achieve this we evaluate two different test cases: The first follows from Heikes and Randall (1995a) and Tomita et al. (2001), henceforth Test Case 0 or TC0, where for $\alpha,\ \beta$ defined as:

$$\alpha = \sin\phi$$
$$\beta = \cos(m\phi)\cos^4(n\theta),$$

where ϕ and θ are the longitude and latitude, respectively, then $\mathbf{u}$ and h are defined:

$$\mathbf{u} = \alpha\nabla\beta \tag{5.9}$$
$$h = \beta. \tag{5.10}$$

We consider in our analysis $m = n = 1$, since it is a smooth particular smooth case with both non-zero vector components, which allows us to evaluate the accuracy of the operators and compare with the literature.

A second case is the Nonlinear Geostrophic testcase, henceforth Test case 1 or TC1, from the toolkit set of Williamson et al. (1992). $\mathbf{u}$ and h are defined as:

$$gh = gb_0 - h_0\sin^2\theta \tag{5.11}$$
$$u = u_0\cos\theta, \tag{5.12}$$

where $gb_0 = 2.94\times10^4$ m^{2}s^{-2}, $h_0 = a\Omega u_0 + u_0^2/2$ m^{2}s^{-2}, $u_0 = 2\pi a/(12$ days$)$ ms^{-1}, $g = 9.81$ ms^{-2} is the acceleration of gravity, $a = 6.371\times10^6$ m is the radius, and $\Omega = 2\pi/86400$ s^{-1} is the angular frequency of earth.

Additionally, in order to compare our results, we define the errors in our domain as $\Delta f = f_r - f_r^{\text{ref}}$, where f_r and f_r^{ref} is the computed and reference function, respectively, for a

mesh element r of the domain. Thus, the maximum and second error norm may be defined as:

$$L_\infty = \frac{\max_r |\Delta f_r|}{\max_f |f_r^{\text{ref}}|} \tag{5.13}$$

$$L_2 = \sqrt{\frac{S(\Delta f^2)}{S((f^{\text{ref}})^2)}} \tag{5.14}$$

where $S(f) = \sum_{r\in\Omega} \Delta f A_r / \sum_{f\in\Omega} A_r$, and A_r is the area of the element, e.g. A_e for the edge, $|K|$ for triangles, or $|\hat{K}|$ for the dual cell.

5.3.1 Divergence

The divergence operator, part of the mass equation, can be defined from the Divergence Theorem. Following it, we can provide a general formula for its discretized version as:

$$(\nabla \cdot \mathbf{u})_i \approx (\mathbf{div}\ u)_i = \frac{1}{|F|} \sum_{e\in\partial F} |e| \mathbf{u} \cdot \mathbf{n}_e n_{e,F}, \tag{5.15}$$

where F is a cell with barycentre i and edges $e \in \partial F$, $n_{e,F} = \{1, -1\}$ is a signed valued aimed to orient the normal velocity $\mathbf{u} \cdot \mathbf{n}_e$ away from the element F.

In order to compute the divergence field, we note that both the A-grid and B-grid schemes compute divergence field at the dual cells (vertices). For the former scheme, we require an interpolation of both the scalar height, (5.2) and (5.3), and vector velocity fields at the dual edge midpoint, in order to compute the divergence at the dual cell, i.e. quasi-hexagonal cell. In the case of the latter scheme, we only require the interpolation of the scalar height field at the primal edge midpoint (5.4), in order to compute the same divergence field at the primal cell.

In the case of the C-grid, there is a substantial difference between the computation of both schemes. MPAS interpolates the scalar height field at the primal edges, similar to B-grid, while ICON uses admissible reconstruction operators of the form $P^T h P u$ to compute the operator.

These differences on the schemes are reflected in our results (Figure 5.5.div). The A-grid for the TC0 testcase displayed an error convergence with an initial rate of second order up to the sixth refinement (g_6). On finer grids, for the L_∞, this scheme has slowed down to first order, while on second order, the scheme remained converging up to second order rate. On the TC1, a more consistent convergence rate was observed, on the L_∞ and L_2, the scheme has displayed a first and second order convergence rate. On other grids, in particular the standard and Spring Dynamics, the A-grid has shown to achieve at least a first order convergence rate (Tomita et al., 2001). Although a direct comparison cannot be provided, since our testcases differ, the scheme on an SCVT has apparently shown to provide a comparable convergence rate to the intended optimized grid on either the L_∞ or the L_2 norm.

Regarding both C-grid schemes, we observe a similar behaviour in the computed operator. In particular, neither scheme displays an increase in accuracy of the divergence field on the L_∞. For the case of ICON, this result has been previously observed in a similar work by

Korn and Linardakis (2018). It was also shown that the *naive* approach to calculate the divergence field still retained a first order increase in accuracy, implying that the main culprit of this inability to increase the accuracy likely lies on Perot's operator itself (Table 4 of Korn and Linardakis (2018)). The authors have not provided a geometrical analysis of their non-uniform grid, but we note that the SCVT grid share some similarities with the standard grid, such as the non convergence of the distance between the primal and dual edge midpoints, which likely has a deleterious effect on the accuracy of the operator. However, on the L_2, the scheme was able to reach at least a first order convergence rate on both testcases.

On the case of MPAS, the inability to provide a decrease in error with grid has been discussed in Peixoto (2016). It is reasoned that since the computation of the divergence is not based on velocities from the Voronoi edge midpoints, the discretization is inconsistent, and a first order convergence is not guaranteed. In contrast, on the L_2, MPAS was able to reach a second order rate up to g_4, but the speed of convergence slows down to first order on TC0, while on TC1 the second order rate is maintained throughout grid refinements.

Finally, B-grid has provided consistent accuracy throughout each testcase. We observed a first and second convergence rate for L_∞ and L_2, respectively, for both testcases. A decrease is observed on TC0, however, this decrease is likely associated with the error approaching the machine truncation error.

When comparing the errors of the schemes, we note that both A- and B-grid schemes display a decrease in speed of accuracy convergence as the grid is refined, with the latter scheme displaying the smallest errors on most of the tested cases and error norms. Additionally, despite ICON providing convergence on some tests, the scheme displays the largest errors of all tested schemes. It is likely that the smaller stencil used in ICON's divergence computation play a role in these larger errors. Another contribution is potentially related to Perot's operator, whose interpolation could act as smoothing the velocity field.

Overall, we note that the structure of the mesh, regarding cell geometry (primal or dual cell) and distortion, plays a contributing factor on approximating the divergence field on all schemes. Both C-grid schemes, in particular, seemed to be the most vulnerable to the grid. In contrast, B-grid's consistency in its accuracy apparently seems to be the least vulnerable to the increase in the distortion of the grid.

5.3.2 Gradient

The gradient operator, from the momentum equation, is a vector field, whose vector points itself to the steepest regions of the original field. The schemes provide different discretizations for this operator:

$$\nabla h \approx \mathbf{grad}\ h = \begin{cases} \sum_{e\in\partial F} h|e|\mathbf{n}_e & \text{A- and B-grid,} \\ \frac{1}{|e|}\sum_{i\in\partial e} h n_e & \text{C-grid.} \end{cases} \tag{5.16}$$

A- and B-grid's schemes provide a complete vector field on our domain by computing the average gradient within the centre of the respective cell F. The C-grid, on the other hand, computes the gradient with respect to the normal vector n_e by computing the difference between the values of the cell neighbouring the edge e. In that regard, the C-grid computation can be perceived as a gradient in the direction of $\mathbf{n}_e$.

In relation to the mesh, the A-grid scheme is computed at the vertices of the mesh, while the B-grid is computed at the barycentre of the triangular cells. On the other hand, both C-grid schemes are computed on the primal edge midpoint of our mesh. However, the MPAS scheme considers the neighbouring vertices to compute the gradient, while ICON considers the neighbouring triangles.

As in the divergence approximation, these differences in computation are as well reflected in our results (Figure 5.5.grad). The A-grid displays for coarser grids a fast convergence rate (second order rate), up to g_5, for both testcases. For finer grids, the L_∞ the decrease in error slows down to a first order convergence, but with the L_2 the convergence rate remains consistent. The analysis made by Tomita et al. (2001) have showed that their grid is capable of displaying a second order error convergence. We again note that although we cannot directly compare our results, due to the differences in testcases used, our results show a comparable error convergence with the authors with the SCVT optimized grid.

Similarly, the B-grid scheme shows a consistent decrease in error on all norms and testcases, similar to the divergence operator results. However, it displays only a first order convergence rate, in contrast to the second order on the divergence operator. The computation of the gradient on the B-grid is analogue to the divergence computation in ICON, therefore a similar argument follows, explaining that the expected convergence rate of such a scheme being a first order.

Comparably, MPAS also displays a consistent convergence rate, but in this case this scheme achieves a second order rate on all norms and testcases. Since the edge midpoint is situated, by definition, at the midpoint between the neighbouring vertices, the discretization is analogue to a centred difference scheme used in traditional quadrilateral grids. Therefore, we can properly achieve a second order convergence rate. The same argument is provided in Peixoto (2016), however the author also argues that when we consider the computation of the gradient of the kinetic energy we do not only reach a convergence rate, but our error diverges with grid refinement. The author reasons that the error of kinetic energy is of zeroth order (to be discussed further), and, thus, its gradient diverges.

On the other hand, the ICON's scheme gradient error displays a near second order convergence rate for coarser grids on the L_∞ norm of the TC0, but this error slows down for further refinements. On the TC1 testcase, the rate of convergence on L_∞ is consistent in first order. However, at the L_2 norm, the scheme has an accuracy of near second order with magnitude similar to that of MPAS.

Finally, we can then draw a comparison from all schemes. The B-grid has displayed the largest errors in magnitude and was the only scheme to achieve a low first order convergence on the L_2. The A-grid L_∞ displays a similar error magnitude and behaviour in convergence with ICON. MPAS has shown the lowest errors among all schemes, and, in the L_2, displayed a comparable magnitude and convergence behaviour with ICON.

Overall, we again observe an impact of the grid structure on our schemes, however, this impact is not as damaging as found in the divergence computation. The directional derivative of MPAS makes it easier to achieve a consistent increase in accuracy, and the mismatch between the edge midpoints, has thwarted ICON's convergence rate. Despite this, the scheme still retained a first order convergence rate.

5.3.3 Curl

The curl operator, part of the vector invariant form of the shallow water velocity equation, is connected to the Coriolis Term. This term requires a careful discretization to allow for Coriolis energy conservation. This operator, in its continuous form, is defined from Stokes Theorem. Its Finite Volume discretization follows from this theorem and a general formulation for all our schemes can be defined as:

$$\nabla \times \mathbf{u}_i \approx |F| \text{vort } u_i = \sum_{i \in \partial F} |e'| \mathbf{u}_i \cdot \mathbf{t}_{e'} t_{e,F}, \tag{5.17}$$

for any F cell with edges e', tangent vector $\mathbf{t}_{e'}$, and $t_{e,F} = \{1, -1\}$ is a signed value guaranteeing that the unit tangent vector is counterclockwise on the cell.

For each scheme, the both A-grid, and B-grid computes the vorticity field on the vertices of the mesh. Since, for the B-grid, the shallow water velocity equation requires the points at the barycentre of the triangle cell, we interpolate the vorticity from the vertices to the barycentre. For the both C-grid schemes, MPAS computes this operator at the circumcentre of the cell, while ICON computes at the vertices, in duality with the divergence operator.

In this context, similarities are observed with the divergence operator. For example, the A-grid convergence rate for both norms and testcases, reach the same order as the divergence operator. On the TC0 testcase, however, throughout all grid refinements the error retain a first order, unlike the divergence operator, which begins with a second order and slows down to a first order. Additionally, on the TC1 testcase, we observe that the vorticity error displays a second order convergence up to g_4 and slows down to first order, unlike the divergence operator (Figure 5.5.Vort).

Similarly, the B-grid scheme displays the same behaviour as in the divergence operator. It displays a first order convergence rate on L_∞ and a rate of second order for L_2 on both testcases.

In contrast, both C-grid schemes display a different behaviour from the divergence operator. MPAS shows a consistent first order convergence rate for both norms on both testcases. Given that this computation is computed on the dual cell centre (red polygon in Figure 5.4), i.e. pentagon or hexagon, we can then achieve a higher accuracy rate of around second order.

ICON, on the other hand, displays a zeroth order convergence on L_∞ for the TC0 testcase. This is likely due to the mismatch of edge midpoints, similar to MPAS's divergence operator. However, on this norm for TC1, the error converges on a first order rate. This difference implies that different testcases will potentially impact the error. On this particular case, we note that the meridional velocity is not present on TC1, which may facilitate the computation of the vorticity. This result is also seen on L_2, while for TC0, the norm converge in first order, for TC1, it converges in second order.

In comparison, we observe that ICON is the only scheme that has trouble in increasing its accuracy when approximating the vorticity operator. In addition, both A- and B-grid schemes were the only to display a second order error rate on the L_2 for both schemes. Although MPAS also has shown an overall convergence, in contrast to ICON, it still has shown a larger error for TC0's L_2 norm and both norms of TC1.

Overall, there are similarities on the error behaviour between both vorticity and divergence scheme due to its similar concepts underlying the discretization. In that regard, we

also observe an impact of the grid structure and the testcase used on the accuracy of the vorticity approximation.

5.3.4 Kinetic Energy

Similar to the vorticity operator, the kinetic energy is part of the vector invariant form of the velocity equation of the shallow water, whose gradient will then be computed. The kinetic energy is defined as:

$$E_k = \frac{1}{2}|\mathbf{u}|^2.$$

The computation of this operator on both A- and B-grid schemes is straightforward, since the vector velocity field is complete on each vertex and barycentre, respectively, of the mesh. However, for the C-grid schemes the vector field is decomposed on the edges of the mesh, therefore require a reconstruction in order to approximate the value of the kinetic energy field. In the particular case of MPAS and ICON, it is difficult to provide a general formula, therefore we individually define:

$$E_k^{(\text{MPAS})} = \frac{1}{2|\hat{K}|}\sum_{e\in\partial\hat{K}}\frac{|e||\hat{e}|}{2}u_e^2, \tag{5.18}$$

$$E_k^{(\text{ICON})} = \frac{|Pu|^2}{2}. \tag{5.19}$$

Both schemes provide some form of interpolation of the velocity on the cell centre, dual for MPAS, primal for ICON. It is observed on this computation that MPAS's and ICON's weights are shown to be: $|e||\hat{e}|/2$, and $|e|d_{e,K}$, where again $d_{e,K}$ is the distance between the edge midpoint e and circumcentre K. We note that for equilateral triangles $d_{e,K} = |\hat{e}|/2$. Another note is that MPAS computes the square of the component of the velocity and then interpolates the resultant on the cell centre, while ICON interpolates the complete vector velocity field on the cell centre, and then computes the kinetic energy.

These difference in computation are reflected on the error of the field (Figure 5.5.Ek). On MPAS scheme, we see that for both testcases it does not converge on L_∞. This result was discussed by Peixoto (2016), as being an inconsistent formulation of the kinetic energy on the SCVT. Part of this inconsistency could partly be due to the computation of the kinetic energy on a single velocity component, as previously mentioned. Despite this, on L_2, MPAS display a second order convergence on TC0, on coarser grids, but it slows down to first order on finer grids. Similarly, on TC1, MPAS displays a first order rate, but throughout all grids.

ICON, in contrast, show a consistent convergence rate on both norms of first order on TC0 and second order on TC1. It can also be observed that, except for TC0's L_2, ICON's error is substantially lower than MPAS. ICON's Perot operator interpolation allows for a higher convergence, in comparison with MPAS, in part due to the vector velocity field interpolated on the cell circumcentre prior to the computation of the kinetic energy.

Overall, both C-grid computations display very distinct error behaviour. On this grid, although on both schemes the kinetic energy formulation allows for energy conservation, MPAS is unable to provide a consistent formulation of the operator. In contrast, ICON is provided with its consistent through the use of its Perot operator.

5.3.5 Perpendicular Velocity

The perpendicular velocity is an important part of the Coriolis Term, which is a forcing that takes into account the non-inertial reference frame of the shallow water equations. In that case, it is important that the Coriolis term of our schemes does not input energy into the system. Similar to the kinetic energy, both the A- and B-grid schemes have their vector velocity defined on the same points, providing an exact value for the perpendicular velocity. However, since C-grid schemes do have their vector velocity decomposed on the edges of the grid, an interpolation is necessary.

This interpolation should be carefully chosen in order to retain the conservation of energy of the system. Following the argument of Peixoto (2016), a reconstruction can be thought as a weighted composition of the neighbouring edges of the cell:

$$u_e^{\perp} = \sum_{e'} w_{e,e'} u_{e'}. \tag{5.20}$$

These weights should be chosen such that this reconstruction is unique and does not provide energy to the system.

Choosing the edges e' from cells that share the same edge e we can define the perpendicular velocity as:

$$u_e^{\perp} = a_{e,F_1} u_{e,F_1}^{\perp} + a_{e,F_2} u_{e,F_2}^{\perp}, \tag{5.21}$$

where a_{e,F_n} are the weights with respect to the cell F_n. This formulation is capable of achieving a unique solution on the edge.

In the case of MPAS's vector interpolation, we define the weights $w_{e,e'}$ as:

$$w_{e,e'} = c_{e,K} \frac{|e'|}{|\hat{e}|} \left(\frac{1}{2} - \sum_{K \in \cup \partial e} \frac{A_{\hat{K},K}}{|\hat{K}|} \right) n_{e',\hat{K}},$$

where $c_{e,\hat{K}}$ and $n_{e',K}$ are sign corrections that guarantee the vector tangent vector is anticlockwise on the for the cell $\hat{K}$ and that the norm vector $n_{e'}$ point outwards of the cell $\hat{K}$; and $A_{\hat{K},K}$ is the sectional area of the triangle cell K formed by the vertex $\hat{K}$ and the neighbouring edges of the circumcentre K in respect to the vertex. Using these weights on (5.20), we can compute $u_{e,K}^{\perp}$. In order to provide a unique reconstruction on edge e we let $a_{e,K} = a_{e,L} = 1$ on (5.21).

In the case of ICON's scheme, we use the interpolation $\hat{P}^T \omega \hat{P} u$. In this case $\hat{P} u_{\hat{K}} = u_{\hat{K}}^{\perp}$, so the weights are defined as:

$$w_{e,e'} = w_{\hat{e},\hat{K}} = \frac{|\hat{e}| d_{\hat{e},\hat{K}}}{|\hat{K}|},$$

giving a unique reconstruction on the centre of the dual cell $\hat{K}$. In order to reduce it back to the edge, we do $a_{e,\hat{K}} = d_{e,\hat{K}}/|e|$. We note that this set of operators allows not only the energy conservation, but also potential enstrophy (Korn and Danilov, 2016; Korn and Linardakis, 2018). We recall, however, that this operator has the potential of producing non-zero frequency geostrophic modes (Peixoto, 2016).

Our results show that MPAS displays a second order convergence rate on L_∞ up to g_6 on TC0, but decrease to a first order for finer grids (Figure 5.5.u$\perp$). On L_2, it shows a second order throughout all refinement. Similarly, on TC1, it also shows a second order rate up to g_7, but decrease near first order to g_8. A similar result is obtained for L_2. This result is similar to Peixoto (2016) showing that MPAS achieves at most a first order convergence rate on the L_∞.

5.4 Shallow Water Time Integration

The time integration of the shallow water equations provides us knowledge about the behaviour and limitations of the model throughout time. In order to gather this understanding, in this section we will put the schemes under a battery of tests. For the purpose of these tests, we chose to use a simple Runge-Kutta (RK44) operator, with 50 seconds timestep for all schemes and grids. Such choices are enough to ensure that the temporal errors are minimal and that the dominating error comes from the spatial discretization. We note that although both C-grid schemes may not require a stabilization term, since their error are expected to be well controlled, both A- and B-grid schemes could excite errors that would potentially destabilize the model. It is possible to use a harmonic ($\nabla^2\mathbf{u}$) or biharmonic ($\nabla^4\mathbf{u}$) term to provide stability of the scheme. In order to be more scale selective and avoid damping physical waves of our simulations we chose to use only the biharmonic, and as it was shown by the original authors of A- and B-grid schemes (Tomita et al., 2001; Danilov et al., 2017) the biharmonic term is enough to provide the necessary stability.

Therefore, the stabilizing operator can be regarded as a composition of Laplace diffusion operators, i.e. $\nabla^4\mathbf{u} = \Delta\Delta\mathbf{u}$. To compute the Laplace diffusion operator, both A- and B-grid schemes are equipped with different approaches in its computation. For the former scheme, the Laplace operator is defined as:

$$\Delta\mathbf{u} = \nabla \cdot \nabla\mathbf{u}. \tag{5.22}$$

Thus, we can approximate the Laplacian operator by $\Delta\mathbf{u} \approx \mathbf{div\ grad\ u}$, using the operators defined in the previous section.

On the other hand, the B-grid scheme, computes the harmonic diffusion for a cell K as:

$$\Delta\mathbf{u} \approx \frac{1}{|K|}\sum_L \frac{|e|}{|\hat{e}|}(\mathbf{u}_L - \mathbf{u}_K), \tag{5.23}$$

where L are all the triangles neighbouring the cell K. For the tested schemes, we used the biharmonic coefficient defined in Table 5.4. Our coefficients are much higher than found in literature (Tomita et al., 2001; Danilov et al., 2017; Majewski et al., 2002; Jablonowski and Williamson, 2011), however both A- and B-grid schemes differ in their discretization and the A-grid scheme is found susceptible to numerical oscillations depending on the choice of grid (Tomita et al., 2001). Therefore, by choosing an intense coefficient, we guarantee that numerical waves will not participate in the comparison of our results.

All schemes will then be evaluated. Firstly, we provide an accuracy analysis of the integrated height and vector velocity fields (Section 5.4.1). Then, we evaluate the linear mode

	A-grid/B-grid (m^2s^{-1})
g_2	10^{22}
g_3	10^{20}
g_4	10^{19}
g_5	10^{18}
g_6	10^{17}
g_7	10^{16}
g_8	10^{15}

Table 5.4: Biharmonic coefficient used for stabilizing the shallow water schemes.

analysis of our schemes (Section 5.4.2). Thirdly, we evaluate the scheme's capacity in maintaining its geostrophic balance (Section 5.4.3). Finally, we evaluate the behaviour of each scheme under a barotropic instability, which is an initial condition that accentuate the nonlinear terms of our schemes (Section 5.4.4).

5.4.1 Time integrated accuracy of variables

Our results demonstrate that both A- and B-grid schemes exhibit improvements in accuracy close to second order for both norms of the height field variable (Figure 5.6). However, for the vector velocity field, the values differ. For L_∞, A-grid is shown to converge near second order, while B-grid, which displays a near second order convergence for coarser grids (up until g_5), only shows a first order for the finer grids. Nevertheless, on L_2, both schemes are shown to display an accuracy increase near second order.

Regarding both C-grid schemes, both of them face problems on increasing their accuracy on L_∞. MPAS does not converge on the height scalar field, but does display a first order convergence rate on L_2. Concerning the vector velocity field on L_∞, MPAS shows a seconder order rate for coarser grids (up until g_6), but decrease to first order in finer grids. However, on L_2, MPAS displays a second order rate consistently for all refinements. This result was also observed in Peixoto (2016), and it is suggested that either the kinetic energy approximation or the divergence, might be responsible for reducing the solution's accuracy.

In contrast, ICON displays a first order convergence rate on both norms for the height scalar field. Nevertheless, the scheme does not seem to convergence on the vector velocity field for the L_∞ norm. In the case of L_2, it displays, for coarser grids, a second order accuracy rate, but from g_7 to g_8 it slows down to a first order rate. Similar to MPAS, some operators, face challenges in converging the solution. In this scheme, the divergence, vorticity, and the perpendicular velocity do not display a convergence of the solution. It is noted that both vorticity and perpendicular velocity are critical components of the Coriolis Term of (5.1b), potentially impacting the convergence of the vector velocity field. Korn and Linardakis (2018) did not observe the same results. Therefore, it is likely that the grid choice is crucial for obtaining convergence on the fields.

Overall, A- and B-grid display similar errors, specially, in the height field. ICON's scheme have showed the largest errors of the tested schemes, except in the height field L_∞, where MPAS did not converge. B-grid show the second-largest magnitude error, only on the vector velocity field. This is likely due to the use of the biharmonic and the notably due to the

gradient operator that is defined on triangles, unlike both A-grid and MPAS, which shows similar magnitudes on L_2. On L_∞, however, MPAS shows a larger error and lower convergence rate, in comparison to the A-grid, likely due to the aforementioned challenges.

5.4.2 Linear Normal Modes

The earth's ocean behaviour is modulated by oscillations that are mostly affected by the earth's rotation. The complete nonlinear equations are difficult to analyse to the high degree of interactions between these oscillations. However, linear analysis can be done by considering (5.1) the following approximations:

$$\begin{aligned} h &= H\nabla \cdot \mathbf{u} \\ \mathbf{u} &= -\nabla h - f\mathbf{u}^{\perp}, \end{aligned} \tag{5.24}$$

where H is a fixed constant. This system still provides a large set of inertia-gravity waves present in either the ocean or atmosphere. In order to calculate the normal modes, we follow the methodology of Weller et al. (2012) by considering a vector $(\mathbf{h}, \mathbf{u}')^T$, where both elements, i.e. $\mathbf{h}$ and $\mathbf{u}$, are scalars, so that we have $(\mathbf{h}, \mathbf{u}')^T = [h_1, h_2, \cdots, h_M, u_1, u_2, \cdots, u_N]$ for M and N elements of height and velocity fields, respectively. In the case of A- and B-grid, the scalar velocity is obtained by decomposing them into zonal and meridional velocity scalars, whereas for both C-grid schemes these scalar fields are obtained directly from the velocity on the edges of the grid.

We run (5.24) $M + N$ times for one timestep of $\Delta t = 10$ seconds on a g_2 grid, with the RK4. The initial conditions used are defined by a unit value on the j-th position of $(\mathbf{h}, \mathbf{u}')^T$, i.e. for the k-th run the initial condition is defined as $(\mathbf{h}_0, \mathbf{u}'_0)^T_k = [\delta^k_j]$, where δ^k_j is the Kronecker delta. We use as parameters: $gH = 10^5$ m^{2}s^{-2}, $f = 1.4584 \times 10^{-4}$ s^{-1} and the radius of the earth $a = 6.371 \times 10^6$.

From these runs, we create a matrix A, where each column is the approximated solution of the initial condition provided. We, then, can calculate the eigenvalues λ of the matrix and, consequently, obtain the frequency of the modes from $\lambda = \alpha e^{i\omega\Delta t}$, where ω is the frequency of the normal modes. We, then, order our results from lowest to maximum frequency. We will have 486 eigenvalues for the A-grid, 642 for both B-grid and MPAS, and 800 for ICON. These values correspond to the total degrees of freedom of our system. There are, in the g_2 grid, 162 vertices, 480 edges, and 320 triangles. For the A-grid, since both mass and vector fields are defined at the vertices, the total DOFs are three times the vertices. In the case of the B-grid, the vector field is defined at the triangles, therefore the total DOFs are the vertices plus twice the triangles. For both C-grid schemes, the vector velocity field is defined at the edges, however MPAS has the mass at the vertices, while ICON has the mass defined at the triangles. In that case, MPAS DOFs are the vertex plus edge points and ICON is the triangle points plus edge points.

The normal modes can be seen in Figure 5.7. A clear difference is observed between frequency representation on all grids. The A-grid shows the slowest representation of inertia-gravity waves, with the maximum frequency of 1.6×10^{-3} s^{-1} s^{-1} on the 119 index. On the other hand, the B-grid scheme shows higher frequencies, with a maximum on the 167 index of around 2.6×10^{-3} s^{-1}.

In contrast, a more accurate representation is obtained by both C-grid schemes. ICON shows a similar, but slightly higher frequencies, compared to the B-grid scheme. However, the highest frequency is obtained on its tail on the 635 index of around 4.2×10^{-3} s^{-1}. Conversely, MPAS displays a more accurate representation of the modal frequency with a maximum on index 320 of around 4.2×10^{-3} s^{-1}.

Overall, our results show similar results with the traditional quadrilateral grids (Arakawa and Lamb, 1977; Randall, 1994). It is known that on these grids, the C-grid schemes represent modes more accurately than the either A- or B-grid schemes, but also B-grid display a higher frequency, and a more accurate representation of inertia-gravity waves, than the A-grid schemes. We highlight that the expected decrease in inertia-gravity representation from the traditional grids is not observed in our results, since we reordered our modes from least to highest frequency. Consequently, higher modes (higher wavenumbers) of both A- and B-grid schemes are not accurately displayed in our results. Despite this, our results demonstrate that the maximum represented frequency of both schemes are indeed lower than that of the C-grid schemes, following the theory.

Regarding both C-grid schemes, our results for MPAS agree with the other authors (Weller et al., 2012; Thuburn et al., 2009; Peixoto, 2016). In addition, we note that ICON's has a less accurate representation of the normal modes in comparison with on MPAS either on the quasi-hexagonal grid or its implementation on triangles (Thuburn et al., 2009). This result in ICON has already been observed (Korn and Danilov, 2016), and it is argued that the filtering property of the divergence on the mass equation might not only remove the intended noise of the triangular mesh, but also some of the higher frequency physical oscillations.

5.4.3 Localized Balanced Flow

An important testcase is to evaluate the model's capability of maintaining its geostrophically balanced state. Our TC1 testcase (Section 5.4.1), allowed us to test whether the models are capable of maintaining their state under small wavenumbers. However, a harder evaluation is to test whether the model have the ability to maintain its state under high wavenumber oscillations. For this reason, we used the testcase developed in Peixoto (2016). This test is particularly important for two main reasons: one of them is that the Perot's operator might not have steady geostrophic modes which may have consequences for the ICON model, the second reason is that both A- and B-grid are unable to maintain their geostrophic balanced state. We evaluate, without the stabilizing term, how all models behave under this testcase.

On that account, we define the testcase as follows:

$$\begin{aligned} h &= h_0(2-\sin^n\theta) \\ u_\phi &= \frac{-F+\sqrt{F^2+4C}}{2}, \end{aligned} \tag{5.25}$$

where h_0 is a constant, such that $gh_0 = 10^5\mathrm{m}^2\mathrm{s}^{-2}$, and $n = 2k+2$ for any positive k. In our particular case, $k = 160$. We also define F and C as:

$$\begin{aligned} F &= af_0\frac{\cos\theta}{\sin\theta} \\ C &= g_0 n\sin^{n-2}(\theta)\cos^2(\theta). \end{aligned}$$

We will also consider the f-sphere with $f_0 = 1.4584 \times 10^{-4}$ s^{-1}. Finally, the grid is rotated so that the nucleus of the depression is centred at 1°E, 3°N.

The parameters used in this testcase will have a timestepping scheme and timestepping value as defined in section 5.4. We will also use a g_6 refinement, where there are abrupt changes on the height field in a very restrict number of cells.

Our results displayed in Figure 5.8 show that both A- and B-grid, without the stabilizing term, are not capable of maintaining the geostrophic balance. For the A-grid, the numerical artefacts, emanated primarily from the pentagons of the grid, destabilize the scheme leading to an exponential growth blowing up the model around the 40 hours integration. In contrast, in the case of the B-grid scheme, there was not detected the presence of fast spurious numerical oscillations. However, the detected numerical dispersion waves were capable of breaking the down the depression up until the 24 hours after the start of the simulation.

Conversely, both C-grid schemes maintain the depression throughout the 5-day period of integration. However, in ICON's case there is a small presence of a noise on the system, but it does not seem to be enough to impact the overall solution.

Overall, the solution of A- and B-grid are impacted from their numerical oscillations. Although in the work of Yu et al. (2020) the A-grid is capable of integrating for a long time, the small wavelength oscillations in this testcase, generated mostly on the pentagons of the mesh, destabilize the integration, blowing up the solution. In contrast, both C-grid schemes solutions do not display damaging oscillations on the solution. MPAS's scheme and Perot's operator on the dual grid for this testcase has been observed by Peixoto (2016) and observed the scheme accurately maintain their geostrophic state. We show are able to show that on the primal grid, ICON, with the use of Perot's formulation, is also able to represent the geostrophic balance state on small scale flows, despite the issues on accuracy of its operators on the SCVT (Section 5.3 and 5.4.1).

5.4.4 Barotropic Instability

Previous testcases aimed in studying the fluid flow under highly controlled experiments, in order to evaluate their accuracies, linear normal modes, and balanced state flow. However, the highly energetic and chaotic nature of the ocean require a more realistic testcase, such a fluid flow instability.

$$\begin{aligned} u &= \begin{cases} \frac{u_{\max}}{e_n} \exp\left[\frac{1}{(\phi-\phi_0)(\phi-\phi_1)}\right] & \phi_0 < \phi < \phi_1 \\ 0 & (\phi-\phi_0)(\phi-\phi_1) > 0 \end{cases} \\ gh(\phi) &= gh_0 - \int_{-\pi/2}^{\phi} au(\phi') \left[f + \frac{\tan(\phi')}{a} u(\phi') \right] d\phi'. \end{aligned} \tag{5.26}$$

where $u_{\max} = 80\text{ms}^{-1}$, $\phi_0 = \pi/7$, $\phi_0 = \pi/2 - \phi_0$, $e_n = \exp[-4/(\phi_1 - \phi_0)^2]$. These initial conditions are under geostrophic balance, but with high potential for fluid instability. In order to trigger it, we add a perturbation to the height field:

$$h'(\theta, \phi) = h_{\max} e^{-(\theta/\alpha)^2} e^{-[(\phi_2 - \phi)/\beta]^2} \cos\phi, \tag{5.27}$$

where $\phi_2 = \pi/4$, $\alpha = 1/3$, $\beta = 1/15$, and $h_{\max} = 120$ m. All schemes are tested on a g_7 refinement with a timestep of 50 seconds under a RK4 timestepping scheme. In order to

avoid the instability, we use a hyperviscosity coefficient of 5×10^{15} and 2×10^{15}, for both A- and B-grid, respectively. These choices of coefficients are in agreement with Tomita and Satoh (2004). We also found that smaller values of these coefficients of each scheme would lead to instability for the A-grid and the appearance of near grid scale oscillations in the B-grid.

The potential vorticity, on the sixth day of integration (Figure 5.9), display the behaviour of the growth of the instability on all the evaluated schemes. Between these schemes, it is observed a clear difference in the representation of the smaller scale features of the instability. Both A-grid and B-grid schemes displays no small scale oscillations present within the vorticity field. Additionally, it is evident that both schemes display slightly coarser features in representing the state of the fields.

Similarly, in both C-grid schemes, we observe more small scale features in this system, helping could potentially aid in the growth of the instability even if no perturbation was added. However, it is evident that in these schemes, near-grid scale oscillations play a role in the physical solutions of the integration. Comparing both C-grid schemes, both schemes seem equally contaminated by numerical noise, however, the small scale oscillations in MPAS display a higher wavenumber than the ICON scheme. MPAS's noise in the vorticity was discussed and argued that the chequerboard noise of the vorticity is the main culprit in the manifestation of this contamination in our physical simulations (Peixoto, 2016). Likewise, we also know that the Perot's operator on the dual grid is capable of manifesting numerical noises on the solutions. Since ICON's divergence operator has the potential to remove small scale oscillations, but the scheme does manifest spurious waves, which was also observed in Korn and Linardakis (2018), therefore, the Perot's dual operator is potentially the main responsible for this manifestation.

Overall, all schemes suffer from the grid scale computational modes. There is, however, the stabilization term for both A- and B-grid schemes, such that the schemes remain stable throughout the integration. Despite both C-grid schemes remaining stable throughout the integration, the solutions are contaminated with noise, that will inevitably require a smoothing term, such as the biharmonic, in order to remove these high wavenumber waves. Additionally, It is observed that the waves from the A-grid to the C-grid schemes, an apparent increase in the effective resolution of the computation, agreeing with the previous results in Section 5.4.2. Following this result, we analyse the kinetic spectrum of these schemes.

5.4.4.1 Kinetic Energy Spectrum

The global kinetic energy spectrum, is a useful tool in evaluating the energy cascade of the fluid. On different scales of the ocean's motion, we observe a power law of k^{-3} for larger scales or $k^{-5/3}$ for smaller scales (Wang et al., 2019). For the 2D case, the former is related to the turbulence of the flow, whereas the latter is related to the reverse energy cascade turbulence. These spectral fluxes provide useful insight into the performance of the models in transferring energy motion between different scales.

Therefore, we define the Kinetic Energy Spectrum as follows:

$$(E_K)_n = \frac{a^2}{4n(n+1)} \left[|\zeta_n^0|^2 + |\delta_n^0|^2 + 2 \sum_{m=1}^{M} \left(|\zeta_n^m|^2 + |\delta_n^m|^2 \right) \right], \tag{5.28}$$

where ζ_n^m, δ_n^m are the spectral coefficient of the vorticity and divergence. These coefficients are defined as:

$$\psi_n^m = \int_{-1}^{1} \frac{1}{2\pi} \mathcal{F}(\psi(\phi,\theta),\phi)\overline{P_n^m}(\theta)d\theta, \tag{5.29}$$

where ψ is the variable to be transformed, $\mathcal{F}(\psi(\phi,\theta),\phi)$ is the Fourier Transform on this variable, and $\overline{P_n^m}(\theta)$ is the normalized associate Legendre polynomial. To evaluate these equations, we use the nearest neighbour to interpolate the original unstructured grid into a quadrilateral grid of 10 km resolution on the equator with the nearest neighbour method.

The energy spectrum of the schemes is shown on Figure 5.10. From the testcase, a small decrease of the spectrum from the wavenumber 1 to 4, and subsequently an increase, reaching a maximum at the wavenumber 6. Afterwards there is a constant decrease of the spectrum with a slope near k^{-3} for all grids. At approximately wavenumber 80, the A-grid scheme has a considerable loss of its power, decreasing more rapidly. Similarly, at wavenumber 90 the B-grid scheme also displays this rapidly loss of energy. With slight higher wavenumber, both A- and B-grid slows its slope until the last evaluated wavenumber.

Comparably, both C-grid schemes extend the physical slope of k^{-3} up to the wavenumber 300. At this wavenumber, ICON display a similar loss of kinetic energy, whereas MPAS maintain a similar slope up to the end of the evaluated wavenumbers.

In summary, we have shown that for smaller wavenumbers there is a good agreement between the models. Additionally, we also have shown that even for the nonlinear time integration of the shallow water system of equations, the schemes behave similar to the linear normal mode analysis, with A-grid having the coarsest effective resolution, and MPAS, on the other extreme, having the highest effective resolution. Additionally, the presence of a slow-down of the loss of the power or even an increase of the spectrum on the highest wavenumbers is likely related to the impact of the interpolation to cause this increase, as it was previously reported in other works (Wang et al., 2019; Rípodas et al., 2009; Juricke et al., 2023).

5.4.5 Models Stability

Our previous results were able to show elementary characteristics of each of the shallow water schemes. Some of our results required the inclusion of a stabilizing term for both A- and B-grid schemes, in order to remove damaging numerical oscillations that participated in the dynamics. Although the same term was not used in the C-grid scheme in our simulations, it is desired to include some sort of filtering, as the simulations may contain numerical waves that could either damage the solution or cause a potential *blow up* of the model.

One particular cause of numerical dispersion is associated with 3D energy-enstrophy conserving models, regardless of the staggering used. The imbalance between the Coriolis and kinetic energy term generates numerical noise, causing near grid-scale oscillations and decreasing the kinetic energy of jets (Hollingsworth et al., 1983). This instability, known as Hollingsworth Instability, also manifests as a destabilized inertia-gravity wave, leading to a blow up of the solution depending on the models' resolution and distortion of the mesh (Bell et al., 2017; Peixoto et al., 2018). Recent ocean models, such as NEMO's model, have shown susceptibility to these oscillations, producing spurious energy transfer to the internal

gravity-waves and dissipation, resulting in corruption of mesoscale currents and submesoscale structures (Ducousso et al., 2017).

Although this instability is 3D in nature, it is possible to mimic it, by considering the ocean model as a layered model, where the vertical flow is associated with one of the thin layers of the ocean (Bell et al., 2017). This can be done by assuming the ocean model is hydrostatic and under a Bousinesq approximation (assumptions made by all ocean models evaluated in this work). In that case, one of the layers, henceforth equivalent depth H, if unstable, will display a strong noise on the horizontal velocity, and, thus, can be analysed with the shallow water equations.

5.4.5.1 2D stability Analysis

In order to examine the instability, we analyse the models under a nonlinear geostrophic testcase, similar to TC1. In this testcase, however, we consider the bathymetry as driving the geostrophic balance. The mass height field will be constant and small to mimic the equivalent depth of the internal modes of the 3D model, as done by Bell et al. (2017), and Peixoto et al. (2018). Furthermore, we apply a linear analysis using the power method (Peixoto et al., 2018):

$$\mathbf{x}^{(k+1)} = \alpha_{k+1}\mathbf{r}^{(k+1)} + \overline{\mathbf{x}}, \tag{5.30}$$

where $\alpha^{(k+1)} = \epsilon/|\mathbf{r}^{(k+1)}|$, $\epsilon = 10^{-5}$ is a small constant, $\overline{\mathbf{x}}$ is the model state under geostrophic balance, $\mathbf{r}^{(k+1)} = \mathbf{x}^* - \overline{\mathbf{x}}$ is the perturbation, $\mathbf{x}^* = \mathbf{G}(x^k) + \mathbf{F}$, $\mathbf{G}(x^k)$ is the model evolution operator, and $\mathbf{F} = \overline{\mathbf{x}} - \mathbf{G}(\overline{\mathbf{x}})$ is a constant forcing. The methods converge, when $\alpha^k \rightarrow^k \alpha$ is found for large enough k. The eigenvalue is then obtained as $\lambda = 1/\alpha$. From there we can compute the E-folding timescale from the growth rate $\nu = \log\lambda/\Delta t$, where Δt is the timestep. We will use, a timestep of 200 seconds.

Ranging from an equivalent depth from 10^{-3} to 100 m we observe a substantial difference between the stability of the evaluated schemes (Figure 5.11). B-grid and ICON show similar e-folding time at around 0.1 and 0.2 days from the shallowest depth up to 1 m. Larger thickness display a stabilization of both schemes. B-grid, in this case, display a faster stabilization than ICON, whose e-folding time remain below 1 day for the 200 m, whilst B-grid show over 2 days e-folding time for the same thickness.

The similarities of both schemes for lower equivalent depths is potentially due to the use of triangular cells on some of their operators. However, the difference between the schemes for larger depths is likely associated with the error created by the reconstruction of the velocity vector field for both Coriolis and Kinetic energy terms in ICON, amplifying the imbalance of the discretization. Additionally, in different grids, ICON is found to be more stable (Korn and Linardakis, 2018), implying that our choice of grid might be a source of a higher instability.

On the other hand, both MPAS and A-grid display overall a more stable scheme. MPAS displayed a 0.6 day e-folding time for the shallowest depths, but showed an increase, reaching around 40 days. Similarly, A-grid displays an even larger stability of around 0.2 day for the shallowest depth. However, contrary to the other schemes, the stability of the A-grid decrease with the increase of the equivalent depth. A-grid's stability loss with depth might be potentially due to different causes of instability being dominant for the equivalent depths,

i.e. for shallower depths, the cause of the instability is likely the Hollingsworth Instability, while for deeper depths, the instability is caused by the excitation of spurious pressure modes.

5.4.5.2 Biharmonic

In order to evaluate the biharmonic effect on the stability of the models, we perform the same analysis for different viscosity coefficients, using an equivalent depth of 1 metre, and a timestep of 200 seconds. For A- and B-grid schemes, we use (5.22) and (5.23), respectively. On C-grid, we use the formulation:

$$\Delta \mathbf{u} = \nabla\nabla \cdot \mathbf{u} - \nabla \times \nabla \times \mathbf{u} \approx \mathbf{grad}\ \mathbf{div}\ u - \mathbf{grad}^{\,T}\mathbf{vort}\ u,$$

where $\mathbf{grad}^{\,T}$ is the transpose gradient operator defined on the dual grid.

Our analysis, shown on Figure 5.12, indicates that all schemes were found to be stable for a viscosity coefficient no more than 10^{15} $\mathrm{m^4 s^{-1}}$. Individually, B-grid and ICON does not display difference in stability for a coefficient up to 10^{13} $\mathrm{m^4 s^{-1}}$. However, increasing the coefficient, shows that the B-grid has, not only a faster stabilization than ICON, but has the fastest of all evaluated schemes, reaching an e-folding time of over 10 days for a coefficient of 1×10^{14} $\mathrm{m^4 s^{-1}}$. ICON, in contrast, shows the slowest stabilization, reaching an e-folding time of 1.1 days for a coefficient of 4×10^{14} $\mathrm{m^4 s^{-1}}$.

Similarly, both A-grid and MPAS schemes display an unchanged e-folding time of up to 10^{13} $\mathrm{m^4 s^{-1}}$ and 10^{14} $\mathrm{m^4 s^{-1}}$, respectively. Additionally, A-grid is shown to stabilize faster than MPAS, reaching an e-folding time of over 20 days for a coefficient of 3×10^{14} $\mathrm{m^4 s^{-1}}$, while MPAS reaches 10 days for the same coefficient.

Overall, we see that despite B-grid showing a lower stability than all schemes, it has the potential to faster achieve stability. Conversely, although ICON obtains a similar stability as the B-grid, it requires a more intense coefficient, in order to stabilize the scheme. The similar behaviour happens with A-grid and MPAS, with MPAS requiring a more intense coefficient for stabilization. This implies that this difficulty is on the C-grid discretization itself, and it is likely associated with either the vector reconstruction of the Coriolis term or the Kinetic Energy discretization.

5.5 ICON-O Model

Given the importance of the biharmonic term in order to stabilize the scheme or, at least, remove spurious computational waves in the system, we, then, aim to bridge the gap between the shallow water model and ICON's operational model. We will first acknowledge that our analysis in this section will be restricted only with ICON-O research model, and will not give light to other models mentioned in this work. However, providing results with ICON-O will be an important step towards understanding the effects of numerical oscillations on research/operational models. Additionally, our simulations presented in this section were not fine-tuned, i.e. the physical parameters and coefficients were not thoroughly calibrated, and, therefore, these simulations may not necessarily represent reality accurately. However, our discussions in this section will be restricted to analyse differences between simulations

with and without the biharmonic filter, so the lack of calibration will not impact the overall analyses of the results.

The research ICON-O model, developed at the Max-Planck Institute for Meteorology, is the oceanic component of the ICON Earth System Model. It uses horizontal discretization described in the earlier sections. Vertically, it extends the triangular cells into prisms, for the use of its z coordinate levels. Additionally, In its 3D formulation, ICON-O uses the hydrostatic and Bousinesq approximations to solve its state vector $\{u, h, T, S\}$, where T and S are temperature and salinity, respectively. These tracers are also imbued with dissipative and subgrid-scale operators, such as isoneutral diffusion and the mesoscale eddy advection Gent-Mcwilliams Korn (2018). The full 3D spatial discretization will be omitted in this section, but the reader can refer to equation (32) of Korn (2017).

For its time integration, ICON-O is discretized using an Adams-Bashforth 2-step predictor-corrector scheme (equation 33, 34, and 35 of (Korn, 2017)). This scheme does not conserve neither energy nor enstrophy (Korn and Linardakis, 2018), but it also contains an implicit diffusion, allowing for more stable simulations.

Our 3D simulations were performed using an HR95 grid with a radial local refinement with the finest resolution, around 14 Km edge length, located near South Africa, and the coarsest resolution, around 80 Km edge length, on the antipode of the earth, i.e. North Pacific (Figure 5.13 upper panel). These locally refined mesh created enumerated distortion spots around the refined region (Figure 5.13 lower panel).

The model was initialized under rest with 128 layers with climatological temperature and salinity from the Polar Science Center Hydrographic Climatology (Steele et al., 2001) and was forced with the German-OMIP climatological forcing, which is derived from the ECMWF reanalysis 15 years dataset. This climatological forcing is daily with a resolution of 1 degree. An initial thirty years spin up was performed under these conditions utilizing a biharmonic coefficient of $2 \times 10^{-1} A_e^{3/2}$, where $A_e = |e||\hat{e}|/2$. In addition, we added a Turbulent Kinetic Energy (TKE) closure scheme, in order to parameterize the turbulent subgrid phenomena on the mesh.

Following the spin up, we, subsequently, ran 2 simulations by 10 years each. One simulated with the same parameters as the spin up, which we will coin as our reference simulation. The other was simulated without the aforementioned biharmonic filter.

The simulation without the filter show a clear decrease in the strength of the currents on the ocean system, e.g. the Gulf, Kuroshio, North Brazil, Agulhas, and Malvinas currents (Figure 5.14). Other regions were found to slightly increase in kinetic energy, in particular, the neighbourhood around the Agulhas Current, near the Antarctic Circumpolar Current, the Equatorial Currents of the Atlantic Ocean and both Northern and Southern of the Pacific Ocean, and the Brazil-Malvinas Confluence. The integrated kinetic energy averaged over these years show that surface kinetic energy loss of around 4.7 $\times 10^{13}$ $\mathrm{km^2 m^2 s^{-2}}$ of its 20 $\times 10^{13}$ $\mathrm{km^2 m^2 s^{-2}}$. Additionally, it is observed, in particular on regions of coarser resolution, such as the Kuroshio Current and Gulf Stream, the presence of a numerical oscillation emanating from the main currents.

Following Ducousso et al. (2017), we show a similar result as that reported by the authors, in the sense that the structure of the Equatorial Undercurrent (EUC) is shown to be more deformed on the simulation without the biharmonic. Although the intensity of the EUC in our results were unchanged, the core of current narrowed vertically and moved from 125 m of

depth to 100 m. According to the authors, the region is subject to barotropic and baroclinic instability, producing waves and vortices which are the main contributors to the current. Although we detect a decrease of EKE on the No Biharmonic run in the southernmost branch of the zonal current (Figure 5.15), we also detect an increase of the EKE over the equatorial countercurrent. Since this decrease in EKE also follows with a decrease in the strength of the core of both northern and southern branches, It is possible that this decrease in EKE is indeed related to a decrease in baroclinic instability, while the increase in EKE over the countercurrent is possibly related to numerical oscillations on the grid, which strengthens the zonal flux over this countercurrent, and, thus, deepening its core.

Other regions of the ocean also display a decrease of the EKE, most notably the Agulhas Current Retroflection, where it meets with the colder water of the South Atlantic Current and Antarctic Circumpolar Current (Figure 5.16). The retroflection region EKE is known to be modulated by the baroclinic instability of the Agulhas current (Zhu et al., 2018).

Additionally, the Agulhas current itself is affected by the absence of biharmonic (Figure 5.17). One observed difference is that the intensity of the surface current is lost. Moreover, the cross-section of the No Biharmonic simulation shows a trail of intense EKE manifesting from the core of the Agulhas Current and propagating southwestward (Figure 5.17.B). These oscillations span from the surface, down to 400 m depth. It is possible that these oscillations absorbs energy from the main current system, adding to the mixing of the water and, consequently, weakening the current.

5.6 Conclusions

In this work, we provided a thorough comparison analysis between different shallow water staggering schemes used in unstructured ocean models and their capability in maintaining a stable integration. Alongside, we also investigated ICON's susceptibility to such numerical instabilities in realistic 3D settings.

The shallow water analyses have shown that all models haves advantages and disadvantages. The NICAM horizontal discretization, from Tomita et al. (2001), is simple to discretize, due to its collocated approach, provides accurate representation of the operators, and presents reasonably stable integrations for complex experiments, for chosen grid optimizations, such as the SCVT. However, similar to the traditional discretization of A-grids on regular grids (Arakawa and Lamb, 1977; Randall, 1994), it displays a low effective resolution, difficulty in maintaining the geostrophic balance, and it is susceptible to the manifestation of numerical oscillations caused by the grid discretization.

Similarly, the FeSOM 2.0 horizontal discretization, from Danilov et al. (2017), also provides a quite simple discretization, accurate approximations of the operators, and a higher effective resolution compared to the A-grid. However, it also has a low effective resolution, and it displays some difficulty in maintaining the geostrophic balance. Additionally, despite not suffering from pressure modes, the B-grid scheme is found to be the least stable scheme, but as shown here and discussed by Danilov (2013), It can be easily fixed by a low coefficient of biharmonic.

Finally, both C-grid schemes, MPAS-O, from (Skamarock et al., 2012), and ICON-O, from Korn (2017), have the most complex discretizations between the evaluated schemes.

Some operators do not accurately approximate the operators of the Shallow Water system. The difficulty for MPAS-O to show convergence in the error was also discussed by Peixoto (2016). Similarly, ICON-O also displays some difficulty in converging some of the operators of the shallow water equations. The lack of convergence of the divergence operator, for example, was also shown in Korn and Linardakis (2018). For both schemes, it is argued that the issue lies in the use of the grid. Therefore, a proper choice of grid optimization should also be taken into consideration when using or using these schemes. Moreover, a dissimilarity between both schemes is seen in their stability. MPAS is shown to have a high stability, as it was discussed in (Peixoto et al., 2018), but ICON, similar to the B-grid, is shown to have a low stability and requires a larger viscosity than B-grid to stabilize the scheme.

Remarkably, in the 3D ICON-O simulation using a grid with Spring Dynamics optimization, the model was found to be stable throughout the simulated years, despite the lack of biharmonic filter. However, near grid oscillations were apparent in the grid and a contribution of these oscillations of the dynamics of the model was apparent. As it was also diagnosed by Ducousso et al. (2017) for the NEMO model, these oscillations seemed to give rise to spurious mixing of the system and also decreases the energy of the ocean's currents. Regions where its strength is derived from baroclinic instability seems more affected by these small scale oscillations. Yet, it is clear the need for further research in this topic. Though the model is stable, it can be affected by these oscillations if the coefficient is not properly adjusted. Moreover, an excess of the viscosity may also decrease the effective resolution of the model, which also is not ideal.

In conclusion, we stress that further research is necessary in order to shed more light into these schemes. We note that all schemes under the shallow water tests have shown to be robust and provide reliable results for their respective purpose. However, testing these schemes under different grids or with more realistic settings might provide greater insights into the performance of the models. Additionally, it seems evident that despite a model being stable without filters, the numerical oscillations in the model may interact with the physical waves, leading to errors or to misinterpretation of the results. It is, therefore, crucial for further investigation on this topic in order to properly make use of filters to avoid these oscillations, but also minimize the damping of physical waves.

5.7 Acknowledgements

We are grateful to the financial support given by the Brazilian Coordination for the Improvement of Higher Education Personnel (CAPES) PRINT project - Call no. 41/2017, Grant 88887.694523/2022-00, the São Paulo Research Foundation (FAPESP) Grant 2021/06176-0, and the Brazilian National Council for Scientific and Technological Development (CNPq), Grants 140455/2019-1 and 303436/2022-0.

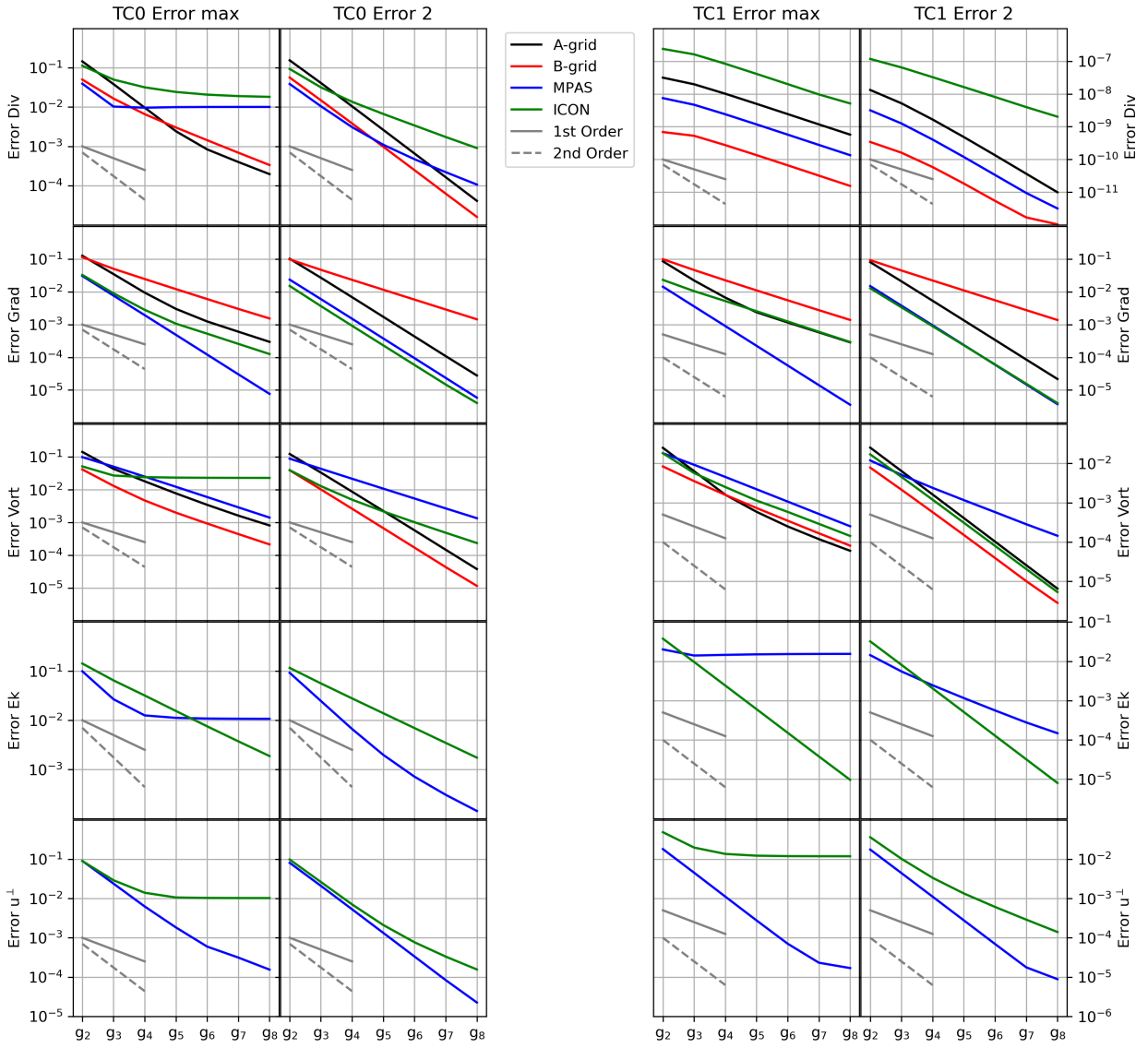

Figure 5.5: TC0 (first and second row panels) and TC1 (third and fourth row panels) operators L_∞ (first and third panels) and L_2 (second and fourth panels) error norms for the A-grid (black lines), B-grid (red lines), MPAS (blue lines), and ICON (green lines).

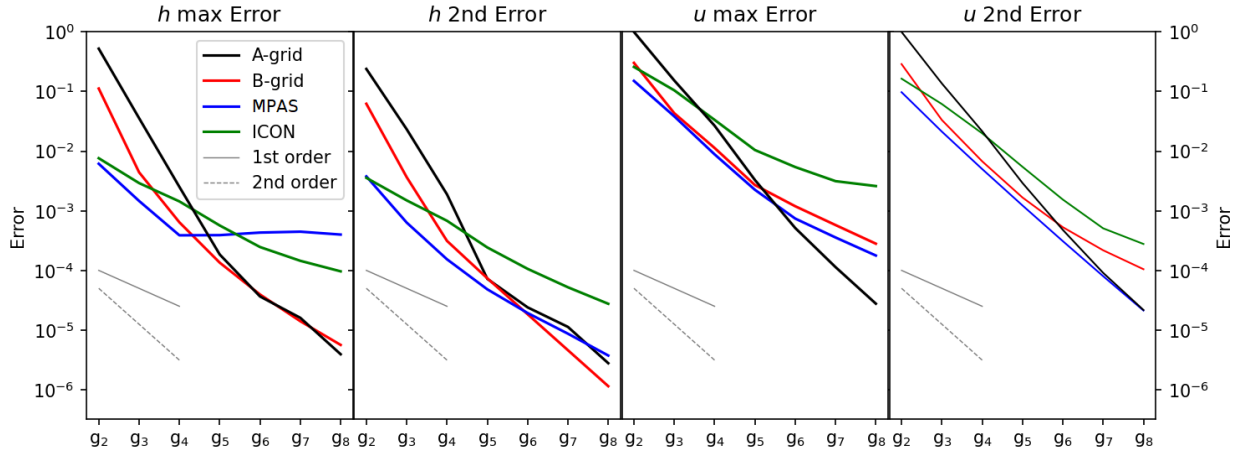

Figure 5.6: h and u error after 15 days.

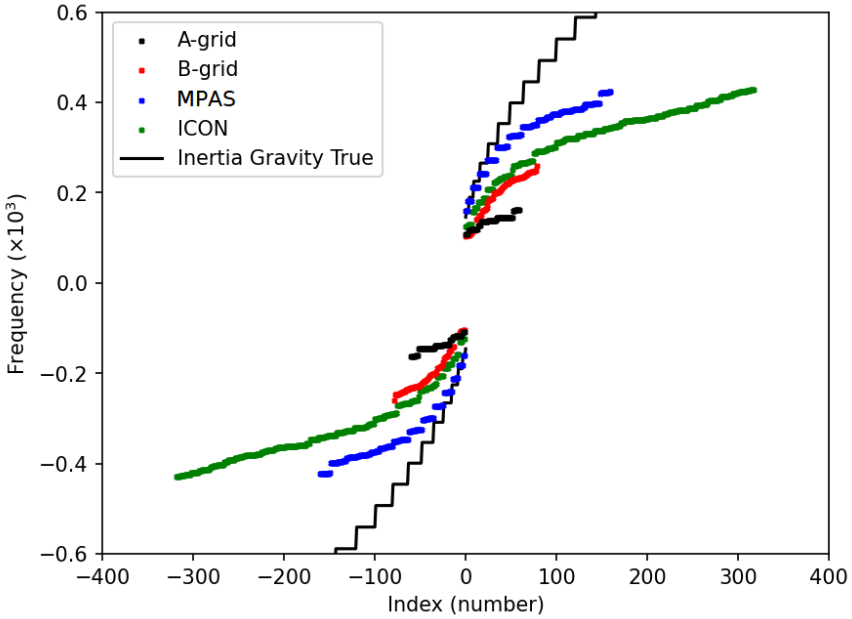

Figure 5.7: Linear normal modes of the considering the linear shallow water equations (5.24) on the f-sphere.

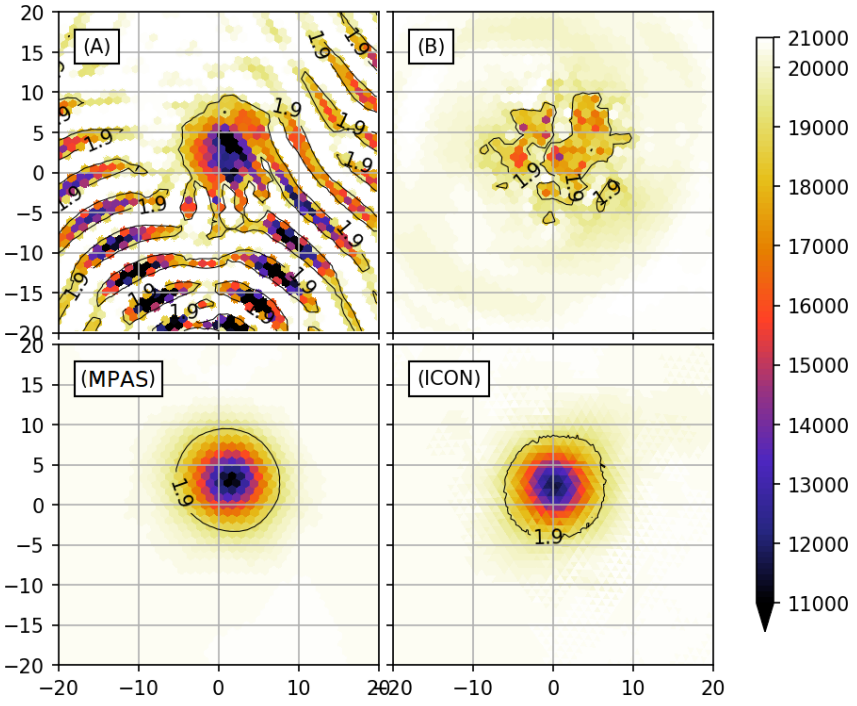

Figure 5.8: Height field of the different schemes for the localized balanced flow testcase without using biharmonic for both A- and B-grid schemes. Using a grid refinement g_6 and a timestep of 50s.

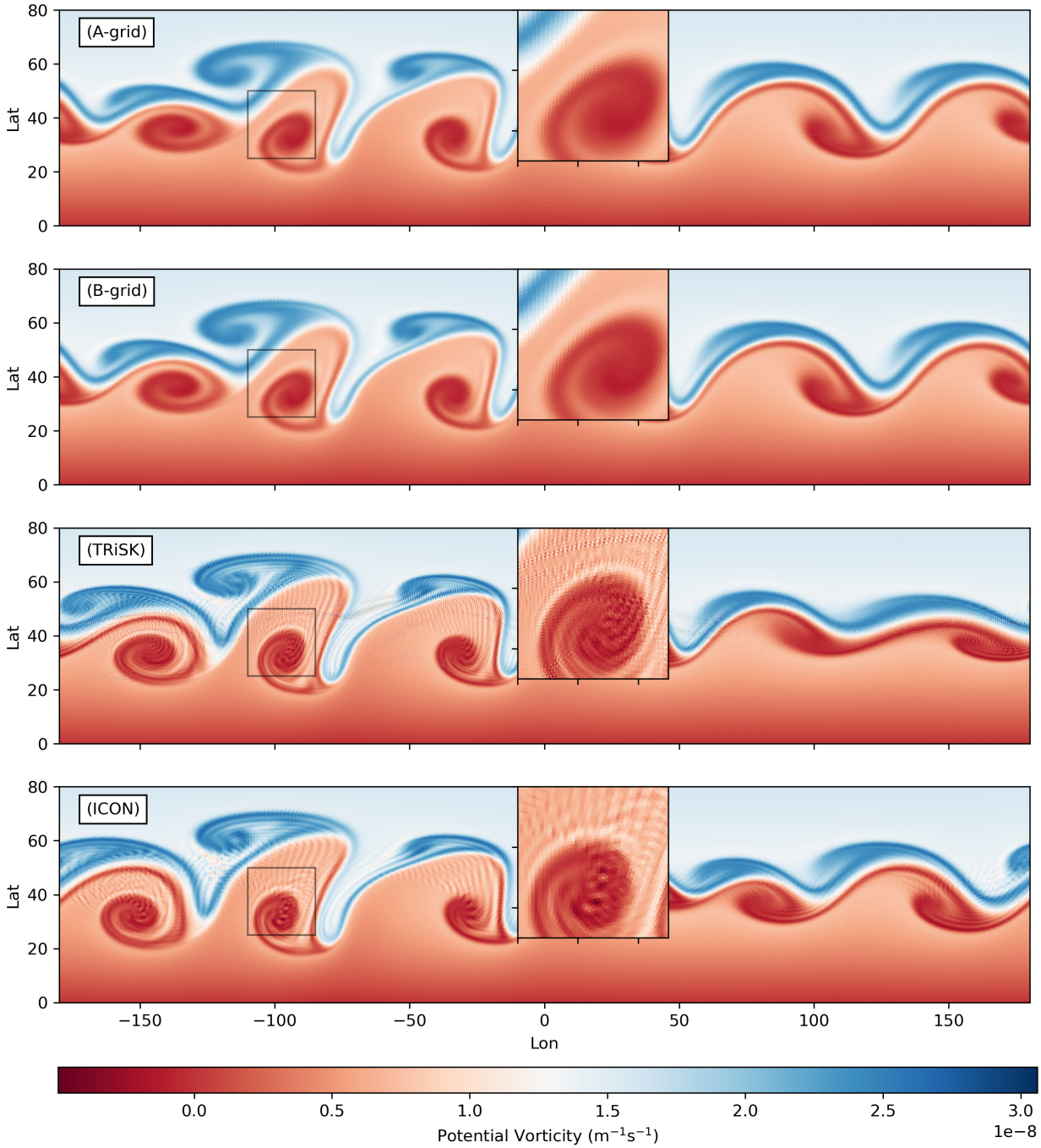

Figure 5.9: Potential Vorticity of all schemes on the 6th day of integration for the barotropic instability testcase with perturbation using a g_7 refinement grid and a respective biharmonic for A- and B-grid schemes, following Table 5.4.

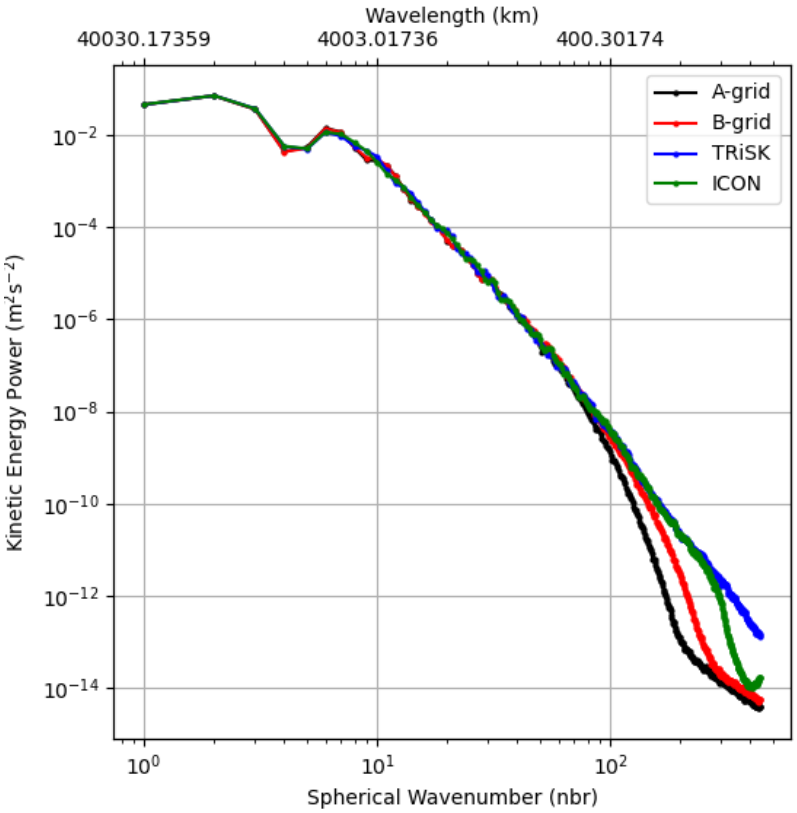

Figure 5.10: Kinetic energy spectra for the Barotropic instability testcase for all schemes as in Figure 5.9.

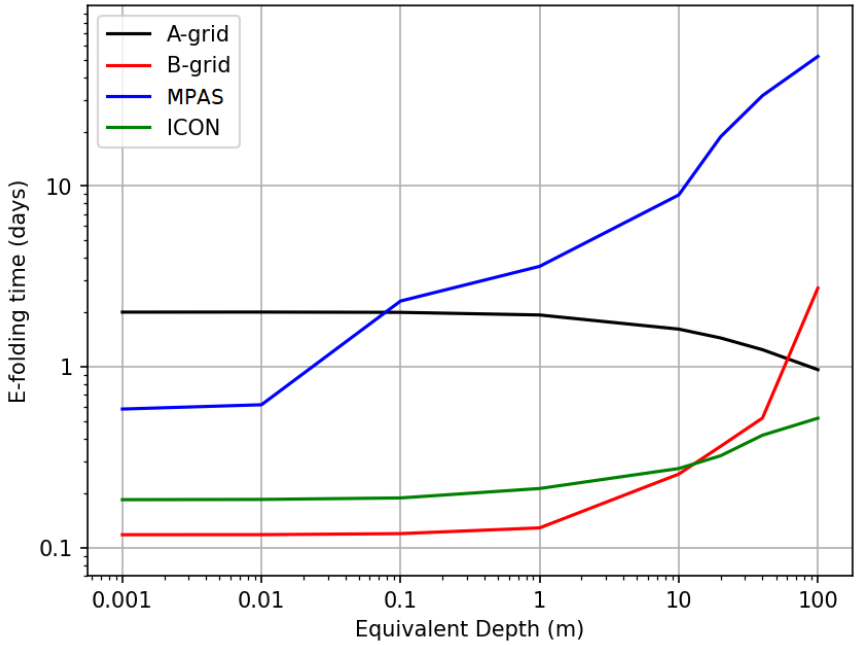

Figure 5.11: E-folding time for the different evaluated schemes, considering a time-step of 200 s in a geostrophic test case where the balanced state is given by the bathymetry, while the height is given by the equivalent depth and constant.

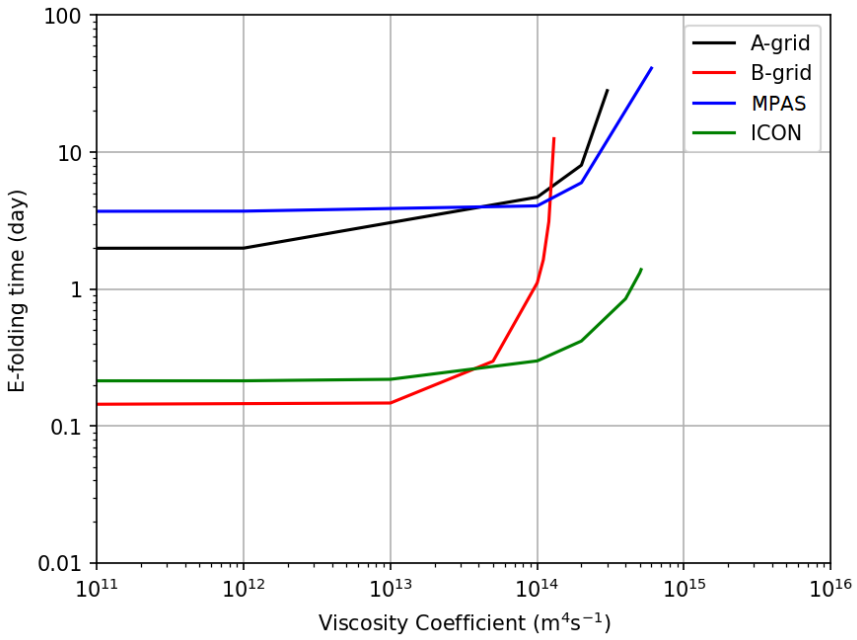

Figure 5.12: E-folding time by viscosity coefficient for each scheme, using a g_6 grid refinement with a timestep of 200 s and a 1 m equivalent depth.

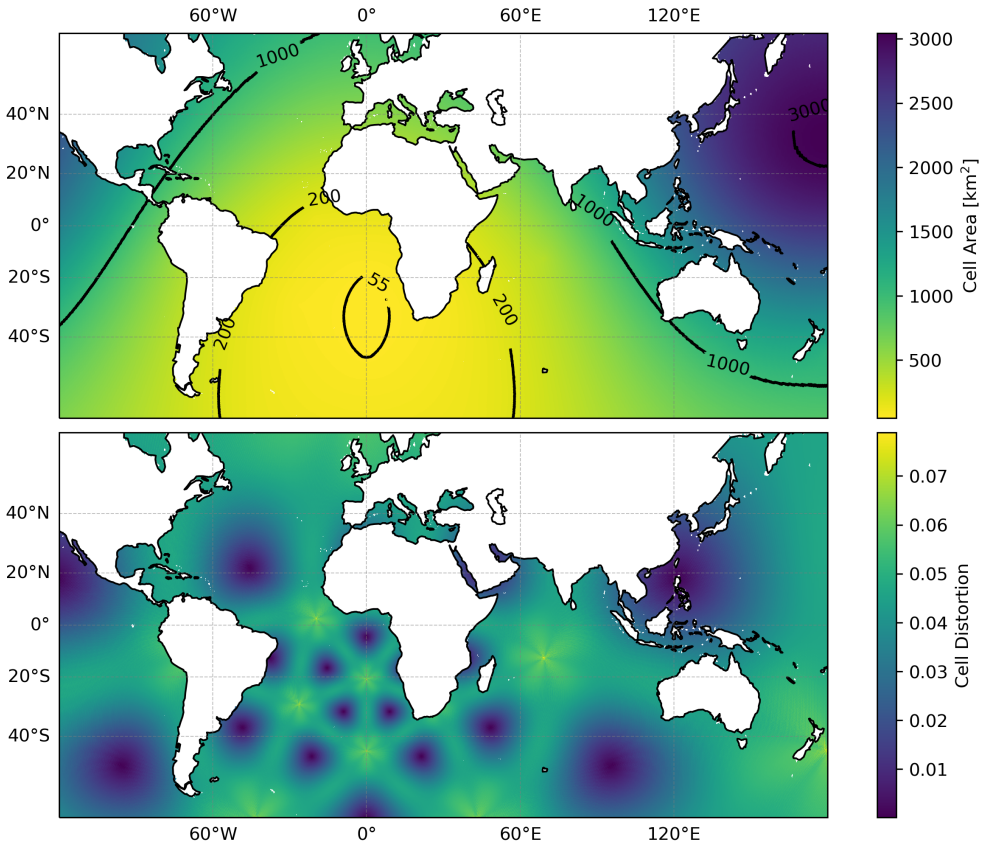

Figure 5.13: The upper panel is the cell area of the spherical grid used in the simulations. The lower panel is the respective cell distortion of the mesh.

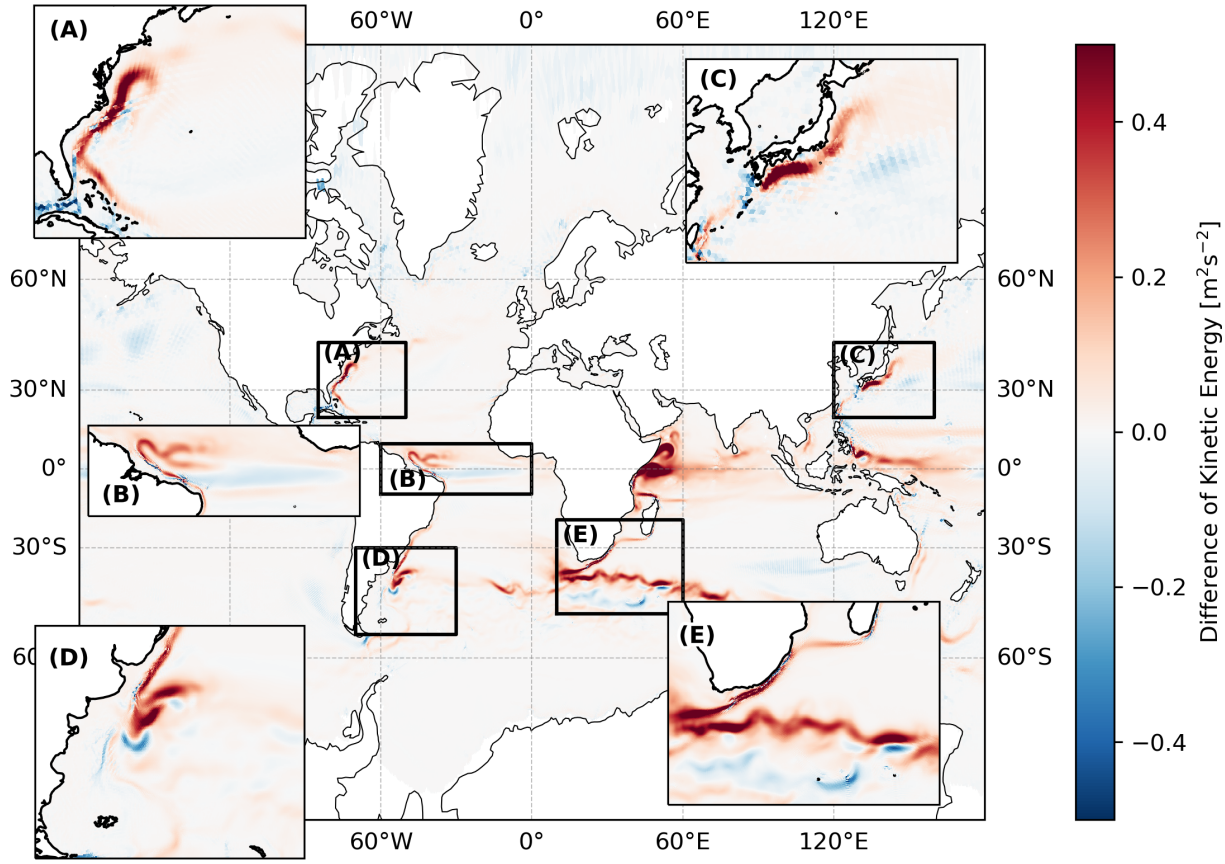

Figure 5.14: Kinetic Energy difference between a reference simulation and simulation without the use of biharmonic, i.e. $E_k^{(\text{ref})} - E_k^{(\text{no bih})}$.

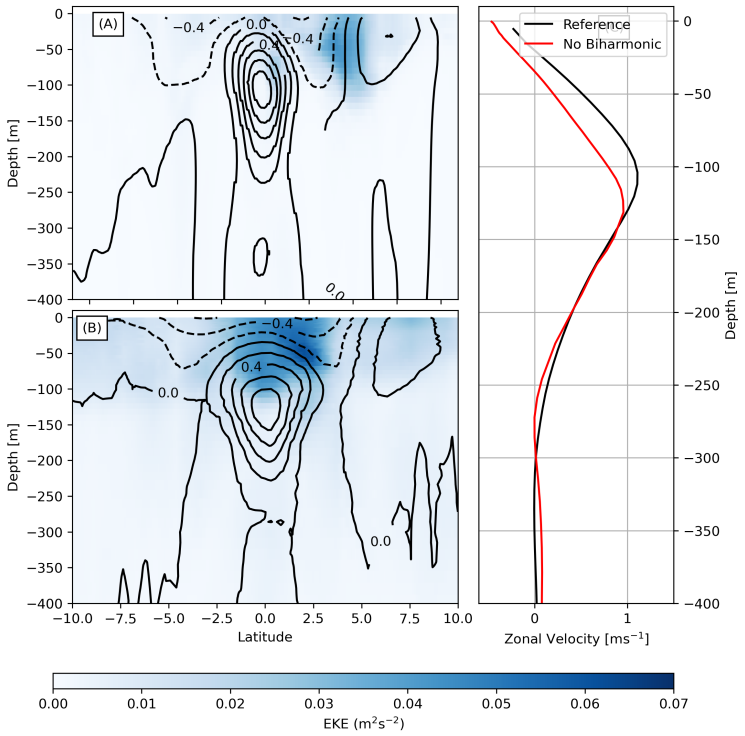

Figure 5.15: Cross-section of the 130°W longitude of the reference (A) and the without biharmonic (B) simulation and a vertical profile of the zonal velocity of both simulation over the 0° Latitude (C).

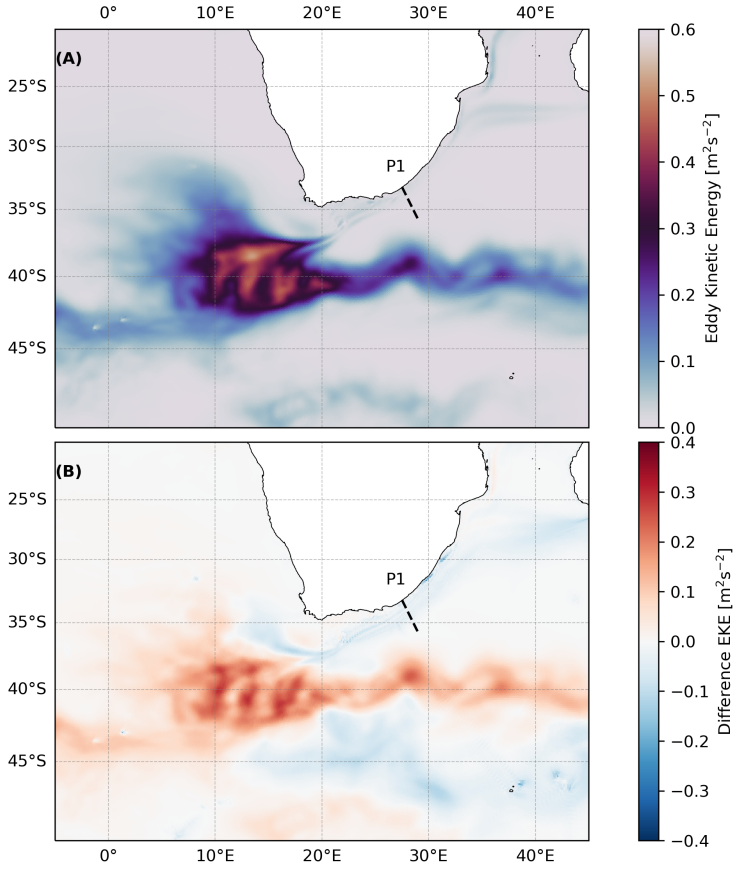

Figure 5.16: Eddy Kinetic Energy (A) and difference between simulations of EKE (B) of the Agulhas Current System.

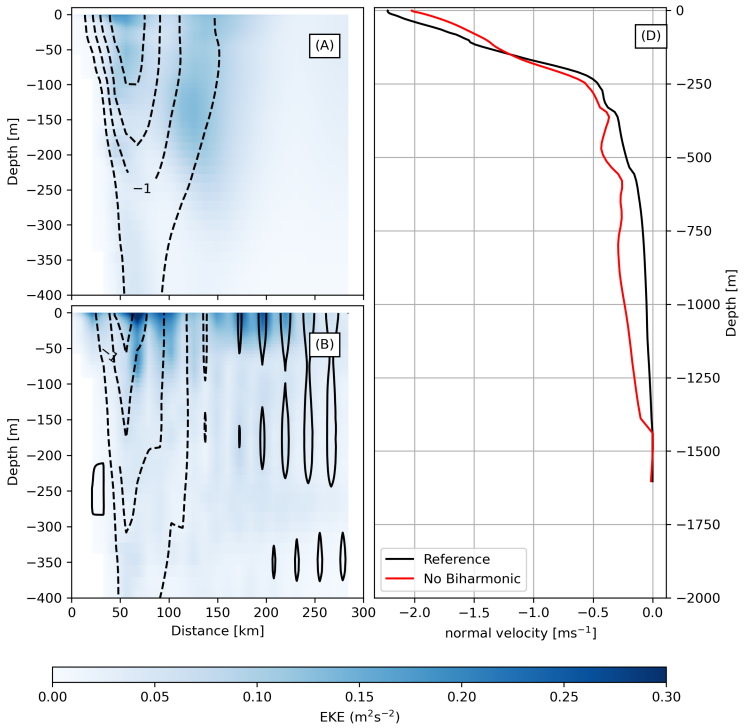

Figure 5.17: P1 Cross-section between the Observational data (A), Reference simulation (B), and No Biharmonic Simulation (C), and the vertical profile of the normal velocity in the 42 km distance (D).

Chapter6

Conclusions

This work aimed to analyse some core properties of global geophysical numerical models. We have provided results for the traits of the modified triangular icosahedral grid (Chapter 2). Using this grid, it was analysed different schemes, where it was tested the accuracy of their operators, and their time integrated solutions (Chapter 3). It was also analysed these schemes' stability to numerical oscillations and how these schemes can increase this stability with a hiperdiffusion filter (Chapter 4). Finally, we incorporated our knowledge in work submitted to the Journal of Ocean Modelling, described in Chapter 5. The overall summary of the results can be seen in Table 6.1.

The modified standard grid (MODSTD) showed overall worse results for the properties tested in this work than the grids tested by Miura and Kimoto (2005). In particular, the grid showed signs of worse distortions. These distortions were more localized than the standard grid, presenting a spatial distribution similar to that of HR95. The SCVT grid used in Chapter 5 displays a lower amount of distortion, and the high distortion cells are localized on the original icosahedral vertices.

These distortions are observed on the operator error spatial distribution. For the A- and B-grid schemes, all operators were able to converge in either first or second order, regardless of grid used (MODSTD in Chapter 3 or SCVT in 5). The error rate of these operators is decreased as the grid is refined, likely due to these distortions, which was pointed out by Peixoto and Barros (2013). On the other hand, the operators defined on the primal cell, i.e. triangular tilling, were mostly first order, with a notable exception to the kinetic energy operator of TRiSK (Chapter 3), which as it was pointed out by Weller et al. (2012) was expected to show better performance than its analogue on the dual quasi-hexagonal cell. In fact, as it was show, TRiSK-MPAS (Chapter 5) displays a 0th order convergence for the SCVT grid, which is in line with the discussed error in Peixoto (2016).

Additionally, some operators, such as the divergence operator on TRiSK and the gradient operator on the B-grid, display an error distribution similar to the chequerboard pattern. For the latter, this was not expected to be a problem, since the model requires the use of a filter, which had removed any signs of noise. For the former, however, this noise would be a problem, since the model can be used without filter. In contrast, ICON's admissible reconstruction operator was able to almost completely remove this noise. In some tests, however, the divergence operator had a worse error than TRiSK, i.e. such as in the case of SCVT grid, where the divergence error does not converge.

These operators influence the simulation test performed on the grids. In the use of the MODSTD grid, the A-grid is contaminated with numerical oscillation despite the use of the biharmonic filter. Its use aid the scheme to stabilize, but have not helped it to remove this noise, which was evident near the areas of larger distortion, thus making the scheme not converge with grid refinement. This was not observed in the SCVT case, since the barycentre

of the dual cell coincide with the vertices of the grid, as it was stated as requisite by Tomita et al. (2001). Regardless, in the mountain case scenario, this scheme on the MODSTD grid has not shown visible oscillations, implying that the scheme could still be used without an instability of the solution. Despite this, it is evident that a grid, such as the Spring Dynamics or the SCVT, is desirable in order to attain optimal results.

On the other hand, B-grid scheme have shown a near first to second order convergence and no signs of visible noise on either the mass nor the velocities fields were detected. Likewise, both C-grid have shown a convergence of its error with refinement on the MODSTD. However, contrary to the B-grid there was some noise detected, in particular, at the mass field. TRiSK was much more affected to this noise, while ICON's use of admissible reconstruction was able to solve this issue. On the SCVT grid, however, it was observed that both C-grid schemes struggle to display a convergence on both mass (h) and vector ($\mathbf{u}$) fields. These likely are related to the difficulty of converging of the aforementioned operators.

Additionally, on ICON, it was observed some drawbacks on the use of its admissible reconstruction. Despite providing a solution to the issue of the chequerboard pattern, it makes the inertia gravity waves underrepresented. This is a similar result obtained by Korn and Danilov (2016). Moreover, the use of the dual reconstruction of ICON manifests non-stationary geostrophic modes, which, as shown by Peixoto (2016), do not display observable damage to the results shown.

Regardless, the ICON's under-representation of inertia-gravity waves could act in favour of the stability of the scheme. Under a thin test case, TRiSK have shown to be the most unstable of the tested schemes. It requires a large diffusivity coefficient to be able to control these spurious waves. It is likely that part of the spurious oscillations that aid the instability are the aforementioned chequerboard pattern. ICON, on the other hand, is more stable than TRiSK, and it requires less diffusion to control the unstable modes. On the dual grid, however, MPAS has shown to be more stable than ICON, implying that the triangular grid still suffer from modes that create instability on the model. Likewise, B-grid is surprisingly more stable than TRiSK and with the use of diffusion it can better control spurious waves than ICON. Additionally, the use of SCVT seems to easier control unstable oscillations in the B-grid than in ICON. One such reason for these results is the necessity of ICON to reconstruct the vector field, which would increase the level of uncertainty in the model. Moreover, the grid distortion on ICON seems to have a higher influence on the results than B-grid.

In contrast, the A-grid was found to be less unstable of those schemes, despite the contamination present in the model. It can be argued that the scheme does not only not require reconstructing the vector field, like B-grid, but also the kinetic energy is almost exactly defined at the necessary points. Not only that, but it is possible that this contamination on the mass field aids in stabilizing the scheme. On the SCVT, however, A-grid scheme display a slightly different behaviour. It still is the least unstable scheme, however, its instability increase with higher equivalent depths. This difference likely lies on the manifestation of the numerical oscillations of the MODSTD grid. In the SCVT grid, the oscillations likely migrate from a Hollingsworth instability to a pressure mode manifestation, which might explain the decrease in stability. On the MODSTD, the manifested waves of the grid are likely present throughout all equivalent depths and are likely the main reason which is making the scheme unstable.

	order of Accuracy	Resolution	Stability
A-grid	1st-2nd	Low	High
B-grid	1st-2nd	Low	Low
TRiSK	-1nd-0th	High	Low
MPAS	0th-1st	High	High
ICON	0th-1st	High	Low

Table 6.1: Summary of different properties analysed for the different schemes used.

Finally, we observe that the full ICON 3D is not found unstable without the biharmonic filter. However, it is observed noticeable impacts on the solution of the integrated model. Although these waves are not amplified in the mode, they contribute to the dynamics, by providing spurious mixing of the currents. The impact is found to be higher on currents, where the main contribution comes with baroclinic instability. With this spurious mixing, there is a decrease in this instability, thus making these currents weaker. We, therefore, note the importance of providing a well-balanced filter, in particular to higher degree of distorted grids, so that we avoid unnecessary damping of higher frequency waves, and are able to avoid the impact of these numerical oscillations, which can lead to erroneous interpretations of the given simulations.

Further work could be done in understanding the behaviour of these schemes. these oscillations can be evaluated in other 3D models. In particular, FESOM 2.0 while displaying different computations of the momentum equations, may provide a better control of these oscillations. Additionally, the work of Perot (2000) also allows for the computation of the advection equation, which is used in ICON may also provide a greater stability. Additionally, the work of Perot and Chartrand (2021), generalize their arguments using harmonic reconstruction. Is it possible, then, to increase the model's stability, and can we remove the non-stationary geostrophic modes of the linearized shallow water simulations?

AppendixA

A-Grid GC

In this chapter, we are going to show the improvement on the operators using an optimized grid. We aimed to follow Tomita et al. (2001) and iterate a grid where both $K^{(b)}$ and $\hat{K}^{(b)}$ are the geometric centres of the primal and dual cell, respectively. The algorithm goes as follows. Assume $\mathbf{v}^{(0)}$ is the vertex of the grid, and $\mathbf{p}^{(0)}$ is the barycentre of the cell calculated normally. We moved the vertex for the kth iteration by a weighted average of the dual cell vertices (triangle barycentre):

$$\mathbf{v}_k^{(k)} = \sum_j \frac{A_j \mathbf{p}_j^{(k-1)}}{A_j} \tag{A.1}$$

where A_j is the area of the triangular cell. With the new vertices, we calculate the new barycentre of the triangular cell. We stop the iteration as $|v^{(k)} - v^{(k-1)}| \leq \epsilon$, $\epsilon > 0$.

Our results show the error for Nonlinear Geostrophic Test Case (TC0 of Chapter 3). The L_2 error is of the order of second order for all operators. The L_∞ error is also near second-order for all operators, except for the divergent operator, which is near first order (Table A.1). Although not expected, it could be due to the initial condition. Other tested cases are near second-order (not shown here).

Table A.1: Maximum error of the operators for the nonlinear geostrophic case.

grid-level	**div**	**grad**	**curl**
g_0	0.0000	$2.6575.10^{0}$	$4.7082.10^{-1}$
g_1	0.0000	$4.1228.10^{-1}$	$1.0153.10^{-1}$
g_2	$5.0024.10^{-8}$	$8.8841.10^{-2}$	$2.4272.10^{-2}$
g_3	$2.9508.10^{-8}$	$2.1833.10^{-2}$	$6.0982.10^{-3}$
g_4	$1.4387.10^{-8}$	$5.4696.10^{-3}$	$1.5289.10^{-3}$
g_5	$6.7665.10^{-9}$	$1.4579.10^{-3}$	$3.8237.10^{-4}$
g_6	$3.1585.10^{-9}$	$6.9593.10^{-4}$	$1.0516.10^{-4}$

All the operators show a pattern near the vertices of the original icosahedron (Figures A.1, A.2), similar to what was obtained by Tomita et al. (2001). This follows the new distortion of the grid.

The variables h and u_θ follow a similar pattern as B-grid (Figure 3.22). The background noise is now much less predominant than the standard grid, but still present. It, however, does not contaminate the grid as did the standard grid. Similar to what was obtained by Tomita et al. (2001).

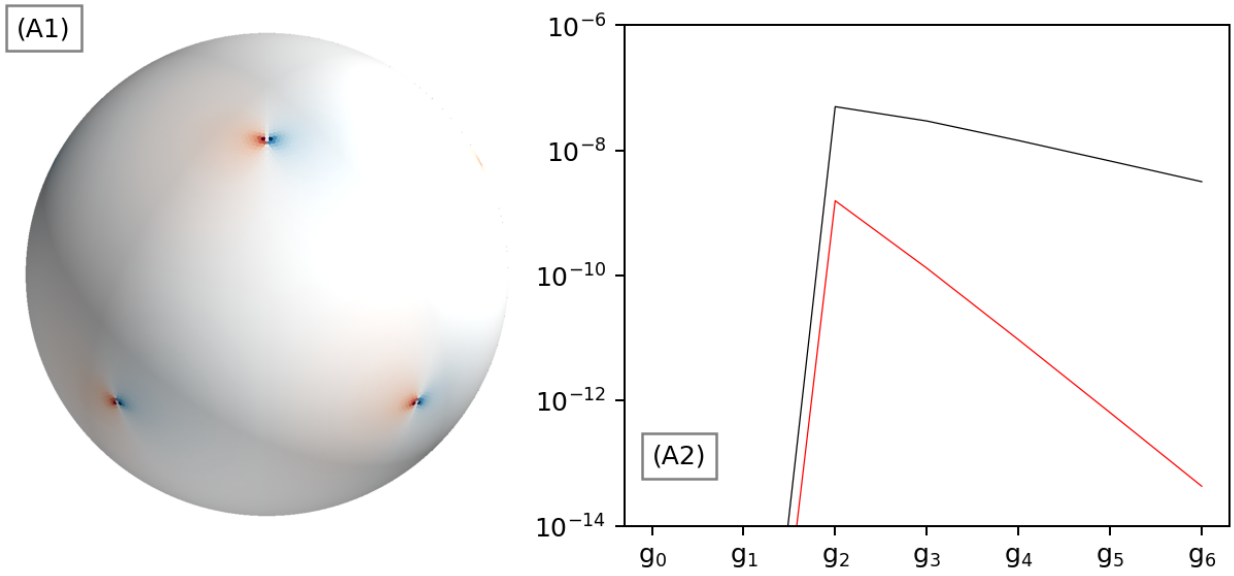

Figure A.1: Divergence error for g_6 (left) and it's L_∞ and L_2 norm.

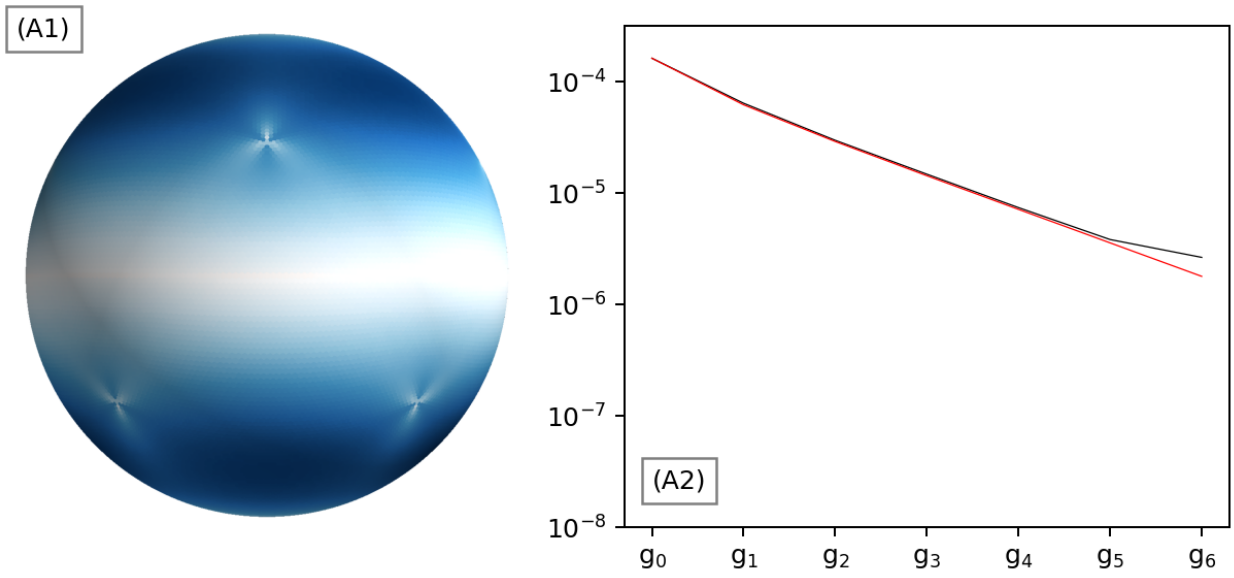

Figure A.2: Gradient operator error for g_6 (left) and it's L_∞ and L_2 norm.

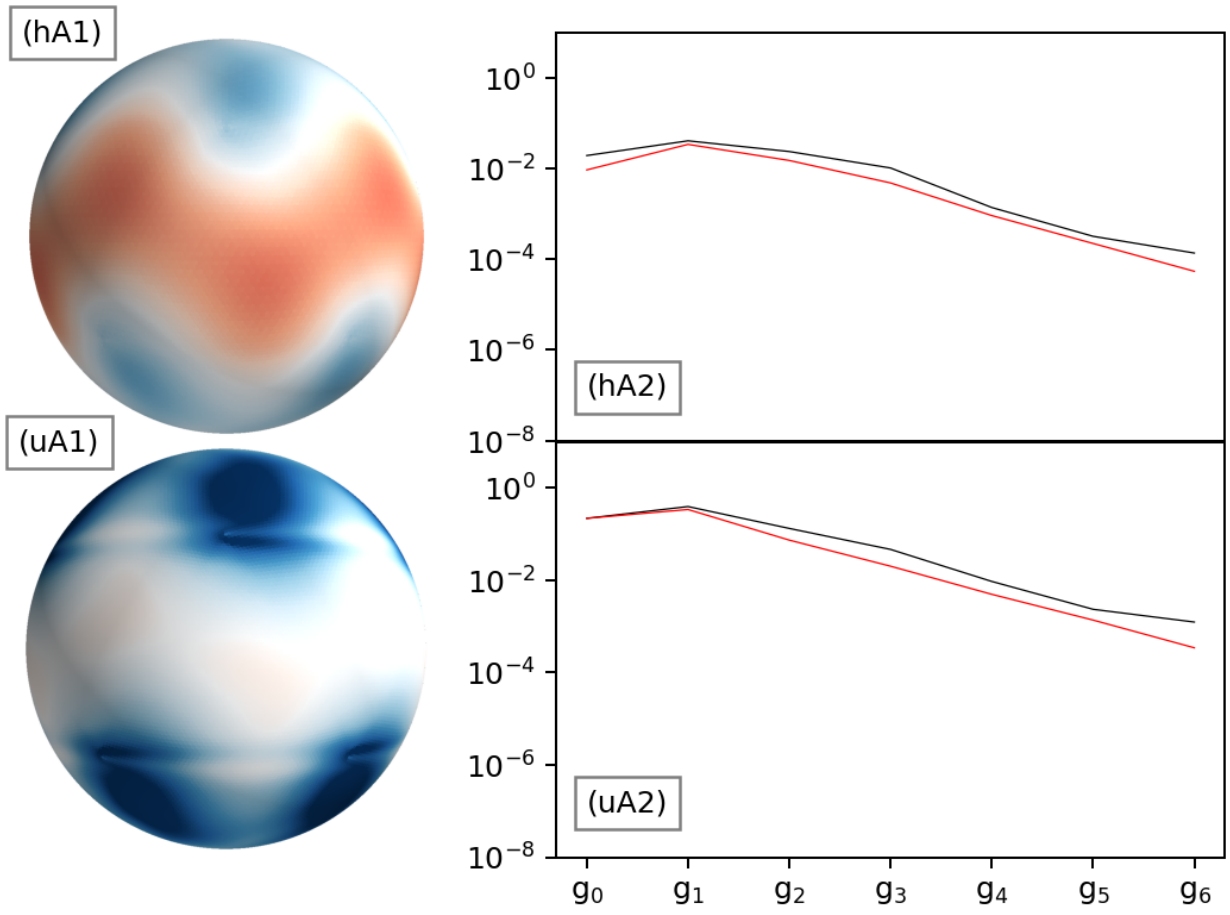

Figure A.3: Variable error for g_6 (left) and L_∞ and L_2 error norms.

AppendixB

Accuracy and Stability Analysis of Horizontal Discretizations used in Unstructured Grid Ocean Models

Below we include the paper submitted to the Journal of Ocean Modelling. This paper compare the shallow water model mentioned in the thesis using the SCVT optimization grid. We note the importance of evaluated the sometimes overlooked accuracy tests and energy tests provided in the submitted paper. Moreover, the use of high resolution grids is now discussed being many research institutes, in which case numerical noises might be more visible in these models. Therefore, we note the importance of evaluating the potential instability of these models and the effects of the numerical noise on the grid.

Graphical Abstract

Accuracy and stability analysis of horizontal discretizations used in unstructured grid ocean models

Fabricio Rodrigues Lapolli, Pedro da Silva Peixoto, Peter Korn

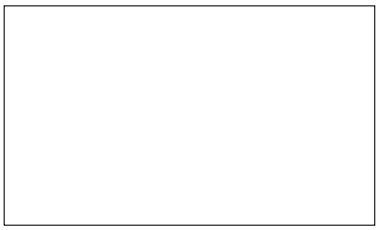

Highlights

Accuracy and stability analysis of horizontal discretizations used in unstructured grid ocean models

Fabricio Rodrigues Lapolli, Pedro da Silva Peixoto, Peter Korn

- Shallow water experiments were performed comparing horizontal discretizations of NICAM (A-grid), FeSOM 2.0 (B-grid), MPAS (C-grid), and ICON (C-grid).
- Schemes' accuracy is investigated, revealing A-grid and B-grid manifest at least a first order accuracy on the operators investigated, while both C-grid schemes display difficulty in convergence for some of the operators due to the used grid.
- C-grid is shown to display the most accurate representation of the energy spectrum from the tested schemes, followed by B- and A-grid schemes, respectively.
- Schemes' stability was investigated, and the necessary filter was evaluated to maintain stability.
- 3D ICON-O operational model was used for evaluating near grid scale instabilities.
- ICON-O was found stable, but susceptible to spurious oscillations participating in the dynamics.

Accuracy and stability analysis of horizontal discretizations used in unstructured grid ocean models

Fabricio Rodrigues Lapolli[a,b], Pedro da Silva Peixoto[a], Peter Korn[b]

[a] *Universidade de Sao Paulo, Rua do Matao, 1010, Cidade Universitaria, Sao Paulo, 05508-090, Sao Paulo, Brazil*
[b] *Max-Planck Institute for Meteorology, Bundestrasse, 53, Hamburg, 20146, , Germany*

Abstract

One important tool at our disposal to evaluate the robustness of Global Circulation Models (GCMs) is to understand the horizontal discretization of the dynamical core under a shallow water approximation. Here, we evaluate the accuracy and stability of different methods used in, or adequate for, unstructured ocean models considering shallow water models. Our results show that the schemes have different accuracy capabilities, with the A- (NICAM) and B-grid (FeSOM 2.0) schemes providing at least 1st order accuracy in most operators and time integrated variables, while the two C-grid (ICON and MPAS) schemes display more difficulty in adequately approximating the horizontal dynamics. Moreover, the theory of the inertia-gravity wave representation on regular grids can be extended for our unstructured based schemes, where from least to most accurate we have: A-, B, and C-grid, respectively. Considering only C-grid schemes, the MPAS scheme has shown a more accurate representation of inertia-gravity waves than ICON. In terms of stability, we see that both A- and C-grid MPAS scheme display the best stability properties, but the A-grid scheme relies on artificial diffusion, while the C-grid scheme doesn't. Alongside, the B-grid and C-grid ICON schemes are within the least stable. Finally, in an effort to understand the effects of potential instabilities in ICON, we note that the full 3D model without a filtering term does not destabilize as it is integrated in time. However, spurious oscillations are responsible for decreasing the kinetic energy of the oceanic currents. Furthermore, an additional decrease of the currents' turbulent kinetic energy is also observed, creating a spurious mixing, which also plays a role in the strength decrease of these oceanic currents.

Keywords: Shallow water model, unstructured ocean models, NICAM, FeSOM 2.0, MPAS-O, ICON-O, Numerical Instability

1. Introduction

Much of the scientific knowledge of the climate is largely due to the development of Earth System Models (ESMs), i.e. coupled models consisting of the atmosphere, ocean, sea ice, and land surface. The ocean, in particular, is a key

component of these ESMs and a driver of the climate. Consequently, it is crucial to develop and improve such ocean models, with particular attention to global models (Randall et al., 2018; Fox-Kemper et al., 2019a).

These efforts, along with the atmospheric modelling community, allowed us to acquire important insights related to these numerical models, such as being able to compartmentalize models into what is termed dynamical cores along with several physical parametrizations (Thuburn, 2008; Staniforth and Thuburn, 2012). Combined, these form the main building blocks of the current operational ESMs. The dynamical core is defined as being responsible for solving the governing equations on the resolved scales of our domain (Randall et al., 2018; Thuburn, 2008). For climate modelling, it is important that these cores are able to mimic important physical properties, such as mass and energy conservation, minimal grid imprinting, increased accuracy, and reliable representation of balanced and adjustment flow, which can be achieved by using a proper grid geometry and horizontal discretization (Staniforth and Thuburn, 2012). However, the use of unstructured grids may pose challenges in fulfilling these properties.

Traditional ocean models commonly used Finite Difference or Finite Volume discretization on regular structured grids (Fox-Kemper et al., 2019b), e.g. NEMO (Gurvan et al., 2022), MOM6 (Adcroft et al., 2019). This approach was useful for the limited regional modelling. However, for global models it posed some problems. The most critical is the presence of singularity points at the poles, which constrained the timestep size for explicit methods, potentially making it unfeasible for use in high resolution models (Sadourny, 1972; Staniforth and Thuburn, 2012; Randall et al., 2018). Therefore, in recent years, a lot of effort has been put on the development of unstructured global oceanic models.

Given the success of triangular grids on coastal ocean models, one popular approach is the use of triangular icosahedral-based global models, i.e. using geodesic triangular grids. However, there are still present issues with triangular grids, in particular with the variable positioning considering a C-grid staggering. The C-grid staggering (Arakawa and Lamb, 1977) considers the velocity decomposed into normal components at the edges of a computational cell. On traditional quadrilateral meshes, this staggering was found to more accurately represent the inertia-gravity waves (Randall, 1994). On unstructured triangular grids, a spurious oscillation is present on the divergence field manifested as a *chequerboard pattern*, and it is present due to the excessive degrees of freedom (DOF) on the vector velocity field (Gassmann, 2011; Le Roux et al., 2005; Danilov, 2019; Weller et al., 2012). In theory, these can lead to incorrect results if not correctly filtered, or can potentially trigger instabilities.

This *chequerboard pattern* issue led modellers to avoid triangular grids. One potential solution, which is used by MPAS-O model, is to use the dual grid, based on hexagonal-pentagonal cells, formed by connecting the circumcentres of the triangles (defining a Voronoi grid dual to the triangulation). By relying on the orthogonality properties between the triangular and the dual quasi-hexagonal grid, the problem of the spurious divergence modes is avoided. However, the noise will appear on the vorticity field, where it is easier to filter (Weller

et al., 2012).

Another potential solution to the chequerboard pattern on triangular grids is the use of filters on the divergence field in order to dampen these oscillations. However, these can potentially break the conservative properties of the model. A solution devised by the ICON-O ocean model community is the implementation of mimetic operators that required the preservation of some physical dynamical core properties, while, simultaneously, filtering the noise of the divergence field (Korn and Danilov, 2017; Korn, 2017; Korn and Linardakis, 2018). However, the added triangle distortion of the grid might not completely remove the noise, and, thus, the filtering property might be at most approximate.

In order to avoid the noise on the divergence field of triangular grids at all, a possibility is to avoid C-grid staggering. FeSOM 2.0 model, for example, uses the (quasi-) B-grid discretization in which the velocity vector field and the height field are allocated at the cells centre and vertices, respectively (Danilov et al., 2017). Alternatively, the NICAM atmospheric model, uses the A-grid discretization, which has all its fields positioned at the vertices of the grid (Tomita et al., 2001; Tomita and Satoh, 2004). Nonetheless, there are drawbacks from this solution. For example, both staggerings display spurious modes that are potentially unstable without treatment (Randall, 1994). The nature of these modes differs for each of the grid designs. The A-grid source of numerical noise is related to the manifestation of spurious pressure modes, whilst the B-grid allows the manifestation of spurious inertial modes due to excessive DOFs of the horizontal velocity (Tomita et al., 2001; Danilov et al., 2017).

Nonetheless, regardless of grid design, other artefacts may also be present. One particular spurious oscillation was detected on an energy-enstrophy conserving scheme (EEN) on an atmospheric model, leading to an instability (Hollingsworth et al., 1983). This kind of instability is dependent on the fastest internal modes of the model, the horizontal velocity and resolution of the model (Bell et al., 2017). Due to the presence of distortion on these newer models, instability might be more easily triggered (Peixoto et al., 2018). This kind of noise is noticeable on atmospheric models, due to the large flow speeds of the atmosphere and the near to kilometre grid resolutions used in their simulations (Skamarock et al., 2012). Although the ocean dynamics are less energetic than the atmosphere, the higher distortion of the grids and the rapid increase of resolution towards submesoscale models make the effects of this noise more relevant. In fact, some models, such as the NEMO's EEN ocean model, identified this noise and its effects, which have shown significant effects on the model's mesoscale jets and submesoscale phenomena (Ducousso et al., 2017).

Considering the challenges discussed, this works aims at investigating and comparing the accuracy and stability of different horizontal discretizations used in global unstructured ocean models. First, the unstructured nature of the model's grid have different implications with respect to the computation of the underlying dynamics operators. As such, can we expect expressive differences in accuracy between A-, B- and C-grid models? Second, each of these grid designs are expected, from the theory, to perform differently when integrating them in time. Therefore, are the inertia-gravity wave dispersion representation

similar to a structured grid case? Third, both the accuracy of the operators and the representation of the phenomena are expected to have an impact on the stability of the model. Consequently, which models are more prone to instability and which are easier to control?

To address these questions, we chose to evaluate both MPAS-O and ICON-O C-grid discretization schemes, due to their robustness and different approaches on computing the necessary operators; the FESOM2.0 for the B-grid scheme; and the NICAM A-grid scheme, which, to our knowledge, currently is not present in ocean models, but could be easily incorporated in existing ones. The investigation will be mostly focused on the rotating shallow water system of equations, but we will also evaluate some properties of the 3D ICON-O model. In section 2, we describe each of the aforementioned schemes. In section 3, we evaluate the accuracy and rate of convergence of each of these schemes. In section 4, we perform a time integration, in order to evaluate the accuracy of the integrated quantities and to observe some important properties of the models, such as the representation of inertia-gravity waves and the manifestation of near-grid scale oscillations under near realistic conditions. Finally, we evaluate the stability of the models under the effects of spurious grid scale oscillations and the effects of these oscillations in a 3D realistic oceanic ICON-O model.

2. Shallow Water models

In order to investigate these models, we test the schemes under the shallow water system of equations (Gill, 1982). This system is as follows:

$$\frac{\partial h}{\partial t} = -\nabla \cdot (\mathbf{u}h) \tag{1a}$$

$$\begin{aligned} \frac{\partial \mathbf{u}}{\partial t} &= -\mathbf{u} \cdot \nabla \mathbf{u} - \nabla \Phi - f\mathbf{u}^{\perp} + F \\ &= -\nabla(\Phi + E_k) - \omega u^{\perp} + F \end{aligned} \tag{1b}$$

where h and $\mathbf{u}$ are the height (scalar) and velocity (vector) fields of the system; f is the Coriolis parameter; $\omega = \zeta + f$ is the absolute vorticity; ζ is the relative vorticity or curl; $\Phi = g(b+h)$ is the geopotential, g is the acceleration of gravity, and b is the bathymetry; $\mathbf{u}^{\perp} = \hat{\mathbf{k}} \times \mathbf{u}$ is the perpendicular vector field $\mathbf{u}$ and $\hat{\mathbf{k}}$ is the vertical unit vector; and $E_k = |\mathbf{u}|^2/2$ is the kinetic energy. The right-hand most side of (1b) is known as the vector invariant form of the system of equations.

On this section, we present an introduction to each model and how they interpolate their quantities of the shallow water operators. On the next section, Section 3, we describe how each model compute each of the shallow water operator.

2.1. Discrete Framework

The models were evaluated with the Spherical Centroidal Voronoi Tessellation (SCVT) optimization (Miura and Kimoto, 2005) between the second (g_2)

and eighth (g_8) refinements of the icosahedral grid (Table 1). This optimization has the property of having its vertices coincide with the barycentre of the dual cells, quasi-hexagonal (red lines of Figure 1). Despite this grid having loss of uniformity with refinement, for oceanic applications, it provides an additional analysis, since the unstructured grid is useful for contouring continental regions of the earth.

	Circ. distance (Km)	Edge length (Km)
g_2	1115	1913
g_3	556	960
g_4	278	480
g_5	139	250
g_6	69	120
g_7	35	60
g_8	17	30

Table 1: Spatial resolution of the SCVT grid, considering the average distance between triangles circumcentre and the average edge length in Km.

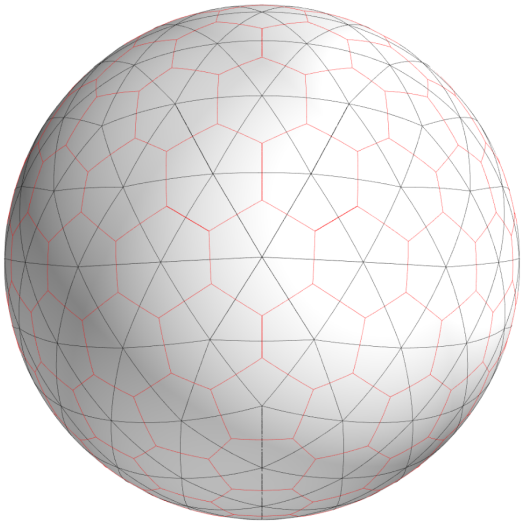

Figure 1: SCVT primal (black lines) and dual (red lines) g_2 grid.

The structure of the grid domain will consist of triangular cells (primal grid) $K \in \mathcal{C}$ with edges $e \in \mathcal{E}$. The set of edges of a particular cell K is represented by ∂K. The vertices in the endpoint of these edges are represented by ∂e. Occasionally, when necessary, the edges may be denoted as $e = K|L$ where it is positioned between cells K and L. The dual cells will be denoted by the $\widehat{(\cdot)}$ symbol. The dual cells and edges, for example, are denoted as $\widehat{K} \in \widehat{\mathcal{C}}$ and $\hat{e} \in \widehat{\mathcal{E}}$,

respectively. Furthermore, the centre/midpoint position of the elements will be denoted by the boldface, e.g. the cell circumcentre position $\mathbf{K}$, and the length or area of the respective elements will be denoted by $|\cdot|$, e.g. $|e|$, $|\widehat{K}|$ is the edge length and dual cell area, respectively.

We note that the relationship between the primal and dual mesh will differ depending on the model discretization definitions. Some models use circumcentre of the triangle to construct the dual mesh. The resulting relationship will be a Delaunay triangulation (for the primal) and a Voronoi diagram (for the dual), making their edges orthogonal to each other, which can be exploited by these models.

Additionally, normal ($\mathbf{n}_e$) and tangent ($\mathbf{t}_e$) vectors are positioned at the edge $\mathbf{e}$ or $\hat{\mathbf{e}}$, such that $\mathbf{n_e} \times \mathbf{t_e} = \mathbf{e}$. The former vector is normal to e, while the latter is parallel to it. These definitions are summarized in Table 2.

Symbol	Description
$\mathcal{C}$	Set of primal cells
$\mathcal{E}$	Set of primal edges
K, L	primal grid cells
∂K	Set of edges of cell K
$e = K\|L$	primal edge
n_e , t_e	Normal and tangent vectors on edge e
∂e	Set of vertices of edge e
$\widehat{\mathcal{C}}$	Set of dual cells
$\widehat{\mathcal{E}}$	Set of dual edges
$\widehat{K}$, $\widehat{L}$	dual grid cells
$\partial\widehat{K}$	Set of edges of cell $\widehat{K}$
$\hat{e} = \widehat{K}\|\widehat{L}$	dual edge
$n_{\hat{e}}$, $t_{\hat{e}}$	Normal and tangent vectors on edge $\hat{e}$
$\partial\hat{e}$	Set of vertices of edge $\hat{e}$

Table 2: Definitions of the grid structure.

2.2. NICAM (A-grid)

The NICAM model is a non-hydrostatic atmospheric-only model developed at AICS, RIKEN. Its development aimed to develop a high-performance global model (Tomita and Satoh, 2004). The model has been shown to produce accurate results for simulations with a 3.5 km mesh size, and recent developments aim to pursue sub-kilometre grid scales (Miyamoto et al., 2013).

NICAM's dynamical core's horizontal component is based on the A-grid discretization, in which all variables are located at the grid vertices (Figure 2). The discretization of this scheme allows only for mass conservation. Other quantities, specially related to the velocity equation, can not be conserved. This is because this scheme allows for spurious pressure modes, which may destabilize the model, thus, requiring filtering.

Additionally, small scale oscillations may also be present due to the grid imprinting, which may also decrease the model's stability (Tomita et al., 2001). These oscillations, however, can be remedied with a proper grid optimization. One important requirement is that the dual cell centre coincide centre of mass coincide with the vertex of the grid, guaranteeing consistency of the discretization of the operators.

Moreover, NICAM's A-grid discretization compared to the MPAS-O shallow water scheme this scheme has been shown to display a higher resilience when non-linearities are present, implying that it can better treat some types of instabilities than other models (Yu et al., 2020). Therefore, despite this scheme not have originally been developed for oceanic purposes, It can be suitably implemented in such applications.

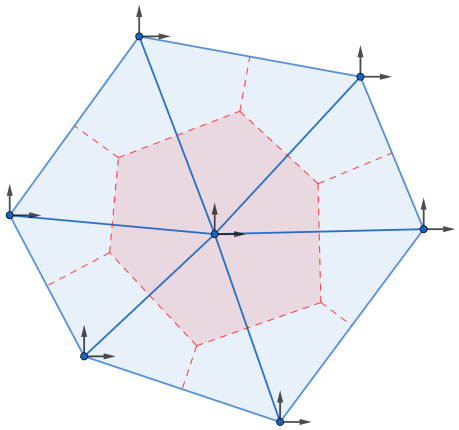

Figure 2: A-grid cell structure. The blue circles on the vertices are the height scalars points and the arrows are the components of the velocity vector points.

2.2.1. Interpolating operators

To compute the operations in the shallow water system, we need that the position of these operators coincide with the variables, i.e., at the vertices. Therefore, the computation must be performed on the dual cell. To do this, it is necessary to interpolate the variables at the dual edge midpoint. We do this by first interpolating at the circumcentre of the primal cell:

$$\widetilde{h}^K = \frac{1}{|K|} \sum_{v \in \partial e_K} w_v h_v, \tag{2a}$$

$$\widetilde{\mathbf{u}}^K = \frac{1}{|K|} \sum_{v \in e_K} w_v \mathbf{u}_v, \tag{2b}$$

where w_v is the sectional triangular area formed by the circumcentre and the opposite vertices of the cell (See Figure 2 of Tomita et al. (2001)). This interpolation, known as the barycentric interpolation, will provide us with a second

order accurate interpolation. A second order interpolation to the edge midpoint can then be met by averaging neighbouring primal cells:

$$\widetilde{h}^{\hat{e}} = \frac{1}{2}(h_K + h_L), \tag{3a}$$

$$\widetilde{\mathbf{u}}^{\hat{e}} = \frac{1}{2}(\mathbf{u}_K + \mathbf{u}_L). \tag{3b}$$

2.3. FESOM (B-grid)

FESOM 2.0, developed in the Alfred Wegener Institute, contains ocean (Danilov et al., 2017) and ice (Danilov et al., 2015, 2023) components only. The model is an update from its previous 1.4 model (Wang et al., 2008). The new model was developed to provide faster simulations compared to its 1.4 predecessor (Scholz et al., 2019), which is partly owed to the change from Finite Element Methods to Finite Volume discretization (Danilov et al., 2017).

In addition to its updated components and faster simulations, FESOM 2.0's horizontal discretization of the dynamical core is based on the Arakawa B-grid staggering (Arakawa and Lamb, 1977). It is important to note that there is no true analogue of the B-grid on triangles (Danilov, 2013), and such a discretization has been coined as quasi-B-grid. However, due to the similarities in the positioning of the fields in the cell, in this work, we will describe this discretization only as B-grid.

Contrary to the aforementioned A-grid, this discretization is free of pressure modes. However, it allows for the presence of spurious inertial modes, due to its excessive degrees of freedom (Danilov et al., 2017). Thus, again, requiring the use of filters to remove these oscillations.

In addition to the B-grid discretization, FESOM's grid design plays a crucial role in computing the operators necessary for FESOM's horizontal discretization. It creates a dual cell by connecting the triangles' barycentre with its edge midpoint, creating a cell with 10 to 12 edges (Figure 3).

2.3.1. Interpolation operators

This grid allows computing the operators by only interpolating the height field at the edges when needed to compute the gradient at the cells' barycentre. Given an edge e, with vertices $\widehat{K}, \widehat{L} \in \partial e$, then the interpolation is defined as:

$$\widetilde{h}^{e} = \frac{1}{2}(h_{\widehat{K}} + h_{\widehat{L}}), \tag{4}$$

thus achieving a second order interpolation on the edge.

FESOM's horizontal momentum discretization is provided with three alternative computations of the momentum equations: two in its flux advective equation form, one computed at the centre of mass of the triangular cell and the other computed at the vertex, and one in a vector-invariant form, which is computed at the vertices of the grid. The two forms computed at the vertices would thus require to be interpolated at the centre of mass of the triangle with (4). It is also argued that the use of the flux advective form of the equation provides

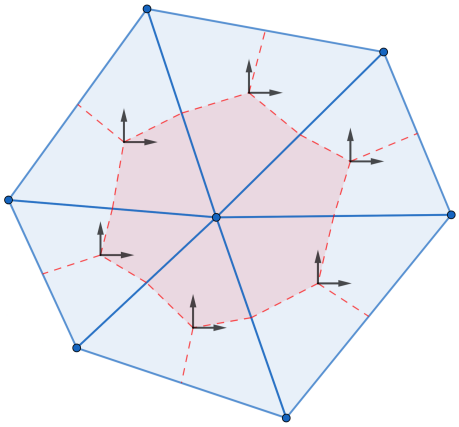

Figure 3: B-grid cell structure. The blue circles on the vertices are the height scalars points, and the arrows on the triangle centre are the components of the velocity vector points.

a small internal diffusion on the system (Danilov et al., 2015). However, there is a surprising lack of published work comparing these forms, indicating a need for a more in-depth research in the future. In this work, in order to ensure a fair comparison with the other schemes, we chose to compute this discretization using the vector invariant form of the equation.

2.4. MPAS-O (C-grid)

MPAS, an ESM from the Climate, Ocean and Sea Ice Modelling (COSIM) and National Center for Atmospheric Research (NCAR), comprises atmospheric, ocean, and ice components (Ringler et al., 2010; Skamarock et al., 2012; Hoffman et al., 2018; Turner et al., 2022). The oceanic component has been shown capable of accurately representing geophysical flows on meshes with a large variation of resolution (Ringler et al., 2013).

The horizontal discretization of the dynamical core of MPAS was developed for arbitrarily sided C-grid polygons (Thuburn et al., 2009; Ringler et al., 2010). It is inspired by the Arakawa and Lamb's scheme (Arakawa and Lamb, 1981), which is capable of providing some conservative properties, such as total energy and potential vorticity, while also providing reliable simulations for these arbitrary grid structures without a breakdown of the time-integrated solutions, which has previously affected schemes using a quasi-hexagonal mesh (Staniforth and Thuburn, 2012).

Although this scheme could potentially be used for any arbitrarily sided polygonal mesh, the icosahedral based hexagonal grid was shown to provide the most accurate and well-behaved solutions (Weller et al., 2012). For example, analysis of this discretization has shown that the scheme can achieve at most first order accuracy for most of the operators, but a stagnation or divergent accuracy for others (Peixoto, 2016). Despite this, the model's noise is well

controlled, while also maintaining its geostrophic modes with zero-frequency (Weller et al., 2012; Peixoto, 2016).

On this C-grid discretization (Figure 4), the velocity vector field is decomposed on the edges of our primal grid (triangular cells), where these velocities are normal to the dual grid (pentagonal or hexagonal cell), while the height field is collocated at the vertices of the grid. This minimizes the use of interpolating variables on this scheme. The only interpolation used is to calculate the perpendicular velocity and the kinetic energy, which will be better discussed in the following sections.

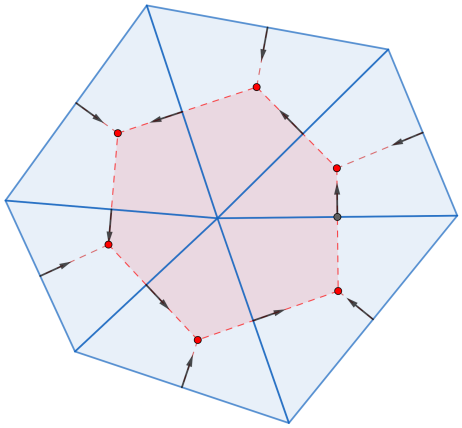

Figure 4: C-grid cell structure. Red circles on the vertices are the height scalar points, and the arrow on the edge midpoint is the decomposed velocity vector field.

2.5. ICON-O (C-grid)

The ICON numerical model is a joint project between the German Weather Service and the Max Planck Institute for Meteorology and consists of atmosphere, ocean (including biogeochemistry), land, and ice components (Giorgetta et al., 2018; Korn, 2017; Jungclaus et al., 2022). The ICON modelling team was not only able to successfully provide an accurate simulation of geophysical flow, but also provided evidence that their model is within reach to accurately simulate ocean submesoscale flow (Hohenegger et al., 2023).

In the particular case of ICON's oceanic component, i.e. ICON-O, its horizontal discretization of the dynamical core is based on the mimetic methods approach, which is a practical way to discretize PDEs while taking into account fundamental properties of these equations (Brezzi et al., 2014). This philosophy, in theory, could allow for ICON depending on the truncation time to achieve the conservation of total energy, relative and potential vorticity, and potential enstrophy to some order of accuracy.

To accomplish these conservation properties under the mimetic methods, ICON-O uses the concept of admissible reconstructions $(\mathcal{P}, \hat{\mathcal{P}}, \hat{\mathcal{P}}^{\dagger})$ (Korn and Linardakis, 2018). These are in charge of connecting variables at different points,

acting as interpolation and reduction operations. They, i.e. the admissible reconstructions, are required to have some properties, such as providing unique and first-order accurate fluxes and having its nullspace coinciding with the space of divergence noise.

2.5.1. Interpolating operators

Operationally, ICON-O model uses the Perot operator. This function reconstructs the velocity field components of the edge midpoint to the triangle centre ($P = \mathcal{P}$), and subsequently project these reconstructed vectors to their original position at the edge midpoint ($P^T\mathcal{P}$) (Perot, 2000):

$$Pu_K = \frac{1}{K} \sum_{e \in \partial K} |e| u_e \mathbf{n}_e, \tag{5}$$

$$P^T u_e = \frac{1}{|\hat{e}|} \sum_{K \in \partial \hat{e}} d_{e,K} u_K \cdot \mathbf{n}_e. \tag{6}$$

The combination of operators is denoted as $M = P^T P$ and is key to compute the operators of the shallow water equations. This mapping, M, was found to filter the divergence noise of triangles without losing the aforementioned physical properties (Korn and Danilov, 2017; Korn, 2017; Korn and Linardakis, 2018). However, the operator has the potential to smooth high wavenumber phenomena (Korn and Danilov, 2017).

Additionally, there is also a set of operators that reconstructs the vector velocity field into the vertices of the grid ($\widehat{P} = \hat{\mathcal{P}}$) and reduce it back into the edge midpoints ($\widehat{P}^\dagger = \hat{\mathcal{P}}^\dagger$). This sequence is defined as:

$$\widehat{P} u_{\hat{K}} = \frac{1}{|\hat{K}|} \sum_{e \in \partial \hat{K}} |\hat{e}| u_e \mathbf{e} \times \mathbf{n}_{\hat{e}}, \tag{7}$$

$$\widehat{P}^\dagger u_e = \frac{1}{|\hat{e}|} \sum_{\hat{K} \in \partial e} d_{e,\hat{K}} u_{\hat{K}} \cdot \mathbf{n}_e. \tag{8}$$

Thus, the sequence $\widehat{M} = \widehat{P}^\dagger \widehat{P}$ allows us to compute the Coriolis term of the shallow water equations. This dual operator has shown to provide a non-zero spurious frequency geostrophic modes, which have been shown to create numerical waves in the system (Peixoto, 2016), and could potentially be damaging to the stability of the scheme (Peixoto et al., 2018). However, due to the filtering property of the operator M, these modes could be removed from the simulation due to their filtering property on the grid scale.

	Institution	Staggering	Components	Conservation
NICAM	AORI, JAMSTEC, AICS	A-grid	Atm	TE
FESOM	AWI	B-grid	Oc	TE
MPAS	COSIM, NCAR	C-grid	Atm/Oc/Ice	PV, TE
ICON	DWD, Max-Planck	C-grid	Atm/Oc/Land/Ice	KE, TE, PV, Enst

Table 3: Summary of the main models to be compared with their respective components: Ocean (Oc), Atmosphere (Atm), Ice Dynamics (Ice) or Land; and their conservation properties: Total energy (TE), Kinetic Energy (KE), Potential vorticity (PV), and Enstrophy (Enst).

3. Accuracy of the Discrete Operators

We aim to analyse the truncation errors of each operator from Nonlinear Shallow Water Equations (1). To achieve this we evaluate two different test cases: The first follows from Heikes and Randall (1995) and Tomita et al. (2001), henceforth Test Case 0 or TC0, where for $\alpha,\ \beta$ defined as:

$$\alpha = \sin\phi$$
$$\beta = \cos(m\phi)\cos^4(n\theta),$$

where ϕ and θ are the longitude and latitude, respectively, then $\mathbf{u}$ and h are defined:

$$\mathbf{u} = \alpha\nabla\beta \tag{9}$$
$$h = \beta. \tag{10}$$

We consider in our analysis $m = n = 1$, since it is a smooth particular smooth case with both non-zero vector components, which allows us to evaluate the accuracy of the operators and compare with the literature.

A second case is the Nonlinear Geostrophic testcase, henceforth Test case 1 or TC1, from the toolkit set of Williamson et al. (1992). $\mathbf{u}$ and h are defined as:

$$gh = gb_0 - h_0\sin^2\theta \tag{11}$$
$$u = u_0\cos\theta, \tag{12}$$

where $gb_0 = 2.94\times10^4$ m^{2}s^{-2}, $h_0 = a\Omega u_0 + u_0^2/2$ m^{2}s^{-2}, $u_0 = 2\pi a/(12\text{ days})$ ms^{-1}, $g = 9.81$ ms^{-2} is the acceleration of gravity, $a = 6.371\times10^6$ m is the radius, and $\Omega = 2\pi/86400$ s^{-1} is the angular frequency of earth.

Additionally, in order to compare our results, we define the errors in our domain as $\Delta f = f_r - f_r^{\text{ref}}$, where f_r and f_r^{ref} is the computed and reference function, respectively, for a mesh element r of the domain. Thus, the maximum

and second error norm may be defined as:

$$L_\infty = \frac{\max_r |\Delta f_r|}{\max_f |f_r^{\text{ref}}|} \tag{13}$$

$$L_2 = \sqrt{\frac{S(\Delta f^2)}{S((f^{\text{ref}})^2)}} \tag{14}$$

where $S(f) = \sum_{r\in\Omega} \Delta f A_r / \sum_{f\in\Omega} A_r$, and A_r is the area of the element, e.g. A_e for the edge, $|K|$ for triangles, or $|\hat{K}|$ for the dual cell.

3.1. Divergence

The divergence operator, part of the mass equation, can be defined from the Divergence Theorem. Following it, we can provide a general formula for its discretized version as:

$$(\nabla \cdot \mathbf{u})_i \approx (\mathbf{div}\ u)_i = \frac{1}{|F|} \sum_{e\in\partial F} |e| \mathbf{u} \cdot \mathbf{n}_e n_{e,F}, \tag{15}$$

where F is a cell with barycentre i and edges $e \in \partial F$, $n_{e,F} = \{1, -1\}$ is a signed valued aimed to orient the normal velocity $\mathbf{u} \cdot \mathbf{n}_e$ away from the element F.

In order to compute the divergence field, we note that both the A-grid and B-grid schemes compute divergence field at the dual cells (vertices). For the former scheme, we require an interpolation of both the scalar height, (2) and (3), and vector velocity fields at the dual edge midpoint, in order to compute the divergence at the dual cell, i.e. quasi-hexagonal cell. In the case of the latter scheme, we only require the interpolation of the scalar height field at the primal edge midpoint (4), in order to compute the same divergence field at the primal cell.

In the case of the C-grid, there is a substantial difference between the computation of both schemes. MPAS interpolates the scalar height field at the primal edges, similar to B-grid, while ICON uses admissible reconstruction operators of the form $P^T h P u$ to compute the operator.

These differences on the schemes are reflected in our results (Figure 5.div). The A-grid for the TC0 testcase displayed an error convergence with an initial rate of second order up to the sixth refinement (g_6). On finer grids, for the L_∞, this scheme has slowed down to first order, while on second order, the scheme remained converging up to second order rate. On the TC1, a more consistent convergence rate was observed, on the L_∞ and L_2, the scheme has displayed a first and second order convergence rate. On other grids, in particular the standard and Spring Dynamics, the A-grid has shown to achieve at least a first order convergence rate (Tomita et al., 2001). Although a direct comparison cannot be provided, since our testcases differ, the scheme on an SCVT has apparently shown to provide a comparable convergence rate to the intended optimized grid on either the L_∞ or the L_2 norm.

Regarding both C-grid schemes, we observe a similar behaviour in the computed operator. In particular, neither scheme displays an increase in accuracy

of the divergence field on the L_∞. For the case of ICON, this result has been previously observed in a similar work by Korn and Linardakis (2018). It was also shown that the *naive* approach to calculate the divergence field still retained a first order increase in accuracy, implying that the main culprit of this inability to increase the accuracy likely lies on Perot's operator itself (Table 4 of Korn and Linardakis (2018)). The authors have not provided a geometrical analysis of their non-uniform grid, but we note that the SCVT grid share some similarities with the standard grid, such as the non convergence of the distance between the primal and dual edge midpoints, which likely has a deleterious effect on the accuracy of the operator. However, on the L_2, the scheme was able to reach at least a first order convergence rate on both testcases.

On the case of MPAS, the inability to provide a decrease in error with grid has been discussed in Peixoto (2016). It is reasoned that since the computation of the divergence is not based on velocities from the Voronoi edge midpoints, the discretization is inconsistent, and a first order convergence is not guaranteed. In contrast, on the L_2, MPAS was able to reach a second order rate up to g_4, but the speed of convergence slows down to first order on TC0, while on TC1 the second order rate is maintained throughout grid refinements.

Finally, B-grid has provided consistent accuracy throughout each testcase. We observed a first and second convergence rate for L_∞ and L_2, respectively, for both testcases. A decrease is observed on TC0, however, this decrease is likely associated with the error approaching the machine truncation error.

When comparing the errors of the schemes, we note that both A- and B-grid schemes display a decrease in speed of accuracy convergence as the grid is refined, with the latter scheme displaying the smallest errors on most of the tested cases and error norms. Additionally, despite ICON providing convergence on some tests, the scheme displays the largest errors of all tested schemes. It is likely that the smaller stencil used in ICON's divergence computation play a role in these larger errors. Another contribution is potentially related to Perot's operator, whose interpolation could act as smoothing the velocity field.

Overall, we note that the structure of the mesh, regarding cell geometry (primal or dual cell) and distortion, plays a contributing factor on approximating the divergence field on all schemes. Both C-grid schemes, in particular, seemed to be the most vulnerable to the grid. In contrast, B-grid's consistency in its accuracy apparently seems to be the least vulnerable to the increase in the distortion of the grid.

3.2. Gradient

The gradient operator, from the momentum equation, is a vector field, whose vector points itself to the steepest regions of the original field. The schemes provide different discretizations for this operator:

$$\nabla h \approx \mathbf{grad}\ h = \begin{cases} \sum_{e \in \partial F} h|e|\mathbf{n}_e & \text{A- and B-grid,} \\ \frac{1}{|e|}\sum_{i \in \partial e} h n_e & \text{C-grid.} \end{cases} \tag{16}$$

A- and B-grid's schemes provide a complete vector field on our domain by computing the average gradient within the centre of the respective cell F. The C-grid, on the other hand, computes the gradient with respect to the normal vector n_e by computing the difference between the values of the cell neighbouring the edge e. In that regard, the C-grid computation can be perceived as a gradient in the direction of $\mathbf{n}_e$.

In relation to the mesh, the A-grid scheme is computed at the vertices of the mesh, while the B-grid is computed at the barycentre of the triangular cells. On the other hand, both C-grid schemes are computed on the primal edge midpoint of our mesh. However, the MPAS scheme considers the neighbouring vertices to compute the gradient, while ICON considers the neighbouring triangles.

As in the divergence approximation, these differences in computation are as well reflected in our results (Figure 5.grad). The A-grid displays for coarser grids a fast convergence rate (second order rate), up to g_5, for both testcases. For finer grids, the L_∞ the decrease in error slows down to a first order convergence, but with the L_2 the convergence rate remains consistent. The analysis made by Tomita et al. (2001) have showed that their grid is capable of displaying a second order error convergence. We again note that although we cannot directly compare our results, due to the differences in testcases used, our results show a comparable error convergence with the authors with the SCVT optimized grid.

Similarly, the B-grid scheme shows a consistent decrease in error on all norms and testcases, similar to the divergence operator results. However, it displays only a first order convergence rate, in contrast to the second order on the divergence operator. The computation of the gradient on the B-grid is analogue to the divergence computation in ICON, therefore a similar argument follows, explaining that the expected convergence rate of such a scheme being a first order.

Comparably, MPAS also displays a consistent convergence rate, but in this case this scheme achieves a second order rate on all norms and testcases. Since the edge midpoint is situated, by definition, at the midpoint between the neighbouring vertices, the discretization is analogue to a centred difference scheme used in traditional quadrilateral grids. Therefore, we can properly achieve a second order convergence rate. The same argument is provided in Peixoto (2016), however the author also argues that when we consider the computation of the gradient of the kinetic energy we do not only reach a convergence rate, but our error diverges with grid refinement. The author reasons that the error of kinetic energy is of zeroth order (to be discussed further), and, thus, its gradient diverges.

On the other hand, the ICON's scheme gradient error displays a near second order convergence rate for coarser grids on the L_∞ norm of the TC0, but this error slows down for further refinements. On the TC1 testcase, the rate of convergence on L_∞ is consistent in first order. However, at the L_2 norm, the scheme has an accuracy of near second order with magnitude similar to that of MPAS.

Finally, we can then draw a comparison from all schemes. The B-grid has displayed the largest errors in magnitude and was the only scheme to achieve

a low first order convergence on the L_2. The A-grid L_∞ displays a similar error magnitude and behaviour in convergence with ICON. MPAS has shown the lowest errors among all schemes, and, in the L_2, displayed a comparable magnitude and convergence behaviour with ICON.

Overall, we again observe an impact of the grid structure on our schemes, however, this impact is not as damaging as found in the divergence computation. The directional derivative of MPAS makes it easier to achieve a consistent increase in accuracy, and the mismatch between the edge midpoints, has thwarted ICON's convergence rate. Despite this, the scheme still retained a first order convergence rate.

3.3. Curl

The curl operator, part of the vector invariant form of the shallow water velocity equation, is connected to the Coriolis Term. This term requires a careful discretization to allow for Coriolis energy conservation. This operator, in its continuous form, is defined from Stokes Theorem. Its Finite Volume discretization follows from this theorem and a general formulation for all our schemes can be defined as:

$$\nabla \times \mathbf{u}_i \approx |F| \text{vort } u_i = \sum_{i \in \partial F} |e'| \mathbf{u}_i \cdot \mathbf{t}_{e'} t_{e,F}, \tag{17}$$

for any F cell with edges e', tangent vector $\mathbf{t}_{e'}$, and $t_{e,F} = \{1, -1\}$ is a signed value guaranteeing that the unit tangent vector is counterclockwise on the cell.

For each scheme, the both A-grid, and B-grid computes the vorticity field on the vertices of the mesh. Since, for the B-grid, the shallow water velocity equation requires the points at the barycentre of the triangle cell, we interpolate the vorticity from the vertices to the barycentre. For the both C-grid schemes, MPAS computes this operator at the circumcentre of the cell, while ICON computes at the vertices, in duality with the divergence operator.

In this context, similarities are observed with the divergence operator. For example, the A-grid convergence rate for both norms and testcases, reach the same order as the divergence operator. On the TC0 testcase, however, throughout all grid refinements the error retain a first order, unlike the divergence operator, which begins with a second order and slows down to a first order. Additionally, on the TC1 testcase, we observe that the vorticity error displays a second order convergence up to g_4 and slows down to first order, unlike the divergence operator (Figure 5.Vort).

Similarly, the B-grid scheme displays the same behaviour as in the divergence operator. It displays a first order convergence rate on L_∞ and a rate of second order for L_2 on both testcases.

In contrast, both C-grid schemes display a different behaviour from the divergence operator. MPAS shows a consistent first order convergence rate for both norms on both testcases. Given that this computation is computed on the dual cell centre (red polygon in Figure 4), i.e. pentagon or hexagon, we can then achieve a higher accuracy rate of around second order.

ICON, on the other hand, displays a zeroth order convergence on L_∞ for the TC0 testcase. This is likely due to the mismatch of edge midpoints, similar to MPAS's divergence operator. However, on this norm for TC1, the error converges on a first order rate. This difference implies that different testcases will potentially impact the error. On this particular case, we note that the meridional velocity is not present on TC1, which may facilitate the computation of the vorticity. This result is also seen on L_2, while for TC0, the norm converge in first order, for TC1, it converges in second order.

In comparison, we observe that ICON is the only scheme that has trouble in increasing its accuracy when approximating the vorticity operator. In addition, both A- and B-grid schemes were the only to display a second order error rate on the L_2 for both schemes. Although MPAS also has shown an overall convergence, in contrast to ICON, it still has shown a larger error for TC0's L_2 norm and both norms of TC1.

Overall, there are similarities on the error behaviour between both vorticity and divergence scheme due to its similar concepts underlying the discretization. In that regard, we also observe an impact of the grid structure and the testcase used on the accuracy of the vorticity approximation.

3.4. Kinetic Energy

Similar to the vorticity operator, the kinetic energy is part of the vector invariant form of the velocity equation of the shallow water, whose gradient will then be computed. The kinetic energy is defined as:

$$E_k = \frac{1}{2}|\mathbf{u}|^2.$$

The computation of this operator on both A- and B-grid schemes is straightforward, since the vector velocity field is complete on each vertex and barycentre, respectively, of the mesh. However, for the C-grid schemes the vector field is decomposed on the edges of the mesh, therefore require a reconstruction in order to approximate the value of the kinetic energy field. In the particular case of MPAS and ICON, it is difficult to provide a general formula, therefore we individually define:

$$E_k^{(\mathrm{MPAS})} = \frac{1}{2|\hat{K}|}\sum_{e\in\partial\hat{K}}\frac{|e||\hat{e}|}{2}u_e^2, \tag{18}$$

$$E_k^{(\mathrm{ICON})} = \frac{|Pu|^2}{2}. \tag{19}$$

Both schemes provide some form of interpolation of the velocity on the cell centre, dual for MPAS, primal for ICON. It is observed on this computation that MPAS's and ICON's weights are shown to be: $|e||\hat{e}|/2$, and $|e|d_{e,K}$, where again $d_{e,K}$ is the distance between the edge midpoint e and circumcentre K. We note that for equilateral triangles $d_{e,K} = |\hat{e}|/2$. Another note is that MPAS computes the square of the component of the velocity and then interpolates

the resultant on the cell centre, while ICON interpolates the complete vector velocity field on the cell centre, and then computes the kinetic energy.

These difference in computation are reflected on the error of the field (Figure 5.Ek). On MPAS scheme, we see that for both testcases it does not converge on L_∞. This result was discussed by Peixoto (2016), as being an inconsistent formulation of the kinetic energy on the SCVT. Part of this inconsistency could partly be due to the computation of the kinetic energy on a single velocity component, as previously mentioned. Despite this, on L_2, MPAS display a second order convergence on TC0, on coarser grids, but it slows down to first order on finer grids. Similarly, on TC1, MPAS displays a first order rate, but throughout all grids.

ICON, in contrast, show a consistent convergence rate on both norms of first order on TC0 and second order on TC1. It can also be observed that, except for TC0's L_2, ICON's error is substantially lower than MPAS. ICON's Perot operator interpolation allows for a higher convergence, in comparison with MPAS, in part due to the vector velocity field interpolated on the cell circumcentre prior to the computation of the kinetic energy.

Overall, both C-grid computations display very distinct error behaviour. On this grid, although on both schemes the kinetic energy formulation allows for energy conservation, MPAS is unable to provide a consistent formulation of the operator. In contrast, ICON is provided with its consistent through the use of its Perot operator.

3.5. Perpendicular Velocity

The perpendicular velocity is an important part of the Coriolis Term, which is a forcing that takes into account the non-inertial reference frame of the shallow water equations. In that case, it is important that the Coriolis term of our schemes does not input energy into the system. Similar to the kinetic energy, both the A- and B-grid schemes have their vector velocity defined on the same points, providing an exact value for the perpendicular velocity. However, since C-grid schemes do have their vector velocity decomposed on the edges of the grid, an interpolation is necessary.

This interpolation should be carefully chosen in order to retain the conservation of energy of the system. Following the argument of Peixoto (2016), a reconstruction can be thought as a weighted composition of the neighbouring edges of the cell:

$$u_e^\perp = \sum_{e'} w_{e,e'} u_{e'}. \tag{20}$$

These weights should be chosen such that this reconstruction is unique and does not provide energy to the system.

Choosing the edges e' from cells that share the same edge e we can define the perpendicular velocity as:

$$u_e^\perp = a_{e,F_1} u_{e,F_1}^\perp + a_{e,F_2} u_{e,F_2}^\perp, \tag{21}$$

where a_{e,F_n} are the weights with respect to the cell F_n. This formulation is capable of achieving a unique solution on the edge.

In the case of MPAS's vector interpolation, we define the weights $w_{e,e'}$ as:

$$w_{e,e'} = c_{e,K}\frac{|e'|}{|\hat{e}|}\left(\frac{1}{2} - \sum_{K\in\cup\partial e}\frac{A_{\hat{K},K}}{|\hat{K}|}\right)n_{e',\hat{K}},$$

where $c_{e,\hat{K}}$ and $n_{e',K}$ are sign corrections that guarantee the vector tangent vector is anticlockwise on the for the cell $\hat{K}$ and that the norm vector $n_{e'}$ point outwards of the cell $\hat{K}$; and $A_{\hat{K},K}$ is the sectional area of the triangle cell K formed by the vertex $\hat{K}$ and the neighbouring edges of the circumcentre K in respect to the vertex. Using these weights on (20), we can compute $u^{\perp}_{e,K}$. In order to provide a unique reconstruction on edge e we let $a_{e,K} = a_{e,L} = 1$ on (21).

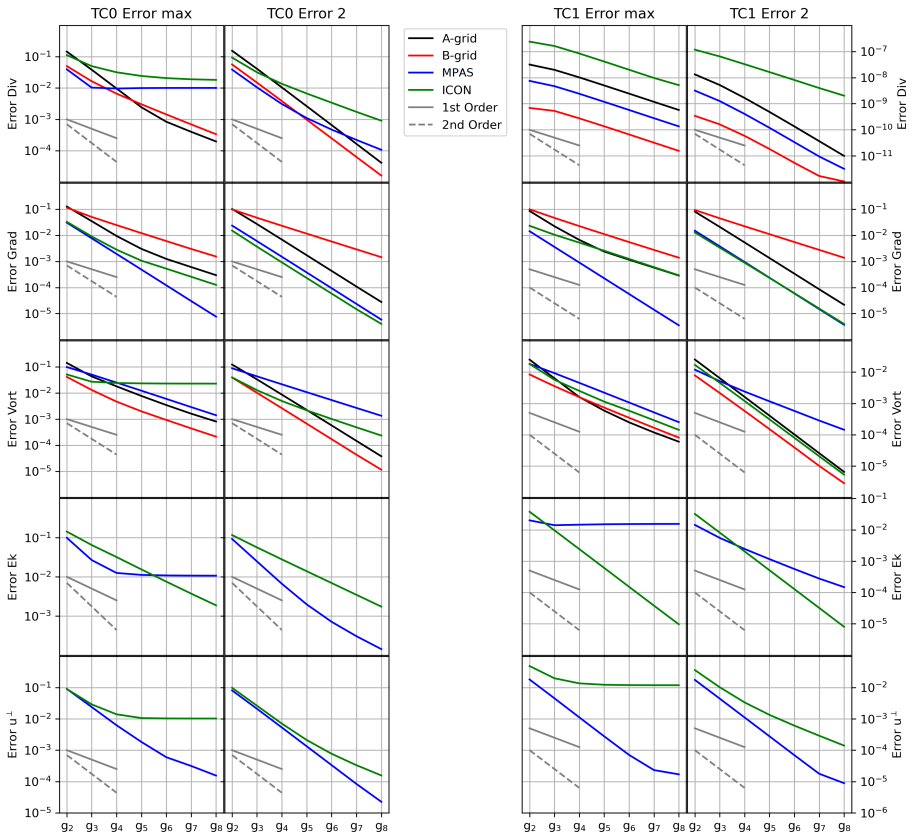

Figure 5: TC0 (first and second row panels) and TC1 (third and fourth row panels) operators L_∞ (first and third panels) and L_2 (second and fourth panels) error norms for the A-grid (black lines), B-grid (red lines), MPAS (blue lines), and ICON (green lines).

In the case of ICON's scheme, we use the interpolation $\hat{P}^T \omega \hat{P} u$. In this case $\hat{P} u_{\hat{K}} = u^{\perp}_{\hat{K}}$, so the weights are defined as:

$$w_{e,e'} = w_{\hat{e},\hat{K}} = \frac{|\hat{e}| d_{\hat{e},\hat{K}}}{|\hat{K}|},$$

giving a unique reconstruction on the centre of the dual cell $\hat{K}$. In order to reduce it back to the edge, we do $a_{e,\hat{K}} = d_{e,\hat{K}}/|e|$. We note that this set of operators allows not only the energy conservation, but also potential enstrophy (Korn and Danilov, 2017; Korn and Linardakis, 2018). We recall, however, that this operator has the potential of producing non-zero frequency geostrophic modes (Peixoto, 2016).

Our results show that MPAS displays a second order convergence rate on L_∞ up to g_6 on TC0, but decrease to a first order for finer grids (Figure 5.u$\perp$). On L_2, it shows a second order throughout all refinement. Similarly, on TC1, it also shows a second order rate up to g_7, but decrease near first order to g_8. A similar result is obtained for L_2. This result is similar to Peixoto (2016) showing that MPAS achieves at most a first order convergence rate on the L_∞.

4. Shallow Water Time Integration

The time integration of the shallow water equations provides us knowledge about the behaviour and limitations of the model throughout time. In order to gather this understanding, in this section we will put the schemes under a battery of tests. For the purpose of these tests, we chose to use a simple Runge-Kutta (RK44) operator, with 50 seconds timestep for all schemes and grids. Such choices are enough to ensure that the temporal errors are minimal and that the dominating error comes from the spatial discretization. We note that although both C-grid schemes may not require a stabilization term, since their error are expected to be well controlled, both A- and B-grid schemes could excite errors that would potentially destabilize the model. It is possible to use a harmonic ($\nabla^2 \mathbf{u}$) or biharmonic ($\nabla^4 \mathbf{u}$) term to provide stability of the scheme. In order to be more scale selective and avoid damping physical waves of our simulations we chose to use only the biharmonic, and as it was shown by the original authors of A- and B-grid schemes (Tomita et al., 2001; Danilov et al., 2017) the biharmonic term is enough to provide the necessary stability.

Therefore, the stabilizing operator can be regarded as a composition of Laplace diffusion operators, i.e. $\nabla^4 \mathbf{u} = \Delta\Delta\mathbf{u}$. To compute the Laplace diffusion operator, both A- and B-grid schemes are equipped with different approaches in its computation. For the former scheme, the Laplace operator is defined as:

$$\Delta \mathbf{u} = \nabla \cdot \nabla \mathbf{u}. \tag{22}$$

Thus, we can approximate the Laplacian operator by $\Delta \mathbf{u} \approx \mathbf{div\ grad\ u}$, using the operators defined in the previous section.

	A-grid/B-grid (m^2s^{-1})
g_2	10^{22}
g_3	10^{20}
g_4	10^{19}
g_5	10^{18}
g_6	10^{17}
g_7	10^{16}
g_8	10^{15}

Table 4: Biharmonic coefficient used for stabilizing the shallow water schemes.

On the other hand, the B-grid scheme, computes the harmonic diffusion for a cell K as:

$$\Delta \mathbf{u} \approx \frac{1}{|K|} \sum_{L} \frac{|e|}{|\hat{e}|} (\mathbf{u}_L - \mathbf{u}_K), \tag{23}$$

where L are all the triangles neighbouring the cell K. For the tested schemes, we used the biharmonic coefficient defined in Table 4. Our coefficients are much higher than found in literature (Tomita et al., 2001; Danilov et al., 2017; Majewski et al., 2002; Jablonowski and Williamson, 2011), however both A- and B-grid schemes differ in their discretization and the A-grid scheme is found susceptible to numerical oscillations depending on the choice of grid (Tomita et al., 2001). Therefore, by choosing an intense coefficient, we guarantee that numerical waves will not participate in the comparison of our results.

All schemes will then be evaluated. Firstly, we provide an accuracy analysis of the integrated height and vector velocity fields (Section 4.1). Then, we evaluate the linear mode analysis of our schemes (Section 4.2). Thirdly, we evaluate the scheme's capacity in maintaining its geostrophic balance (Section 4.3). Finally, we evaluate the behaviour of each scheme under a barotropic instability, which is an initial condition that accentuate the nonlinear terms of our schemes (Section 4.4).

4.1. Time integrated accuracy of variables

Our results demonstrate that both A- and B-grid schemes exhibit improvements in accuracy close to second order for both norms of the height field variable (Figure 6). However, for the vector velocity field, the values differ. For L_∞, A-grid is shown to converge near second order, while B-grid, which displays a near second order convergence for coarser grids (up until g_5), only shows a first order for the finer grids. Nevertheless, on L_2, both schemes are shown to display an accuracy increase near second order.

Regarding both C-grid schemes, both of them face problems on increasing their accuracy on L_∞. MPAS does not converge on the height scalar field, but does display a first order convergence rate on L_2. Concerning the vector velocity field on L_∞, MPAS shows a seconder order rate for coarser grids (up until g_6), but decrease to first order in finer grids. However, on L_2, MPAS displays a second order rate consistently for all refinements. This result was also observed in

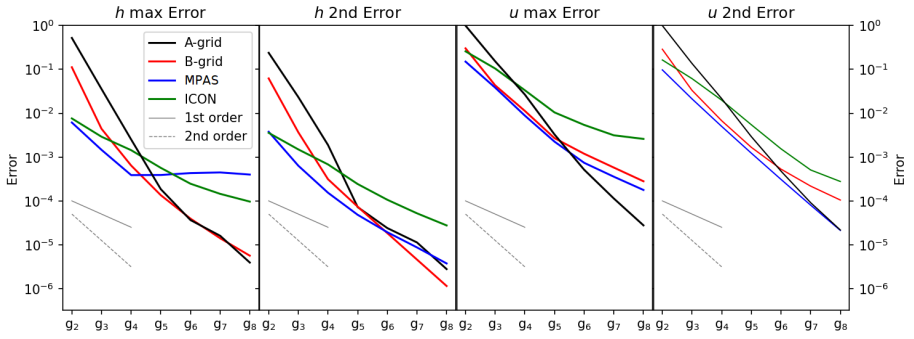

Figure 6: h and u error after 15 days.

Peixoto (2016), and it is suggested that either the kinetic energy approximation or the divergence, might be responsible for reducing the solution's accuracy.

In contrast, ICON displays a first order convergence rate on both norms for the height scalar field. Nevertheless, the scheme does not seem to convergence on the vector velocity field for the L_∞ norm. In the case of L_2, it displays, for coarser grids, a second order accuracy rate, but from g_7 to g_8 it slows down to a first order rate. Similar to MPAS, some operators, face challenges in converging the solution. In this scheme, the divergence, vorticity, and the perpendicular velocity do not display a convergence of the solution. It is noted that both vorticity and perpendicular velocity are critical components of the Coriolis Term of (1b), potentially impacting the convergence of the vector velocity field. Korn and Linardakis (2018) did not observe the same results. Therefore, it is likely that the grid choice is crucial for obtaining convergence on the fields.

Overall, A- and B-grid display similar errors, specially, in the height field. ICON's scheme have showed the largest errors of the tested schemes, except in the height field L_∞, where MPAS did not converge. B-grid show the second-largest magnitude error, only on the vector velocity field. This is likely due to the use of the biharmonic and the notably due to the gradient operator that is defined on triangles, unlike both A-grid and MPAS, which shows similar magnitudes on L_2. On L_∞, however, MPAS shows a larger error and lower convergence rate, in comparison to the A-grid, likely due to the aforementioned challenges.

4.2. Linear Normal Modes

The earth's ocean behaviour is modulated by oscillations that are mostly affected by the earth's rotation. The complete nonlinear equations are difficult to analyse to the high degree of interactions between these oscillations. However, linear analysis can be done by considering (1) the following approximations:

$$\begin{aligned} h &= H\nabla \cdot \mathbf{u} \\ \mathbf{u} &= -\nabla h - f\mathbf{u}^{\perp}, \end{aligned} \tag{24}$$

where H is a fixed constant. This system still provides a large set of inertia-gravity waves present in either the ocean or atmosphere. In order to calculate the normal modes, we follow the methodology of Weller et al. (2012) by considering a vector $(\mathbf{h}, \mathbf{u}')^T$, where both elements, i.e. $\mathbf{h}$ and $\mathbf{u}$, are scalars, so that we have $(\mathbf{h}, \mathbf{u}')^T = [h_1, h_2, \cdots, h_M, u_1, u_2, \cdots, u_N]$ for M and N elements of height and velocity fields, respectively. In the case of A- and B-grid, the scalar velocity is obtained by decomposing them into zonal and meridional velocity scalars, whereas for both C-grid schemes these scalar fields are obtained directly from the velocity on the edges of the grid.

We run (24) $M + N$ times for one timestep of $\Delta t = 10$ seconds on a g_2 grid, with the RK4. The initial conditions used are defined by a unit value on the j-th position of $(\mathbf{h}, \mathbf{u}')^T$, i.e. for the k-th run the initial condition is defined as $(\mathbf{h}_0, \mathbf{u}'_0)^T_k = [\delta^k_j]$, where δ^k_j is the Kronecker delta. We use as parameters: $gH = 10^5$ m^{2}s^{-2}, $f = 1.4584 \times 10^{-4}$ s^{-1} and the radius of the earth $a = 6.371 \times 10^6$.

From these runs, we create a matrix A, where each column is the approximated solution of the initial condition provided. We, then, can calculate the eigenvalues λ of the matrix and, consequently, obtain the frequency of the modes from $\lambda = \alpha e^{i\omega\Delta t}$, where ω is the frequency of the normal modes. We, then, order our results from lowest to maximum frequency. We will have 486 eigenvalues for the A-grid, 642 for both B-grid and MPAS, and 800 for ICON. These values correspond to the total degrees of freedom of our system. There are, in the g_2 grid, 162 vertices, 480 edges, and 320 triangles. For the A-grid, since both mass and vector fields are defined at the vertices, the total DOFs are three times the vertices. In the case of the B-grid, the vector field is defined at the triangles, therefore the total DOFs are the vertices plus twice the triangles. For both C-grid schemes, the vector velocity field is defined at the edges, however MPAS has the mass at the vertices, while ICON has the mass defined at the triangles. In that case, MPAS DOFs are the vertex plus edge points and ICON is the triangle points plus edge points.

The normal modes can be seen in Figure 7. A clear difference is observed between frequency representation on all grids. The A-grid shows the slowest representation of inertia-gravity waves, with the maximum frequency of 1.6×10^{-3} s^{-1} s^{-1} on the 119 index. On the other hand, the B-grid scheme shows higher frequencies, with a maximum on the 167 index of around 2.6×10^{-3} s^{-1}.

In contrast, a more accurate representation is obtained by both C-grid schemes. ICON shows a similar, but slightly higher frequencies, compared to the B-grid scheme. However, the highest frequency is obtained on its tail on the 635 index of around 4.2×10^{-3} s^{-1}. Conversely, MPAS displays a more accurate representation of the modal frequency with a maximum on index 320 of around 4.2×10^{-3} s^{-1}.

Overall, our results show similar results with the traditional quadrilateral grids (Arakawa and Lamb, 1977; Randall, 1994). It is known that on these grids, the C-grid schemes represent modes more accurately than the either A- or B-grid schemes, but also B-grid display a higher frequency, and a more accurate representation of inertia-gravity waves, than the A-grid schemes. We highlight

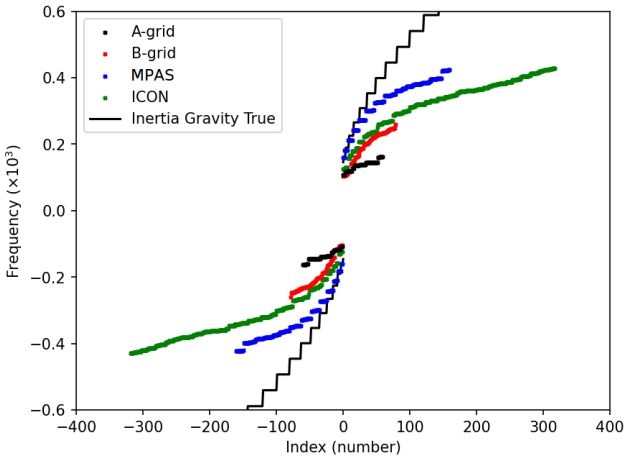

Figure 7: Linear normal modes of the considering the linear shallow water equations (24) on the f-sphere.

that the expected decrease in inertia-gravity representation from the traditional grids is not observed in our results, since we reordered our modes from least to highest frequency. Consequently, higher modes (higher wavenumbers) of both A- and B-grid schemes are not accurately displayed in our results. Despite this, our results demonstrate that the maximum represented frequency of both schemes are indeed lower than that of the C-grid schemes, following the theory.

Regarding both C-grid schemes, our results for MPAS agree with the other authors (Weller et al., 2012; Thuburn et al., 2009; Peixoto, 2016). In addition, we note that ICON's has a less accurate representation of the normal modes in comparison with on MPAS either on the quasi-hexagonal grid or its implementation on triangles (Thuburn et al., 2009). This result in ICON has already been observed (Korn and Danilov, 2017), and it is argued that the filtering property of the divergence on the mass equation might not only remove the intended noise of the triangular mesh, but also some of the higher frequency physical oscillations.

4.3. Localized Balanced Flow

An important testcase is to evaluate the model's capability of maintaining its geostrophically balanced state. Our TC1 testcase (Section 4.1), allowed us to test whether the models are capable of maintaining their state under small wavenumbers. However, a harder evaluation is to test whether the model have the ability to maintain its state under high wavenumber oscillations. For this reason, we used the testcase developed in Peixoto (2016). This test is particularly important for two main reasons: one of them is that the Perot's operator might not have steady geostrophic modes which may have consequences for the ICON model, the second reason is that both A- and B-grid are unable to

maintain their geostrophic balanced state. We evaluate, without the stabilizing term, how all models behave under this testcase.

On that account, we define the testcase as follows:

$$\begin{aligned} h &= h_0(2 - \sin^n \theta) \\ u_\phi &= \frac{-F + \sqrt{F^2 + 4C}}{2}, \end{aligned} \tag{25}$$

where h_0 is a constant, such that $gh_0 = 10^5 \mathrm{m}^2\mathrm{s}^{-2}$, and $n = 2k + 2$ for any positive k. In our particular case, $k = 160$. We also define F and C as:

$$\begin{aligned} F &= af_0 \frac{\cos\theta}{\sin\theta} \\ C &= g_0 n \sin^{n-2}(\theta)\cos^2(\theta). \end{aligned}$$

We will also consider the f-sphere with $f_0 = 1.4584 \times 10^{-4}\ \mathrm{s}^{-1}$. Finally, the grid is rotated so that the nucleus of the depression is centred at 1°E, 3°N.

The parameters used in this testcase will have a timestepping scheme and timestepping value as defined in section 4. We will also use a g_6 refinement, where there are abrupt changes on the height field in a very restrict number of cells.

Our results displayed in Figure 8 show that both A- and B-grid, without the stabilizing term, are not capable of maintaining the geostrophic balance. For the A-grid, the numerical artefacts, emanated primarily from the pentagons of the grid, destabilize the scheme leading to an exponential growth blowing up the model around the 40 hours integration. In contrast, in the case of the B-grid scheme, there was not detected the presence of fast spurious numerical oscillations. However, the detected numerical dispersion waves were capable of breaking the down the depression up until the 24 hours after the start of the simulation.

Conversely, both C-grid schemes maintain the depression throughout the 5-day period of integration. However, in ICON's case there is a small presence of a noise on the system, but it does not seem to be enough to impact the overall solution.

Overall, the solution of A- and B-grid are impacted from their numerical oscillations. Although in the work of Yu et al. (2020) the A-grid is capable of integrating for a long time, the small wavelength oscillations in this testcase, generated mostly on the pentagons of the mesh, destabilize the integration, blowing up the solution. In contrast, both C-grid schemes solutions do not display damaging oscillations on the solution. MPAS's scheme and Perot's operator on the dual grid for this testcase has been observed by Peixoto (2016) and observed the scheme accurately maintain their geostrophic state. We show are able to show that on the primal grid, ICON, with the use of Perot's formulation, is also able to represent the geostrophic balance state on small scale flows, despite the issues on accuracy of its operators on the SCVT (Section 3 and 4.1).

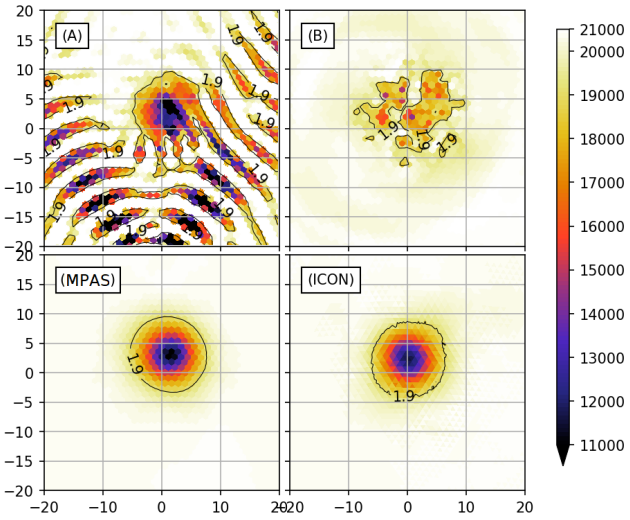

Figure 8: Height field of the different schemes for the localized balanced flow testcase without using biharmonic for both A- and B-grid schemes. Using a grid refinement g_6 and a timestep of 50s.

4.4. Barotropic Instability

Previous testcases aimed in studying the fluid flow under highly controlled experiments, in order to evaluate their accuracies, linear normal modes, and balanced state flow. However, the highly energetic and chaotic nature of the ocean require a more realistic testcase, such a fluid flow instability.

$$u = \begin{cases} \frac{u_{\max}}{e_n} \exp\left[\frac{1}{(\phi-\phi_0)(\phi-\phi_1)}\right] & \phi_0 < \phi < \phi_1 \\ 0 & (\phi-\phi_0)(\phi-\phi_1) > 0 \end{cases}$$
$$gh(\phi) = gh_0 - \int_{-\pi/2}^{\phi} au(\phi') \left[f + \frac{\tan(\phi')}{a} u(\phi')\right] d\phi'. \tag{26}$$

where $u_{\max} = 80\text{ms}^{-1}$, $\phi_0 = \pi/7$, $\phi_0 = \pi/2 - \phi_0$, $e_n = \exp[-4/(\phi_1 - \phi_0)^2]$. These initial conditions are under geostrophic balance, but with high potential for fluid instability. In order to trigger it, we add a perturbation to the height field:

$$h'(\theta, \phi) = h_{\max} e^{-(\theta/\alpha)^2} e^{-[(\phi_2 - \phi)/\beta]^2} \cos\phi, \tag{27}$$

where $\phi_2 = \pi/4$, $\alpha = 1/3$, $\beta = 1/15$, and $h_{\max} = 120$ m. All schemes are tested on a g_7 refinement with a timestep of 50 seconds under a RK4 timestepping scheme. In order to avoid the instability, we use a hyperviscosity coefficient of 5×10^{15} and 2×10^{15}, for both A- and B-grid, respectively. These choices of coefficients are in agreement with Tomita and Satoh (2004). We also found that smaller values of these coefficients of each scheme would lead to instability for the A-grid and the appearance of near grid scale oscillations in the B-grid.

The potential vorticity, on the sixth day of integration (Figure 9), display the behaviour of the growth of the instability on all the evaluated schemes. Between these schemes, it is observed a clear difference in the representation of the smaller scale features of the instability. Both A-grid and B-grid schemes displays no small scale oscillations present within the vorticity field. Additionally, it is evident that both schemes display slightly coarser features in representing the state of the fields.

Similarly, in both C-grid schemes, we observe more small scale features in this system, helping could potentially aid in the growth of the instability even if no perturbation was added. However, it is evident that in these schemes, near-grid scale oscillations play a role in the physical solutions of the integration. Comparing both C-grid schemes, both schemes seem equally contaminated by numerical noise, however, the small scale oscillations in MPAS display a higher wavenumber than the ICON scheme. MPAS's noise in the vorticity was discussed and argued that the chequerboard noise of the vorticity is the main culprit in the manifestation of this contamination in our physical simulations (Peixoto, 2016). Likewise, we also know that the Perot's operator on the dual grid is capable of manifesting numerical noises on the solutions. Since ICON's divergence operator has the potential to remove small scale oscillations, but the scheme does manifest spurious waves, which was also observed in Korn and Linardakis (2018), therefore, the Perot's dual operator is potentially the main responsible for this manifestation.

Overall, all schemes suffer from the grid scale computational modes. There is, however, the stabilization term for both A- and B-grid schemes, such that the schemes remain stable throughout the integration. Despite both C-grid schemes remaining stable throughout the integration, the solutions are contaminated with noise, that will inevitably require a smoothing term, such as the biharmonic, in order to remove these high wavenumber waves. Additionally, It is observed that the waves from the A-grid to the C-grid schemes, an apparent increase in the effective resolution of the computation, agreeing with the previous results in Section 4.2. Following this result, we analyse the kinetic spectrum of these schemes.

4.4.1. Kinetic Energy Spectrum

The global kinetic energy spectrum, is a useful tool in evaluating the energy cascade of the fluid. On different scales of the ocean's motion, we observe a power law of k^{-3} for larger scales or $k^{-5/3}$ for smaller scales (Wang et al., 2019). For the 2D case, the former is related to the turbulence of the flow, whereas the latter is related to the reverse energy cascade turbulence. These spectral fluxes provide useful insight into the performance of the models in transferring energy motion between different scales.

Therefore, we define the Kinetic Energy Spectrum as follows:

$$(E_K)_n = \frac{a^2}{4n(n+1)} \left[|\zeta_n^0|^2 + |\delta_n^0|^2 + 2 \sum_{m=1}^{M} \left(|\zeta_n^m|^2 + |\delta_n^m|^2 \right) \right], \tag{28}$$

where ζ_n^m, δ_n^m are the spectral coefficient of the vorticity and divergence. These coefficients are defined as:

$$\psi_n^m = \int_{-1}^{1} \frac{1}{2\pi} \mathcal{F}(\psi(\phi,\theta),\phi)\overline{P_n^m}(\theta)d\theta, \tag{29}$$

where ψ is the variable to be transformed, $\mathcal{F}(\psi(\phi,\theta),\phi)$ is the Fourier Transform on this variable, and $\overline{P_n^m}(\theta)$ is the normalized associate Legendre polynomial. To evaluate these equations, we use the nearest neighbour to interpolate the original unstructured grid into a quadrilateral grid of 10 km resolution on the equator with the nearest neighbour method.

The energy spectrum of the schemes is shown on Figure 10. From the test-case, a small decrease of the spectrum from the wavenumber 1 to 4, and subsequently an increase, reaching a maximum at the wavenumber 6. Afterwards there is a constant decrease of the spectrum with a slope near k^{-3} for all grids. At approximately wavenumber 80, the A-grid scheme has a considerable loss of its power, decreasing more rapidly. Similarly, at wavenumber 90 the B-grid scheme also displays this rapidly loss of energy. With slight higher wavenumber, both A- and B-grid slows its slope until the last evaluated wavenumber.

Comparably, both C-grid schemes extend the physical slope of k^{-3} up to the wavenumber 300. At this wavenumber, ICON display a similar loss of kinetic energy, whereas MPAS maintain a similar slope up to the end of the evaluated wavenumbers.

In summary, we have shown that for smaller wavenumbers there is a good agreement between the models. Additionally, we also have shown that even for the nonlinear time integration of the shallow water system of equations, the schemes behave similar to the linear normal mode analysis, with A-grid having the coarsest effective resolution, and MPAS, on the other extreme, having the highest effective resolution. Additionally, the presence of a slow-down of the loss of the power or even an increase of the spectrum on the highest wavenumbers is likely related to the impact of the interpolation to cause this increase, as it was previously reported in other works (Wang et al., 2019; Rípodas et al., 2009; Juricke et al., 2023).

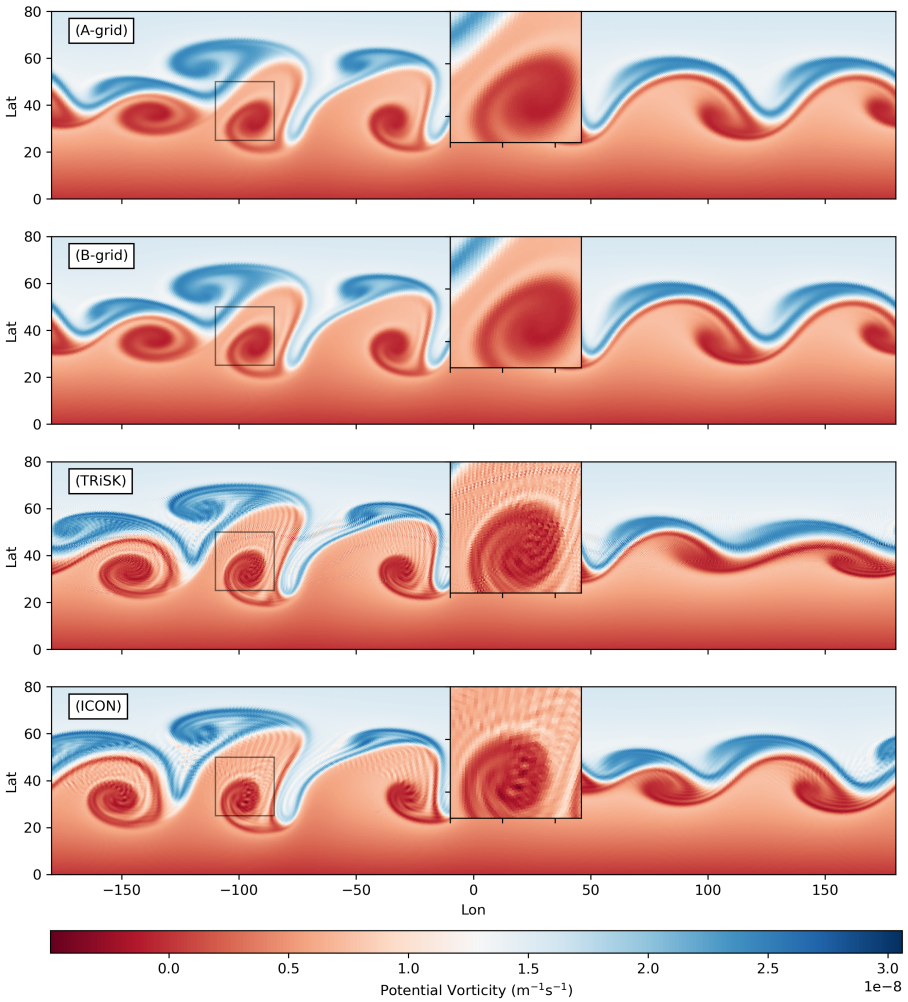

Figure 9: Potential Vorticity of all schemes on the 6th day of integration for the barotropic instability testcase with perturbation using a g_7 refinement grid and a respective biharmonic for A- and B-grid schemes, following Table 4.

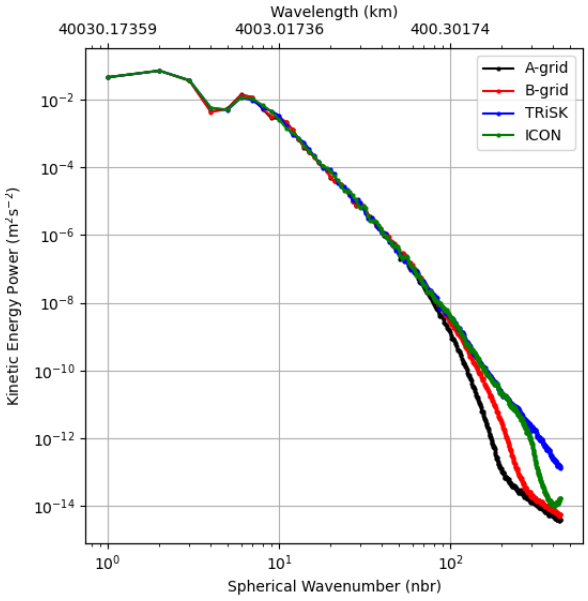

Figure 10: Kinetic energy spectra for the Barotropic instability testcase for all schemes as in Figure 9.

4.5. Models Stability

Our previous results were able to show elementary characteristics of each of the shallow water schemes. Some of our results required the inclusion of a stabilizing term for both A- and B- grid schemes, in order to remove damaging numerical oscillations that participated in the dynamics. Although the same term was not used in the C-grid scheme in our simulations, it is desired to include some sort of filtering, as the simulations may contain numerical waves that could either damage the solution or cause a potential *blow up* of the model.

One particular cause of numerical dispersion is associated with 3D energy-enstrophy conserving models, regardless of the staggering used. The imbalance between the Coriolis and kinetic energy term generates numerical noise, causing near grid-scale oscillations and decreasing the kinetic energy of jets (Hollingsworth et al., 1983). This instability, known as Hollingsworth Instability, also manifests as a destabilized inertia-gravity wave, leading to a blow up of the solution depending on the models' resolution and distortion of the mesh (Bell et al., 2017; Peixoto et al., 2018). Recent ocean models, such as NEMO's model, have shown susceptibility to these oscillations, producing spurious energy transfer to the internal gravity-waves and dissipation, resulting in corruption of mesoscale currents and submesoscale structures (Ducousso et al., 2017).

Although this instability is 3D in nature, it is possible to mimic it, by considering the ocean model as a layered model, where the vertical flow is associated with one of the thin layers of the ocean (Bell et al., 2017). This can be done by assuming the ocean model is hydrostatic and under a Bousinesq approximation (assumptions made by all ocean models evaluated in this work). In that case, one of the layers, henceforth equivalent depth H, if unstable, will display a strong noise on the horizontal velocity, and, thus, can be analysed with the shallow water equations.

4.5.1. 2D stability Analysis

In order to examine the instability, we analyse the models under a nonlinear geostrophic testcase, similar to TC1. In this testcase, however, we consider the bathymetry as driving the geostrophic balance. The mass height field will be constant and small to mimic the equivalent depth of the internal modes of the 3D model, as done by Bell et al. (2017), and Peixoto et al. (2018). Furthermore, we apply a linear analysis using the power method (Peixoto et al., 2018):

$$\mathbf{x}^{(k+1)} = \alpha_{k+1}\mathbf{r}^{(k+1)} + \overline{\mathbf{x}}, \tag{30}$$

where $\alpha^{(k+1)} = \epsilon/|\mathbf{r}^{(k+1)}|$, $\epsilon = 10^{-5}$ is a small constant, $\overline{\mathbf{x}}$ is the model state under geostrophic balance, $\mathbf{r}^{(k+1)} = \mathbf{x}^* - \overline{\mathbf{x}}$ is the perturbation, $\mathbf{x}^* = \mathbf{G}(x^k) + \mathbf{F}$, $\mathbf{G}(x^k)$ is the model evolution operator, and $\mathbf{F} = \overline{\mathbf{x}} - \mathbf{G}(\overline{\mathbf{x}})$ is a constant forcing. The methods converge, when $\alpha^k \rightarrow^k \alpha$ is found for large enough k. The eigenvalue is then obtained as $\lambda = 1/\alpha$. From there we can compute the E-folding timescale from the growth rate $\nu = \log\lambda/\Delta t$, where Δt is the timestep. We will use, a timestep of 200 seconds.

Ranging from an equivalent depth from 10^{-3} to 100 m we observe a substantial difference between the stability of the evaluated schemes (Figure 11). B-grid and ICON show similar e-folding time at around 0.1 and 0.2 days from the shallowest depth up to 1 m. Larger thickness display a stabilization of both schemes. B-grid, in this case, display a faster stabilization than ICON, whose e-folding time remain below 1 day for the 200 m, whilst B-grid show over 2 days e-folding time for the same thickness.

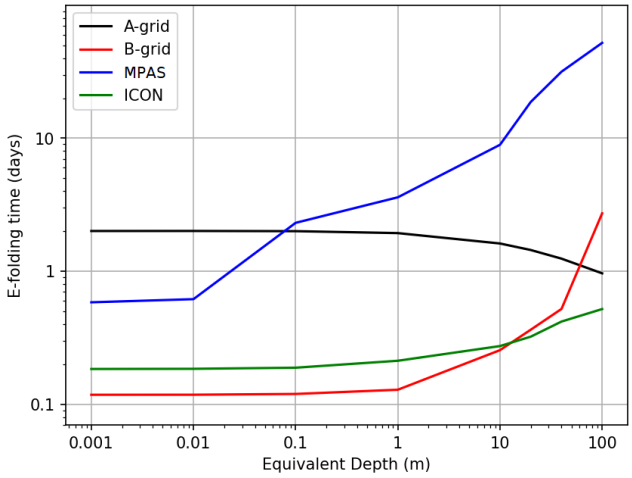

Figure 11: E-folding time for the different evaluated schemes, considering a time-step of 200 s in a geostrophic test case where the balanced state is given by the bathymetry, while the height is given by the equivalent depth and constant.

The similarities of both schemes for lower equivalent depths is potentially due to the use of triangular cells on some of their operators. However, the difference between the schemes for larger depths is likely associated with the error created by the reconstruction of the velocity vector field for both Coriolis and Kinetic energy terms in ICON, amplifying the imbalance of the discretization. Additionally, in different grids, ICON is found to be more stable (Korn and Linardakis, 2018), implying that our choice of grid might be a source of a higher instability.

On the other hand, both MPAS and A-grid display overall a more stable scheme. MPAS displayed a 0.6 day e-folding time for the shallowest depths, but showed an increase, reaching around 40 days. Similarly, A-grid displays an even larger stability of around 0.2 day for the shallowest depth. However, contrary to the other schemes, the stability of the A-grid decrease with the increase of the equivalent depth. A-grid's stability loss with depth might be potentially due to different causes of instability being dominant for the equivalent depths, i.e. for shallower depths, the cause of the instability is likely the Hollingsworth Instability, while for deeper depths, the instability is caused by the excitation of spurious pressure modes.

4.5.2. Biharmonic

In order to evaluate the biharmonic effect on the stability of the models, we perform the same analysis for different viscosity coefficients, using an equivalent depth of 1 metre, and a timestep of 200 seconds. For A- and B-grid schemes, we use (22) and (23), respectively. On C-grid, we use the formulation:

$$\Delta \mathbf{u} = \nabla\nabla \cdot \mathbf{u} - \nabla \times \nabla \times \mathbf{u} \approx \mathbf{grad}\ \mathbf{div}\ u - \mathbf{grad}^{\,T}\mathbf{vort}\ u,$$

where $\mathbf{grad}^{\,T}$ is the transpose gradient operator defined on the dual grid.

Our analysis, shown on Figure 12, indicates that all schemes were found to be stable for a viscosity coefficient no more than 10^{15} $\mathrm{m^4 s^{-1}}$. Individually, B-grid and ICON does not display difference in stability for a coefficient up to 10^{13} $\mathrm{m^4 s^{-1}}$. However, increasing the coefficient, shows that the B-grid has, not only a faster stabilization than ICON, but has the fastest of all evaluated schemes, reaching an e-folding time of over 10 days for a coefficient of 1×10^{14} $\mathrm{m^4 s^{-1}}$. ICON, in contrast, shows the slowest stabilization, reaching an e-folding time of 1.1 days for a coefficient of 4×10^{14} $\mathrm{m^4 s^{-1}}$.

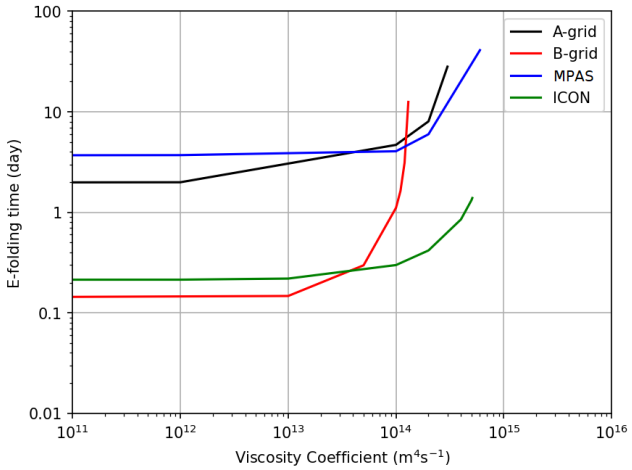

Figure 12: E-folding time by viscosity coefficient for each scheme, using a g_6 grid refinement with a timestep of 200 s and a 1 m equivalent depth.

Similarly, both A-grid and MPAS schemes display an unchanged e-folding time of up to 10^{13} $\mathrm{m^4 s^{-1}}$ and 10^{14} $\mathrm{m^4 s^{-1}}$, respectively. Additionally, A-grid is shown to stabilize faster than MPAS, reaching an e-folding time of over 20 days for a coefficient of 3×10^{14} $\mathrm{m^4 s^{-1}}$, while MPAS reaches 10 days for the same coefficient.

Overall, we see that despite B-grid showing a lower stability than all schemes, it has the potential to faster achieve stability. Conversely, although ICON obtains a similar stability as the B-grid, it requires a more intense coefficient, in order to stabilize the scheme. The similar behaviour happens with A-grid

and MPAS, with MPAS requiring a more intense coefficient for stabilization. This implies that this difficulty is on the C-grid discretization itself, and it is likely associated with either the vector reconstruction of the Coriolis term or the Kinetic Energy discretization.

5. ICON-O Model

Given the importance of the biharmonic term in order to stabilize the scheme or, at least, remove spurious computational waves in the system, we, then, aim to bridge the gap between the shallow water model and ICON's operational model. We will first acknowledge that our analysis in this section will be restricted only with ICON-O research model, and will not give light to other models mentioned in this work. However, providing results with ICON-O will be an important step towards understanding the effects of numerical oscillations on research/operational models. Additionally, our simulations presented in this section were not fine-tuned, i.e. the physical parameters and coefficients were not thoroughly calibrated, and, therefore, these simulations may not necessarily represent reality accurately. However, our discussions in this section will be restricted to analyse differences between simulations with and without the biharmonic filter, so the lack of calibration will not impact the overall analyses of the results.

The research ICON-O model, developed at the Max-Planck Institute for Meteorology, is the oceanic component of the ICON Earth System Model. It uses horizontal discretization described in the earlier sections. Vertically, it extends the triangular cells into prisms, for the use of its z coordinate levels. Additionally, In its 3D formulation, ICON-O uses the hydrostatic and Bousinesq approximations to solve its state vector $\{u, h, T, S\}$, where T and S are temperature and salinity, respectively. These tracers are also imbued with dissipative and subgrid-scale operators, such as isoneutral diffusion and the mesoscale eddy advection Gent-Mcwilliams Korn (2018). The full 3D spatial discretization will be omitted in this section, but the reader can refer to equation (32) of Korn (2017).

For its time integration, ICON-O is discretized using an Adams-Bashforth 2-step predictor-corrector scheme (equation 33, 34, and 35 of (Korn, 2017)). This scheme does not conserve neither energy nor enstrophy (Korn and Linardakis, 2018), but it also contains an implicit diffusion, allowing for more stable simulations.

Our 3D simulations were performed using an HR95 grid with a radial local refinement with the finest resolution, around 14 Km edge length, located near South Africa, and the coarsest resolution, around 80 Km edge length, on the antipode of the earth, i.e. North Pacific (Figure 13 upper panel). These locally refined mesh created enumerated distortion spots around the refined region (Figure 13 lower panel).

The model was initialized under rest with 128 layers with climatological temperature and salinity from the Polar Science Center Hydrographic Climatology (Steele et al., 2001) and was forced with the German-OMIP climatological

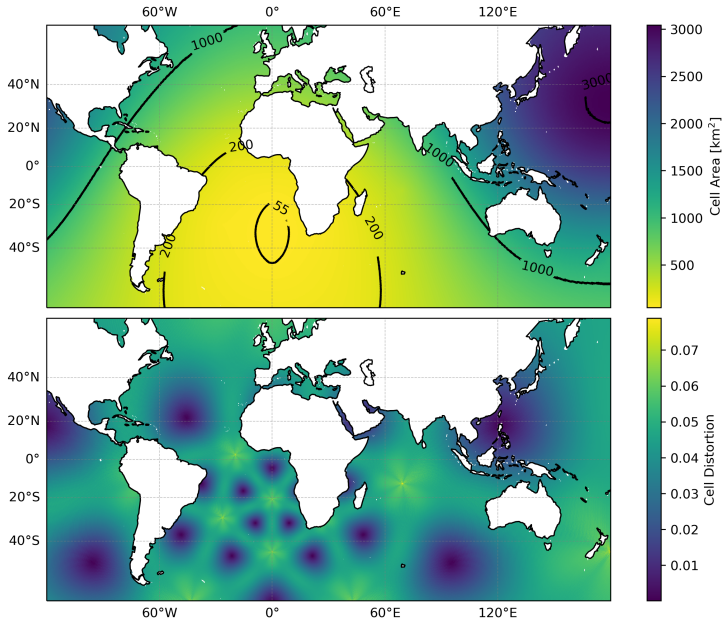

Figure 13: The upper panel is the cell area of the spherical grid used in the simulations. The lower panel is the respective cell distortion of the mesh.

forcing, which is derived from the ECMWF reanalysis 15 years dataset. This climatological forcing is daily with a resolution of 1 degree. An initial thirty years spin up was performed under these conditions utilizing a biharmonic coefficient of $2 \times 10^{-1} A_e^{3/2}$, where $A_e = |e||\hat{e}|/2$. In addition, we added a Turbulent Kinetic Energy (TKE) closure scheme, in order to parameterize the turbulent subgrid phenomena on the mesh.

Following the spin up, we, subsequently, ran 2 simulations by 10 years each. One simulated with the same parameters as the spin up, which we will coin as our reference simulation. The other was simulated without the aforementioned biharmonic filter.

The simulation without the filter show a clear decrease in the strength of the currents on the ocean system, e.g. the Gulf, Kuroshio, North Brazil, Agulhas, and Malvinas currents (Figure 14). Other regions were found to slightly increase in kinetic energy, in particular, the neighbourhood around the Agulhas Current, near the Antarctic Circumpolar Current, the Equatorial Currents of the Atlantic Ocean and both Northern and Southern of the Pacific Ocean, and the Brazil-Malvinas Confluence. The integrated kinetic energy averaged over these years show that surface kinetic energy loss of around 4.7 $\times 10^{13}$ $\mathrm{km^2 m^2 s^{-2}}$ of its 20 $\times 10^{13}$ $\mathrm{km^2 m^2 s^{-2}}$. Additionally, it is observed, in particular on regions of coarser resolution, such as the Kuroshio Current and Gulf Stream, the presence of a numerical oscillation emanating from the main currents.

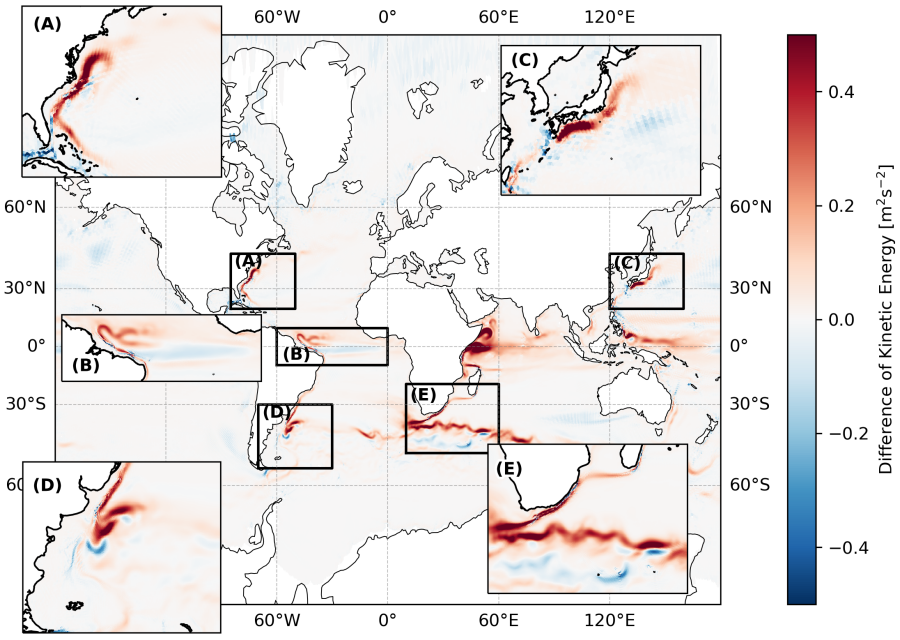

Figure 14: Kinetic Energy difference between a reference simulation and simulation without the use of biharmonic, i.e. $E_k^{(\text{ref})} - E_k^{(\text{no bih})}$.

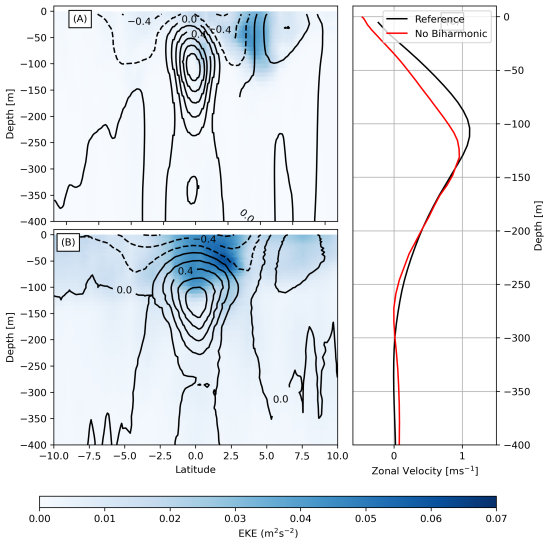

Figure 15: Cross-section of the 130°W longitude of the reference (A) and the without biharmonic (B) simulation and a vertical profile of the zonal velocity of both simulation over the 0° Latitude (C).

Following Ducousso et al. (2017), we show a similar result as that reported by the authors, in the sense that the structure of the Equatorial Undercurrent (EUC) is shown to be more deformed on the simulation without the biharmonic. Although the intensity of the EUC in our results were unchanged, the core of current narrowed vertically and moved from 125 m of depth to 100 m. According to the authors, the region is subject to barotropic and baroclinic instability, producing waves and vortices which are the main contributors to the current. Although we detect a decrease of EKE on the No Biharmonic run in the southernmost branch of the zonal current (Figure 15), we also detect an increase of the EKE over the equatorial countercurrent. Since this decrease in EKE also follows with a decrease in the strength of the core of both northern and southern branches, It is possible that this decrease in EKE is indeed related to a decrease in baroclinic instability, while the increase in EKE over the countercurrent is possibly related to numerical oscillations on the grid, which strengthens the zonal flux over this countercurrent, and, thus, deepening its core.

Other regions of the ocean also display a decrease of the EKE, most notably the Agulhas Current Retroflection, where it meets with the colder water of the South Atlantic Current and Antarctic Circumpolar Current (Figure 16). The retroflection region EKE is known to be modulated by the baroclinic instability of the Agulhas current (Zhu et al., 2018).

Additionally, the Agulhas current itself is affected by the absence of biharmonic (Figure 17). One observed difference is that the intensity of the surface current is lost. Moreover, the cross-section of the No Biharmonic simulation

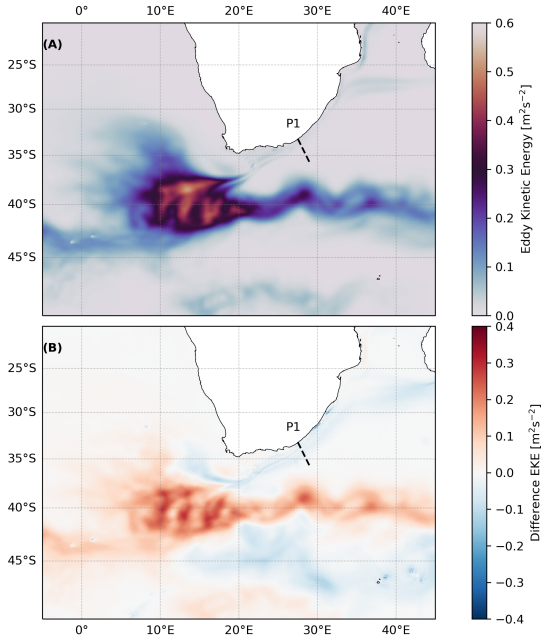

Figure 16: Eddy Kinetic Energy (A) and difference between simulations of EKE (B) of the Agulhas Current System.

shows a trail of intense EKE manifesting from the core of the Agulhas Current and propagating southwestward (Figure 17.B). These oscillations span from the surface, down to 400 m depth. It is possible that these oscillations absorbs energy from the main current system, adding to the mixing of the water and, consequently, weakening the current.

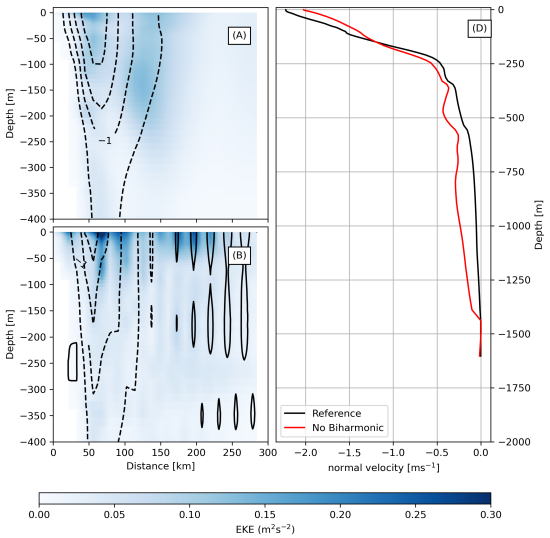

Figure 17: P1 Cross-section between the Observational data (A), Reference simulation (B), and No Biharmonic Simulation (C), and the vertical profile of the normal velocity in the 42 km distance (D).

6. Conclusions

In this work, we provided a thorough comparison analysis between different shallow water staggering schemes used in unstructured ocean models and their capability in maintaining a stable integration. Alongside, we also investigated ICON's susceptibility to such numerical instabilities in realistic 3D settings.

The shallow water analyses have shown that all models haves advantages and disadvantages. The NICAM horizontal discretization, from Tomita et al. (2001), is simple to discretize, due to its collocated approach, provides accurate representation of the operators, and presents reasonably stable integrations for complex experiments, for chosen grid optimizations, such as the SCVT. However, similar to the traditional discretization of A-grids on regular grids (Arakawa and Lamb, 1977; Randall, 1994), it displays a low effective resolution, difficulty in maintaining the geostrophic balance, and it is susceptible to the manifestation of numerical oscillations caused by the grid discretization.

Similarly, the FeSOM 2.0 horizontal discretization, from Danilov et al. (2017), also provides a quite simple discretization, accurate approximations of the operators, and a higher effective resolution compared to the A-grid. However, it also has a low effective resolution, and it displays some difficulty in maintaining the geostrophic balance. Additionally, despite not suffering from pressure modes, the B-grid scheme is found to be the least stable scheme, but as shown here and discussed by Danilov (2013), It can be easily fixed by a low coefficient of biharmonic.

Finally, both C-grid schemes, MPAS-O, from (Skamarock et al., 2012), and

ICON-O, from Korn (2017), have the most complex discretizations between the evaluated schemes. Some operators do not accurately approximate the operators of the Shallow Water system. The difficulty for MPAS-O to show convergence in the error was also discussed by Peixoto (2016). Similarly, ICON-O also displays some difficulty in converging some of the operators of the shallow water equations. The lack of convergence of the divergence operator, for example, was also shown in Korn and Linardakis (2018). For both schemes, it is argued that the issue lies in the use of the grid. Therefore, a proper choice of grid optimization should also be taken into consideration when using or using these schemes. Moreover, a dissimilarity between both schemes is seen in their stability. MPAS is shown to have a high stability, as it was discussed in (Peixoto et al., 2018), but ICON, similar to the B-grid, is shown to have a low stability and requires a larger viscosity than B-grid to stabilize the scheme.

Remarkably, in the 3D ICON-O simulation using a grid with Spring Dynamics optimization, the model was found to be stable throughout the simulated years, despite the lack of biharmonic filter. However, near grid oscillations were apparent in the grid and a contribution of these oscillations of the dynamics of the model was apparent. As it was also diagnosed by Ducousso et al. (2017) for the NEMO model, these oscillations seemed to give rise to spurious mixing of the system and also decreases the energy of the ocean's currents. Regions where its strength is derived from baroclinic instability seems more affected by these small scale oscillations. Yet, it is clear the need for further research in this topic. Though the model is stable, it can be affected by these oscillations if the coefficient is not properly adjusted. Moreover, an excess of the viscosity may also decrease the effective resolution of the model, which also is not ideal.

In conclusion, we stress that further research is necessary in order to shed more light into these schemes. We note that all schemes under the shallow water tests have shown to be robust and provide reliable results for their respective purpose. However, testing these schemes under different grids or with more realistic settings might provide greater insights into the performance of the models. Additionally, it seems evident that despite a model being stable without filters, the numerical oscillations in the model may interact with the physical waves, leading to errors or to misinterpretation of the results. It is, therefore, crucial for further investigation on this topic in order to properly make use of filters to avoid these oscillations, but also minimize the damping of physical waves.

7. Acknowledgements

We are grateful to the financial support given by the Brazilian Coordination for the Improvement of Higher Education Personnel (CAPES) PRINT project - Call no. 41/2017, Grant 88887.694523/2022-00, the São Paulo Research Foundation (FAPESP) Grant 2021/06176-0, and the Brazilian National Council for Scientific and Technological Development (CNPq), Grants 140455/2019-1 and 303436/2022-0.

References

Adcroft, A., Anderson, W., Balaji, V., Blanton, C., Bushuk, M., Dufour, C.O., Dunne, J.P., Griffies, S.M., Hallberg, R., Harrison, M.J., Held, I.M., Jansen, M.F., John, J.G., Krasting, J.P., Langenhorst, A.R., Legg, S., Liang, Z., McHugh, C., Radhakrishnan, A., Reichl, B.G., Rosati, T., Samuels, B.L., Shao, A., Stouffer, R., Winton, M., Wittenberg, A.T., Xiang, B., Zadeh, N., Zhang, R., 2019. The gfdl global ocean and sea ice model om4.0: Model description and simulation features. Journal of Advances in Modeling Earth Systems 11, 3167–3211.

Arakawa, A., Lamb, V.R., 1977. Computational design of the basic dynamical processes of the UCLA General Circulation Model, in: Chang, J. (Ed.), General Circulation Models of the Atmosphere. Elsevier. volume 17 of *Methods in Computational Physics: Advances in Research and Applications*, pp. 173–265.

Arakawa, A., Lamb, V.R., 1981. A potential enstrophy and energy conserving scheme for the shallow water equations. Monthly Weather Review 109, 18 – 36.

Bell, M.J., Peixoto, P.S., Thuburn, J., 2017. Numerical instabilities of vector-invariant momentum equations on rectangular C-grids. Quarterly Journal of the Royal Meteorological Society 143, 563–581.

Brezzi, F., Buffa, A., Manzini, G., 2014. Mimetic scalar products of discrete differential forms. Journal of Computational Physics 257, 1228–1259.

Danilov, S., 2013. Ocean modeling on unstructured meshes. Ocean Modelling 69, 195–210.

Danilov, S., 2019. On utility of triangular C-grid type discretization for numerical modeling of large-scale ocean flows. Ocean Dynamics 60, 1361–1369.

Danilov, S., Mehlmann, C., Sidorenko, D., Wang, Q., 2023. CD-type discretization for sea ice dynamics in FESOM version 2. Geoscientific Model Development Discussions 2023, 1–17.

Danilov, S., Sidorenko, D., Wang, Q., Jung, T., 2017. The Finite-volumE Sea ice–Ocean Model (FESOM2). Geoscientific Model Development 10, 765–789.

Danilov, S., Wang, Q., Timmermann, R., Iakovlev, N., Sidorenko, D., Kimmritz, M., Jung, T., Schröter, J., 2015. Finite-element sea ice model (FESIM), version 2. Geoscientific Model Development 8, 1747–1761.

Ducousso, N., Le Sommer, J., Molines, J.M., Bell, M., 2017. Impact of the "Symmetric Instability of the Computational Kind" at mesoscale- and submesoscale-permitting resolutions. Ocean Modelling 120, 18–26.

Fox-Kemper, B., Adcroft, A., Böning, C.W., Chassignet, E.P., Curchitser, E., Danabasoglu, G., Eden, C., England, M.H., Gerdes, R., Greatbatch, R.J., Griffies, S.M., Hallberg, R.W., Hanert, E., Heimbach, P., Hewitt, H.T., Hill, C.N., Komuro, Y., Legg, S., Le Sommer, J., Masina, S., Marsland, S.J., Penny, S.G., Qiao, F., Ringler, T.D., Treguier, A.M., Tsujino, H., Uotila, P., Yeager, S.G., 2019a. Challenges and prospects in ocean circulation models. Frontiers in Marine Science 6.

Fox-Kemper, B., Adcroft, A., Böning, C.W., Chassignet, E.P., Curchitser, E., Danabasoglu, G., Eden, C., England, M.H., Gerdes, R., Greatbatch, R.J., Griffies, S.M., Hallberg, R.W., Hanert, E., Heimbach, P., Hewitt, H.T., Hill, C.N., Komuro, Y., Legg, S., Le Sommer, J., Masina, S., Marsland, S.J., Penny, S.G., Qiao, F., Ringler, T.D., Treguier, A.M., Tsujino, H., Uotila, P., Yeager, S.G., 2019b. Challenges and prospects in ocean circulation models. Frontiers in Marine Science 6.

Gassmann, A., 2011. Inspection of hexagonal and triangular c-grid discretizations of the shallow water equations. Journal of Computational Physics 230, 2706–2721.

Gill, A.E., 1982. Atmosphere-ocean dynamics. volume 30. Academic press, San Diego, Calif.

Giorgetta, M.A., Brokopf, R., Crueger, T., Esch, M., Fiedler, S., Helmert, J., Hohenegger, C., Kornblueh, L., Köhler, M., Manzini, E., Mauritsen, T., Nam, C., Raddatz, T., Rast, S., Reinert, D., Sakradzija, M., Schmidt, H., Schneck, R., Schnur, R., Silvers, L., Wan, H., Zängl, G., Stevens, B., 2018. ICON-A, the atmosphere component of the ICON Earth System Model: I. Model Description. Journal of Advances in Modeling Earth Systems 10, 1613–1637.

Gurvan, M., Bourdallé-Badie, R., Chanut, J., Clementi, E., Coward, A., Ethé, C., Iovino, D., Lea, D., Lévy, C., Lovato, T., Martin, N., Masson, S., Mocavero, S., Rousset, C., Storkey, D., Müeller, S., Nurser, G., Bell, M., Samson, G., Mathiot, P., Mele, F., Moulin, A., 2022. NEMO ocean engine.

Heikes, R., Randall, D.A., 1995. Numerical integration of the shallow-water equations on a twisted icosahedral grid. part i: Basic design and results of tests. Monthly Weather Review 123, 1862 – 1880.

Hoffman, M.J., Perego, M., Price, S.F., Lipscomb, W.H., Zhang, T., Jacobsen, D., Tezaur, I., Salinger, A.G., Tuminaro, R., Bertagna, L., 2018. MPAS-Albany Land Ice (MALI): a variable-resolution ice sheet model for Earth system modeling using Voronoi grids. Geoscientific Model Development 11, 3747–3780.

Hohenegger, C., Korn, P., Linardakis, L., Redler, R., Schnur, R., Adamidis, P., Bao, J., Bastin, S., Behravesh, M., Bergemann, M., Biercamp, J., Bockelmann, H., Brokopf, R., Brüggemann, N., Casaroli, L., Chegini, F., Datseris, G., Esch, M., George, G., Giorgetta, M., Gutjahr, O., Haak, H., Hanke,

M., Ilyina, T., Jahns, T., Jungclaus, J., Kern, M., Klocke, D., Kluft, L., Kölling, T., Kornblueh, L., Kosukhin, S., Kroll, C., Lee, J., Mauritsen, T., Mehlmann, C., Mieslinger, T., Naumann, A.K., Paccini, L., Peinado, A., Praturi, D.S., Putrasahan, D., Rast, S., Riddick, T., Roeber, N., Schmidt, H., Schulzweida, U., Schütte, F., Segura, H., Shevchenko, R., Singh, V., Specht, M., Stephan, C.C., von Storch, J.S., Vogel, R., Wengel, C., Winkler, M., Ziemen, F., Marotzke, J., Stevens, B., 2023. ICON-Sapphire: simulating the components of the Earth system and their interactions at kilometer and subkilometer scales. Geoscientific Model Development 16, 779–811.

Hollingsworth, A., Kållberg, P., Renner, V., Burridge, D.M., 1983. An internal symmetric computational instability. Quarterly Journal of the Royal Meteorological Society 109, 417–428.

Jablonowski, C., Williamson, D.L., 2011. The Pros and Cons of Diffusion, Filters and Fixers in Atmospheric General Circulation Models. Springer Berlin Heidelberg, Berlin, Heidelberg. pp. 381–493.

Jungclaus, J.H., Lorenz, S.J., Schmidt, H., Brovkin, V., Brüggemann, N., Chegini, F., Crüger, T., De-Vrese, P., Gayler, V., Giorgetta, M.A., Gutjahr, O., Haak, H., Hagemann, S., Hanke, M., Ilyina, T., Korn, P., Kröger, J., Linardakis, L., Mehlmann, C., Mikolajewicz, U., Müller, W.A., Nabel, J.E.M.S., Notz, D., Pohlmann, H., Putrasahan, D.A., Raddatz, T., Ramme, L., Redler, R., Reick, C.H., Riddick, T., Sam, T., Schneck, R., Schnur, R., Schupfner, M., von Storch, J.S., Wachsmann, F., Wieners, K.H., Ziemen, F., Stevens, B., Marotzke, J., Claussen, M., 2022. The ICON Earth System Model Version 1.0. Journal of Advances in Modeling Earth Systems 14.

Juricke, S., Bellinghausen, K., Danilov, S., Kutsenko, A., Oliver, M., 2023. Scale analysis on unstructured grids: Kinetic energy and dissipation power spectra on triangular meshes. Journal of Advances in Modeling Earth Systems 15.

Korn, P., 2017. Formulation of an unstructured grid model for global ocean dynamics. Journal of Computational Physics 339, 525–552.

Korn, P., 2018. A structure-preserving discretization of ocean parametrizations on unstructured grids. Ocean Modelling 132, 73–90.

Korn, P., Danilov, S., 2017. Elementary dispersion analysis of some mimetic discretizations on triangular C-grids. Journal of Computational Physics 330, 156–172.

Korn, P., Linardakis, L., 2018. A conservative discretization of the shallow-water equations on triangular grids. Journal of Computational Physics 375, 871–900.

Le Roux, D., Sène, A., Rostand, V., Hanert, E., 2005. On some spurious mode issues in shallow-water models using a linear algebra approach. Ocean Modelling 10, 83–94.

Majewski, D., Liermann, D., Prohl, P., Ritter, B., Buchhold, M., Hanisch, T., Paul, G., Wergen, W., Baumgardner, J., 2002. The operational global icosahedral–hexagonal gridpoint model gme: Description and high-resolution tests. Monthly Weather Review 130, 319 – 338.

Miura, H., Kimoto, M., 2005. A comparison of grid quality of optimized spherical hexagonal–pentagonal geodesic grids. Monthly Weather Review 133, 2817 – 2833.

Miyamoto, Y., Kajikawa, Y., Yoshida, R., Yamaura, T., Yashiro, H., Tomita, H., 2013. Deep moist atmospheric convection in a subkilometer global simulation. Geophysical Research Letters 40, 4922–4926.

Peixoto, P.S., 2016. Accuracy analysis of mimetic finite volume operators on geodesic grids and a consistent alternative. Journal of Computational Physics 310, 127–160.

Peixoto, P.S., Thuburn, J., Bell, M.J., 2018. Numerical instabilities of spherical shallow-water models considering small equivalent depths. Quarterly Journal of the Royal Meteorological Society 144, 156–171.

Perot, B., 2000. Conservation properties of unstructured staggered mesh schemes. Journal of Computational Physics 159, 58–89.

Randall, D.A., 1994. Geostrophic adjustment and the finite-difference shallow-water equations. Monthly Weather Review 122, 1371 – 1377.

Randall, D.A., Bitz, C.M., Danabasoglu, G., Denning, A.S., Gent, P.R., Gettelman, A., Griffies, S.M., Lynch, P., Morrison, H., Pincus, R., Thuburn, J., 2018. 100 years of earth system model development. Meteorological Monographs 59, 12.1 – 12.66.

Ringler, T., Petersen, M., Higdon, R.L., Jacobsen, D., Jones, P.W., Maltrud, M., 2013. A multi-resolution approach to global ocean modeling. Ocean Modelling 69, 211–232.

Ringler, T., Thuburn, J., Klemp, J., Skamarock, W., 2010. A unified approach to energy conservation and potential vorticity dynamics for arbitrarily-structured C-grids. Journal of Computational Physics 229, 3065–3090.

Rípodas, P., Gassmann, A., Förstner, J., Majewski, D., Giorgetta, M., Korn, P., Kornblueh, L., Wan, H., Zängl, G., Bonaventura, L., Heinze, T., 2009. Icosahedral Shallow Water Model (ICOSWM): results of shallow water test cases and sensitivity to model parameters. Geoscientific Model Development 2, 231–251.

Sadourny, R., 1972. Conservative finite-difference approximations of the primitive equations on quasi-uniform spherical grids. Monthly Weather Review 100, 136 – 144.

Scholz, P., Sidorenko, D., Gurses, O., Danilov, S., Koldunov, N., Wang, Q., Sein, D., Smolentseva, M., Rakowsky, N., Jung, T., 2019. Assessment of the finite-volume sea ice-ocean model (fesom2.0) – part 1: Description of selected key model elements and comparison to its predecessor version. Geoscientific Model Development 12, 4875–4899.

Skamarock, W.C., Klemp, J.B., Duda, M.G., Fowler, L.D., Park, S.H., Ringler, T.D., 2012. A multiscale nonhydrostatic atmospheric model using centroidal voronoi tesselations and c-grid staggering. Monthly Weather Review 140, 3090 – 3105.

Staniforth, A., Thuburn, J., 2012. Horizontal grids for global weather and climate prediction models: a review. Quarterly Journal of the Royal Meteorological Society 138, 1–26.

Steele, M., Morley, R., Ermold, W., 2001. PHC: A global ocean hydrography with a high-quality Arctic Ocean. Journal of Climate 14, 2079 – 2087.

Thuburn, J., 2008. Numerical wave propagation on the hexagonal C-grid. Journal of Computational Physics 227, 5836–5858.

Thuburn, J., Ringler, T., Skamarock, W., Klemp, J., 2009. Numerical representation of geostrophic modes on arbitrarily structured C-grids. Journal of Computational Physics 228, 8321–8335.

Tomita, H., Satoh, M., 2004. A new dynamical framework of nonhydrostatic global model using the icosahedral grid. Fluid Dynamics Research 34, 357.

Tomita, H., Tsugawa, M., Satoh, M., Goto, K., 2001. Shallow water model on a modified icosahedral geodesic grid by using spring dynamics. Journal of Computational Physics 174, 579–613.

Turner, A.K., Lipscomb, W.H., Hunke, E.C., Jacobsen, D.W., Jeffery, N., Engwirda, D., Ringler, T.D., Wolfe, J.D., 2022. MPAS-Seaice (v1.0.0): sea-ice dynamics on unstructured Voronoi meshes. Geoscientific Model Development 15, 3721–3751.

Wang, L., Zhang, Y., Li, J., Liu, Z., Zhou, Y., 2019. Understanding the performance of an unstructured-mesh global shallow water model on kinetic energy spectra and nonlinear vorticity dynamics. Journal of Meteorological Research 33, 2198–0934.

Wang, Q., Danilov, S., Schröter, J., 2008. Finite element ocean circulation model based on triangular prismatic elements, with application in studying the effect of topography representation. Journal of Geophysical Research: Oceans 113.

Weller, H., Thuburn, J., Cotter, C.J., 2012. Computational modes and grid imprinting on five quasi-uniform spherical C grids. Monthly Weather Review 140, 2734 – 2755.

Williamson, D.L., Drake, J.B., Hack, J.J., Jakob, R., Swarztrauber, P.N., 1992. A standard test set for numerical approximations to the shallow water equations in spherical geometry. Journal of Computational Physics 102, 211–224.

Yu, Y.G., Wang, N., Middlecoff, J., Peixoto, P.S., Govett, M.W., 2020. Comparing numerical accuracy of icosahedral a-grid and c-grid schemes in solving the shallow-water model. Monthly Weather Review 148, 4009 – 4033.

Zhu, Y., Qiu, B., Lin, X., Wang, F., 2018. Interannual eddy kinetic energy modulations in the agulhas return current. Journal of Geophysical Research: Oceans 123, 6449–6462.

Bibliography

A. Adcroft, W. Anderson, V. Balaji, C. Blanton, M. Bushuk, C. O. Dufour, J. P. Dunne, S. M. Griffies, R. Hallberg, M. J. Harrison, I. M. Held, M. F. Jansen, J. G. John, J. P. Krasting, A. R. Langenhorst, S. Legg, Z. Liang, C. McHugh, A. Radhakrishnan, B. G. Reichl, T. Rosati, B. L. Samuels, A. Shao, R. Stouffer, M. Winton, A. T. Wittenberg, B. Xiang, N. Zadeh, and R. Zhang. The gfdl global ocean and sea ice model om4.0: Model description and simulation features. *Journal of Advances in Modeling Earth Systems*, 11 (10):3167–3211, 2019.

A. Arakawa and V. R. Lamb. Computational design of the basic dynamical processes of the ucla general circulation model. In J. CHANG, editor, *General Circulation Models of the Atmosphere*, volume 17 of *Methods in Computational Physics: Advances in Research and Applications*, pages 173 – 265. Elsevier, 1977. doi: 10.1016/B978-0-12-460817-7.50009-4.

A. Arakawa and V. R. Lamb. A potential enstrophy and energy conserving scheme for the shallow water equations. *Monthly Weather Review*, 109(1):18 – 36, 1981. doi: 10.1175/1520-0493(1981)109⟨0018:APEAEC⟩2.0.CO;2.

M. J. Bell, P. S. Peixoto, and J. Thuburn. Numerical instabilities of vector-invariant momentum equations on rectangular c-grids. *Quarterly Journal of the Royal Meteorological Society*, 143(702):563–581, 2017. doi: 10.1002/qj.2950.

G. J. Boer. Homogeneous and isotropic turbulence on the sphere. *Journal of Atmospheric Sciences*, 40(1):154 – 163, 1983. doi: 10.1175/1520-0469(1983)040⟨0154:HAITOT⟩2.0.CO;2.

F. Brezzi, A. Buffa, and G. Manzini. Mimetic scalar products of discrete differential forms. *Journal of Computational Physics*, 257:1228–1259, 2014. ISSN 0021-9991. doi: 10.1016/j.jcp.2013.08.017. Physics-compatible numerical methods.

K. Bryan. A numerical investigation of a nonlinear model of a wind-driven ocean. *Journal of Atmospheric Sciences*, 20(6):594 – 606, 1963.

K. Bryan and M. D. Cox. A numerical investigation of the oceanic general circulation. *Tellus*, 19(1):54–80, 1967. doi: 10.1111/j.2153-3490.1967.tb01459.x.

J. A. Carton, B. S. Giese, and S. A. Grodsky. Sea level rise and the warming of the oceans in the simple ocean data assimilation (soda) ocean reanalysis. *Journal of Geophysical Research: Oceans*, 110(C9), 2005. doi: 10.1029/2004JC002817.

J. G. Charney, R. FjÖrtoft, and J. V. Neumann. Numerical integration of the barotropic vorticity equation. *Tellus*, 2(4):237–254, 1950. doi: 10.3402/tellusa.v2i4.8607.

J. A. Church and N. J. White. A 20th century acceleration in global sea-level rise. *Geophysical Research Letters*, 33(1), 2006. doi: 10.1029/2005GL024826.

R. Courant, K. Friedrichs, and H. Lewy. Uber die partiellen differenzengleichungen der mathematischen physik. *Mathematische Annalen*, 100, 1928. ISSN 1432-1807. doi: 10.1007/BF01448839.

R. Courant, K. Friedrichs, and H. Lewy. On the partial difference equations of mathematical physics. *IBM Journal of Research and Development*, 11(2):215–234, March 1967. ISSN 0018-8646. doi: 10.1147/rd.112.0215.

K. Cowtan, Z. Hausfather, E. Hawkins, P. Jacobs, M. E. Mann, S. K. Miller, B. A. Steinman, M. B. Stolpe, and R. G. Way. Robust comparison of climate models with observations using blended land air and ocean sea surface temperatures. *Geophysical Research Letters*, 42(15):6526–6534, 2015. doi: 10.1002/2015GL064888.

L. B. da Veiga, K. Lipnikov, and G. Manzini. *The mimetic finite difference method for elliptic problems*, volume 11. Springer, 2014.

S. Danilov. Ocean modeling on unstructured meshes. *Ocean Modelling*, 69:195–210, 2013. doi: 10.1016/j.ocemod.2013.05.005.

S. Danilov. On utility of triangular c-grid type discretization for numerical modeling of large-scale ocean flows. *Ocean Dynamics*, 60:1361–1369, 2019. doi: 10.1007/s10236-010-0339-6.

S. Danilov, Q. Wang, R. Timmermann, N. Iakovlev, D. Sidorenko, M. Kimmritz, T. Jung, and J. Schröter. Finite-element sea ice model (fesim), version 2. *Geoscientific Model Development*, 8(6):1747–1761, 2015. doi: 10.5194/gmd-8-1747-2015.

S. Danilov, D. Sidorenko, Q. Wang, and T. Jung. The finite-volume sea ice–ocean model (fesom2). *Geoscientific Model Development*, 10(2):765–789, 2017. doi: 10.5194/gmd-10-765-2017.

S. Danilov, C. Mehlmann, D. Sidorenko, and Q. Wang. Cd-type discretization for sea ice dynamics in fesom version 2. *Geoscientific Model Development Discussions*, 2023: 1–17, 2023. doi: 10.5194/gmd-2023-37. URL `https://gmd.copernicus.org/preprints/gmd-2023-37/`.

N. Ducousso, J. Le Sommer, J.-M. Molines, and M. Bell. Impact of the "symmetric instability of the computational kind" at mesoscale- and submesoscale-permitting resolutions. *Ocean Modelling*, 120:18–26, 2017. ISSN 1463-5003. doi: 10.1016/j.ocemod.2017.10.006.

J. K. Dukowicz. Mesh effects for rossby waves. *Journal of Computational Physics*, 119(1): 188–194, 1995. ISSN 0021-9991. doi: 10.1006/jcph.1995.1126.

D. Engwirda. *Locally optimal Delaunay-refinement and optimisation-based mesh generation*. Doctor of philosophy ph.d., School of Mathematics and Statistics, 2014.

B. Fox-Kemper, A. Adcroft, C. W. Böning, E. P. Chassignet, E. Curchitser, G. Danabasoglu, C. Eden, M. H. England, R. Gerdes, R. J. Greatbatch, S. M. Griffies, R. W. Hallberg, E. Hanert, P. Heimbach, H. T. Hewitt, C. N. Hill, Y. Komuro, S. Legg, J. Le Sommer,

S. Masina, S. J. Marsland, S. G. Penny, F. Qiao, T. D. Ringler, A. M. Treguier, H. Tsujino, P. Uotila, and S. G. Yeager. Challenges and prospects in ocean circulation models. *Frontiers in Marine Science*, 6, 2019. ISSN 2296-7745. doi: 10.3389/fmars.2019.00065.

A. Gassmann. Inspection of hexagonal and triangular c-grid discretizations of the shallow water equations. *Journal of Computational Physics*, 230(7):2706 – 2721, 2011. ISSN 0021-9991. doi: 10.1016/j.jcp.2011.01.014.

A. Gassmann. A global hexagonal c-grid non-hydrostatic dynamical core (icon-iap) designed for energetic consistency. *Quarterly Journal of the Royal Meteorological Society*, 139(670): 152–175, 2013. doi: 10.1002/qj.1960.

A. Gassmann. Discretization of generalized coriolis and friction terms on the deformed hexagonal c-grid. *Quarterly Journal of the Royal Meteorological Society*, 144(716):2038–2053, 2018. doi: 10.1002/qj.3294.

A. E. Gill. *Atmosphere-ocean dynamics*, volume 30. Academic press, San Diego, Calif, 1982.

M. A. Giorgetta, R. Brokopf, T. Crueger, M. Esch, S. Fiedler, J. Helmert, C. Hohenegger, L. Kornblueh, M. Köhler, E. Manzini, T. Mauritsen, C. Nam, T. Raddatz, S. Rast, D. Reinert, M. Sakradzija, H. Schmidt, R. Schneck, R. Schnur, L. Silvers, H. Wan, G. Zängl, and B. Stevens. Icon-a, the atmosphere component of the icon earth system model: I. model description. *Journal of Advances in Modeling Earth Systems*, 10(7):1613–1637, 2018. doi: 10.1029/2017MS001242.

M. Gurvan, R. Bourdallé-Badie, J. Chanut, E. Clementi, A. Coward, C. Ethé, D. Iovino, D. Lea, C. Lévy, T. Lovato, N. Martin, S. Masson, S. Mocavero, C. Rousset, D. Storkey, S. Müeller, G. Nurser, M. Bell, G. Samson, P. Mathiot, F. Mele, and A. Moulin. Nemo ocean engine, 2022.

Z. Hausfather, H. F. Drake, T. Abbott, and G. A. Schmidt. Evaluating the performance of past climate model projections. *Geophysical Research Letters*, 47(1):e2019GL085378, 2020. doi: 10.1029/2019GL085378. e2019GL085378 2019GL085378.

R. Heikes and D. A. Randall. Numerical integration of the shallow-water equations on a twisted icosahedral grid. part i: Basic design and results of tests. *Monthly Weather Review*, 123(6):1862 – 1880, 1995a. doi: 10.1175/1520-0493(1995)123⟨1862:NIOTSW⟩2.0.CO;2.

R. Heikes and D. A. Randall. Numerical integration of the shallow-water equations on a twisted icosahedral grid. part ii. a detailed description of the grid and an analysis of numerical accuracy. *Monthly Weather Review*, 123(6):1881 – 1887, 1995b. doi: 10.1175/1520-0493(1995)123⟨1881:NIOTSW⟩2.0.CO;2.

M. J. Hoffman, M. Perego, S. F. Price, W. H. Lipscomb, T. Zhang, D. Jacobsen, I. Tezaur, A. G. Salinger, R. Tuminaro, and L. Bertagna. Mpas-albany land ice (mali): a variable-resolution ice sheet model for earth system modeling using voronoi grids. *Geoscientific Model Development*, 11(9):3747–3780, 2018. doi: 10.5194/gmd-11-3747-2018.

C. Hohenegger, P. Korn, L. Linardakis, R. Redler, R. Schnur, P. Adamidis, J. Bao, S. Bastin, M. Behravesh, M. Bergemann, J. Biercamp, H. Bockelmann, R. Brokopf, N. Brüggemann, L. Casaroli, F. Chegini, G. Datseris, M. Esch, G. George, M. Giorgetta, O. Gutjahr, H. Haak, M. Hanke, T. Ilyina, T. Jahns, J. Jungclaus, M. Kern, D. Klocke, L. Kluft, T. Kölling, L. Kornblueh, S. Kosukhin, C. Kroll, J. Lee, T. Mauritsen, C. Mehlmann, T. Mieslinger, A. K. Naumann, L. Paccini, A. Peinado, D. S. Praturi, D. Putrasahan, S. Rast, T. Riddick, N. Roeber, H. Schmidt, U. Schulzweida, F. Schütte, H. Segura, R. Shevchenko, V. Singh, M. Specht, C. C. Stephan, J.-S. von Storch, R. Vogel, C. Wengel, M. Winkler, F. Ziemen, J. Marotzke, and B. Stevens. Icon-sapphire: simulating the components of the earth system and their interactions at kilometer and subkilometer scales. *Geoscientific Model Development*, 16(2):779–811, 2023. doi: 10.5194/gmd-16-779-2023.

A. Hollingsworth and P. Kallberg. Spurious energy conversions in an energy/enstrophy conserving finite difference scheme. Internal Report 22, ECMWF, Shinfield Park, Reading, 1979.

A. Hollingsworth, P. Kållberg, V. Renner, and D. M. Burridge. An internal symmetric computational instability. *Quarterly Journal of the Royal Meteorological Society*, 109(460): 417–428, 1983. doi: 10.1002/qj.49710946012.

M. Hortal and A. J. Simmons. Use of reduced gaussian grids in spectral models. *Monthly Weather Review*, 119(4):1057 – 1074, 1991. doi: 10.1175/1520-0493(1991)119⟨1057:UORGGI⟩2.0.CO;2.

C. Jablonowski and D. L. Williamson. *The Pros and Cons of Diffusion, Filters and Fixers in Atmospheric General Circulation Models*, pages 381–493. Springer Berlin Heidelberg, Berlin, Heidelberg, 2011. ISBN 978-3-642-11640-7. doi: 10.1007/978-3-642-11640-7_13.

R. Jakob-Chien, J. J. Hack, and D. L. Williamson. Spectral transform solutions to the shallow water test set. *Journal of Computational Physics*, 119(1):164–187, 1995. ISSN 0021-9991. doi: 10.1006/jcph.1995.1125.

J. H. Jungclaus, S. J. Lorenz, H. Schmidt, V. Brovkin, N. Brüggemann, F. Chegini, T. Crüger, P. De-Vrese, V. Gayler, M. A. Giorgetta, O. Gutjahr, H. Haak, S. Hagemann, M. Hanke, T. Ilyina, P. Korn, J. Kröger, L. Linardakis, C. Mehlmann, U. Mikolajewicz, W. A. Müller, J. E. M. S. Nabel, D. Notz, H. Pohlmann, D. A. Putrasahan, T. Raddatz, L. Ramme, R. Redler, C. H. Reick, T. Riddick, T. Sam, R. Schneck, R. Schnur, M. Schupfner, J.-S. von Storch, F. Wachsmann, K.-H. Wieners, F. Ziemen, B. Stevens, J. Marotzke, and M. Claussen. The icon earth system model version 1.0. *Journal of Advances in Modeling Earth Systems*, 14(4), 2022. doi: 10.1029/2021MS002813.

S. Juricke, K. Bellinghausen, S. Danilov, A. Kutsenko, and M. Oliver. Scale analysis on unstructured grids: Kinetic energy and dissipation power spectra on triangular meshes. *Journal of Advances in Modeling Earth Systems*, 15(1), 2023. doi: 10.1029/2022MS003280.

Y. Kodama, T. Odajima, E. Arima, and M. Sato. Evaluation of power management control on the supercomputer fugaku. In *2020 IEEE International Conference on Cluster Computing (CLUSTER)*, pages 484–493, 2020. doi: 10.1109/CLUSTER49012.2020.00069.

C. S. Konor and D. A. Randall. Impacts of the horizontal and vertical grids on the numerical solutions of the dynamical equations – part 1: Nonhydrostatic inertia–gravity modes. *Geoscientific Model Development*, 11(5):1753–1784, 2018a. doi: 10.5194/gmd-11-1753-2018.

C. S. Konor and D. A. Randall. Impacts of the horizontal and vertical grids on the numerical solutions of the dynamical equations - Part 2: Quasi-geostrophic Rossby modes. *Geoscientific Model Development*, 11(5):1785–1797, 2018b. doi: 10.5194/gmd-11-1785-2018.

P. Korn. Formulation of an unstructured grid model for global ocean dynamics. *Journal of Computational Physics*, 339:525 – 552, 2017. ISSN 0021-9991. doi: 10.1016/j.jcp.2017.03.009.

P. Korn. A structure-preserving discretization of ocean parametrizations on unstructured grids. *Ocean Modelling*, 132:73–90, 2018. ISSN 1463-5003.

P. Korn and S. Danilov. Elementary dispersion analysis of some mimetic discretizations on triangular c-grids. *Journal of Computational Physics*, 330:156–172, 2016. ISSN 0021-9991. doi: 10.1016/j.jcp.2016.10.059.

P. Korn and L. Linardakis. A conservative discretization of the shallow-water equations on triangular grids. *Journal of Computational Physics*, 375:871 – 900, 2018. ISSN 0021-9991. doi: /10.1016/j.jcp.2018.09.002.

D. Le Roux, A. Sène, V. Rostand, and E. Hanert. On some spurious mode issues in shallow-water models using a linear algebra approach. *Ocean Modelling*, 10(1):83 – 94, 2005. ISSN 1463-5003. doi: 10.1016/j.ocemod.2004.07.008. The Second International Workshop on Unstructured Mesh Numerical Modelling of Coastal, Shelf and Ocean Flows.

D. Majewski, D. Liermann, P. Prohl, B. Ritter, M. Buchhold, T. Hanisch, G. Paul, W. Wergen, and J. Baumgardner. The operational global icosahedral–hexagonal gridpoint model gme: Description and high-resolution tests. *Monthly Weather Review*, 130(2):319 – 338, 2002. doi: 10.1175/1520-0493(2002)130⟨0319:TOGIHG⟩2.0.CO;2.

S. Manabe and K. Bryan. Climate calculations with a combined ocean-atmosphere model. *Journal of Atmospheric Sciences*, 26(4):786 – 789, 1969. doi: 10.1175/1520-0469(1969)026⟨0786:CCWACO⟩2.0.CO;2.

H. Miura and M. Kimoto. A comparison of grid quality of optimized spherical hexagonal–pentagonal geodesic grids. *Monthly Weather Review*, 133(10):2817 – 2833, 2005. doi: 10.1175/MWR2991.1.

Y. Miyamoto, Y. Kajikawa, R. Yoshida, T. Yamaura, H. Yashiro, and H. Tomita. Deep moist atmospheric convection in a subkilometer global simulation. *Geophysical Research Letters*, 40(18):4922–4926, 2013. doi: 10.1002/grl.50944.

W. Munk. On the wind-driven ocean circulation. *Journal of Atmospheric Sciences*, 7(2):80 – 93, 1950. doi: 10.1175/1520-0469(1950)007⟨0080:OTWDOC⟩2.0.CO;2.

P. Peixoto. *Analise de discretizacoes e interpolacoes em malhas icosaedricas e aplicacoes em modelos de transporte semi-lagrangianos*. PhD thesis, Universidade de Sao Paulo, 2013.

P. S. Peixoto. Accuracy analysis of mimetic finite volume operators on geodesic grids and a consistent alternative. *Journal of Computational Physics*, 310:127 – 160, 2016. ISSN 0021-9991. doi: 10.1016/j.jcp.2015.12.058.

P. S. Peixoto and S. R. Barros. Analysis of grid imprinting on geodesic spherical icosahedral grids. *Journal of Computational Physics*, 237:61 – 78, 2013. ISSN 0021-9991. doi: 10.1016/j.jcp.2012.11.041.

P. S. Peixoto, J. Thuburn, and M. J. Bell. Numerical instabilities of spherical shallow-water models considering small equivalent depths. *Quarterly Journal of the Royal Meteorological Society*, 144(710):156–171, 2018. doi: 10.1002/qj.3191.

B. Perot. Conservation properties of unstructured staggered mesh schemes. *Journal of Computational Physics*, 159(1):58–89, 2000. ISSN 0021-9991. doi: 10.1006/jcph.2000.6424.

J. B. Perot and C. Chartrand. A mimetic method for polygons. *Journal of Computational Physics*, 424:109853, 2021. ISSN 0021-9991. doi: 10.1016/j.jcp.2020.109853.

N. A. Phillips. A map projection system suitable for large-scale numerical weather prediction. *Journal of the Meteorological Society of Japan. Ser. II*, 35A:262–267, 1957.

M. K. Rajpoot, S. Bhaumik, and T. K. Sengupta. Solution of linearized rotating shallow water equations by compact schemes with different grid-staggering strategies. *Journal of Computational Physics*, 231(5):2300–2327, 2012. ISSN 0021-9991. doi: 10.1016/j.jcp.2011.11.025.

D. A. Randall. Geostrophic adjustment and the finite-difference shallow-water equations. *Monthly Weather Review*, 122(6):1371 – 1377, 1994.

D. A. Randall, C. M. Bitz, G. Danabasoglu, A. S. Denning, P. R. Gent, A. Gettelman, S. M. Griffies, P. Lynch, H. Morrison, R. Pincus, and J. Thuburn. 100 years of earth system model development. *Meteorological Monographs*, 59:12.1 – 12.66, 2018a. doi: 10.1175/AMSMONOGRAPHS-D-18-0018.1.

D. A. Randall, C. M. Bitz, G. Danabasoglu, A. S. Denning, P. R. Gent, A. Gettelman, S. M. Griffies, P. Lynch, H. Morrison, R. Pincus, and J. Thuburn. 100 years of earth system model development. *Meteorological Monographs*, 59:12.1 – 12.66, 2018b. doi: 10.1175/AMSMONOGRAPHS-D-18-0018.1.

E. Rignot and R. H. Thomas. Mass balance of polar ice sheets. *Science*, 297(5586):1502–1506, 2002. ISSN 0036-8075. doi: 10.1126/science.1073888.

T. Ringler, J. Thuburn, J. Klemp, and W. Skamarock. A unified approach to energy conservation and potential vorticity dynamics for arbitrarily-structured c-grids. *Journal of Computational Physics*, 229(9):3065 – 3090, 2010. ISSN 0021-9991. doi: 10.1016/j.jcp.2009.12.007.

T. Ringler, M. Petersen, R. L. Higdon, D. Jacobsen, P. W. Jones, and M. Maltrud. A multi-resolution approach to global ocean modeling. *Ocean Modelling*, 69:211–232, 2013. ISSN 1463-5003. doi: 10.1016/j.ocemod.2013.04.010.

T. D. Ringler and D. A. Randall. The zm grid: An alternative to the z grid. *Monthly Weather Review*, 130(5):1411 – 1422, 2002. doi: 10.1175/1520-0493(2002)130⟨1411:TZGAAT⟩2.0.CO;2.

P. Rípodas, A. Gassmann, J. Förstner, D. Majewski, M. Giorgetta, P. Korn, L. Kornblueh, H. Wan, G. Zängl, L. Bonaventura, and T. Heinze. Icosahedral shallow water model (icoswm): results of shallow water test cases and sensitivity to model parameters. *Geoscientific Model Development*, 2(2):231–251, 2009. doi: 10.5194/gmd-2-231-2009.

A. Robinson and H. Stommel. The oceanic thermocline and the associated thermohaline circulation1. *Tellus*, 11(3):295–308, 1959.

RSAS. Integrating innovation and climate with economic growth. *Royal Swedish Academy of Sciences*, 2018.

RSAS. Press release: The nobel prize in physics 2021. *Royal Swedish Academy of Sciences*, 2021.

R. M. Russell. The cray-1 computer system. *Commun. ACM*, 21(1):63–72, Jan. 1978. ISSN 0001-0782. doi: 10.1145/359327.359336.

R. Sadourny. Conservative finite-difference approximations of the primitive equations on quasi-uniform spherical grids. *Monthly Weather Review*, 100(2):136 – 144, 1972.

R. Sadourny, A. Arakawa, and Y. Mintz. Integration of the nondivergent barotropic vorticity equation with an icosahedral-hexagonal grid for the sphere. *Monthly Weather Review*, 96 (6):351 – 356, 1968. doi: 10.1175/1520-0493(1968)096⟨0351:IOTNBV⟩2.0.CO;2.

R. R. Schaller. Moore's law: past, present and future. *IEEE Spectrum*, 34(6):52–59, 1997. doi: 10.1109/6.591665.

P. Scholz, D. Sidorenko, O. Gurses, S. Danilov, N. Koldunov, Q. Wang, D. Sein, M. Smolentseva, N. Rakowsky, and T. Jung. Assessment of the finite-volume sea ice-ocean model (fesom2.0) – part 1: Description of selected key model elements and comparison to its predecessor version. *Geoscientific Model Development*, 12(11):4875–4899, 2019. doi: 10.5194/gmd-12-4875-2019.

W. C. Skamarock, J. B. Klemp, M. G. Duda, L. D. Fowler, S.-H. Park, and T. D. Ringler. A multiscale nonhydrostatic atmospheric model using centroidal voronoi tesselations and c-grid staggering. *Monthly Weather Review*, 140(9):3090 – 3105, 2012. doi: 10.1175/MWR-D-11-00215.1.

A. Staniforth and J. Thuburn. Horizontal grids for global weather and climate prediction models: a review. *Quarterly Journal of the Royal Meteorological Society*, 138(662):1–26, 2012. doi: 10.1002/qj.958.

M. Steele, R. Morley, and W. Ermold. Phc: A global ocean hydrography with a high-quality arctic ocean. *Journal of Climate*, 14(9):2079 – 2087, 2001. doi: 10.1175/1520-0442(2001)014⟨2079:PAGOHW⟩2.0.CO;2.

H. Stommel. The westward intensification of wind-driven ocean currents. *Eos, Transactions American Geophysical Union*, 29(2):202–206, 1948. doi: 10.1029/TR029i002p00202.

H. Sverdrup. Wind-driven currents in a baroclinic ocean; with application to the equatorial currents of the eastern pacific. *Proc Natl Acad Sci USA*, 33:318–326, 1947. doi: 10.1073/pnas.33.11.318.

J. Thuburn. Numerical wave propagation on the hexagonal c-grid. *Journal of Computational Physics*, 227(11):5836 – 5858, 2008. ISSN 0021-9991. doi: 10.1016/j.jcp.2008.02.010.

J. Thuburn, T. Ringler, W. Skamarock, and J. Klemp. Numerical representation of geostrophic modes on arbitrarily structured c-grids. *Journal of Computational Physics*, 228(22):8321 – 8335, 2009. ISSN 0021-9991. doi: 10.1016/j.jcp.2009.08.006.

J. Thuburn, C. J. Cotter, and T. Dubos. A mimetic, semi-implicit, forward-in-time, finite volume shallow water model: comparison of hexagonal–icosahedral and cubed-sphere grids. *Geoscientific Model Development*, 7(3):909–929, 2014. doi: 10.5194/gmd-7-909-2014.

H. Tomita and M. Satoh. A new dynamical framework of nonhydrostatic global model using the icosahedral grid. *Fluid Dynamics Research*, 34(6):357, jun 2004. doi: 10.1016/j.fluiddyn.2004.03.003.

H. Tomita, M. Tsugawa, M. Satoh, and K. Goto. Shallow water model on a modified icosahedral geodesic grid by using spring dynamics. *Journal of Computational Physics*, 174(2):579–613, 2001. ISSN 0021-9991. doi: 10.1006/jcph.2001.6897.

A. K. Turner, W. H. Lipscomb, E. C. Hunke, D. W. Jacobsen, N. Jeffery, D. Engwirda, T. D. Ringler, and J. D. Wolfe. Mpas-seaice (v1.0.0): sea-ice dynamics on unstructured voronoi meshes. *Geoscientific Model Development*, 15(9):3721–3751, 2022. doi: 10.5194/gmd-15-3721-2022.

G. Veronis. An Analysis of Wind-Driven Ocean Circulation with a Limited Number of Fourier Components. *Journal of Atmospheric Sciences*, 20(6):577–593, Nov. 1963.

L. Wang, Y. Zhang, J. Li, Z. Liu, and Y. Zhou. Understanding the performance of an unstructured-mesh global shallow water model on kinetic energy spectra and nonlinear vorticity dynamics. *Journal of Meteorological Research*, 33(6):1075–1097, 2019. doi: 10.1007/s13351-019-9004-2.

Q. Wang, S. Danilov, and J. Schröter. Finite element ocean circulation model based on triangular prismatic elements, with application in studying the effect of topography representation. *Journal of Geophysical Research: Oceans*, 113(C5), 2008. doi: 10.1029/2007JC004482.

H. Weller, J. Thuburn, and C. J. Cotter. Computational Modes and Grid Imprinting on Five Quasi-Uniform Spherical C Grids. *Monthly Weather Review*, 140(8):2734–2755, 2012. ISSN 0027-0644. doi: 10.1175/MWR-D-11-00193.1.

D. White, A. J. Kimerling, K. Sahr, and L. Song. Comparing area and shape distortion on polyhedral-based recursive partitions of the sphere. *International Journal of Geographical Information Science*, 12(8):805–827, 1998. doi: 10.1080/136588198241518.

D. L. Williamson. Integration of the barotropic vorticity equation on a spherical geodesic grid. *Tellus*, 20(4):642–653, 1968. doi: 10.1111/j.2153-3490.1968.tb00406.x.

D. L. Williamson. The evolution of dynamical cores for global atmospheric models. *J. Meteorol. Soc. Japan*, 85B:241–269, 2007. doi: 10.2151/jmsj.85B.241.

D. L. Williamson, J. B. Drake, J. J. Hack, R. Jakob, and P. N. Swarztrauber. A standard test set for numerical approximations to the shallow water equations in spherical geometry. *Journal of Computational Physics*, 102(1):211 – 224, 1992. ISSN 0021-9991. doi: 10.1016/S0021-9991(05)80016-6.

P. J. Wolfram and O. B. Fringer. Mitigating horizontal divergence "checker-board" oscillations on unstructured triangular c-grids for nonlinear hydrostatic and nonhydrostatic flows. *Ocean Modelling*, 69:64–78, 2013. ISSN 1463-5003. doi: 10.1016/j.ocemod.2013.05.007.

N. Wood, A. Staniforth, A. White, T. Allen, M. Diamantakis, M. Gross, T. Melvin, C. Smith, S. Vosper, M. Zerroukat, and J. Thuburn. An inherently mass-conserving semi-implicit semi-lagrangian discretization of the deep-atmosphere global non-hydrostatic equations. *Quarterly Journal of the Royal Meteorological Society*, 140(682):1505–1520, 2014. doi: 10.1002/qj.2235.

Y. G. Yu, N. Wang, J. Middlecoff, P. S. Peixoto, and M. W. Govett. Comparing numerical accuracy of icosahedral a-grid and c-grid schemes in solving the shallow-water model. *Monthly Weather Review*, 148(10):4009 – 4033, 2020. doi: 10.1175/MWR-D-20-0024.1.

Y. Zhu, B. Qiu, X. Lin, and F. Wang. Interannual eddy kinetic energy modulations in the agulhas return current. *Journal of Geophysical Research: Oceans*, 123(9):6449–6462, 2018. doi: 10.1029/2018JC014333.